

The crystal chemistry of iron oxides and oxyhydroxides at extreme conditions: implications for the deep Earth's oxygen cycle

DISSERTATION

zur Erlangung des akademischen Grades eines
Doktors der Naturwissenschaften (Dr. rer. nat.)
an der Bayreuther Graduiertenschule für Mathematik und
Naturwissenschaften (BayNAT) der Universität Bayreuth

vorgelegt von

Egor Koemets

aus Omsk (Russland)

Bayreuth, 2020

This doctoral thesis was prepared at the Bavarian Research Institute of Experimental Geochemistry and Geophysics (BGI) at the University of Bayreuth from 10/2016 until 03/2020 and was supervised by Prof. Dr. Leonid Dubrovinsky.

This is a full reprint of the thesis submitted to obtain the academic degree of Doctor of Natural Sciences (Dr. rer. nat.) and approved by the Bayreuth Graduate School of Mathematical and Natural Sciences (BayNAT) of the University of Bayreuth

Date of submission: 17.03.2020

Date of defence: 27.04.2020

Acting director: Prof. Dr. Markus Lippitz

Doctoral committee:

Prof. Dr. Leonid Dubrovinsky (reviewer)

Prof. Dr. Daniel Frost (reviewer)

PD Dr. Catherine McCammon (chair)

PD Dr. Gerd Steinle-Neumann

Zusammenfassung

Diese kumulative Arbeit beschreibt eine experimentelle Untersuchung des Verhaltens des Eisen-Sauerstoff-Systems (Fe-O) unter Bedingungen, die für den unteren Erdmantel relevant sind. Das Fe-O-System zeigt unter extremen Bedingungen ein komplexes kristallchemisches Verhalten, welches sich auf die Eigenschaften der Materialien, aus denen das Erdinnere besteht, sowie auf die innerhalb der Erde ablaufenden Redoxprozesse auswirkt. Das Hochdruckverhalten von Eisenoxiden spielt eine entscheidende Rolle für das Verständnis des tiefen Erdinneren, da Eisenoxide die Endglieder von Materialien darstellen, die den Erdmantel aufbauen (FeO für zweiwertiges Eisen (Fe^{2+}) und Fe_2O_3 für dreiwertiges Eisen (Fe^{3+}) im Erdmantel). Die reinen Eisenoxide und -oxyhydroxide sind auch Hauptbestandteile der sogenannten gebänderten Eisenerze und können durch die Subduktion von tektonischen Platten bis in den unteren Erdmantel transportiert werden. Daher sind diese Phasen nicht nur als Modellsysteme von großem Interesse, sondern auch als natürliche Proben, die an der Dynamik der Erde beteiligt sind.

Das Ziel dieser Arbeit ist die Untersuchung des Stabilitätsfeldes von α -FeOOH (Mineral Goethit) unter Subduktions-Bedingungen und die Beschreibung der strukturellen und chemischen Eigenschaften von Hochdruckeisenoxiden, insbesondere FeO_2 , welche durch die Zersetzung von α -FeOOH entstehen. Die verwendete experimentelle Technik ist die *In-situ*-Einkristall-Röntgenbeugung (SC-XRD) in der laserbeheizten Diamantstempelzelle (LH-DAC). Durch die Bestimmung und Verfeinerung der Atompositionen liefert diese Methode Informationen über die Kristallstruktur, Zusammensetzung, chemische Bindung und die elastischen Eigenschaften von Proben bei extremen Drücken und Temperaturen. Zusätzliche Analysetechniken zur Bestimmung der physikalischen Eigenschaften verschiedener Hochdruck-Fe-O-Phasen sind Mößbauer- und Röntgenabsorptionsspektroskopie.

Eine Reihe von Experimenten mit FeOOH wurde bei 40-107 GPa und 1200-2500 K durchgeführt, um die realistischen Bedingungen innerhalb der subduzierten Platten abzudecken, die in den unteren Mantel transportiert werden. Zunächst wurden die methodischen Aspekte bei der Auswahl eines geeigneten druckübertragenden Mediums für Experimente mit FeOOH geklärt. Das oft verwendete Druckübertragungsmedium NaCl reagierte mit FeOOH und kontaminierte daher das Fe-O-System. Durch die chemische Reaktion zwischen NaCl und FeOOH bei 107 (2) GPa und 2000 (200) K wurde eine neue orthorhombische $\text{Na}_2\text{FeCl}_4\text{OH}_x$ Phase gebildet (Raumgruppe # 55, Pbam). Die Bildung einer solchen Verbindung ist selbst in geringen Mengen nachteilig: Ihr Vorhandensein beeinflusst die Chemie des Fe-O-Systems und erschwert die Interpretation spektroskopischer Daten. Daher wurde in nachfolgenden Experimenten mit FeOOH Neon (Ne) als Druckübertragungsmedium verwendet.

Das Stabilitätsfeld von in Ne geladenem α -FeOOH wurde in einer Reihe von Experimenten bei 40-82 GPa und 1200-2500 K untersucht. FeOOH zersetzte sich unter diesen Bedingungen und bildete unter der Freisetzung von Wasser und Sauerstoff eine Vielzahl von reinen Hochdruckeisenoxiden. Unter den Zersetzungsprodukten wurden die bereits bekannten Hochdruck Eisenoxidphasen ι -Fe₂O₃, η -Fe₂O₃ HP-Fe₃O₄, Fe₅O₇, und FeO₂H_x, sowie mehrere neue Phasen beobachtet. Wir haben diese neuen Phasen untersucht, ihre Kristallstrukturen ermittelt und verfeinert: Fe₇O₁₀ (Raumgruppe Cmc₂m) und Fe_{6.32}O₉ (Raumgruppe P6₃/m). Wir haben auch eine detaillierte Studie über ihre strukturellen Veränderungen bei verschiedenen Drücken durch kalte Kompression und Dekompression (Kompressibilität und Eisen-Spin-Zustandsübergänge) durchgeführt. Der Zerfall von FeOOH zeigt die Instabilität dieser Phase bei der Subduktion von Platten bei Bedingungen an, die einer Tiefe von 1000 km entsprechen. Unsere Ergebnisse legen nahe, dass das Rückführen von FeOOH in den Erdmantel zur Freisetzung oxidierender Flüssigkeiten führt, welches eine Änderung des Redoxzustandes bewirkt. Wir nehmen an, dass der Transport dieser Flüssigkeiten (oder des oxidierten Mantelmaterials) zur Erdoberfläche den sporadischen Anstieg des Sauerstoffgehalts vor dem großen Oxidationsereignis erklären könnte, der mit der Bildung großer magmatischer Provinzen in Verbindung gebracht wird. Unsere Hypothese impliziert, dass die Bildung der sauerstoffreichen Erdatmosphäre auf Prozessen in der frühen anaeroben Biosphäre, der Plattentektonik und der Zersetzung von Eisen(III)-oxyhydroxiden im Erdmantel beruht.

Eine detaillierte Untersuchung von FeO₂H_x wurde durchgeführt, über das vor kurzem in der Literatur als Eisenperoxid des „Pyrit-Strukturtyps“ berichtet wurde. Wir synthetisierten auch FeO₂, das isostrukturell mit FeO₂H_x ist, durch direkte Wechselwirkung zwischen Eisen und Sauerstoff, um die Eigenschaften dieses Materials im Hinblick auf die Definition der Oxidationsstufe von Eisen und der FeO Bindungseigenschaften zu erforschen. Dabei wurde festgestellt, dass FeO₂ und FeO₂H_x nicht zum Pyrit-Strukturtyp gehören, sondern stattdessen zum Strukturtyp HP-PdF₂. Mit Hilfe eines multimethodischen Ansatzes, der Mößbauer-Spektroskopie, XANES Spektroskopie und eine erweiterte theoretische Analyse (DFT+DMFT) umfasste, konnten wir überraschende Ergebnisse ermitteln: kubisches FeO₂ und FeO₂H_x enthalten dreiwertiges Eisen (3+) und Sauerstoff weist formal einen Oxidationszustand 1.5- auf. Diese Beobachtung machte eine erneute Überprüfung der Kristallchemie der Hauptphasen des Erdmantels, (Fe,Al)-haltigen Silikat-Perowskit (Bridgmanit) und Post-Perowskit erforderlich, die erhebliche Veränderungen in ihrem Verhalten bei Bedingungen des untersten Erdmantels aufzeigten. Wir beobachteten die Abweichung der Oxidationsstufe von Sauerstoff (2-) in diesen Phasen. Diese Effekte können unser Verständnis der geochemischen und geophysikalischen Prozesse sowohl im unteren Erdmantel als auch auf globaler Ebene verändern.

Summary

This cumulative thesis describes an experimental investigation of the behavior of the iron-oxygen (Fe-O) system at conditions relevant to Earth's lower mantle. The Fe-O system shows complex crystallochemical behavior at extreme conditions that impacts the properties of materials constituting Earth's interior and redox processes operating within the planet. The high-pressure behavior of iron oxides plays a vital role in understanding the deep Earth since iron oxides represent the end-members of materials that constitute Earth's mantle (FeO and Fe₂O₃ for ferrous (Fe²⁺) and ferric (Fe³⁺) states of iron in the mantle, respectively). Also, pure iron oxides and oxyhydroxides contained in banded iron formations can be transported into the lower mantle through the subduction of slabs; therefore, these phases are of great interest not only as model systems but also as natural samples involved in the dynamics of Earth.

The thesis research aims to investigate the stability field of α -FeOOH (mineral goethite) at conditions of subducting slabs and describe the structural and chemical properties of high-pressure iron oxides, particularly FeO₂, resulting from the decomposition of this material. The cornerstone technique used is *in situ* single-crystal X-ray diffraction (SC-XRD) in laser-heated diamond anvil cells (LH-DACs). Through structure solutions and refinements, this method gives the information on the crystal structure, composition, chemical bonding, and elastic properties of samples at extreme pressures and temperatures. Additional analytical techniques applied in determining the physical properties of various high-pressure Fe-O phases are Mössbauer and X-ray absorption spectroscopies.

A series of experiments on FeOOH were performed at 40-107 GPa and 1200-2500 K to cover the likely conditions inside subducting slabs being transported into the lower mantle. Firstly, the methodological aspects of selecting a proper pressure-transmitting medium for experiments with FeOOH were addressed. The popular NaCl pressure-transmitting medium reacted with FeOOH and therefore contaminated the Fe-O system. As a result of chemical reaction between NaCl and FeOOH at 107(2) GPa and 2000(200) K, a novel orthorhombic Na₂FeCl₄OH_x phase was formed (space group #55, Pbam). The formation of such a compound, even in small quantities, is detrimental: its presence affects the chemistry of Fe-O system and complicates the interpretation of spectroscopic data. Therefore, in subsequent experiments on FeOOH, a neon (Ne) pressure-transmitting medium was used.

The stability field of α -FeOOH loaded in Ne was investigated in a series of experiments at 40-82 GPa and 1200-2500 K. FeOOH decomposed at these conditions, forming a variety of pure high-pressure iron oxides with release of water and oxygen. Observed among the decomposition products were the already known high-pressure iron oxide phases ι -Fe₂O₃, η -Fe₂O₃, HP-Fe₃O₄, Fe₅O₇, and FeO₂H_x, as well as several new phases. We studied these novel phases, solved and refined their structures: Fe₇O₁₀ (space group Cmcm) and Fe_{6.32}O₉ (space group P6₃/m). We also made a detailed study on their structural changes at various pressures via cold compression and decompression (compressibility and iron spin state transitions). The decomposition of FeOOH indicates the instability of this phase in subducting slabs at conditions corresponding to 1000 km depth. Our results suggest that the recycling of FeOOH in Earth's mantle leads to a release of oxidizing fluids, causing a change in redox conditions. We hypothesize that the transport of these fluids (or oxidized mantle material) to Earth's surface could explain the sporadic increase of oxygen levels before the Great Oxidation Event, which is linked to the formation of large igneous provinces. Our hypothesis implies that the formation of Earth's oxygen-rich atmosphere resulted from processes in the early anaerobic biosphere, plate tectonics, and decomposition of ferric iron oxyhydroxides in Earth's mantle.

A detailed study of FeO₂H_x was performed, which was recently reported in the literature as a "pyrite-type" iron peroxide. We also synthesized FeO₂ isostructural to FeO₂H_x from direct interaction between iron and oxygen to explore the properties of these materials with a focus on defining the oxidation state of iron and Fe-O bonding features. It was found that FeO₂ and FeO₂H_x do not belong to the pyrite-type structure, but belong instead to HP-PdF₂ type. Using a multimethodological approach that included Mössbauer spectroscopy, XANES spectroscopy, and advanced theoretical analysis (DFT + DMFT), we discovered surprising results: cubic FeO₂ and FeO₂H_x contain ferric (3+) iron and oxygen has the formal oxidation state 1.5-. This observation required a reconsideration of the crystal chemistry of the major Earth's mantle phases, (Fe,Al)-bearing silicate perovskite (bridgmanite) and post-perovskite, that revealed considerable changes in their behavior at conditions of the lowermost mantle. We observed the deviation of the oxidation state of oxygen (2-) in these phases. These effects may change our understanding of geochemical and geophysical processes in both the lower mantle and on a global scale.

Acknowledgments

I would like to thank my supervisors, Prof. Dr. Leonid Dubrovinsky, Prof. Dr. Natalia Dubrovinskaia, Prof. Dr. Eiji Ohtani and Dr. Catherine McCammon for their guidance. I am grateful for the support and inspiration I gained through our discussions and meetings, for the patience and wonderful working environment.

With a lot of synchrotron experiments performed, I acknowledge the support and assistance of local contacts. I am thankful for the help I received from Michael Hanfland, Hanns-Peter Liermann, Konstantin Glazyrin, Vitali Prakapenka, Angelika Rosa, Gaston Garbarino, Volodymyr Svitluk, Alexander Chumakov, Valerio Cerantola. Without them, this work would be hardly possible.

I would like to thank the support staff of BGI, Petra Buchert, Janina Potzel, Lydia Kison-Herzing, Anna Dinius, Nicole Fischer, Stefan Übelhack, Detlef Krausse and Dr. Stefan Keyssner for their help and support in administrative and technical issues.

I'm so grateful to my *senpais*, Elena Bykova, Maxim Bykov, George Aprilis, and Stella Chariton. Thank you so much for all those things that you taught me and for sharing your expertise with me. It was especially valuable in receiving new skills and knowledge for me. Thank you a lot!

Special thanks to comrades-in-arms and friends, Timofey Fedotenko, Saiana Khandarkhaeva, Alexander Kurnosov, Joana Polednia, Sumith Abeykoon, Artem Chanyshev, Giacomo Criniti, Druzhbin Dmitry, Denis Vasiukov, Serena Dominijanni, Catherina Melai, Dominique Laniel, Andy Adams, Johannes Buchen, Dmitry Bondar. Thank you ever so much for the things you helped me, your cheers and the time we spent together.

I am truly grateful to Dr. Florian Heidelberg and Joana Polednia for translating the abstract of this thesis in German.

I would like to express my gratitude to all the members of the International research training group "Deep Earth volatile cycles". Special thanks to people involved in organization of this big international program. It was a great opportunity to learn new things, to do exiting research worldwide and to meet wonderful people.

I am thankful to my wife, Iuliia Koemets. Thank you for being by my side, for your support and optimism, which energized me all these years!

I would like to thank my parents, Tatiana Koemets and Nikolai Shevkunov for encouraging my interest in science from childhood and to this day.

Table of Contents

CHAPTER 1. INTRODUCTION.....	15
1.1. THE EARTH'S FORMATION	15
1.2. MODERN EARTH'S STRUCTURE: THE ROLE OF THE FE-O SYSTEM.....	16
1.3. IRON OXIDES AND SUBDUCTION OF BIFS.....	20
1.4. COMPLEX HIGH PRESSURE CRYSTALLOCHEMISTRY OF THE FE-O SYSTEM	21
1.5. FeOOH AND FeO ₂ H _x AT DEEP EARTH CONDITIONS	25
CHAPTER 2. EXPERIMENTAL METHODS	31
2.1. GENERATING EXTREME PRESSURES AND TEMPERATURES USING DIAMOND ANVIL CELLS (DAC)	31
2.1.1. <i>Basic principles of DAC and variations of design</i>	31
2.1.2. <i>Pressure-transmitting media</i>	33
2.1.3. <i>Cryogenic loading of pressure-transmitting media</i>	35
2.1.4. <i>Pressure determination</i>	36
2.1.5. <i>Heating in DACs</i>	37
2.2. IN SITU XRD IN LASER-HEATED DIAMOND ANVIL CELLS.....	40
2.2.1. <i>Basics of the X-ray diffraction technique</i>	40
2.2.2. <i>Phase problem and structure solution</i>	42
2.2.3. <i>Methodology for XRD experiments in DAC: features and limitations</i>	44
2.2.4. <i>Before the experiment</i>	45
2.2.5. <i>DAC alignment on goniometer</i>	45
2.2.6. <i>Step-scans and wide-scans</i>	47
2.2.7. <i>X-ray contrast maps</i>	48
2.2.8. <i>Step-scans during laser heating</i>	49
2.2.9. <i>Single-crystal XRD data processing</i>	51
2.3. MÖSSBAUER SPECTROSCOPY	56
2.4. X-RAY ABSORPTION SPECTROSCOPY	61
CHAPTER 3. SYNOPSIS	64
3.1. SUMMARY AND LINKAGE OF RESEARCH STUDIES	64
3.1.1. <i>Summary of Chapter 4: Interaction between FeOOH and NaCl at extreme conditions: synthesis of novel Na₂FeCl₄OH_x compound</i>	65
3.1.2. <i>Summary of Chapter 5: Role of FeOOH in oxygen recycling in early Earth's history</i>	66
3.1.3. <i>Summary of Chapter 6: Variation of oxygen oxidation state at the base of the Earth's mantle</i> 71	

3.1.4.	<i>Summary of Chapter 7: Diamond anvils with a round table (DART-anvils) designed for high-pressure experiments in DAC</i>	76
3.2.	BRIEF OUTLOOK AND PERSPECTIVES	78
3.3.	LIST OF MANUSCRIPTS AND STATEMENT OF AUTHORS' CONTRIBUTION	79
CHAPTER 4.	INTERACTION BETWEEN FEOOH AND NA₂FECL₄OH_x COMPOUND	81
4.1.	ABSTRACT	81
4.2.	INTRODUCTION.....	81
4.3.	MATERIALS AND METHODS	82
4.4.	RESULTS.....	83
4.5.	DISCUSSION	88
4.6.	CONCLUSIONS	91
4.7.	SUPPLEMENTARY MATERIALS.....	92
CHAPTER 5.	ROLE OF FEOOH IN OXYGEN RECYCLING IN EARLY EARTH'S HISTORY	94
5.1.	ABSTRACT	94
5.2.	INTRODUCTION.....	94
5.3.	EXPERIMENTAL RESULTS	96
5.4.	DISCUSSION	100
5.5.	METHODS	105
5.5.1.	<i>Sample preparation and DAC assembly</i>	105
5.5.2.	<i>X-ray diffraction</i>	105
5.5.3.	<i>Data analysis</i>	106
5.6.	SUPPLEMENTARY INFORMATION	107
5.6.1.	<i>Compressibility of novel Fe₇O₁₀ and Fe_{6.32}O₉</i>	109
5.6.2.	<i>Crystallochemical discussion on novel Fe₇O₁₀ iron oxide</i>	111
5.6.3.	<i>Crystallochemical discussion on novel Fe₇O₁₀ iron oxide</i>	112
5.6.4.	<i>Computational details</i>	112
CHAPTER 6.	VARIATION OF OXYGEN OXIDATION STATE AT THE BASE OF THE EARTH'S MANTLE	116
6.1.	ABSTRACT	116
6.2.	INTRODUCTION.....	116
6.3.	RESULTS.....	117
6.4.	DISCUSSION	124
6.5.	ACKNOWLEDGMENTS	127

6.6.	EXPERIMENTAL.....	127
6.6.1.	<i>Materials</i>	127
6.6.2.	<i>DAC preparations</i>	128
6.6.3.	<i>Data acquisition</i>	128
6.6.4.	<i>Structure solution and refinement</i>	129
6.6.5.	<i>Computational details</i>	130
6.6.6.	<i>Evolution of the crystal structure parameters with pressure</i>	131
6.7.	SUPPLEMENTARY INFORMATION	131
6.7.1.	<i>Pyrite vs HP-PdF₂-type structures</i>	131
6.7.2.	<i>Electronic structure of FeO₂</i>	132
6.7.3.	<i>Electronic structure of Fe(Si_{0.75}Fe_{0.25})O₃</i>	133
6.7.4.	<i>Electronic structure of MgO₂</i>	133
6.7.5.	<i>Composition of Fe-bearing silicate post-perovskite at conditions of the Earth's lower mantle.</i> 134	
6.7.6.	<i>Figures and Tables</i>	136
CHAPTER 7. DIAMOND ANVILS WITH A ROUND TABLE (DART-ANVILS) DESIGNED FOR HIGH-PRESSURE		
EXPERIMENTS IN DAC 154		
7.1.	ABSTRACT	154
7.2.	INTRODUCTION.....	155
7.3.	DIAMOND ANVIL WITH A ROUND TABLE (DART-ANVIL)	157
7.4.	EXAMPLES OF APPLICATIONS OF DART-ANVILS	160
7.4.1.	<i>Performance of DART-anvils on compression at ambient temperature</i>	161
7.4.2.	<i>Single-crystal XRD data collection during laser heating at IDD-13 at GSECARS (APS, USA)</i>	162
7.4.3.	<i>Single-crystal XRD data collection during laser heating at Extreme Conditions Beam Line (ECB P02.2) at PETRA III (DESY, Germany)</i>	165
7.5.	CONCLUSIONS.....	167
7.6.	ACKNOWLEDGMENTS	168
CHAPTER 8. BIBLIOGRAPHY 171		

Chapter 1. Introduction

1.1. The Earth's formation

The understanding of the Earth's structure and evolution relies on the multi-disciplinary scientific fields. For example, geophysical, geochemical and cosmochemical observations, studies of natural samples brought to the surface from greater depths, propagation of seismic waves passing through the planet and laboratory experiments at extreme pressures and temperatures all give insights into the processes that take place within our planet, past and present.

The Earth was formed through the accretion from a solar nebula as it condensed, evaporated and fractionated (1, 2). The initial bulk composition of the early Earth was set up very similar to the average of the solar system (Figure 1.1-1) (3). The exceptions are the volatile elements and compounds (such as hydrogen, helium, neon, nitrogen, light hydrocarbons, etc.) major part of which was possibly outflowed by the activity of solar wind (4, 5). The heat produced by accretion caused Earth's early matter to reach temperatures high enough to melt heavy siderophile elements (1). This has led to the segregation of a primitive mantle and metallic core in the Earth's interior, while the outer layer of the planet cooled forming a thin solid crust; which, in turn, resulted in the formation of a layered structure of the Earth. After the collision with a large planetoid body (~4.5 Ga), the portion of Earth's material was ejected into space forming the Moon; this event changed the Earth's composition (6). Volcanic activity and mantle outgassing produced the primordial atmosphere, while small, outer solar bodies brought water to Earth during the heavy bombardment, which produced oceans (7–9). The onset of plate tectonics between 3.2 Ga and 2.5 Ga caused significant changes in the Earth's structure (10). As an example, the movement of continental plates led to an exchange of matter and energy between the mantle and the Earth's surface, through the subduction of slabs and volcanic activity at the plates boundaries (10, 11).

Over time, the Earth has developed and continues to change. As the most abundant elements, both iron and oxygen have played vital roles in Earth's evolution. The next chapters are dedicated to the structure of modern Earth, and the importance of the Fe-O system for the understanding of processes operating in the Earth's interior.

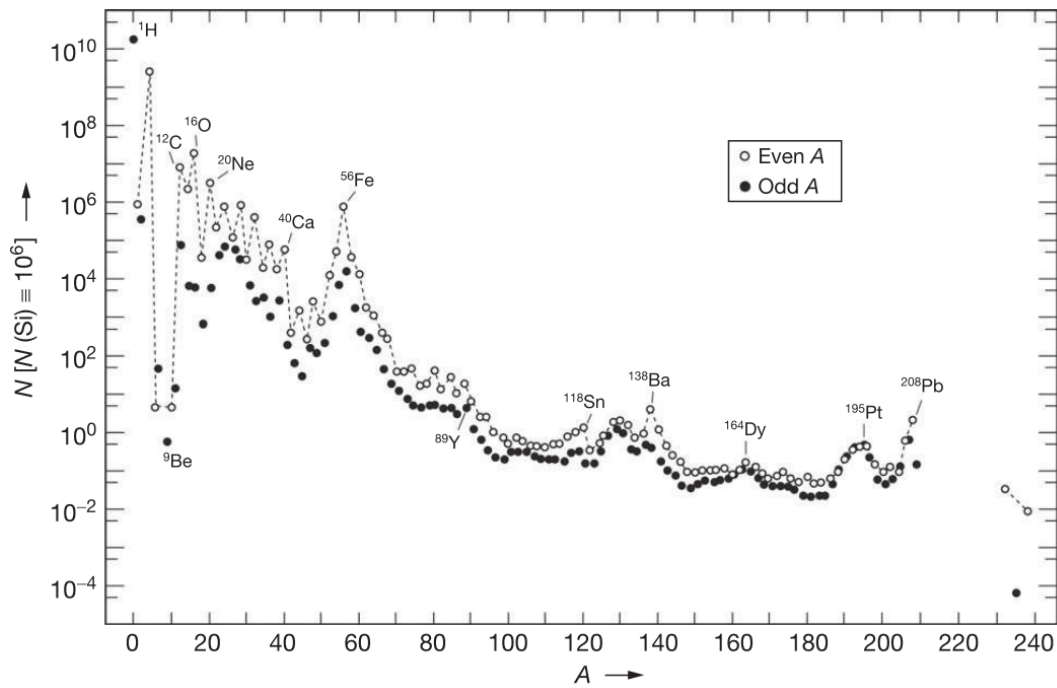


Figure 1.1-1 The abundance of chemical elements in the solar system by mass number (A) (3). Atoms with even masses are more abundant than those with odd masses (Oddo–Harkins rule).

1.2. Modern Earth's structure: the role of the Fe-O system

The bulk elemental composition of modern Earth is (by mass): iron (Fe, 32.1%), oxygen (O, 30.1%), silicon (Si, 15.1%), magnesium (Mg, 13.9%), sulfur (S, 2.9%), nickel (Ni, 1.8%), calcium (Ca, 1.5%), aluminum (Al, 1.4%) and other elements (1.2%) (12, 13). The distribution of these elements within the Earth's interior is not homogeneous. Seismological data suggests that modern Earth still has several distinct layers with different densities and elastic properties: lithosphere (crust), asthenosphere and upper mantle, transition zone, lower mantle, and the

outer and inner core (Figure 1.2-1) (14, 15). As the first-order approximation, those regions differ by the chemical and phase compositions.

The mantle, divided into the upper mantle, transition zone, and the lower mantle, is mostly composed of silicate minerals (13, 15). The upper mantle is dominantly peridotite, made of the minerals olivine ($\text{Mg}^{2+}, \text{Fe}^{2+}$) $_2\text{SiO}_4$, pyroxenes (monoclinic and orthorhombic), and an aluminous phase (16). The latter transforms with increasing depth: at the uppermost part it is plagioclase, followed by spinel, and then the garnet. The transition zone, which divides the upper and lower mantle, starts from 440 km depth. The minerals constituting that region are wadsleyite and ringwoodite, which originate through the isochemical transformation of olivine, at corresponding pressures and temperatures. The transition zone continues down to around 660 km, where the lower mantle region starts. At this depth, ringwoodite decomposes into silicate perovskite (mineral bridgmanite, with a general formula $(\text{Mg,Fe})(\text{Si,Al})\text{O}_3$), and iron-magnesium oxide ferropericlase, $(\text{Mg,Fe})\text{O}$ (16, 17). Bridgmanite is considered the main constituent (~75%) of the Earth's lower mantle, whereas the ferropericlase makes up a fraction (~20%); with the remainder being minor amounts of calcium perovskite and, in some models, stishovite (1). At the lowermost part of the mantle (D'' layer), the high-pressure modification of bridgmanite with a CaIrO_3 -type structure is dominant ("post-perovskite" phase, PPv) (18). This layer has a thickness of approximately 200 km and borders the core at a depth of about 2900 km. The Earth's core is divided into two parts: a liquid outer, and a solid inner. The outer core is a liquid layer about 2,260 kilometers thick, composed predominantly of Fe, with minor amounts of Ni and light elements. Convection of metal in the outer core gives rise to Earth's magnetic field (19). The inner solid core is expected to have almost the same composition as the outer core with the difference is that it is solidified due to the extreme pressures. The transition between the inner solid core and outer liquid core occurs at approximately 5,000 km beneath the Earth's surface.

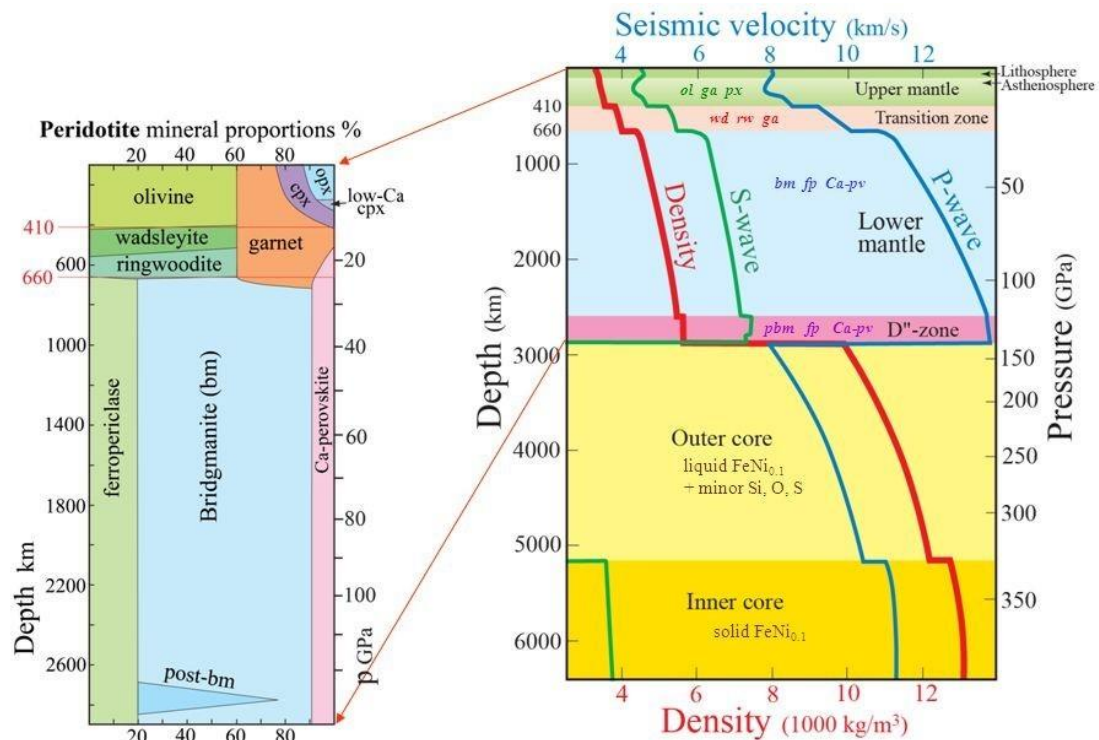


Figure 1.2-1 The structure of the Earth and mineral composition of the Earth's mantle. The data is from (14), the illustration is modified after (20). The right part of the illustration represents the Earth's layers, density, and seismic velocities. The left part represents the mineral proportions in the mantle, depending on depth.

As described above, all of the Earth's layers contain significant amounts of iron and oxygen. The distribution and interaction of these elements define the physical and chemical properties of the materials that constitute Earth and affect the dynamics and evolution of the planet. Iron is heaviest among prevalent elements in Earth's mantle and transition zone, so variations of its concentration in the mantle materials significantly affect their sound velocities. Changes in the spin states of iron influence the density (for example, the spin transitions of iron in ferropericlase and bridgmanite over a range of depths from 1000 to 2200 km), and therefore, rheology, and thermal conductivity of mantle minerals (21–28). Among all of the geochemically abundant elements in the Earth's interior, only iron is considered to have the variable oxidation state (Fe^0 - metallic, Fe^{2+} - ferrous or Fe^{3+} - ferric). Therefore, Fe influences the chemistry of the mantle through the control of oxygen fugacity $f(\text{O}_2)$. It acts to buffer the chemical potential of oxygen, establishing the $f(\text{O}_2)$ of the entire system (29) which exerts an impact on fundamental

geochemical processes. The oxygen fugacity influences the mantle convection and affects the onset of partial melting. The stabilities of carbonates and OH-bearing phases are also linked to $f(\text{O}_2)$ (30, 31).

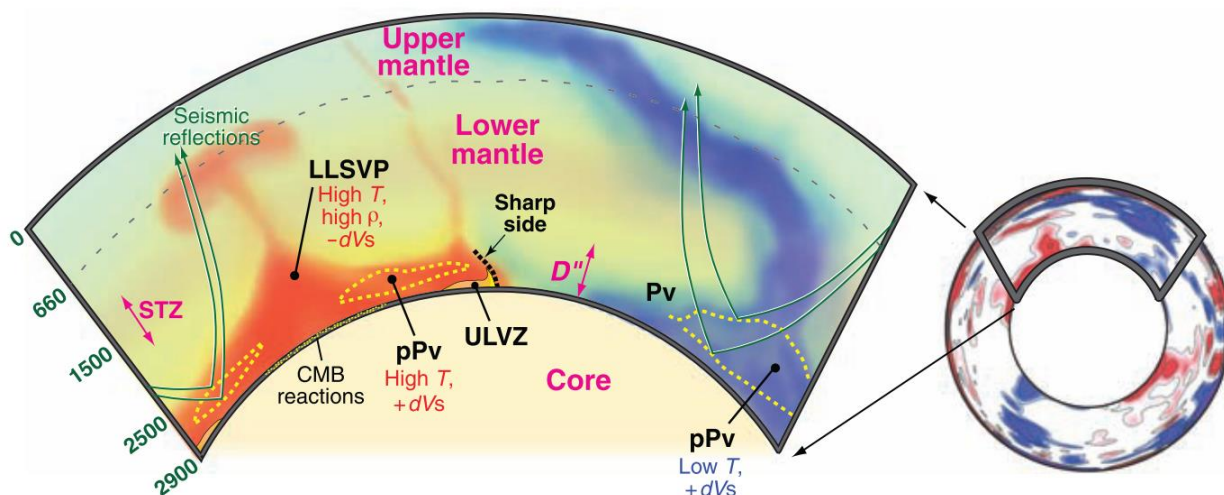


Figure 1.2-2. Schematic representation of tomography-derived seismic anomalies (equatorial cross-section, right) and enlarged illustration depicting features of D'' region (left). A large low-shear-velocity province (LLSVP) existing beneath the Pacific Ocean and Africa has a high density and temperature with sharp-sides velocities contrast relative to the surrounding mantle. The reflectors observed beneath the subduction and overlapping with LLSVP is consistent with the perovskite to post-perovskite phase transition (marked with dashed yellow lines) locally raising the shear velocities. Ultralow-velocity zone (ULVZ, yellow) is located on the core-mantle boundary possibly relating to chemical reactions between the mantle and core. The spin transition zone (STZ) centered near 1500 km depth represents a change in the iron spin state and may also affect lower-mantle densities and velocities (44, 45). The illustration is from (32).

The deep Earth's interior contains regions which are possessing density and sound velocity anomalies such as large low-shear velocity provinces and ultra-low velocity zones (LLSVP and ULVZ, Figure 1.2-2) (18, 33, 34). Despite the lack of data on their exact composition, it is expected that both iron and oxygen involved in altering properties of minerals in these regions. For example, the compositional models explained the elevated density of LLSVP by enrichment of iron because of its higher mass (35, 36). It was also proposed that the spin state of iron in the ferropericlase could affect the morphology of LLSVP influencing the surrounding mantle

convection (37, 38). The ULVZ, in turn, are located right on the top of the core-mantle boundary and also expected to contain the anomalous amount of both iron and oxygen (37, 39–41).

The investigation of the Fe-O system behavior at extreme conditions is crucial for understanding of Earth's interior and especially for the redox processes operating within the planet. Obviously, the properties of iron oxides play a vital role in guiding those processes. Pure iron oxides represent the end-members of the materials that constitute the Earth's mantle: FeO and Fe₂O₃ have long been considered as the main end-members of the ferrous (Fe²⁺) and ferric (Fe³⁺) states of iron in the mantle, respectively (42). In addition, pure iron oxides and oxyhydroxides participate in the subduction processes; therefore, they are of great interest not only as model systems but also as real samples involved in the dynamics of the Earth.

1.3. Iron oxides and subduction of BIFs

“If gold rusts, what then can iron do?” — wrote Geoffrey Chaucer, an English poet in the XIV century. Without delving into the depths of this metaphor and answering the question directly – to rust too.

At ambient conditions, iron oxidizes readily in the presence of oxygen. Three different iron oxides are known to exist since a long time ago: Fe₂O₃ (particularly mineral hematite), Fe₃O₄ (oldest known magnetic material, magnetite), and FeO (wüstite) (43). Those are phases that have vast technological uses including semiconductors, pigments, catalysts, biomedical applications and iron extraction (44, 45). Approximately 60% of global iron reserves are accounted for in the sedimentary rocks consisting of repeated layers of iron oxides and iron-poor shales with cherts called Banded Iron Formations



Figure 1.3-1 A 2.5-Gyr-old banded iron formation from Hamersley, Australia. The grey bands predominantly contain the iron oxide hematite and the brown bands are rich in siliceous chert. The picture is modified after (48).

(BIFs, Figure 1.3-1) (46). Vast volumes of BIFs were deposited ca. 2.6 Ga to the Great Oxygenation Event (GOE) with some evidence for possible earlier formation (~3.7Ga) (47). As was mentioned in the previous section, the BIFs and iron oxides, accordingly, are involved in the subduction as part of the ocean floor which started to recycle into the Earth's interior with an onset of plate tectonics (48).

It was argued, that the melting point for iron oxides would be above the geotherm in the entire mantle and therefore they should remain solid in slabs and could reach the depths of the CMB (49, 50). Dobson and Brodholt (49) proposed that ULVZ are composed out of the deep BIF assemblage, primarily iron oxides. This hypothesis, introduced in 2005, was based on the assumption that mineralogy and chemical composition of iron oxides at ambient and extreme conditions would remain similar. However, later findings demonstrate that the chemical behavior of the iron-oxygen system is drastically different at the extreme pressures and temperatures (51–55).

1.4. Complex high pressure crystallochemistry of the Fe-O system

Mineral physics and chemistry directly concern on *how exactly* materials behave while exposed to extreme conditions. This question applies to the many aspects of matter's properties but one of the most important would be the information about the crystal structure, composition/chemical bonding, and elastic properties. For the conditions of a lower mantle, *in situ* high pressure – high temperature (HP-HT) studies of minerals and Earth-related compounds in the diamond anvil cells (DACs) can address such questions.

Extreme pressures and temperatures can cause chemical, structural, electronic and magnetic changes in a matter. Material exposed to the HP-HT can undergo phase transitions and to exhibit unexpected chemical behavior. The iron oxides are not an exception and their behavior is one of a vibrant example of the complexity of chemistry and physics at extreme conditions. First, the iron oxides known to exist at ambient conditions could transform into high-pressure polymorphs through the isochemical phase transitions. As an example, FeO at ambient conditions has NaCl-

type structure which converts into the NiAs-type structure at ~ 70 GPa and 1000 K (51); magnetite Fe_3O_4 adopts the CaTi_2O_4 -type structure (space group Bbmm) after laser heating between 1000 K and 1200 K and 41 GPa (52). By far, the largest number of known HP polymorphs belongs to the hematite: the detailed study by Bykova et al. (53) reports at least 4 various HP Fe_2O_3 types which could exist in the pressure range up to 115 GPa as it was revealed by the means of *in-situ* single-crystal XRD in a DACs (see Figure 1.4-1). Generally speaking, the crystal structure defines the physical properties of crystalline matter (54). The HP polymorphs of Fe_2O_3 exhibit, for example, different magnetic properties: the antiferromagnetic orthorhombic α - Fe_2O_3 becomes paramagnetic at the elevated temperatures (~ 1000 K), Rh_2O_3 -type ι - Fe_2O_3 and η - Fe_2O_3 possesses the transition from magnetic to paramagnetic at ~ 900 K and 700 K correspondingly, while ζ - Fe_2O_3 is reported to be paramagnetic at temperatures > 500 K (55). Possibly existing in the subduction zones, the magnetic properties of hematite and its HP polymorphs are proposed to impact the Earth's geomagnetic field and cause its heterogeneities in the West Pacific region (55).

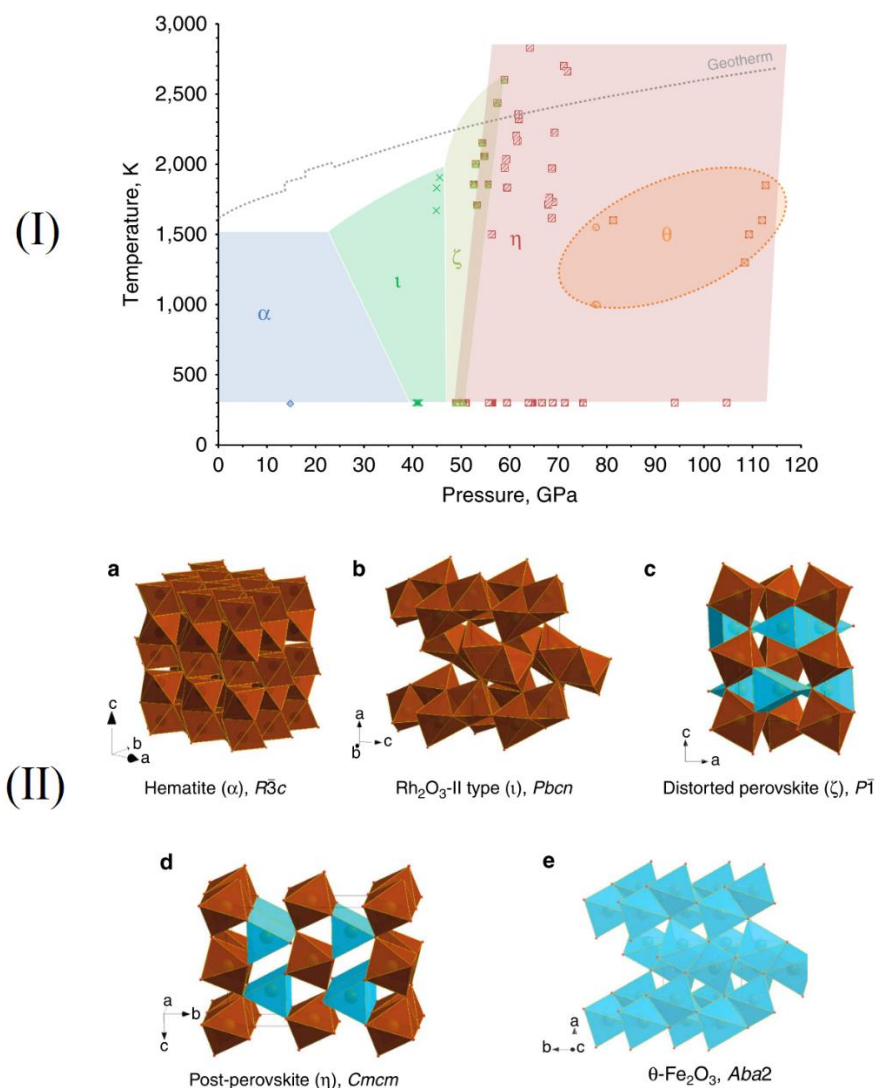


Figure 1.4-1 Phase diagram of Fe_2O_3 HP polymorphs (I) and their crystal structures (II). The coordination polyhedra of Fe are represented as brown and blue octahedrons. Hematite (II-a) structure is composed of FeO_6 octahedra connected in a corundum-like motif; each octahedron connects with three neighbors via edges, and layers are interconnected through common triangular faces of octahedra. The l - Fe_2O_3 structure (II-b): each two FeO_6 octahedra are connected through a common triangular face; such units are packed in a herringbone pattern with a shift along the c -direction having common edges. In distorted perovskite ζ - Fe_2O_3 (II-c) octahedra connect through common vertices and prisms share only common edges. Post-perovskite η - Fe_2O_3 has a structure where prisms are connected through common triangular faces, while octahedra connect only via shared edges. θ - Fe_2O_3 (II-e) adopts the packing motif from l - Fe_2O_3 but is composed of FeO_6 prisms instead of octahedra. The illustration is modified after (53).

Additional complexity of iron oxides' crystal chemistry is caused by the great variety of stoichiometries possible at extreme conditions. Several new mixed-valence iron oxides (containing both ferric and ferrous iron) were synthesized and exist at the wide P-T range possessing unusual crystal structures and stoichiometries. For example, orthorhombic phases Fe_4O_5 and Fe_5O_6 (56–58), monoclinic Fe_5O_7 (53) and Fe_7O_9 (59), hexagonal $\text{Fe}_{25}\text{O}_{32}$ (53). The stoichiometry of these new iron oxides can be expressed as $n\text{Fe}_2\text{O}_3 \cdot m\text{FeO}$ (where n and m are integers), where their crystal structures change by addition of FeO_6 octahedral blocks into a “basic” post-perovskite Fe_2O_3 type of structure (Figure 1.4-2) (53, 59–61).

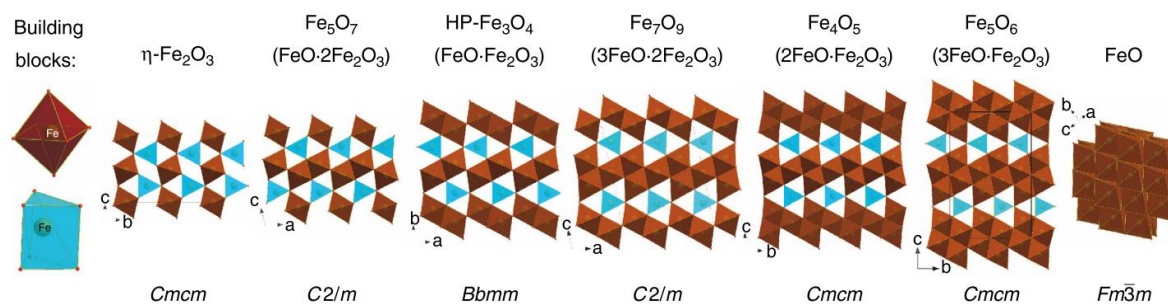


Figure 1.4-2 Crystal structures of high-pressure iron oxide phases synthesized at HP-HT conditions described by the common formula $n\text{FeO} \cdot m\text{Fe}_2\text{O}_3$. The structures are assembled from two building blocks, FeO_6 octahedra and trigonal prisms (monocapped or bicapped, not shown for simplicity). Those polyhedra are represented in brown and blue colors, correspondingly. These polyhedra form parallel columns of face-shared prisms and edge-shared octahedra arranged in different motifs represented by structures viewed from the top of the columns. Increasing Fe^{2+} content favors octahedral packing over mixed octahedral and prismatic packing. This requires denser packing of FeO_6 octahedra and, as a result, columns of octahedra condense in slabs by sharing common edges. In particular, $\eta\text{-Fe}_2\text{O}_3$ has ordinary columns of prisms and octahedra with a chessboard-like arrangement; Fe_5O_7 has ordinary and doubled columns of octahedra; $\text{HP-Fe}_3\text{O}_4$ possesses only doubled columns; Fe_7O_9 has doubled columns and tripled columns organized in zigzag slabs; Fe_4O_5 possesses only tripled and Fe_5O_6 only quadruple zigzag slabs. The endmember of the homologous series wüstite (FeO) consists of octahedra with a maximum of 12 edge-shared neighbors. The illustration is modified after (53)

An exotic species of iron oxides as synthesized in laboratory HP-HT conditions could also exist in the Earth's interior. Reports on superdeep diamonds suggest that some phases observed within their inclusions (magnesiowüstite and Fe^{3+} -rich phases) could be relicts of high-pressure

iron oxides such as Fe_4O_5 and Fe_5O_6 (62), formed together with carrying diamonds. Additionally, it has also been demonstrated that Fe_4O_5 and Fe_7O_9 form solid solutions with Mg, with end-members such as $\text{Mg}_2\text{Fe}_2\text{O}_5$ and $\text{Mg}_3\text{Fe}_4\text{O}_9$, which affirms the possible existence of complicated Mg-Fe oxides in the deep mantle (60, 63, 64).

1.5. FeOOH and FeO_2H_x at deep Earth conditions

Another iron-bearing chemical compound potentially important for the understanding of the history of our planet is iron oxyhydroxide, FeOOH . Mineral goethite, $\alpha\text{-FeOOH}$, is a major component among oxidized iron species, called “rust”, formed as a product of metabolism of anoxygenic prokaryotes ~ 3.8 Ga (65, 66). Along with hematite, maghemite ($\gamma\text{-Fe}_2\text{O}_3$) and lepidocrocite ($\gamma\text{-FeOOH}$), $\alpha\text{-FeOOH}$ constitutes the majority of crystalline ferric oxides and oxyhydroxides at Earth’s surface. Goethite is abundant in soils, banded iron formations, iron ores, and hydrothermal deposits (67). Related to the pure iron oxides, iron hydrous oxide and its high-pressure polymorphs are of great interest to the experimental geoscience community. Recent studies suggest that, similarly to hematite, FeOOH present in BIFs could be transported to the Earth’s deep interior with subducting slabs (68–70). Hu et al. (69) and Nishi et al. (71) reported that FeOOH remains stable until it reaches the lowermost part of the lower mantle. By means of *in situ* powder X-ray diffraction it was revealed that at pressures corresponding to depths of $\sim 1500\text{--}1800$ km and at moderately high temperatures, FeOOH undergoes a phase transition to form the stable pyrite-type phase FeO_2H_x with $0 \leq x \leq 1$ (“Py-phase”, see Figure 1.5-1) (69, 72). Goethite and its high-pressure polymorphs have therefore been considered to be candidates for water and/or hydrogen transfer to the lower mantle and the core-mantle boundary (68, 69, 72).

Generally, water-bearing species affect properties of mantle minerals and cause large-scale global phenomena such as arc volcanism and plate tectonics (73–75). The partial dehydrogenation of FeOOH during its transformation into the Py-phase could lead to hydrogen saturation in subducting materials and upward migration of hydrogen (water) (42, 69, 71, 72, 76, 77). The release of water could influence chemical and physical properties of mantle minerals,

change the redox conditions of the lower mantle, melting temperatures of silicates, affect sound velocities and viscosity of mantle minerals and enhance the rate of phase transformations (73–75, 78–84). Cubic FeO_2H_x phase could be also synthesized by the reaction between water and iron as shown in (39, 85, 86). That implies that FeO_2H_x could be formed at the CMB by at least two different mechanisms: through the phase transition of FeOOH and through the chemical interaction between the water brought to the CMB by various hydrous phases. While FeOOH was intensively studied at the conditions of the upper mantle and core-mantle boundary, there is a lack of data on its behavior at the conditions in between. The investigation of phase stability of FeOOH in this region, possible changes in its structure and crystal chemistry are crucial for understanding if that material could contribute to the origin of ULVZ. The existence of possible decomposition products is also important for the understanding of the fundamental HP chemistry of the Fe-O system. These are key points describing our motivations behind the results presented in Chapter 5.

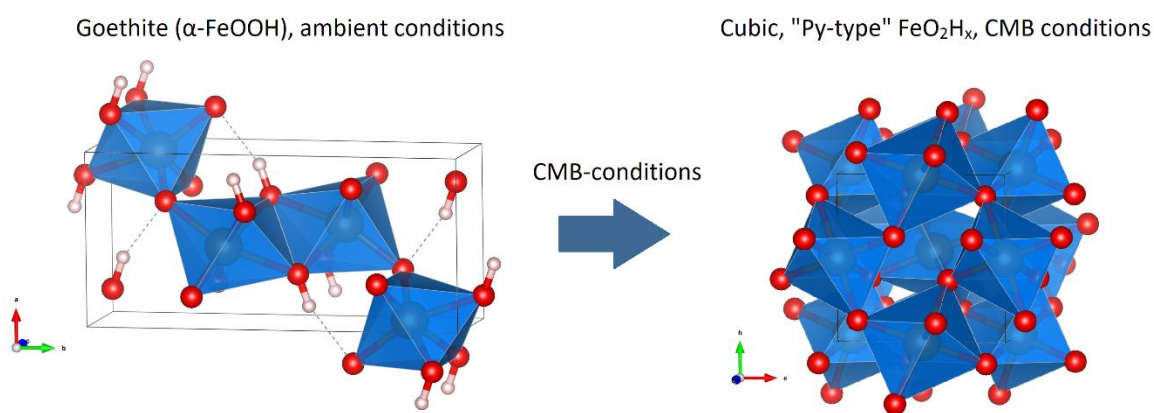


Figure 1.5-1 The crystal structures of goethite (left) and cubic high-pressure FeO_2H_x phase. The white, red and blue spheres represent the hydrogen, oxygen and iron atoms. In the case of FeO_2H_x , the hydrogen is not denoted for simplicity. The coordination polyhedra of Fe atoms are represented in blue color.

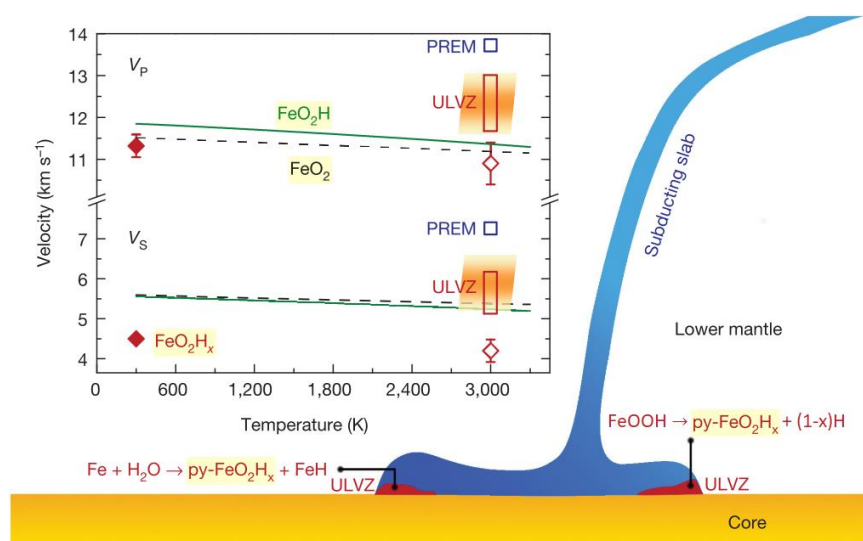


Figure 1.5-2. The possible formation of ULVZ through the synthesis of the FeO₂H_x phase at the CMB. Two possible routes are suggested: interaction of iron from the core with water brought by subducting slabs and decomposition of FeOOH in subducted BIFs. The inset shows the sound velocities of FeO₂H_x at high pressure and high temperature. The solid and dashed curves are the theoretical calculations for FeO₂H and FeO₂ at 130 GPa. Filled diamonds show FeO₂H_x at 133 GP from NRIXS experiments; open diamonds show FeO₂H_x extrapolated to 3,000 K and CMB pressures. Shaded areas show the extrapolated V_P and V_S of FeO₂H_x-bearing domains for a mixture of 40%–50% FeO₂H_x with the ambient mantle based on PREM (blue squares); the red rectangles indicate the reduction in V_P (5%–15%) and V_S (15%–30%) observed in ULVZs. The illustration is modified after (87)

Despite the obvious importance for water transfer and explanation of ULVZ genesis, the chemical nature of FeO₂ and FeO₂H_x phases has yet to be clarified. Initially, the hydrogen-free FeO₂ was obtained by reaction of Fe₂O₃ and O₂ above ~78 GPa in laser-heated diamond anvil cell (DAC). Its cubic symmetry and space group (Pa3-) was established by multigrain analysis and crystal structure was refined from powder diffraction data (69, 69). The structural model and DFT calculations suggested that material belongs to the peroxides, in which iron is ferrous, Fe²⁺O₂²⁻ (69). However, the interpretation of the oxidation state of iron could be complicated because the refinement of atomic coordinates from powder XRD data cannot provide enough accuracy. Additionally, for peroxides (in molecular or crystalline forms), distances between closest oxygen atoms at ambient pressure are very characteristic – from about 1.2 to 1.5 Å (88), and with

compression, these distances are not expected to increase. Reported shortest O-O contact in pyrite-type FeO_2 is $\sim 1.9 \text{ \AA}$ (69). This is too much large value for peroxides, but too short for cubic dioxides with a high-pressure PdF_2 -type structure (HP- PdF_2). For the later, the shortest O-O distance is $\sim 2.5 \text{ \AA}$ at ambient conditions and they are characterized by low compressibility (89, 90).

Different possible forms of the compound – from dioxide (no direct chemical bonds between O^{2-} oxygen atoms) to peroxide (covalent bonds between oxygen atoms forming O_2^{2-} anions) were assigned by (91–93). In some cases, FeO_2 was interpreted to exist ‘in-between’ the dioxides and peroxides with the unusual formal oxidation state of oxygen: FeO_2^{3-} . Thus, one could expect that FeO_2 also form dioxide, not peroxide. The problem of oxidation state of iron in FeO_2 is closely linked to the conditions at which this compound could be formed, particularly if excess of oxygen is necessary to oxidize iron above Fe^{3+} , or compound contains only Fe^{2+} and competitive to other oxides with ferrous iron (53, 57, 58, 94). The X-ray Absorption Spectroscopy (XAS) (77, 95), and synchrotron Mössbauer scattering (SMSc) (77) were used to argue that iron is ferrous in FeO_2H_x , even at strongly oxidizing conditions. However, the results of XAS and SMSc are internally inconstant – while XAS data were interpreted as proof for Fe^{2+} (77, 95), the SMSc of cubic FeO_2 (77) shows unrealistic central shift for any ferrous oxides ($\sim 0.15 \text{ mm/s}$ at 80 GPa). Additionally, the formation of a complex phase content in the sample (due to the interactions between the pressure-transmitting medium and the sample, temperature gradients, etc.) could also lead to the misinterpretation of spectroscopic data. For example, some of the reported studies on FeOOH and FeO_2H_x were performed in a KCl pressure-transmitting medium. That motivated us to study possible chemical interaction(s) between the iron oxyhydroxides and alkali metal halides at HP-HT conditions (see Chapter 4).

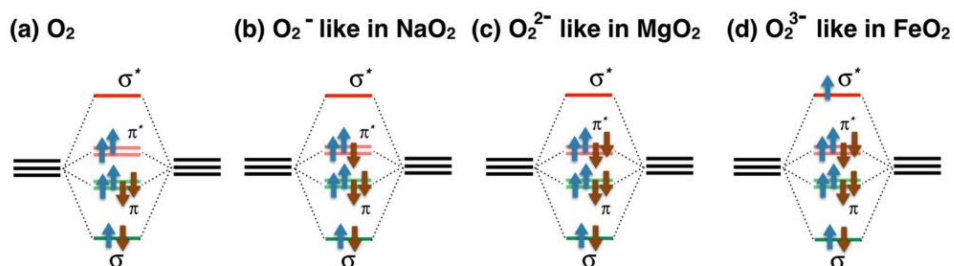


Figure 1.5-3 Occupation of oxygen 2p orbitals in different compounds with O_2 dimers and possible electronic configuration in FeO_2 proposed by (91) The system gains (loses) energy by occupation of green bonding (red antibonding) bonds.

It is of great importance to clarify the oxidation state of oxygen in FeO_2 and to understand if it could deviate from -2 and whether this effect could be pronounced in the other Fe-O interactions at HP, particularly in mantle minerals. This question is addressed in the study presented in Chapter 6.

Existing information on the HP crystallochemistry of iron oxides underline incompleteness of our understanding of chemically simple and at the same time very complex binary system. There is a fundamental interest to explore its behavior at high pressures and temperatures utilizing high-resolution structural studies performed *in situ*. This could allow getting insights into the fundamental chemistry, deep Earth processes and global volatile cycles. In the present thesis, we address this by employing a combination of advanced *in situ* single-crystal XRD technique performed in laser-heated diamond anvil cells coupled with Mössbauer spectroscopy and X-ray absorption spectroscopy.

The laser-heated diamond anvil cells technique coupled with X-ray diffraction is one of the most powerful techniques to describe the samples' properties. However, the data collection of *single-crystal* XRD dataset from a DAC *during* the laser heating of a sample is an extremely difficult task requiring solutions of many engineering problems (for example, placing the whole laser-heating setup on the goniometer which rotates both DAC and optics simultaneously; for more details please see Section 2.2). At present, the only synchrotron beamline equipped with such a system (96) is P02.2 at DESY. Within the framework of Ph.D. studies, we have developed a special type of diamond anvils,

DART (diamond anvils with a round table) which aims to overcome the technological limitations and allows to perform *in situ* single-crystal XRD data collection at HP-HT conditions at beamlines equipped with ordinary, non-rotating laser-heating setup. This is the main motivation for the work presented in Chapter 7.

Chapter 2. Experimental Methods

2.1. Generating extreme pressures and temperatures using diamond anvil cells (DAC)

2.1.1. Basic principles of DAC and variations of design

Established in the 1950s, the DAC technique became one of the most successful approaches for the generation of high-pressure high-temperature conditions. It also provides the opportunity for *in situ* studies and analysis of the matter at extreme conditions. A wide range of methods could be applied to the sample, for example, X-ray diffraction; optical, X-ray and γ -ray spectroscopies, as well as methods based on the photon's inelastic scattering. The range of static pressure generation with a DAC extends to 1 TPa (97), which is high above the estimated pressures of the Earth's inner core (~360 GPa). A detailed description and historical overview of a diamond anvil cell development and principal designs, as well as its major application fields, can be found in the publication of Bassett (98).

The fundament of the DAC is a pair of diamonds with polished tips (anvils) which are driven against each other, compressing a sample that is located in a sample chamber between the anvils. Thin metal plate (Re or steel), named 'gasket', with an indentation cavity and small hole in its center, is placed between the two opposing diamond anvils; this assemblage forms a sealed pressure chamber. The anvils are fixed on hard-material seats (tungsten carbide, for example) and placed inside a metallic cell, which could be driven mechanically (Figure 2.1-1). The compression of two diamonds transfers the load onto the sample which is located in a sample chamber (Figure 2.1-2).

A great variety of different DACs' designs exists. There are both commercial (by Diacell, Almax easyLab, Syntek) and academic research solutions available (Merrill-Basset 3-pin DAC (99), BX90 and BX90mini (100), Mao-Bell-type DAC (101), Le Toullec type DAC (102), ETH-type DAC (103)). The majority of studies presented in a thesis, we performed in a BX90 type DACs, which were

designed and machined in Bayerisches Geoinstitut (BGI) (100). This DAC provides an easy alignment, a stable pressurization, and maintains the pressure constant for a long time. For several synchrotron experiments at the European Synchrotron Facility (ESRF), we used a membrane driven Le Toullec type DAC (102).

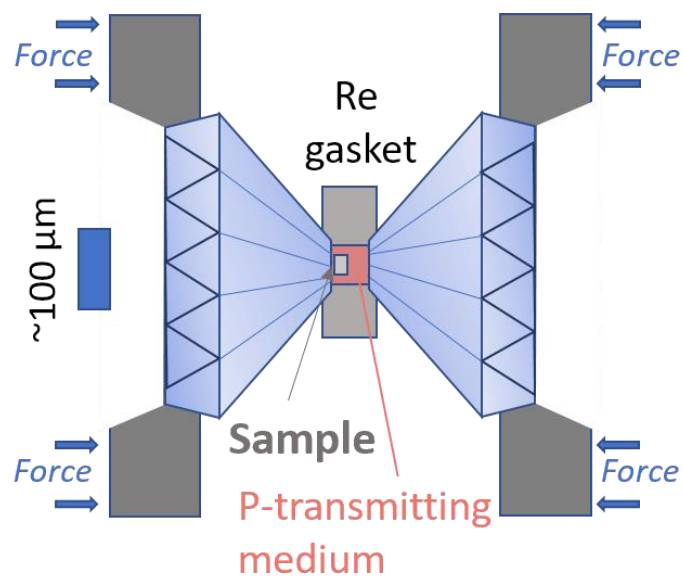


Figure 2.1-1. The principal scheme of extreme pressure generation using a Diamond Anvil Cell. The sample and pressure-transmitting medium are sealed within the small hole in the pre-indented metal gasket. The application of force to the diamond anvils leads to the dramatic increase of pressure between the anvils due to the tiny area of their tips (cullets).

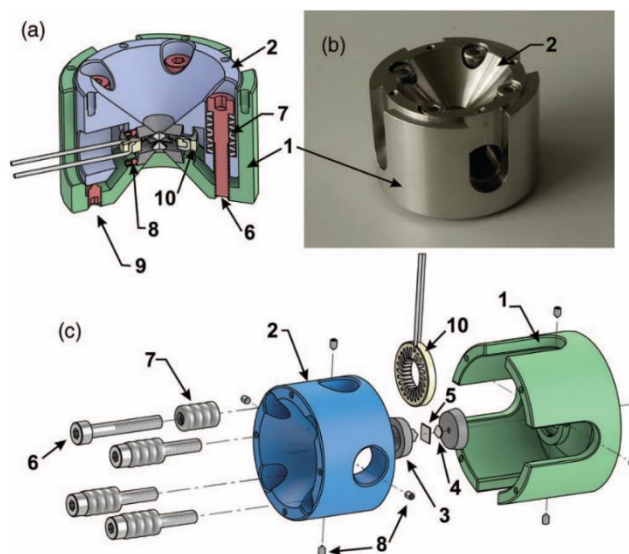


Figure 2.1-2 BX-90 diamond anvil cell design. a – Section view, b – photograph of a loaded cell, c – exploded-view scheme. 1 – Outer cylinder part, 2 – inner piston part, 3 – diamond supporting plates, 4 – diamond anvils, 5 – metallic gasket, 6 – M4 screws for generating loading force, 7 – pack of conical spring washers (Belleville springs), 8 – setscrews for diamond anvils alignment, 9 – safety setscrews, 10 – optional miniature resistive heater. Illustration is modified after (100).

2.1.2. Pressure-transmitting media

Pressure transmitting (P-transmitting) medium serves as an environment transferring the load of the diamond anvils' tips (culets) to the entire surface of a sample. A sample compressed without medium would be squeezed along one direction and, in case of a single-crystal, could be destroyed. Also, the principal construction of the DAC assumes a uniaxial compression and the pressure medium helps to make it isotropic (often referred to as hydrostatic). Uniaxial stress would cause shear strains in the sample which could be undesirable, depending on the scientific task. For example, in the case of XRD experiments, this could cause the broadening of the diffraction reflections. However, the real hydrostaticity at conditions above 15 GPa and ambient temperature is not possible due to the lack of known compounds possessing liquid state at such conditions. Some noble gases loaded into the pressure chamber shows the best approximation to the hydrostatic behavior; due to their properties, they create a quasi-hydrostatic environment upon a pressure-induced solidification to at least 150 GPa (104).

In most cases, the P-transmitting medium should also be chemically inert against the sample. However, depending on the scientific task, it can also be used as a substance to react with a sample. The part of the work in the present thesis was performed using a Ne pressure medium for experiments on the FeOOH samples. Another part of the studies was performed on the ^{57}Fe loaded in the solid oxygen, which served both pressure-transmitting medium and a reactant.

The Ne was loaded into the sample chamber using an HP-vessel gas loading system developed and installed in Bayerisches Geoinstitut (105). The system operates as follows: a DAC is placed inside the vessel and then the desired gas is pumped inside up to 1.5 kbar pressure; next, the DAC is being closed by the piston-driving mechanism trapping the dense gas inside the sample chamber. Afterward, the pressure inside the vessel is released to the atmosphere, while the mechanical load is keeping the DAC closed. Next, the operator tightens the DAC's screws, releases the system's mechanical load and removes the DAC from the pressure vessel.

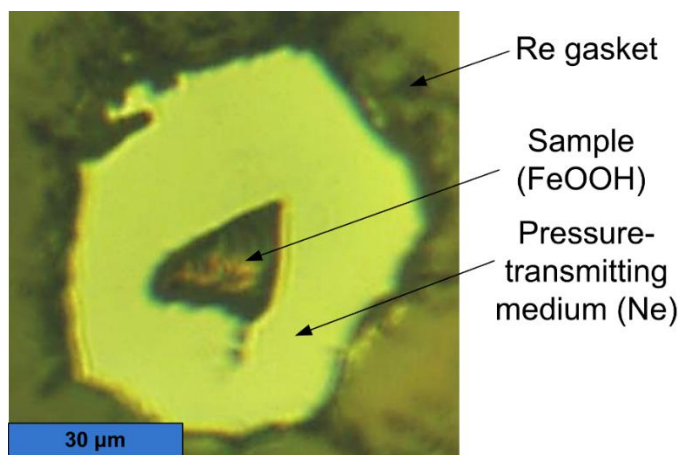


Figure 2.1-3. A microphotograph of a DAC's sample chamber after loading taken through the diamond anvils. The FeOOH sample is located (with lateral sizes $\sim 25 \mu\text{m}$) in the center, surrounded by a transparent Ne pressure-transmitting medium with Re gasket around. The pressure inside a sample chamber is $\sim 45 \text{ GPa}$.

2.1.3. Cryogenic loading of pressure-transmitting media

Another approach to load a DAC with a pressure-transmitting media is a usage of liquefaction of substances at low temperatures, which was used in the present thesis for loading oxygen into the sample chamber. The schematic representation of a cryogenic DAC loading system used is provided in Figure 2.1-4. The prepared DAC (with a rhenium gasket and a sample) is placed into the sealed loading chamber. After the flushing of the chamber's atmosphere, the desired substance (e.g. oxygen) is pumped through. Then the loading chamber is cooled down in a cryogenic bath, for example, liquid nitrogen. After cooling to the liquefaction temperature, the pressure medium is liquefied. At this stage, DAC should be closed so the pressure medium is trapped inside the sample chamber, between diamonds. During the cooling process, it is important to keep the pressure inside the loading chamber higher than the atmospheric to avoid nitrogen coming inward. The usage of such a system allows loading of possibly dangerous P-transmitting medium (for example, flammable gases) safely.

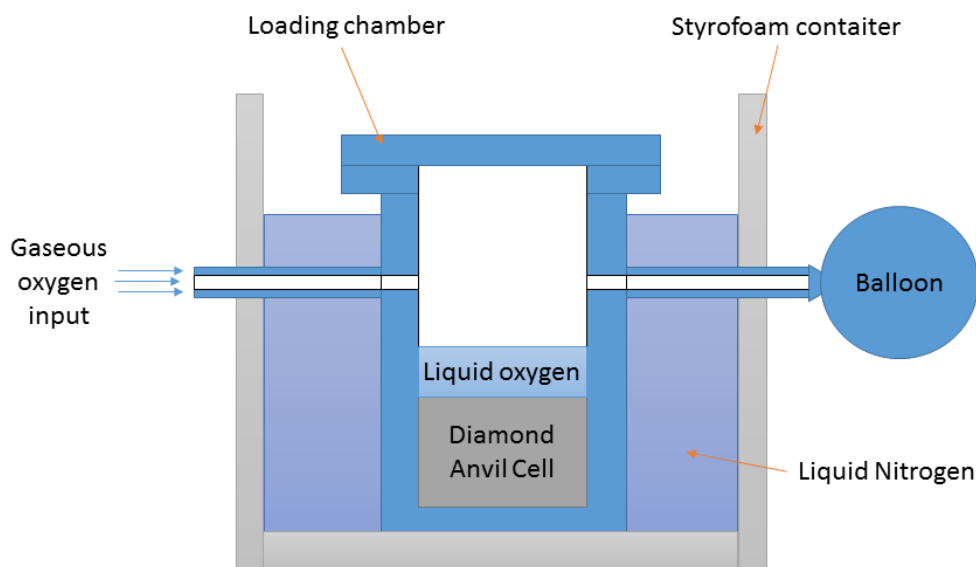


Figure 2.1-4. The schematic representation of a cryogenic DAC loading setup used in a process of loading oxygen as a pressure-transmitting medium/reactant.

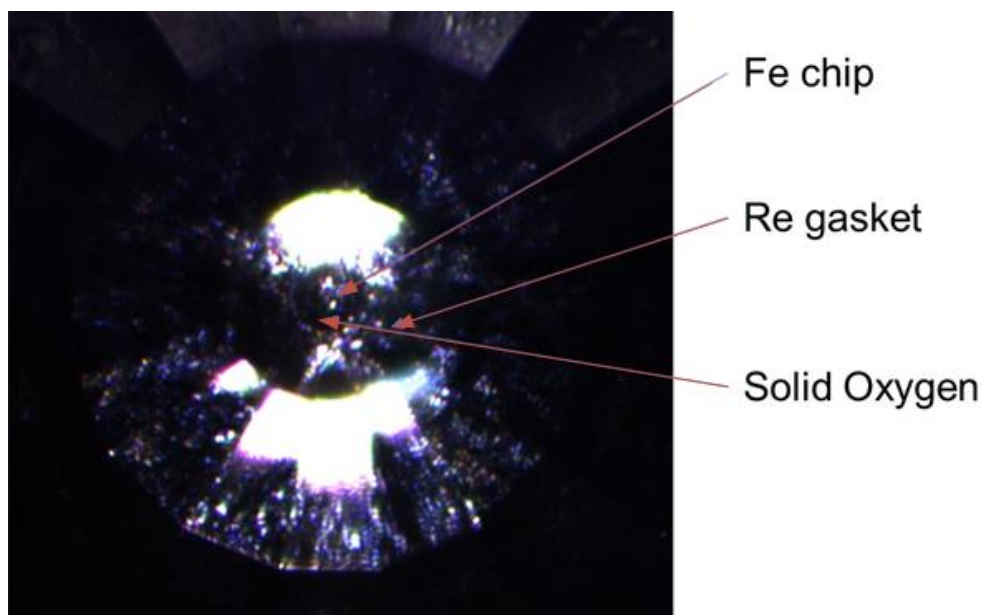


Figure 2.1-5. An example of a DAC's sample chamber after cryogenic loading with oxygen at 65 GPa. A microphotograph is taken through the diamond anvil.

2.1.4. Pressure determination

For the experiments performed in DACs, the proper pressure determination inside the sample chamber is required. Several approaches were developed which can be used separately or simultaneously depending on the design of a particular experiment:

1. **Laser-induced fluorescence.** The pressure standards (such as Cr-doped Al_2O_3 or $\text{Y}_3\text{Al}_5\text{O}_{12}$) are loaded into the sample chamber together with a sample. Measuring R1 spectral line of Ruby or Y1 line in Sm-doped garnet, one can obtain information of pressure conditions by analyzing the shift of these lines (106–108)
2. **Diamond anvil's Raman shift.** Determination of pressure using Raman spectroscopy of diamond anvils. The high-frequency edge of the Raman band is correlated with the normal stress at the anvils' culet face. The calibration of the diamond Raman edge frequency against the equation of state (EOS) of Pt up to 250 GPa allows to use it for pressure determination (109).

3. **EOS of standard material.** The standard material is loaded into the sample chamber along with a sample. Measuring the unit cell volume (V) with XRD one can compare it to the values reported in literature. The most widely used materials serving as an EOS standard are metals (Au, Pt, Mo) or simple binary compounds (MgO, NaCl, KCl, KBr) (110–113). These compounds usually remain inert and demonstrate relatively high compressibility. Some pressure transmitting media, such as Ne or Ar (after the solidification) and NaCl are widely used as the standards (111).

In the present thesis, the combination of pressure determination methodologies listed above was used. While spectroscopic approach was used typically for preliminary pressure estimations (during an increase or increase of the pressure in the DAC, for example), XRD data and EOS of Ne or Fe were used for the precise pressure determination during the cold-compression studies as well as laser-heating experiments.

2.1.5. Heating in DACs

For the studies on the Earth-related materials, the generation of high temperatures in the sample compressed to extreme pressures is required to recreate the conditions of the planet's interior. Generally, two widespread techniques are used in a DAC experiment to increase the temperature of the sample: external electrical resistive heating and heating with focused laser radiation.

In the first case, the small metal coil and thermocouple(s) are placed around the diamond anvils and the sample chamber. The supply of electrical current through the coil warms it up while the thermocouple's feedback is controlling the stability of the desired temperature. The resistive heating provides precise temperature determination and allows minimizing thermal gradients within the sample. Unfortunately, the practical temperature limit accessible with heating coils is around 1100K. At such "close-to-the-limit" temperatures diamond anvils start to degrade and, therefore, pressure stability in a sample chamber decreases drastically.

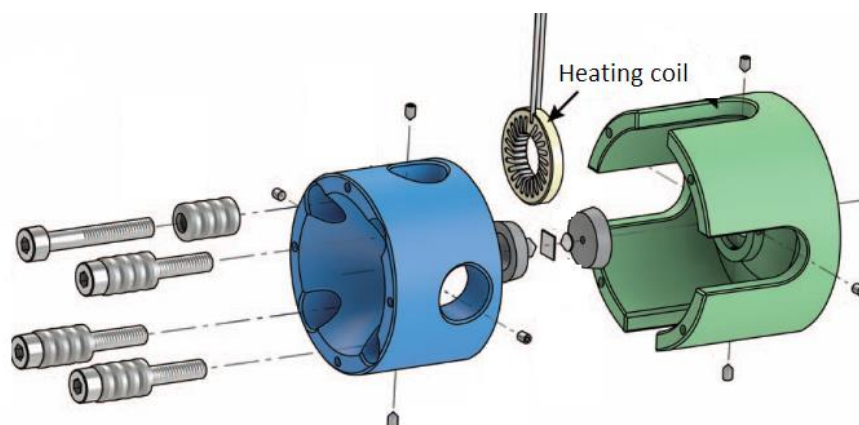


Figure 2.1-6. A principal scheme of a BX-90 type DAC with a heating coil to be placed around the diamond anvils. The illustration is modified after (100).

The laser-heating of a sample in a DAC, in turn, can be applied for the generation of temperatures high above 1100 K allowing to cover the temperatures of the Earth's core and reach even higher values. The heating of a sample with a lasers is carried out by focusing the radiation to the small spot on a sample, which absorbs infrared or near-infrared radiation. Despite its apparent simplicity, such a method requires building complex optical systems. Additionally, the method does not provide the precise temperature determination (temperatures are usually measured spectrometrically using the grey-body approximation, which practically leads to at least ~ 100 K uncertainty). Moreover, it generates large thermal gradients within the sample especially in the case of one side heating. To decrease the latter problem, a double-sided laser heating is used often.

Generalizing the laser-heating setups' designs, it is possible to divide them into 2 different groups depending on the type of optical elements used: reflective and refractive (114). Both of them have advantages and disadvantages. The refractive optics is usually easier to align and the quality of the observed image is high, but the material of lenses introduces the chromatic aberrations to the thermal radiation spectra so the precision of temperature determination decreases. The reflective systems, in turn, introduce much less chromatic aberrations but they are usually more complicated in operation and alignment. A detailed comparison of these

approaches could be found in the work of Giampaoli et al. (115), while explicit description of laser-heating system designs is reported in (114, 116–119).

In the present thesis, most of the in-house laser heating was performed on the refractive systems developed in BGI (Figure 2.1-7) which are described in (118, 119).

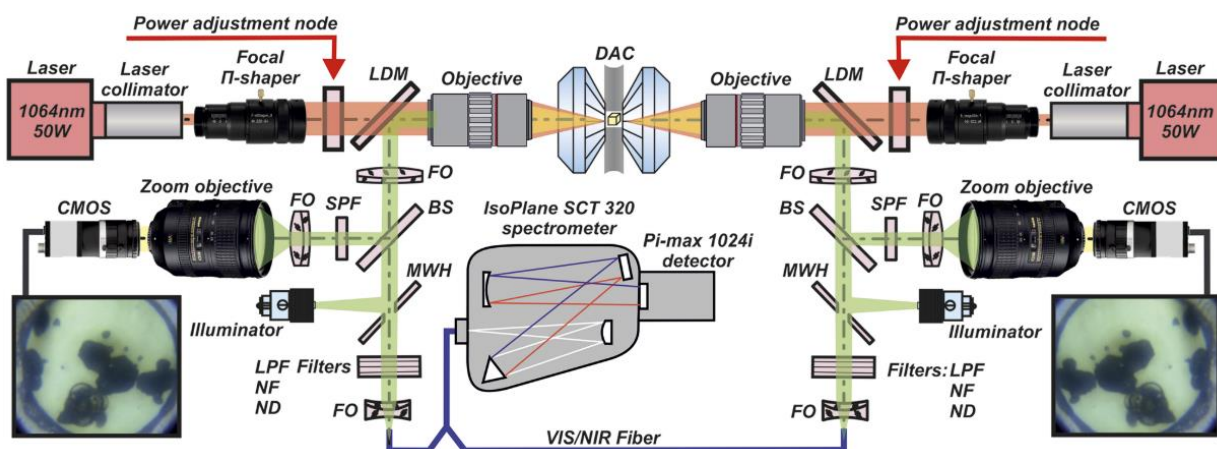


Figure 2.1-7. A principal scheme of a refractive double-sided laser-heating setup for diamond anvil cells used in the present thesis. LDMs are the long-pass dichroic mirrors; FOs are the focusing optics; BSs are 50/50 beam splitters; SPFs are the short-pass filters with a cutoff at 800 nm; CMOS are the cameras for optical observation; MWHs are the mirrors with a hole; LPFs are the long-pass filters with a cut-on wavelength of 550 nm; NFs are the notch filters for 1064 nm, and NDs are neutral density filters. The illustration is modified after (118)

2.2. In situ XRD in laser-heated diamond anvil cells

2.2.1. Basics of the X-ray diffraction technique

Established at the beginning of an XX century, the X-ray diffraction technique has acted as the cornerstone of twentieth-century science (120). Being a powerful non-destructive method for analysis of a solid matter, it allows to obtain information on the crystal structure of a sample and to perform the phase analysis (121). Still, it is being actively developed and the application areas have expanded dramatically over time. The development of powerful X-ray sources, sensitive detectors, and the possibility to perform *in situ* experiments with different sample environments (furnaces, chemical reactors, DACs, etc. (122–124)) significantly expanded the investigation opportunities, while the base of the technique remains the same: the diffraction phenomenon.

The diffraction is a result of the interaction of electromagnetic waves with scattering objects when they ordered with characteristic repeating features comparable to the wavelength of electromagnetic radiation. In the case of crystalline material, the scattering objects would be electrons of atoms that are ordered in a 3-dimensional periodic structure with interatomic distances comparable to the wavelength of X-rays.

The diffraction conditions for the crystalline materials are described according to the Bragg's law (or Wulff-Bragg's condition):

$$2d \sin \theta = n\lambda \quad \text{Eq. (1)}$$

where d – is a distance between family of hkl crystallographic planes, θ – the incident angle of X-rays with the wavelength λ , n denotes the reflection order (integer number). If we consider the lattice planes acting as mirrors for the incident X-ray beams, the latter would reflect from specific hkl planes distance between which is a d . This would cause a phase difference due to the different path length of reflected X-rays. The interference maxima then appears where the phase

difference is equal to the integer number of wavelengths. The illustration of this simplified model for a diffraction phenomenon is presented in Figure 2.2-1.

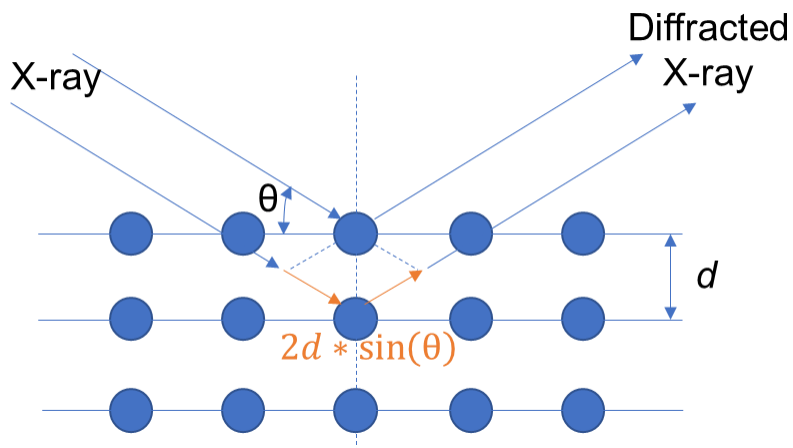


Figure 2.2-1 Schematic illustration of a simplified model for Bragg's law (Eq. (1)). Blue circles represent the atoms, while blue and orange arrows represent the travel path of X-ray radiation. Coherent waves reflecting from the family of hkl planes and interfere with each other. The interference maxima are appearing when the phase difference is equal to the integer number of wavelengths.

Thereby, the crystalline matter causes an incident X-rays to diffract into specific directions defined by the structure. By measuring the angles and intensities of diffracted radiation, it is possible to solve the inverse problem: to establish the three-dimensional distribution of electrons within the crystal. Through the value of electron density obtained, the determination of the atomic positions within a crystal is possible, and, the length of chemical bonds between them, information on the crystallographic disorder and other valuable properties.

Traditionally, the XRD technique is divided into two approaches: powder and single-crystal XRD. Powder X-ray diffraction, trivially, is based on working with powders (numerous fine grains) of crystalline material. Possessing random orientations, a portion of crystallites fulfilling the Bragg's law will be present in a sample, producing a diffraction signal as Debye-Scherrer rings. Defining the d-spacings of the sample's diffraction peaks allows using this set of values as a fingerprint for the phase identification and definition of unit cell parameters. Unfortunately, this approach meets difficulties when the new phases and structures are present in the sample (the

direct structure solution is almost impossible due to the loss of data on the reciprocal vectors). The single-crystal XRD is a more complicated technique to operate. The single-crystal XRD patterns consist of a number of diffraction spots at a certain distance between each other. Since the Bragg conditions for a given d-spacings and a wavelength would be met only at the defined theta angles, the crystal should be irradiated with a different orientation relative to the incident X-ray beam so all the reflections could be measured. The main advantage of SC-XRD over the powder XRD is the possibility to obtain the information on the atoms' distribution within the unit cell (crystal structure) since it is carried in the intensities of Bragg reflections.

2.2.2. Phase problem and structure solution

The diffracted X-rays carry not only the information on the reciprocal vectors but also information on the electronic density within the unit cell of a sample. The collected experimental squared amplitudes F_{hkl}^2 are related to the intensities by the following formula:

$$F_{hkl}^2 = \frac{I_{hkl}}{k \cdot Lp \cdot A} \quad \text{Eq. (2)}$$

where k is a scale factor, Lp is Lorentz-polarization correction, A is a transmission factor; those are related as special corrections.

The X-rays diffracted from crystal lattice planes are described by the following expression for the structure factor:

$$\mathbf{F}_{hkl} = F_{hkl} \exp(i\alpha_{hkl}) = \sum_j f_j \exp \left[-B_j \left(\frac{\sin\theta}{\lambda} \right)^2 \right] \exp[2\pi i(hx_j + ky_j + lz_j)] \quad \text{Eq. (3)}$$

where the summing is made for the atoms within the unit cell; x_j, y_j, z_j are the coordinates of the j^{th} atom; f_j is the scattering factor of the j^{th} atom; α_{hkl} is the phase of the diffracted beam;

B_j is a B -factor directly related to the mean square isotropic displacement of the j^{th} atom; θ is the scattering angle and λ is the X-ray wavelength.

The electron density (ρ_{xyz}) then could be derived by applying the inverse Fourier transform resulting in the following equation:

$$\rho_{xyz} = \frac{1}{V} \sum_{hkl} F_{hkl} \exp[-2\pi i(hx + ky + lz)] \quad \text{Eq. (4)}$$

where V is a unit cell volume.

Thus, it is possible to determine the electronic density and, therefore, position all the atoms within the unit cell. Based on a set of experimental structural amplitudes, F_{hkl}^2 , the structure solution process could be described as a calculation of atomic coordinates within the unit cell and their thermal parameters (isotropic or anisotropic displacement parameters). Unfortunately, the experimental values of F_{hkl}^2 are real numbers, while F_{hkl} required for calculation of electronic density is a complex function. Therefore, direct determination of F_{hkl} phase is impossible (the exponential multiplier, referred to as “phase”, $\exp[-2\pi i(hx + ky + lz)]$ in Eq. (3)). This barrier for direct obtaining of electron density is called a “phase problem”. However, this issue is possible to overcome and the phase problem could be solved with automated phasing procedures such as the Patterson syntheses, direct methods, heavy-atom methods, charge flipping algorithms, dual-space methods and others that are implemented in various software (125, 126). After applying one of these methods, the electronic density is established; and the starting structural model is built. Next, the structural model is being refined against the experimental dataset by variation of adjustable parameters (for example, atomic coordinates, their occupancies, atomic displacement parameters) with a least-squares minimization. Firstly, the missing atoms are found from the comparison of model and experimental electron density maps; their position and occupancies are refined as well as anisotropic displacement parameters.

The agreement between the model and experimental data is defined by R -factors, which represent the quality of the refined structural model:

$$R_1 = \frac{\sum |F_{obs}| - |F_{calc}|}{\sum |F_{obs}|} \quad \text{Eq. (5)}$$

$$wR_2 = \left[\frac{\sum w |F_{obs}^2 - F_{calc}^2|}{\sum w F_{obs}^2} \right]^{1/2} \quad \text{Eq. (6)}$$

where F_{obs} –the observed structure factor amplitude, F_{calc} – the calculated structure factor amplitude based on the model; and w –weighting factor derived for each measured reflection based on its standard uncertainty.

2.2.3. Methodology for XRD experiments in DAC: features and limitations

Compared to a routine XRD experiment at ambient conditions, the application of this technique for LH-DACs is more complex. First, the sample environment gives an additional XRD signal: the solidified pressure-transmitting media, a pair of diamond anvils and a gasket material contaminate the signal from a sample. Second, the metallic body of a DAC shadows more than 60% of the Bragg reflections, worsening the statistics on the collected data. The third issue is the size of a sample: for the DAC experiments at pressures higher than 40 GPa, the sample size is usually about 10-20 μm . This, of course, imposes strong requirements for the goniometer's and sample stage's motors precision and reproducibility of movement for aligning the sample to the X-ray beam. On synchrotrons, for example, the X-ray beam could be focused down to the spot with a diameter of several micrometers so even the small deviation of a sample from the axis of rotation of goniometer could result in bad quality data collection. The last, but not least, is a sample's content inside the DAC after laser-heating procedure: decomposition of a sample and chemical reactions could cause the appearance of dozens of small (even sub-micron sized) crystallites of different phases. Each of these crystallites would act as a single-crystal and give

their own set of spotty Bragg's reflections. Thus, the sample in LH-DACS is usually in-between the powder XRD and single-crystal XRD approaches (some groups refer to that state of a sample as "multigrain" or "polycrystalline"). Of course, the list of limitations and difficulties is longer, but the problems listed above are the most crucial. The brief description of some strategies of overcoming difficulties in a synchrotron-based XRD experiment with LH-DACs is described in the next subsections.

2.2.4. Before the experiment

After a victory in the proposal competition and arrival to the synchrotron facility, the experimental hardware should be prepared prior to any data collection. After the alignment of the X-ray optics and maintenance of the goniometer, performed by beamline stuff, the calibration of the experimental setup is made. The information on the X-ray wavelength, sample-detector distance, pixel size and tilt/yaw angles of detector, the x-y coordinates of a primary beam is obtained, which is crucial for further correct data processing. This information is usually extracted from the XRD signal obtained from a powder XRD signal of standard materials (such as CeO_2 , LaB_6 or other suitable well-studied substances) with further refinement of these parameters from an SC-XRD dataset. The latter is usually collected on high-quality crystals of phases with large unit cell parameters (which helps to collect a large number of Bragg reflections). Additionally, the SC-XRD standards should have chemical/temporal sustainability (not to degrade over time; for example, enstatite, MgSiO_3 satisfies all the requirements). After calibration is done, the experiments with the desired samples could be started.

2.2.5. DAC alignment on goniometer

Both sizes of sample and the X-ray spot are of an order of a few micrometers, therefore a high precision alignment procedure based on the absorption of X-rays is performed. Placed in a holder, DAC is positioned on the goniometer's sample stage, which can move the DAC in a submillimeter ranges in y and z directions while the intensity of the X-ray beam passing through the DAC is recorded by a Si-diode (Figure 2.2-2). The resulted absorption curve has usually a

characteristic profile that is related to the different X-ray absorption by different DAC's parts: tungsten carbide seats, a bulk gasket, indented gasket, sample chamber and the sample itself. If the sample has a high absorption coefficient, it is possible to directly find its position from the absorption curve. If the sample does not give a signal on the latter, it is still possible to align the center of a sample chamber with X-rays (via y and z scans) and then bring the sample to the beam using an optical microscope.

The next, most important step of alignment for SC-XRD data collection in DACs, is bringing the desired sample area to the goniometer's axis of rotation. Since both beam and sample sizes are usually of a few micrometers, it is necessary that the sample stays in the X-ray beam during the rotations. The triangulation procedure performed by scanning the sample or sample chamber along the y-axis at two different goniometer's angles (increasing iteratively from $\pm 1^\circ$ to $\pm 20^\circ$) allows correcting DAC's position along the x-direction and bringing it to the rotation axis.

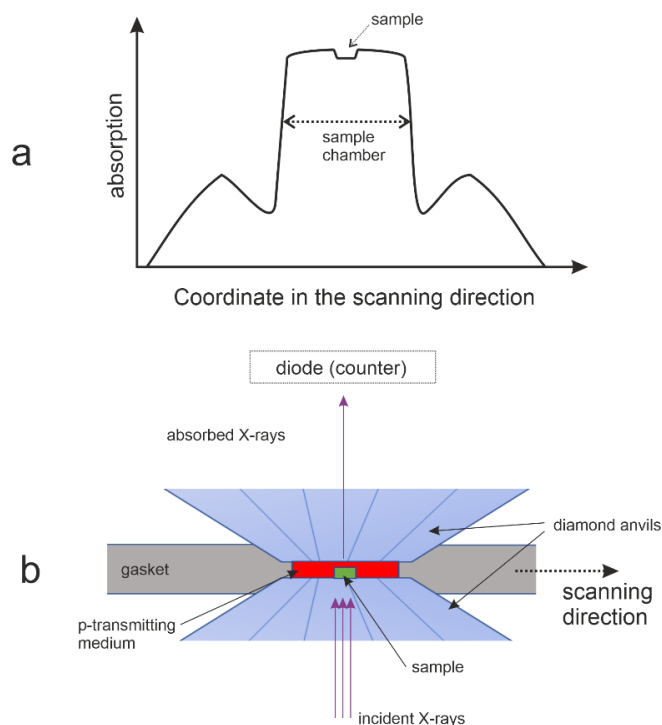


Figure 2.2-2 A schematic representation of an X-ray absorption curve (a) after scanning the DAC and its content (b). Small humps on the sides of the absorption curve are caused by the deformation of diamonds and the corresponding gasket's thickness.

2.2.6. Step-scans and wide-scans

After the alignment of a sample on a beamline, the actual XRD measurements could be performed. Depending on the tasks, several types of XRD data could be recorded. The first type, still-scan, is registered by the detector as a single shot of desired exposure with a stationary DAC. Being fast, such an exposure could be useful when the time is limited (measurements during the laser heating, during the fast compression or just for the estimations of signal quality or sample state). Next is a wide scan: the DAC rotates from $-w$ to $+w$, where w denotes the desired angle, which is typically 20° . It takes usually longer than a still scan, but allows collecting good statistics on the powder rings and can show more complete picture for the single-crystal Bragg reflections. The last type of scan, "step-scan", is a collection of single-crystal data. The photographs are taken by flat-panel detector each 0.5° of continuous DAC rotation with equal exposure time, laying typically from 1 to 10 seconds. The angular range is usually selected as the maximum of the DAC angular opening (from -38° to 38° degrees for BX-90 DAC) since it defines the number of Bragg's reflections collected and, therefore, the quality of dataset for the further structure solution. Typically, still-scans or wide-scans are the first to measure. Further, they serve as a reference point for preliminary sample checks and for adjusting the parameters (beam intensity, exposure time, rotation angles) of SC-XRD data collection, step-scans.

Within the framework of the presented thesis, the new design of DAC was designed to increase the angular opening accessible with X-rays (Figure 2.2-3, a). The design was based on the BX-90 DAC (100), leaving the outer diameter and operating principle similar, shape modifications were made. By decreasing the distance from the diamond anvil's culet to the surface of the tungsten carbide seat and increasing the diameter of the latter for its stability during the load (Figure 2.2-3, b). The angular opening with this new DAC, named BX-120, could reach 120° total if using a special cut of diamond anvils, and approximately 105° when using a standard Bohler-Almax anvil's cut. The usage of the BX-120 can significantly improve the statistics of the single-crystal XRD dataset, give more precise structural refinements and could be crucial in some special cases (for example, refining the hydrogen atomic positions).

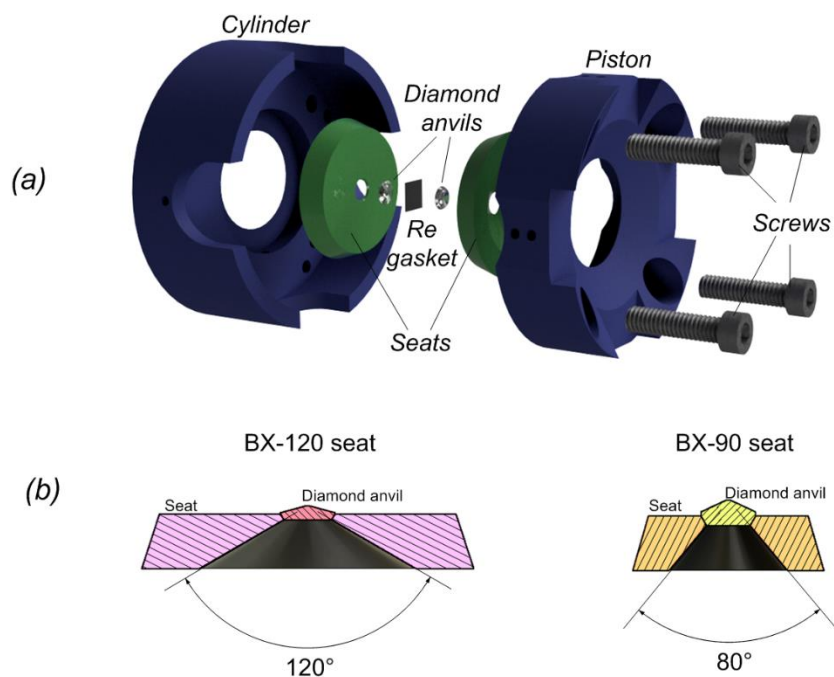


Figure 2.2-3 The BX-120 DAC render image (a) and the comparative incision of seats with anvils for BX-120 and BX-90 (b). Decreasing the culet-seat surface distance, a 1.5 times larger angular opening compared to BX-90 was obtained. The usage of special anvils, however, is not necessary, and experiments can be performed with the standard Boehler-Almax cut anvils which will decrease the accessible angle to about 105°.

2.2.7. X-ray contrast maps

In an LH-DAC experiment, the sample often represents the multigrain assemblage of crystallites belonging to several different phases which could be non-homogeneously distributed within the sample. To find the best spot for the single-crystal XRD data collection, or to obtain the exact information on the distribution of phases, XRD mapping can be collected. The operator set-ups a script that changes a DAC position relative to the X-ray beam by small steps in y and z directions, and on each step still XRD images, or w-scans are being collected. Such a dataset can be imported in a software (for example, XDI (127)) which builds a contrast maps based on the intensity of selected d-spacing (the user needs to find the unique non-overlapping peaks for each phase) and therefore allows to observe a phase distribution in the sample (Figure 2.2-4)

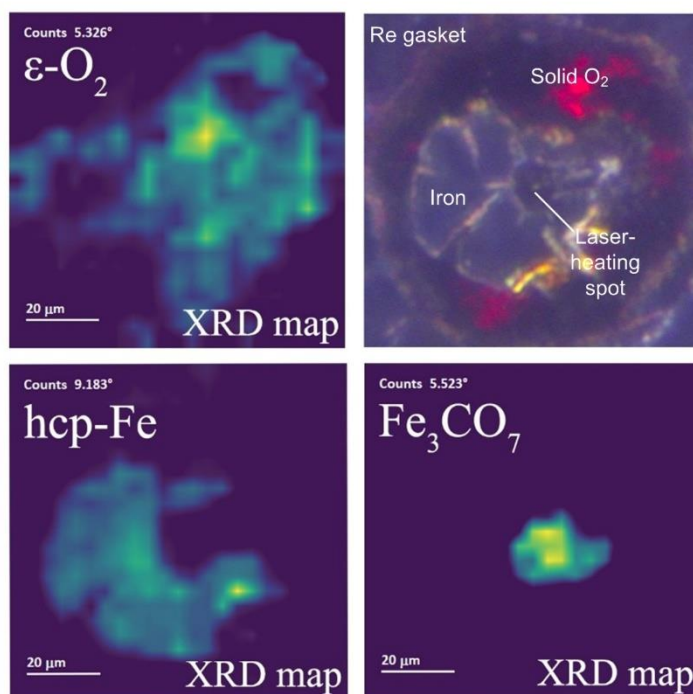


Figure 2.2-4. The optical (upper right) and XRD-mapping images of various phases in the experiment on Fe loaded with O₂ pressure-transmitting medium after laser-heating to 2200(200) K at 44(2) GPa. The 2 θ values defining the d-spacings of unique non-overlapping peaks for each phase are on the upper-left part of each panel.

2.2.8. Step-scans during laser heating

The high demand on the performance of *in situ* HP-HT X-ray diffraction led to the equipping of most beamlines dedicated to high-pressure with online laser-heating systems which are coupled with X-ray goniometers (BL10XU at Spring-8, LH setup of P02.2 at DESY, ID24 and 27 at ESRF, IDD-13 at APS, etc. (114, 119, 122, 128–131)). Most of the XRD experiments, which can be performed on these facilities with *in situ* laser heating, are imposed by restriction of a DAC rotation. Due to the high refractive index of a diamond, any rotation of DAC relatively to the laser beam will shift the laser-heating spot away from the sample. Therefore, while the sample is heated with lasers, only the XRD still-images can be collected from a heating spot. Even it can be useful for the identification of known phase(s), phase transitions, melting and determination of unit cell parameters *in situ* at HP-HT, in most cases such a data are insufficient. If the sample is

single-crystal or multi-grain, the whole set of Bragg reflections cannot be observed and, in turn, it is practically impossible to extract any structural information or solve a structure of novel compounds.

The recent development of the laser-heating setup which rotates along with a DAC removes that restrictions (96). The P02.2 beamline at DESY, equipped with the rotational laser setup allows the users to collect the *in situ* HP-HT single-crystal XRD datasets. This is, no doubt, is of great importance: this methodology allows obtaining the crystallochemical behavior of matter at the conditions relevant to the Earth's interior directly. Composed of two "UniHead" blocks and X-ray transparent graphite mirrors, the system is placed on a goniometer and allows stable laser-heating of a sample during its rotation. Still, the fine adjustments of laser-beams, X-ray beams and sample and alignment of them in one spot is delicate and complex work, which requires a high level of expertise from users.

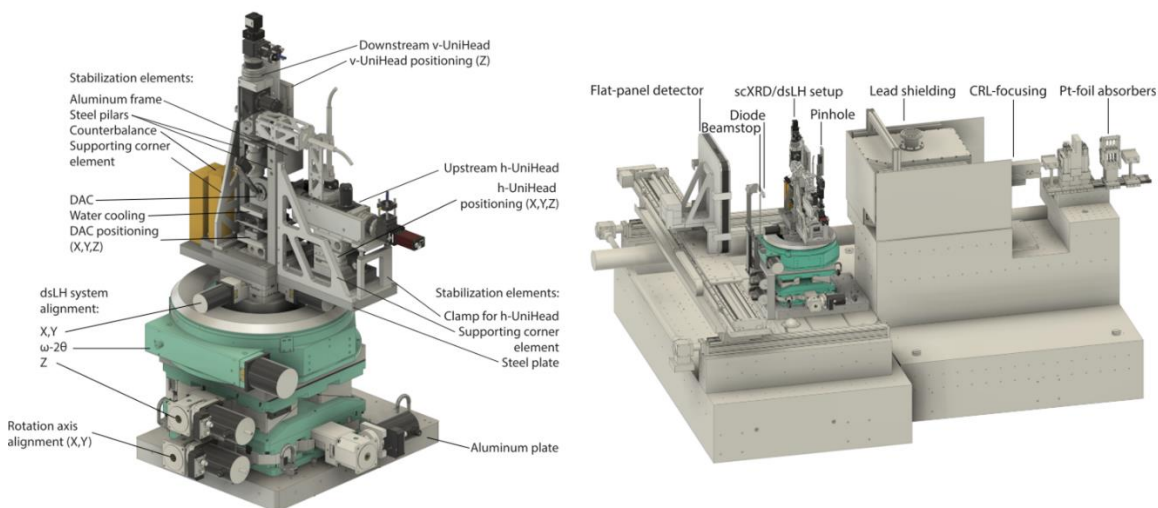


Figure 2.2-5. Rotational laser-heating setup for *in situ* single-crystal XRD data collection in laser-heated DACs at P02.2 beamline, DESY. The illustration is modified after (96).

2.2.9. Single-crystal XRD data processing

Since most of the present thesis was based on the single-crystal XRD, and powder XRD was used as an auxiliary method, the focus of this section will be devoted to the data processing routine of SC-XRD datasets. In the present thesis, most of the single-crystal XRD data reductions were performed using the self-written Python scripts and CrysAlis^{PRO} software (132). Structure solution and refinement was performed in the SHELX package (126, 133) and Xseed GUI (134) with some portions of work made in JANA2006 (125). A detailed tutorial for the data processing of single-crystal XRD datasets collected in DACs using CrysAlis^{PRO} could be found in (135). The following section briefly describes the main steps in the data processing.

1) Data conversion and calibration

The images registered by the detector should be converted to the CrysAlisPro format files first. The importing wizard is called through the 'rd p' command in the software's cmd. Depending on a detector used, the information on the format of images and encoding parameters should be applied: the number of header bytes, pixel data type (long, short, float), etc. During this step, calibration files and detector masks (if necessary) are applied. After the conversion is finished, the inspection of frames should be made so the actual DAC opening is checked and the utmost frames containing trash diffraction from the anvil's seats are not involved in the experimental dataset.

2) Peak hunting

A peak hunting procedure called by 'ph s' command starts an extraction of peaks from the image frames as implemented in CrysAlisPro software. After input of a frame range, the extraction algorithm should be chosen: automatic, traditional (user defines the threshold for the intensities for the peaks and the area size around it) and a smart peak hunting option. The algorithmic models are hidden in the software, but empirically the 'smart peakhunt' option fits best in the most cases for the data collected with following detectors: MAR165 (ID27 beamline at ESRF), Perkin Elmer (P02.2 beamline at Petra III, ID27 beamline at ESRF) and Pilatus (13-IDD

beamline at APS). Further, the software reconstructs the position of peaks in a reciprocal space, which is required for the next steps of data processing. The resulting list of peaks can be observed via 'pt e' command that calls a window where hkl and xyz coordinates of each software-defined experimental Bragg's reflections are listed, as well as their intensity and other attributes. The file containing that information is saved under the *.tabbin resolution in a project folder.

3) Cleaning of a reciprocal space

The basic algorithms responsible for the search of peaks on experimental diffraction images do not recognize the "trash" diffraction from diamonds, gasket, dead pixels and powder profiles of P-transmitting media or phases present in the sample. This leads to the high contamination of the reciprocal space which should be further cleaned as much as possible. The smart peak hunting has a more advanced peak profile analysis algorithm, but unfortunately for the experiments performed in a DAC experiments, it is still far from perfect.

Within the present thesis, in collaboration with Dr. M.Bykov, the algorithm, which allows simplifying the dataset by cleaning the 'trash' peaks found by CrysAlisPro was developed. First versions were realized in a python-based software, "peakCleanerPro" (the project could be found on the GitHub page: '<https://github.com/maxbyk/PeakCleaner>'). While this software remains open for further developments by the community, the last version of CrysAlisPro has a built-in feature based on the algorithm developed. It could be called by pressing the 'advanced filtering' button in the Ewald Explorer of CrysAlisPro.

The idea behind the algorithm is rather simple: the peaks from single-crystal grains of a sample should appear and disappear as the sample rotates. At the same time, the powder components and pixels oversaturated by diamond reflections will remain the same position on detector independent of a sample orientation. Therefore, if there are peaks with the same (or close) X-Y coordinates on the detector frames made at subsequent ω angles of a DAC rotation, then, most probably, they belong to the 'trash' signal. The algorithm analyses the distribution of peaks found for each x-y coordinate of a detector for the whole set of step-scan dataset. Further, it flags the

peaks, which present at the same position in most frames as ‘unused’. Such a cleaning procedure was tested in the number of experiment datasets successfully and accelerated the data processing significantly which is crucial for fast, online data processing.

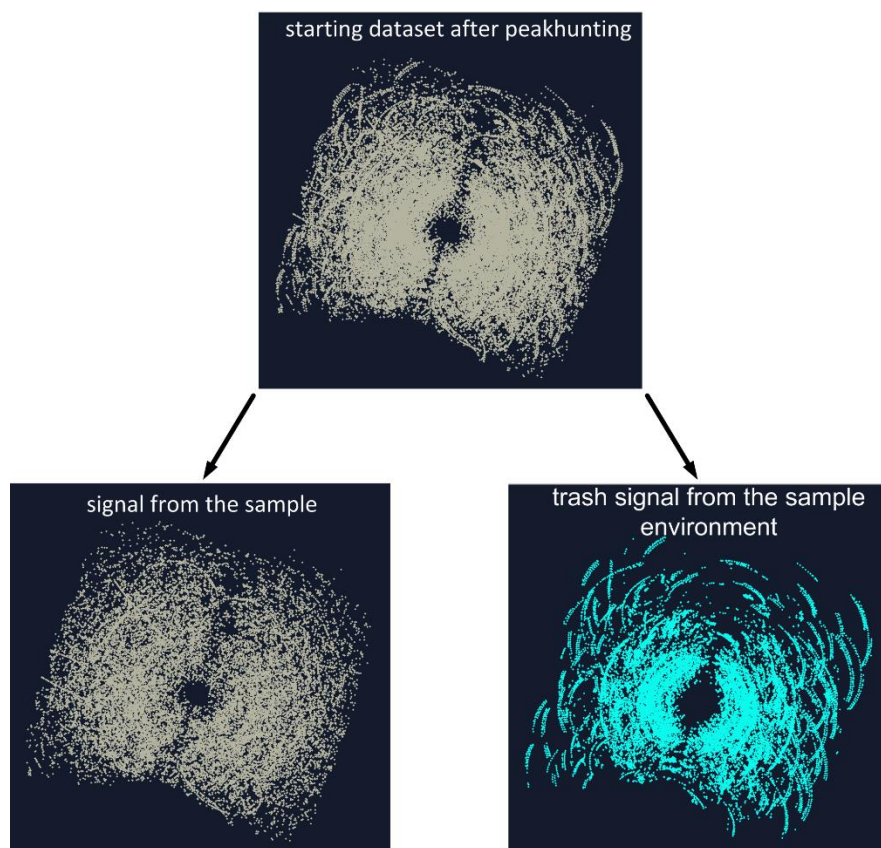


Figure 2.2-6 The result of cleaning the reciprocal space for the SC-XRD dataset collected in DACs by the developed algorithm.

4) Unit cell finding

After the reciprocal space is satisfactorily cleaned from the ‘trash’ signal, it is usually still full of peaks raised from the different crystallites present in the sample. The user’s task in the next step is to define the Bragg peaks that belong to one single crystalline grain. They form regular patterns within the reciprocal space so by rotating the reciprocal space, a user finds these peaks and manually selects them. If at least several peaks from several different ‘rows’ of single grain’s reflections are selected, the unit cell finding algorithm (called by ‘um tt’ command),

implemented in CrysAlisPro, can find the unit cell and index the rest of the peaks belonging to this grain of a specific phase (um i). The orientation matrix for the grain is also defined at this step and could be called by 'um s' command. In such a way all the sets of Bragg's reflections for all the crystalline grains in the sample could be found, divided into different groups and treated separately (Figure 2.2-7). However, the search of the starting peaks for the unit cell finding is still a complex task, which requires attentiveness and keen eyes of experienced users.

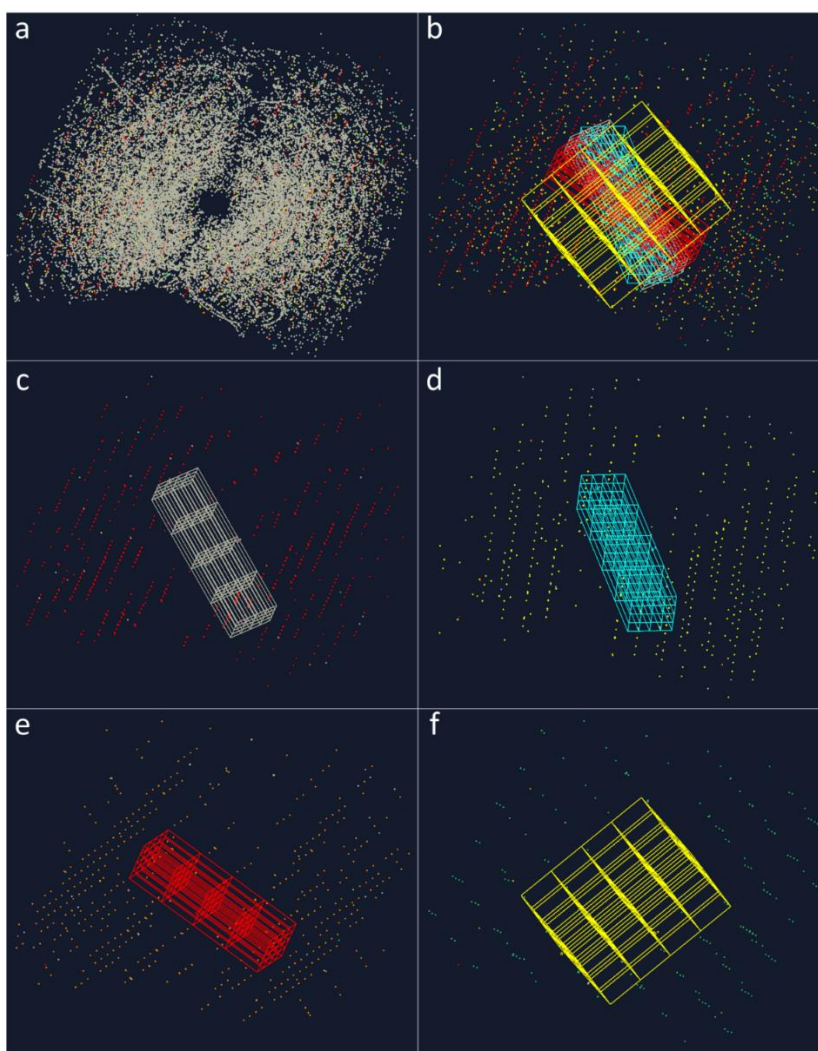


Figure 2.2-7 An example of initial dataset (a) in a reciprocal space, the sets of Bragg's reflections for different crystallites (b) and separate presentation of each of these sets (c-f). The dots represent the reflections, colored cells – orientation and unit cells for different crystallites (c-e) and different phases (c-e) and (f).

5) Integration

For the given orientation matrix (UB-matrix), the precise extraction of Bragg's peaks intensities for a certain crystallite is started with 'dc proffit' command. CrysAlisPro predicts the positions of the reflections based on the UB-matrix and extracts their intensities from the raw detector images, taking into account their shape and the background level. Analyzing the systematic absences, the software suggests a space group that could be assigned to the given crystallite and the user inspects the quality of the data by observing values reported by software after the procedure: R_{int} , absolute intensities value and the frame-scaling curve. If the user is not satisfied with a quality of integration, it is possible to run the process again changing the variables, which define the treatment of detector images: background correction, masking of reflections, integration range, etc. After that process, called data reduction, the software produces a file that lists all the hkl reflections with their intensities which is further used by a separate structure solution software.

6) Data finalization

The last step made in a CrysAlisPro is a data finalization, the step that is performed after the user reached a good quality of integration. The user checks again the error factors and systematic absences and defines the space group. Following that procedure, CrysAlisPRO writes down files containing information on the performed data treatment. Among them, the most important are standard reflection and instruction files recognizable with the structure-solution software: with file types .hkl, .cif-od, .cif and .ins.

7) Structure solution with JANA, X-SEED

The files generated in the previous step (reflection files and instruction files) are next imported into the software dedicated to the structure solution. Particularly, into the JANA2006 and X-SEED (125, 126, 136) as they were used intensively.

2.3. Mössbauer spectroscopy

In γ -radiation resonance absorption, the two nuclei are required: the one in the excited state which is emitting the γ photon through the relaxation and the second, same isotope in the ground state which should absorb this photon. For the free nuclei the emission of a γ -photon with momentum $p_\gamma = \frac{E_\gamma}{c}$ (where E_γ is a photon energy and c is a speed of light) will cause the recoil of the emitting system due to the high energy of a γ -photon. Since the nuclear mass M will recoil with an opposite momentum, the energy of a γ -photon will be diminished by the value of recoil energy:

$$E_R = \frac{p^2}{2M} = \frac{E_\gamma^2}{2Mc^2} \quad \text{Eq. (7)}$$

Similarly, the free absorbing nucleus will experience the recoil. Therefore, $2E_R$ energy difference is distancing the emission and absorption energies, whereas their overlap is required to get the resonance fluorescence (137).

The finding of Rudolf L. Mössbauer, made in 1958, allowed overcoming this energy “barrier”. If nuclei are located in crystal lattices, the emission and absorption of γ -rays could take place with no nuclear recoil: the recoil momentum is transferred to the crystal lattice and therefore the photon energy changes caused by recoil energy are negligible. Thus, the nuclei transition in a crystal could be used as a source of γ -rays to induce a reverse transition in nuclei, which are being probed. This phenomenon gave a raise to the Mössbauer spectroscopy. The strong resonance observed due to the Mössbauer effect allows precise measuring of very small energy changes in nuclei, atoms, and crystals induced by electrical, magnetic, or gravitational fields. This sensitivity is enough to detect differences in the atomic environment of a crystal lattice through the small changes in the energy levels of the nucleus (138).

The small changes in the atomic environment causes the nuclei energy level shifts and splitting. Though Mössbauer spectroscopy is a short-range probe, which is sensitive in the best cases to the first two coordination shells, the small energy deviations induced by electrical, magnetic and gravitational fields could be precisely measured due to extremely high energy resolution. Three physical phenomena contribute to the number, location and width of observed absorption peaks in Mössbauer spectra: the isomer shift, quadrupole splitting, and hyperfine splitting (139). The isomer shift consists of the relative change of the value of resonance energy that could be caused, for example, by the change of the oxidation state of atom which holds a nucleus. Quadrupole splitting is observed whereas the nucleus is experiencing electric field gradients. Nuclei in states with angular quantum number (I) higher than $1/2$ have a nuclear quadrupole moment. In this case, an asymmetric electric field (produced by an asymmetric electronic charge distribution) splits the nuclear energy levels. Resulting is removing the spin-state degeneracy and causing different spin states to possess different energy levels. The last, hyperfine splitting is caused by the presence of a magnetic field dividing the nucleus spin state into $(2I+1)$ sublevels with different energies.

Several elements have isotopes appropriate for a Mössbauer spectroscopy. Among them, ^{57}Fe with its nuclear transition at 14.4 keV, is one of the most frequently studied due to the convenience of use and its importance of iron in technology and fundamental sciences, especially for geology-related fields.

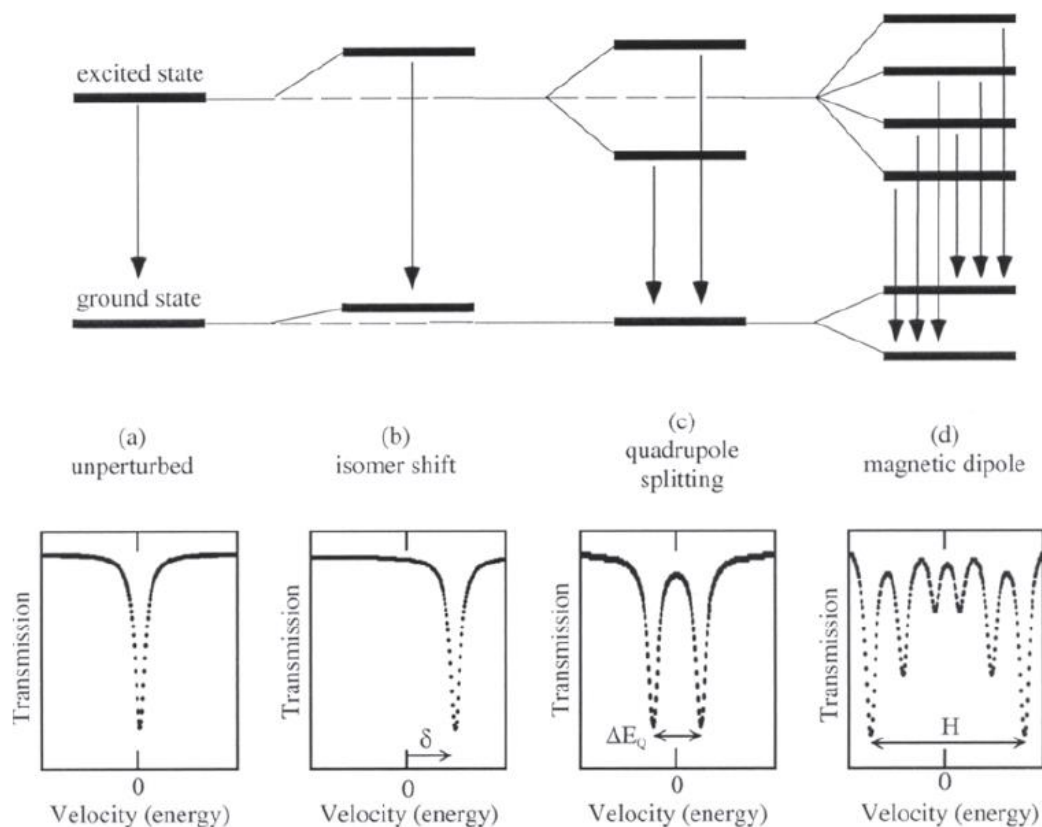


Figure 2.3-1 An illustration of the different effects observed on the Mössbauer spectra due to different types of ^{57}Fe nuclei interactions with an atomic environment. (a) Unperturbed nucleus. (b) Change in center shift (c) Quadrupole splitting. (d) Magnetic dipole interaction. Each interaction is accompanied by a resulting Mössbauer spectrum. Modified after (140).

The Mössbauer spectroscopy experiments require the source of γ -rays, the sample and the detector (counter). Usually, the source should consist of the same nucleus as in the sample but in the excited state so the required resonance energy could be achieved. The laboratory source for ^{57}Fe , for example, is ^{57}Co , decays due to electron capture to an excited state of ^{57}Fe ; relaxation of latter results in the emission of photons of the appropriate energy to excite the sample's nuclei. Since the nuclei levels of the sample could vary due to the effects described above, to resolve their energies a small variation of wavelengths of an incident beam is required. To perform that, the source is placed on the drive oscillating towards and backward the sample (absorber). The Doppler effect causes the tiny variations in the energy of emitted photons from

the source depending on the instant speed of a drive (140). However, the value of these energy differences is sufficient to resolve the fine and hyperfine splitting of the sample's core energy levels with high precision. Synchronization of a detector counting the photons with the oscillating drive allows assigning an energy level of each photon coming. The velocities of a source are usually at the order of a few mm/s speed so it became a standard way of representation of energy (mm/s instead of neV).

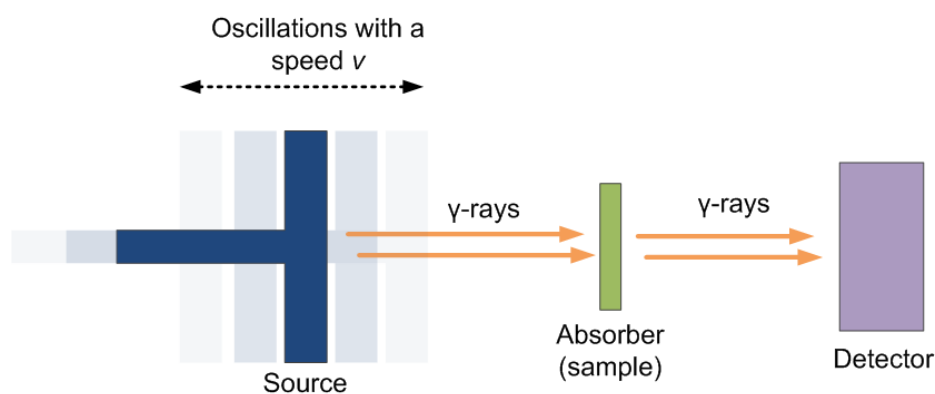


Figure 2.3-2 Schematic view of a Mössbauer spectrometer showing various possibilities for the source, absorber, and detector. Nearly all the individual configurations are independent, enabling numerous combinations to be made. Modified after (140).

Conventional laboratory Mössbauer spectroscopy was a powerful tool for studying the properties of various materials for decades. However, this approach meets barriers when samples of a small size, like in the DAC experiments are being measured. The focusing of γ -rays with the laboratory sources is problematic resulting in a low count rate and signal/noise ratio leading to very long exposure times, especially for the studies performed in the DACs.

However, the development of synchrotron-based Mössbauer spectroscopy allowed to overcome the limitations listed above perfectly. The experimental setup developed at the Nuclear Resonance Beamline of ESRF (ID18) (141) allows conducting Mössbauer spectroscopy (known as Synchrotron Mössbauer Source, SMS) experiments in LH-DACs at HP and HT conditions. It is based on the usage of $^{57}\text{FeBO}_3$ crystal (142) which allows the nuclear diffraction at the specific Bragg condition. Therefore, the usage of iron borate allows cutting the

synchrotron's hard radiation and achieving the required resonance energy of photons with a narrow linewidth. Similarly to the lab sources, the crystal is mounted on an oscillating drive for adjusting the photon energies probing the sample.

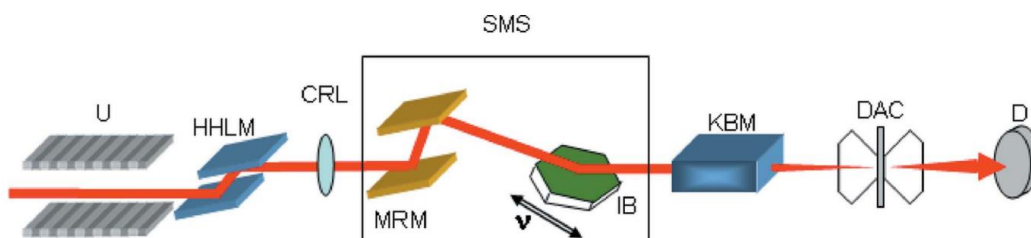


Figure 2.3-3. Optical scheme for a high-pressure experiment with DACs using the Synchrotron Mössbauer Source (SMS) at ID18 of the ESRF. U: undulator; HLM: high-heat-load monochromator; CRL: compound refractive lens; MRM: medium-resolution monochromator; IB: iron borate ($^{57}\text{FeBO}_3$) crystal; KBM: Kirkpatrick-Baez mirrors; DAC: diamond anvil cell; D: avalanche photodiode detector. Modified after (141).

High radiation intensity and the small focus distinguish the SMS from the conventional laboratory setup with obvious benefits for the DAC experiments: the small exposure times, high signal/noise ratio and a possibility to study the phases which are of $\sim 10\ \mu\text{m}$ lateral size.

2.4. X-ray absorption spectroscopy

X-ray Absorption Spectroscopy (XAS) is a technique based on the interaction of X-ray radiation with a matter causing the excitation of the inner-shell electrons. During the excitation, the photons of specific energy are absorbed depending on the geometric and electronic structure of a sample. The chance of an incident X-ray photon to be absorbed increases rapidly when its energy is close enough for the transmission of specific core electron to valence bound states or to the continuum, which results in the creation of photoelectron. This process causes a sharp changes in the absorption spectra, called an absorption edge. The value of energy level (and the absorption edge position, correspondingly, is characteristic for different elements and every electron shell in them). The different absorption edges are named according to the principal quantum numbers ($n = 1, 2$ and 3 correspond to K-, L- and M-edges, respectively). The present thesis focuses on the K-edge of iron at 7112 eV, corresponding to the excitation of 1s electrons.

The spectral features carry information about the electronic state of the atoms of the selected element in the sample, which in turn reflects the properties of the electronic configuration (such as oxidation state) and the local atomic environment (for example, coordination of a cation). The XAS spectra are usually separated into two main regions: X-ray absorption near-edge structure (XANES) and extended X-ray absorption fine structure (EXAFS) regions.

The XANES operates with a region near the absorption edge, where energy at which a sharp rise in the absorption coefficient of X-rays occurs. The characteristics of the absorption spectra at this range provide information on the oxidation state of the atom, its site symmetry and coordination and the degree of distortion of coordination polyhedra (octahedral, tetrahedral, prismatic coordination). Generally hard to describe theoretically, the XANES could be used as a “fingerprint” method for establishing, for example, the oxidation state of atoms through a well-recognizable shift of an edge position.

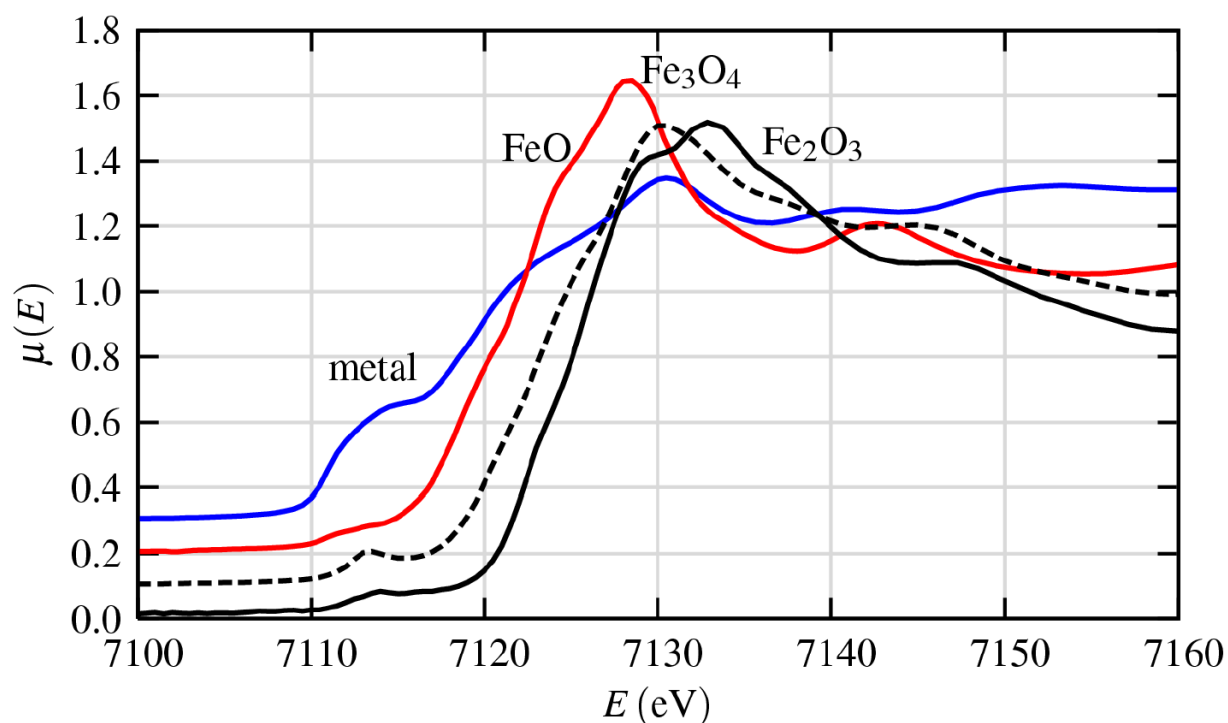


Figure 2.4-1 Fe K-edge XANES of Fe metal and several Fe oxides. A clear relationship between edge position and formal valence state could be noted. The shapes, positions, and intensities of pre-edge peaks can also be correlated to the oxidation state. The illustration is modified after (143).

EXAFS technique is applied for the higher energies than the one of XANES. This region is related to the multiple scattering of photoelectrons on the surrounding atoms causing the interference patterns to appear. Fourier transformation applied to that region and fitting of a model allows obtaining information on the radial distribution function (the variation of electron density around the absorbing atom as a function of distance), providing information about the local interatomic distances around the absorber. A more detailed description of both these techniques could be found in references (143–146).

In the present thesis, we applied the XANES technique for Fe K-edge at extreme pressures to withdraw the oxidation state of iron in the FeO_2 phase. The XAS data presented were collected at the Energy Dispersive X-ray Absorption Spectroscopy (ED-XAS) beamline at the ESRF (ID24). The setup of ID24 uses a silicon polychromator to focus the ‘pink beam’ radiation composed of

different energies on a small spot on a sample as small as $1\ \mu\text{m}$ at full-width half-maximum. A detector collects the incident radiation that was not absorbed by the sample and allows the collection of X-ray absorption spectra with a single exposure. The fast spectrum collection and the small spot size allows performing X-ray absorption mapping inside the DAC (147). The experimental setup is coupled with a laser heating system allowing for XAS measurements at high temperatures and pressures (129).

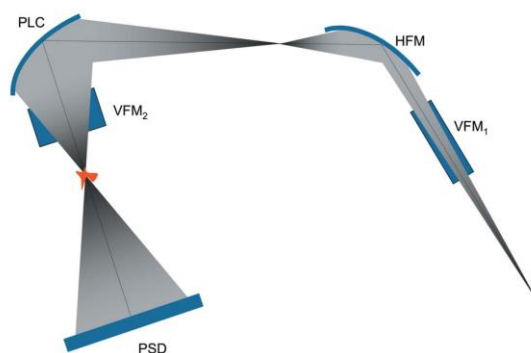


Figure 2.4-2. Experimental setup for Energy Dispersive X-ray Absorption Spectroscopy (ED-XAS) at ID24 at the ESRF. The incident beam is chromatically dispersed using a polychromator crystal (PLC) and the whole range of energies around the selected absorption edge is collected simultaneously from a position-sensitive detector (PSD) in a single exposure. The optical scheme consists of mirrors in a Kirkpatrick–Baez geometry for vertical (VFM_1) and horizontal focusing (HFM). A second vertically focusing mirror (VFM_2) downstream of the polychromator is used to refocus the beam onto the sample. Modified from (147).

Chapter 3. Synopsis

3.1. Summary and linkage of research studies

With the present thesis, we report our results on the investigation of FeOOH and FeO₂ behavior at pressures and temperatures relevant to the deep Earth interior. The Fe-O system shows complex crystallochemical behavior at extreme conditions that influence the properties of materials constituting Earth's interior and redox processes operating within the planet. The determination of structural and physical properties, chemical stability of FeOOH and its decomposition products has important implications for the deep hydrogen and oxygen cycle and the dynamical processes which dictate the Earth's evolution.

This part shortly presets an overview of the results presented in Chapters 5 to 8. Each of these chapters is a research article prepared in the framework of the Ph.D. project. They are either published (Chapters 5 and 8) or submitted and currently under review (Chapters 6 and 7).

Chapter 4 is dedicated to the clarification of the methodology for studying the FeOOH system. Alkali metal halides such as NaCl and KCl are widely used as a P-transmitting medium and therefore their chemical inertness is necessary for all experimental studies on FeOOH performed in DACs. We employ single-crystal XRD in LH-DACs to investigate the chemical interaction between FeOOH and NaCl at extreme P-T conditions. We observe the chemical interaction resulting in a formation of Na₂FeCl₄OH_x phase and describe its properties. Chapter 5 is devoted to the HP-HT treatment of FeOOH loaded in Ne pressure-transmitting medium. Applying *in situ* SC-XRD in LH-DACs we explore the stability field of FeOOH at conditions relevant for slabs subducted to the lower mantle. We observed the decomposition of initial FeOOH and the formation of various HP iron oxides, including two novel ones: Fe₇O₁₀ and Fe_{6.32}O₉. We describe the crystallochemical properties of these phases and hypothesize on the impact of the decomposition of FeOOH on the Early Earth's mantle and atmosphere. Chapter 6 summarizes the exploration of the physical properties of FeO₂ and isostructural FeO₂H_x by a multimethodological approach: single-crystal XRD, Mössbauer and X-ray absorption

spectroscopy, and advanced theoretical calculations (DFT+DMFT). We established the unusual oxygen behavior in these species: in FeO_2 , the formal oxidation state of oxygen is $\text{O}^{1.5-}$. We imply this surprising finding in the Fe-O chemistry to the lower-mantle related materials (bridgmanite). Chapter 7 is dedicated to the methodological improvements for the *in-situ* HP-HT single-crystal X-ray diffraction. We developed diamond anvil with a round table (DARTs), a new type of diamond anvils allowing collection of XRD datasets which require rotation of DAC relative to the X-ray beam with simultaneous laser heating. The application of DARTs allows the *in situ* SC-XRD data collection at both HP-HT conditions at the beamlines equipped with a stationary laser-heating setups.

3.1.1. Summary of Chapter 4: *Interaction between FeOOH and NaCl at extreme conditions: synthesis of novel $\text{Na}_2\text{FeCl}_4\text{OH}_x$ compound*

The alkali metal chlorides (for example, NaCl and KCl) are widely used as a pressure-transmitting media in LH-DAC experiments and considered to be chemically inert. However, at high pressures and temperatures, the chemical behavior of materials may change and these species could interact with samples. As a methodological aspect required for the investigations of FeOOH behavior, it is of great importance to verify that the presence of alkali metal chlorides does not influence Fe-O chemistry. Due to the absence of literature data on the possible reactions between FeOOH and alkali metal halides at extreme P-T conditions, we performed a single-crystal XRD study in LH-DAC exploring this system. A FeOOH sample was loaded in NaCl P-transmitting medium and was heated at 107(2) GPa to 2000(200) K. Using *in situ* single-crystal XRD, we

established that the formation of cubic FeO_2H_x phase occurs reported before in the literature as well as the formation of two novel phases. For one of them, we were able to collect a good quality dataset and perform the structure solution, establishing the novel phase as an orthorhombic compound (space group #44 $\text{Imm}2$, $a=2.5467(5)$ Å, $b=9.640(2)$ Å, $c=11.580(2)$ Å) $\text{Na}_2\text{FeCl}_4\text{OH}_x$ with an unusual coordination of Na cations (Figure 3.1-1). Our results demonstrate that at high P-T conditions the alkali metal halides could interact with hydrous phases. The alkali metal halides can influence the Fe-O chemistry; formation of phases with a complex elemental composition could, in turn, significantly complicate the interpretation of spectroscopical studies. Thus, alkali metal halides (NaCl, KCl, etc) are not suitable as a pressure transmitting and thermal insulating medium in DAC experiments dedicated to studies of hydroxyl or water-bearing materials at high P-T. Therefore, in subsequent experiments on FeOOH , a neon (Ne) pressure-transmitting medium was used.

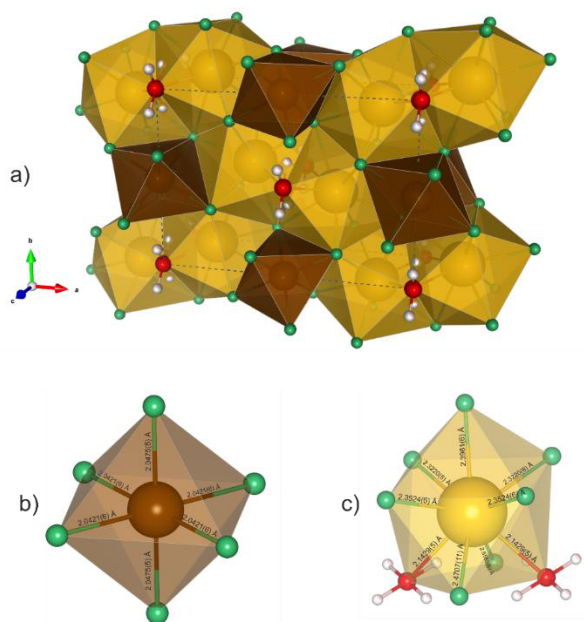


Figure 3.1-1 The crystal structure of $\text{Na}_2\text{FeCl}_4\text{OH}_x$ at 107(2) GPa. (a) Yellow spheres – Na atoms, brown spheres – Fe atoms, Cl and O atoms shown as green and red spheres, correspondingly. Yellow and brown polyhedra represent the coordination of Na and Fe irons. White spheres show possible (partially occupied) positions of H atoms. Fe and Na (b and c, correspondingly) coordination polyhedra with bond lengths.

3.1.2. Summary of Chapter 5: *Role of FeOOH in oxygen recycling in early Earth's history*

Water or water-bearing species have a strong impact not only on life on our planet but also on numerous processes in Earth's interior (29, 148). The presence of water affects the physical properties of mantle minerals and causes different global phenomena such as arc volcanism and

plate tectonics (73–75). Mechanisms of water circulation between geospheres are crucial for understanding our planet's dynamics and chemistry but remain debated and discussed actively (148). Recent studies suggest that iron-bearing minerals present in Banded Iron Formations (BIFs), such as goethite (α -FeOOH), could transport some quantities of water to the deep Earth interior with subducting slabs (68, 69, 71, 72). It was reported that FeOOH (mineral goethite and its HP polymorphs) remains stable in the sinking slab until it reaches the bottom part of the lower mantle. By means of *in situ* powder XRD it was revealed that at pressures corresponding to the depths of ~1500-1800 km and at moderately high temperatures FeOOH undergoes a phase transition to form a stable pyrite-type phase FeO_2H_x with $0 \leq x \leq 1$ (69, 72). Therefore, goethite and its HP polymorph are considered to be candidates for water and/or hydrogen transfer to the lower mantle and the core-mantle boundary (68).

We performed a series of *in situ* synchrotron single-crystal XRD experiments in LH-DACs on the stability field of α -FeOOH loaded in Ne at 40-82 GPa and 1200-2500 K (Figure 3.1-2). Heating of a starting goethite to 1500(100) K at 40(2) GPa, which corresponds to the PT conditions of a cold slab at ~1000 km depth, led to a transformation of initial α -FeOOH to ϵ -FeOOH and its partial decomposition to the Rh_2O_3 -II type structured iron oxide ι - Fe_2O_3 . At a slightly higher temperature of 1600(100) K at 41(2) GPa, the decomposition yields two iron oxides - ι - Fe_2O_3 and monoclinic Fe_5O_7 . Heating at 52(1) GPa and 1200 K resulted in the formation of three iron oxides - previously known Fe_5O_7 and η - Fe_2O_3 (CaIrO₃-type Fe_2O_3), and an additional hexagonal phase. This phase, according to our single-crystal X-ray diffraction data analysis, is a novel mixed-valenced $\text{Fe}_{6.32}\text{O}_9$ iron oxide, which has a hollandite-like structure (space group $P6_3/m$). Heating of another goethite crystal in the same DAC at 1550(100) K leads to the formation of η - Fe_2O_3 and Fe_5O_7 , while no traces of $\text{Fe}_{6.3}\text{O}_9$ were detected. Treatment of goethite at about 2000 K at 52(1) GPa leads to the formation of a single iron oxide, orthorhombic HP- Fe_3O_4 . During experiments at 64(2) GPa, we registered the decomposition of FeOOH with a formation of η - Fe_2O_3 at 1500(100) K. On further iterative sample heating up to 2100(100) K we observe the formation of η - Fe_2O_3 and novel orthorhombic iron oxide, Fe_7O_{10} (space group Cmcm) as its structure was refined. Upon laser

heating to 1500(100) K at 81(2) GPa and goethite transformed into cubic FeO_2H_x and partially decomposes to $\eta\text{-Fe}_2\text{O}_3$ and $\text{Fe}_{6.32}\text{O}_9$.

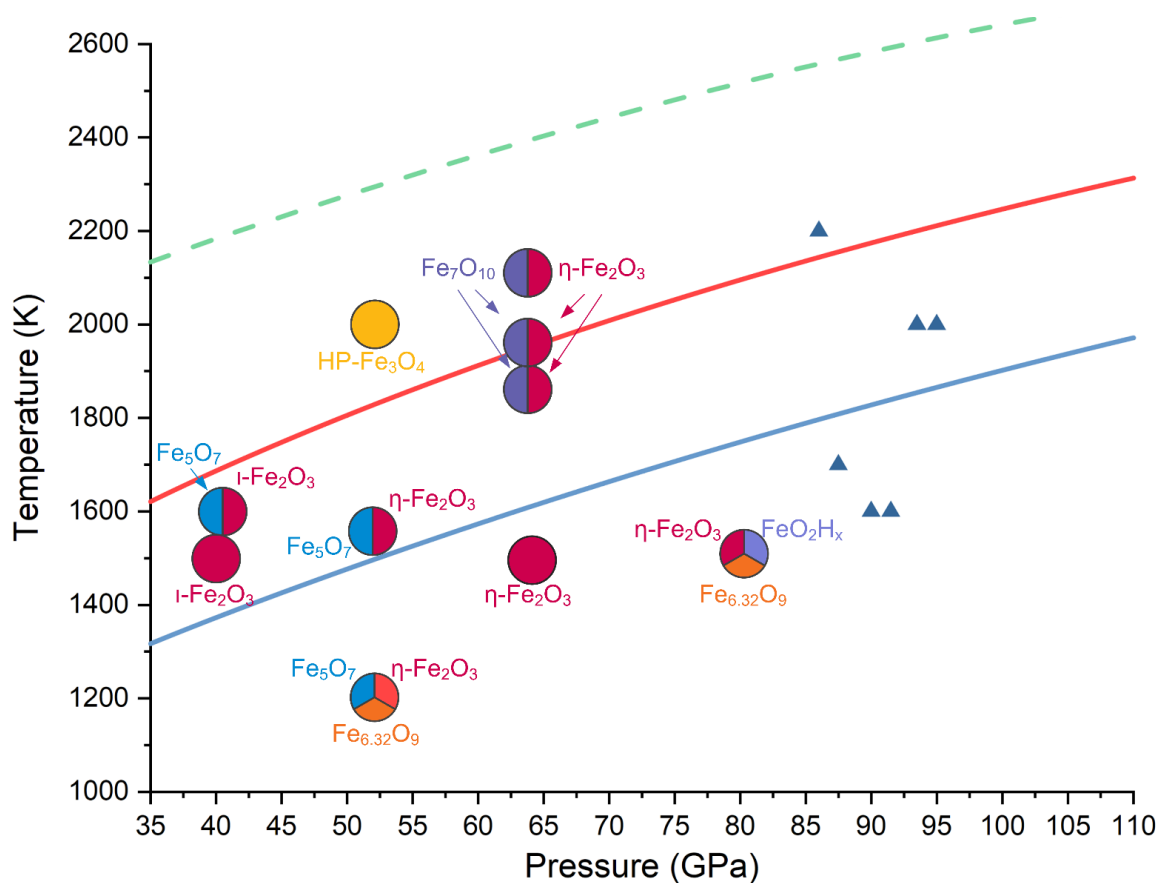


Figure 3.1-2 Experimental conditions of high P-T treatment of starting $\alpha\text{-FeOOH}$ and results of phase analysis obtained in present work. The position of filled circles represents P-T conditions of FeOOH treatment; different colors represent phases synthesized at these P-T conditions (sector size is arbitrary). Error bars of pressure are within the size of the symbols. Blue solid triangles represent the synthesis conditions of FeO_2H_x according to (70). The dashed green line is a mantle geotherm (149), while solid red and blue lines are the calculated lowest temperatures across slabs sinking at vertical speeds of 1 and 2 cm/year, respectively. We observed goethite decomposition that formed previously described $l\text{-Fe}_2\text{O}_3$, $\eta\text{-Fe}_2\text{O}_3$, $\text{HP-Fe}_3\text{O}_4$, and Fe_5O_7 , and newly reported mixed-valence iron oxides Fe_7O_{10} and $\text{Fe}_{6.32}\text{O}_9$.

A detailed study on the structural changes of novel Fe_7O_{10} and $\text{Fe}_{6.32}\text{O}_9$ iron oxides at various pressures via cold compression and decompression was made. Fe_7O_{10} has unusually large unit cell parameters and continues the homological series of $n\text{FeO} \cdot m\text{Fe}_2\text{O}_3$ high-pressure iron oxides.

The spin transition of iron in Fe_7O_{10} occurred at 43(2) GPa with a 7% volume collapse, and a 3rd order Birch-Murnaghan equation of state was obtained for this phase with high-spin iron ($V_0=609(9) \text{ \AA}^3$, $K_0=222(25) \text{ GPa}$, and $K'=4 \text{ GPa}$). The crystal structure of novel non-stoichiometric $\text{Fe}_{6.32}\text{O}_9$ differs from any known compound in the Fe-O system: it has infinite hexagonal channels along the c direction, where iron atoms partially occupy their positions. A spin transition of iron in $\text{Fe}_{6.32}\text{O}_9$ was observed to occur between 37 and 43 GPa and Birch-Murnaghan 3rd order EOS parameters were obtained as follows: $V_0=313(7) \text{ \AA}^3$, $K_0=157(31) \text{ GPa}$ for high-spin iron and $V_0=287(3) \text{ \AA}^3$, $K_0=209(16) \text{ GPa}$ for low-spin iron (K' is fixed to 4 in both cases).

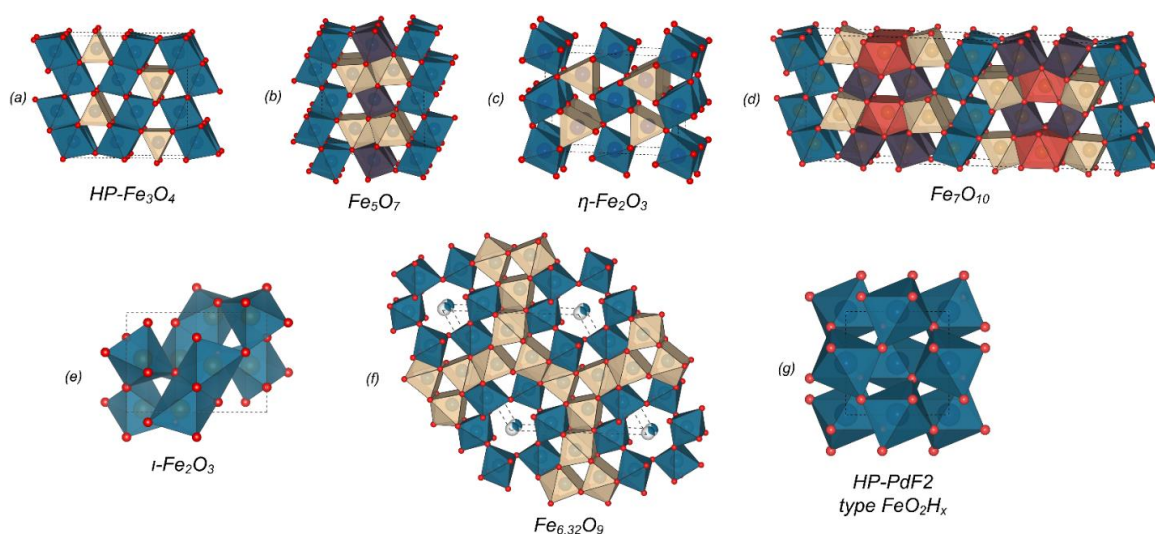
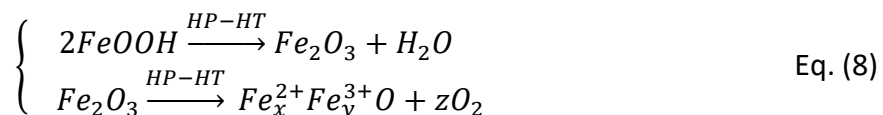


Figure 3.1-3 Structures of iron oxides synthesized from goethite during high P-T treatment based on in situ single-crystal XRD. Blue spheres are iron atoms while red spheres are oxygen atoms. Building blocks are octahedra (blue and dark purple) and trigonal prisms (pale yellow and orange). (a) HP-Fe₃O₄ (Bbmm) with the CaTi₂O₄ structural type, where edge-shared FeO₆ octahedra are ordered in a zigzag motif and interconnected via stacking layers of triangular prisms with shared bases; (b) Fe₅O₇; (c) post-perovskite η-Fe₂O₃; (d) novel Fe₇O₁₀ (η-Fe₂O₃ and Fe₇O₁₀ are members of the homologous series FeO · mFe₂O₃ (53), where prisms are connected through common triangular faces and octahedra are connected only via shared edges); (e) l-Fe₂O₃ with the Rh₂O₃-II structure type (25, 53); (f) novel Fe_{6.32}O₉ which can be described as hexagonal hollandite-like, with chains of apices-sharing FeO₆ octahedra forming hexagonal channels that are partially occupied by iron cations. A three-dimensional framework of mono-capped prisms separates the channels. (g) FeO₂H_x (Pa-3) with the HP-PdF₂-type structure. The apices-sharing FeO₆ octahedra form a framework in which the shortest O-O distance is 2.267(5) Å at 82(1) GPa. For details of the crystal structures of Fe₇O₁₀, Fe_{6.32}O₉, and FeO₂H_x see Supplementary Materials.

According to currently well-established theories (see, for example, the seminal book by D.E. Canfield, (150)), before the advent of oxygenic photosynthesis, Earth's biosphere was driven by anaerobic metabolism starting from about 3.8 Ga ago. During this period, iron(III) oxyhydroxides were a common byproduct of the vital functions of iron-oxidizing phototrophs. A simple estimate shows that the sedimentation of FeOOH would have taken less than 5 Ma to accumulate the amount of oxygen present in the modern atmosphere (65, 66). Over hundreds of millions of years, a huge amount of FeOOH was buried and, when plate tectonics became active (currently considered to have started 3.2 to 2.5 Ga ago), the subduction brought oxyhydroxides down to the Earth's deep interior (151).

Our in situ synchrotron single-crystal X-ray diffraction experiments demonstrate that at pressure-temperature conditions corresponding to the depth of about 1000 km, FeOOH in the sediments decomposes to iron oxides (known Fe₂O₃ and Fe₅O₇, and reported for the first time Fe₇O₁₀ and Fe_{6.32}O₉) and an oxygen-rich fluid. Schematically, this process could be represented as the following chemical equation (however, the exact decomposition pathway is still not clarified):



First, the initial FeOOH decomposes to water and Fe₂O₃ whereas the further decomposition of the latter leads to the formation of mixed-valence iron oxides and oxygen (see Eq. (8)), in agreement with a report by Bykova et al (53). Our results suggest that the recycling of FeOOH in Earth's mantle leads to a release of oxidizing fluids, causing a change in redox conditions. We hypothesize that the transport of these fluids (or oxidized mantle material) to the Earth's surface could explain the sporadic increase of oxygen levels before the Great Oxidation Event, which is linked to the formation of large igneous provinces. Our hypothesis implies that the formation of Earth's oxygen-rich atmosphere resulted from processes in the early anaerobic biosphere, plate tectonics, and decomposition of ferric iron oxyhydroxides in the Earth's mantle.

3.1.3. Summary of Chapter 6: *Variation of oxygen oxidation state at the base of the Earth's mantle*

Iron, the most abundant element by mass on the Earth, until recently was considered to be the only geochemically abundant element in Earth's interior with a variable oxidation state. While oxygen (most abundant element by number of atoms) is also known to form species with several oxidation states (for example, O^0 in atmosphere, O^{2-} in oxides and silicates, O_2^{2-} in peroxides, O_2^{3-} in electrochemically oxidized transition metals oxides (152, 153), so far only valence state -2 was considered for materials forming Earth mantle. Synthesis of numerous iron oxides with unexpected compositions (25, 26, 57, 58) at high pressures and high temperatures (for example, Fe_4O_5 , Fe_5O_6 , Fe_7O_9 , Fe_5O_7 , $Fe_{25}O_{32}$, and especially FeO_2), their unusual crystal structures, and intriguing physical properties, indicate that oxygen may have variable oxidation states in the deep Earth interior. X-ray Absorption Spectroscopy (XAS, (77, 95)) and synchrotron Mössbauer scattering (SMSc, (77)) studies of cubic high-pressure FeO_2H_x ($x=0$ to 1) compounds were used to argue that iron is ferrous even at strongly oxidized conditions and thus oxygen can form peroxide (O^{2-}) ions under deep mantle conditions.

However, the chemical nature of the FeO_2 (and FeO_2H_x) compound remains uncertain: some theoretical works (91, 92, 154) suggest that iron is ferric; experimental structural data come from powder diffraction data (71, 155) (making accurate analysis of O-O distances difficult); results of XAS and SMSc are internally inconsistent – while XAS data were interpreted as proof for Fe^{2+} (77, 95), the SMSc of cubic FeO_2 (77) shows unrealistic for any ferrous oxides central shift (~ 0.15 mm/s at 80 GPa). Even if peroxide anion form stable iron compound(s) at high-pressure, it is not clear whether this would affect the behavior of the major Earth mantle phases (ferropericlase, bridgmanite, silicate post-perovskite).

Thus, the goals of the present work are to clarify (particularly on the example of FeO_2) what is the nature of the variable oxidation state of oxygen and describe its electronic properties. To achieve these goals, we employed synchrotron *in situ* single-crystal X-ray diffraction, Mössbauer

and XANES spectroscopies to investigate the properties of FeO₂ synthesized by laser-heating in DACs. The synthesis of FeO₂ for subsequent investigation of properties was performed by a direct reaction between iron and oxygen in LH-DAC at 46(1) GPa and 1200(100) K. Single-crystal XRD analysis allowed to identify the cubic FeO₂ phase (with unit cell parameter $a = 4.4313(14)$ Å, in agreement with previous studies (69, 92)) and to solve and refine its structure.

The structural analysis performed at various pressures showed that the shortest O-O distance varies from 2.203(4)Å to 2.090(10) Å within the pressure range ~36 to ~73 GPa. From the crystal-chemical point of view, such a long interatomic distance suggests the absence of chemical bonding between these oxygen atoms. Thus, the cubic FeO₂ structure belongs to the HP-PdF₂ structure type (89, 90), rather than to the pyrite-type and it does not belong to peroxides (Fe²⁺O₂²⁻). DFT+DMFT calculations confirm that the oxidation state of Fe in HP-PdF₂-type FeO₂ is close to 3+ and that there is a noticeable absence of O-O bonding to at least 180 GPa. Mössbauer spectroscopy data are consistent with iron in the Fe³⁺ state (53, 156), in good agreement with (77). Results of the XANES study of isostructural FeO₂H_x phase also indicate the ferrous state of iron contrary to the reported data in (95).

Our experimental and theoretical results thus imply that the oxidation state of oxygen in HP-PdF₂-type FeO₂ is equal to 1.5- due to oxygen-metal negative charge transfer. Such a charge transfer is expected to shorten the Fe-O distance and consequently the volume of FeO₆ octahedra, which should lead to both iron polyhedra and the entire structure to become very incompressible. Indeed, fitting the pressure-volume data for cubic FeO₂ with the 3rd order Birch-Murnaghan equation of state (EoS) gave EoS parameters with a large bulk modulus: $V_0=97.6(3)$ Å³/unit cell, bulk modulus $K_0=305(9)$ GPa, and $K'=4.0$ (fixed). Compressibility of FeO₆ octahedra is very low ($K_{0,\text{octahedron}}=350(4)$ GPa) and their volume is significantly smaller than that is known for any other compound, including those with ferric iron Fe³⁺ in the low-spin state.

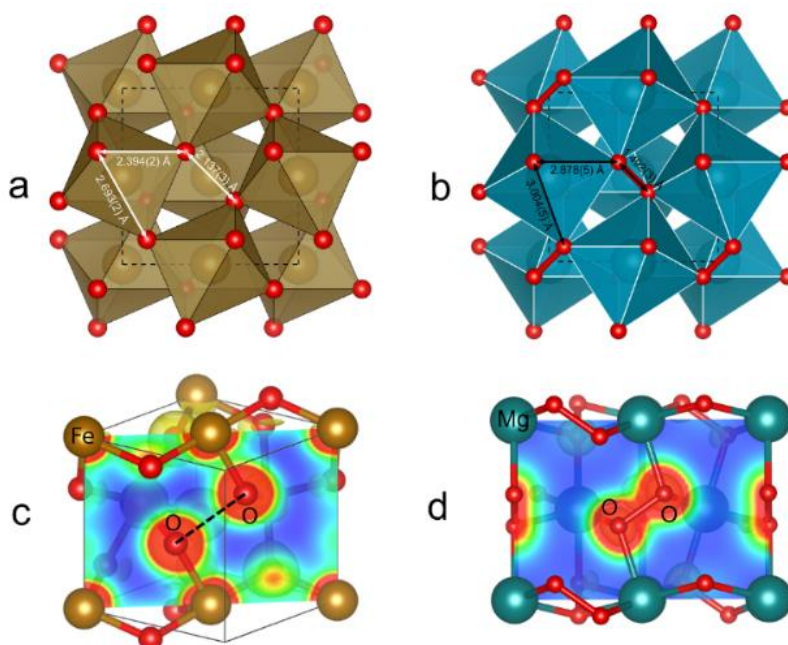


Figure 3.1-4. Comparison of crystal structures of HP-PdF₂-type FeO₂ and pyrite-type MgO₂ peroxide. (a) Crystal structure of cubic (HP-PdF₂-type) FeO₂ as refined from single-crystal XRD data (iron – brown, oxygen – red). XRD data were taken from the temperature quenched sample obtained after heating iron in oxygen at 58(2) GPa and 1800(100) K in a DAC (Tables S1, S2). The shortest experimentally determined O-O distance is 2.137(2) Å, which is too large for a peroxide-type structure. (b) Crystal structure of pyrite-type MgO₂ peroxide (magnesium atoms are blue-green) at ambient conditions (26). The shortest O-O distance is 1.492(3) Å. (c) Valence electron density plot for cubic FeO₂ for the unit cell volume 83.0 Å³ (corresponding to 69 GPa). The theory confirms that the shortest O-O bond length even at 180 GPa remains sufficiently large (1.86 Å), suggesting the absence of covalent ‘molecular’ (O₂)³⁻ bonding in FeO₂. (d) Valence electron density plot for cubic MgO₂ for the unit cell volume 113.3 Å³ (ambient pressure) as obtained by DFT (HSE03) calculations. For MgO₂ the formation of ‘molecular’ (O₂)²⁻ bonds, with 21% of a maximal electron density value in the center of the O-O contact, is evident. For cubic FeO₂ the value is only 5% and thus the calculations support the Fe³⁺(O^{1.5-})₂ electronic configuration.

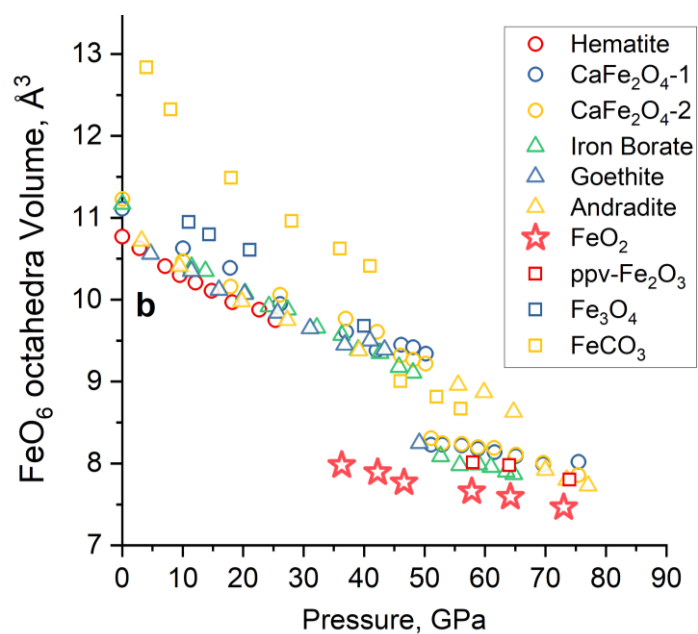


Figure 3.1-5 Pressure dependence of volumes of FeO_6 octahedra in various compounds according to (30) and references therein. Red stars designate the data for HP-PdF₂-structured cubic FeO_2 ; red circles – hematite (α - Fe_2O_3); blue and yellow circles – two different octahedra in calcium ferrite (CaFe_2O_4 -1) and (CaFe_2O_4 -2), respectively; green triangles – iron borate (FeBO_3); blue triangles – goethite (α - FeOOH); yellow triangles – andradite ($\text{Ca}_3\text{Fe}_2(\text{SiO}_4)_3$); red squares – CaIrO_3 -type structured η - Fe_2O_3 (ppv- Fe_2O_3); blue squares – magnetite (Fe_3O_4); yellow squares – iron carbonate (FeCO_3).

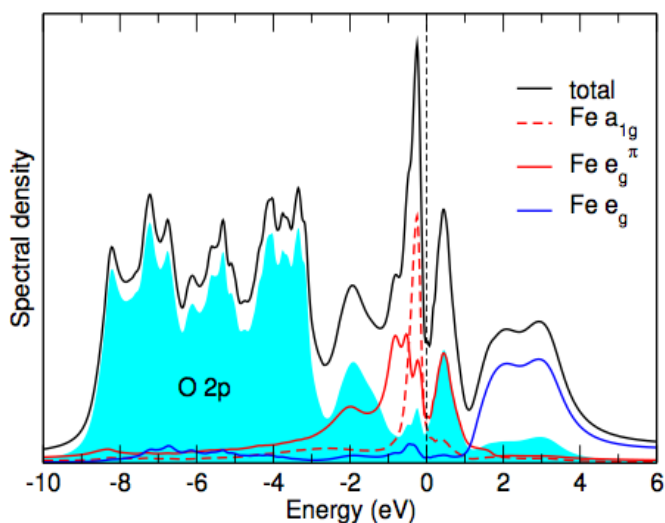


Figure 3.1-6 Orbitaly-resolved spectral functions of FeO_2 for Fe 3d (delineated by colored lines) and O 2p (blue shaded area) obtained by DFT+DMFT at 1160 K and ~ 70 GPa. The Fermi energy ($E_F = 0$ eV) is taken as energy zero and is shown by a vertical dashed line. Due to distorted FeO_6 octahedron symmetry, the Fe t_{2g} states split into an a_{1g} singlet and e_g doublet. Fe e_g orbitals are empty and are located well above the Fermi level between 1 to 4 eV. Fe t_{2g} states form weakly renormalized ($m/m^* \sim 1.6$) quasiparticle bands near E_F . The bonding-antibonding splitting of the O 2p orbitals is ~ 2 -3 eV. The bonding σ states appear at ~ -2 eV, while the anti-bonding σ^* states due to mixing with the Fe t_{2g} states at the Fermi level split into the $t_{2g} \pm \sigma^*$ combinations (two peaks at -1 and +1 eV). Note the empty $t_{2g} - \sigma^*$ O-O band located ~ 1 eV above the Fermi level. Our results show the O 2p states crossing the Fermi level, implying that FeO_2 belongs to the class of negative charge-transfer gap materials in the Zaanen-Sawatzky-Allen scheme (excitation energy for the transfer of electrons from the O 2p to Fe 3d states is negative). In such materials, instead of having an electronic configuration corresponding to the formal valence state, e.g. Fe^{4+} ($3d^4$) and O^{2-} ($2p^6$) configuration in FeO_2 , the system prefers to have a configuration with higher occupation of the 3d-shell, creating holes on oxygen. This behavior can be attributed to the known high resistance of transition metal ions to extremely elevated valence (which is energetically unfavorable, e.g., due to a large Coulomb interaction U value between the electrons in the 3d shell) and prefer to retain a lower valence (higher occupation of the 3d-shell) at the expense of creating holes on oxygen.

Generalizing our observations on the cubic HP-PdF₂-structured FeO_2 and FeO_2H_x phases, and taking into account that compounds with x up to 1 were previously described in the literature, we conclude that at pressures above ~ 50 GPa oxidation state of oxygen could significantly deviate from -2. Prominent changes in oxygen chemistry could affect the behavior of major lower mantle phases, particularly those containing iron (such as bridgmanite, Brg), and the effect should be

most pronounced (and easier detected) for iron-rich compounds. We consider the impact of this effect on silicate post-perovskite and (Fe,Al)-bearing bridgmanite and discuss it in the results section of Chapter 6.

3.1.4. Summary of Chapter 7: *Diamond anvils with a round table (DART-anvils) designed for high-pressure experiments in DAC*

The performance of *in situ* HP-HT single-crystal XRD experiments would significantly benefit to the geoscience since it allows obtaining the structural information on the phases existing in conditions relevant to the deep Earth interior. However, the collection of single-crystal XRD data in DACs at *in situ* HT-regime, i.e. during the laser heating, is a technically complicated task. Conventional anvils have “flat plate” geometry, and rotation of a cell at any angle relative to the stationary laser beam leads to strong refraction, as diamond is a material with a high refractive index ($n = 2.425$ at 532 nm). This will result in the shift of laser-heating spot from the desired sample area, which is being probed by X-rays. Therefore, for the data collection, which requires a DAC rotations relatively to the X-rays (like, for example, in case of single-crystal XRD), the simultaneous laser-heating with stationary systems cannot be performed.

Within this thesis, we present a new Diamond Anvils with a Round Table (DART-anvils) for DACs that allow the single-crystal XRD data collection (with rotations of a DAC) during laser heating. The main features of the new DART-anvil design are a spherical shape of both the crown and the table of a diamond serving as a lens with a focal point exactly in the center of a culet. Due to that modification, the parallel laser beam passing through the DACs is always brought in the focal point independently of a DAC orientation relative to the beam. The performance of DART-anvils was tested in several high-pressure high-temperature (HP-HT) experiments at different synchrotron facilities. These experiments have demonstrated a number of advantages, which are unavailable with any of hitherto known anvils designs. Use of DART-anvils enables to perform *in situ* single-crystal X-ray diffraction experiments with laser heating using stationary laser-heating setups with which almost all high-pressure beamlines are equipped.

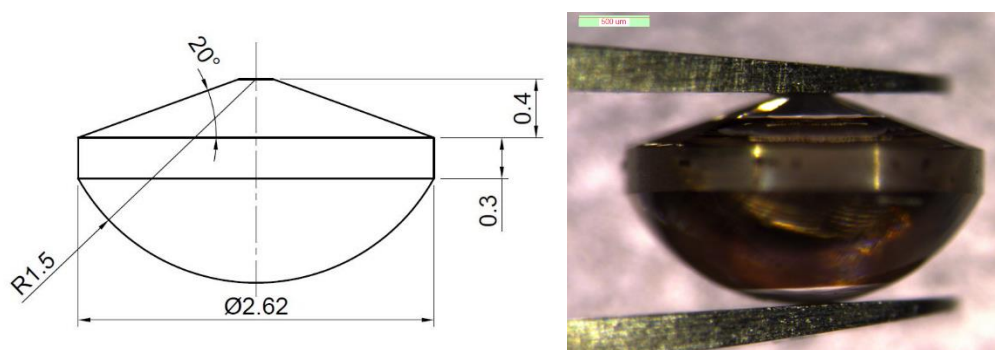


Figure 3.1-7 A schematic (left, dimensions are in mm) and a microscope image (right) of the DART-anvil (Diamond Anvil with a Round Table). (Dimensions may be scaled/adjusted in accordance with experimental needs.)



Figure 3.1-8 A series of photographs of a sample in a DAC (an iron foil in silicate perovskite at ~ 35 GPa) taken with a five-degree interval upon rotation of the DAC about the ω -axis. Beforehand the cell was aligned with respect to the rotational centre of the goniometer at 13-IDB beamline at the APS (USA). The position of the X-ray beam is marked by the yellow square. No visible changes in the position of the sample were detected upon rotation.

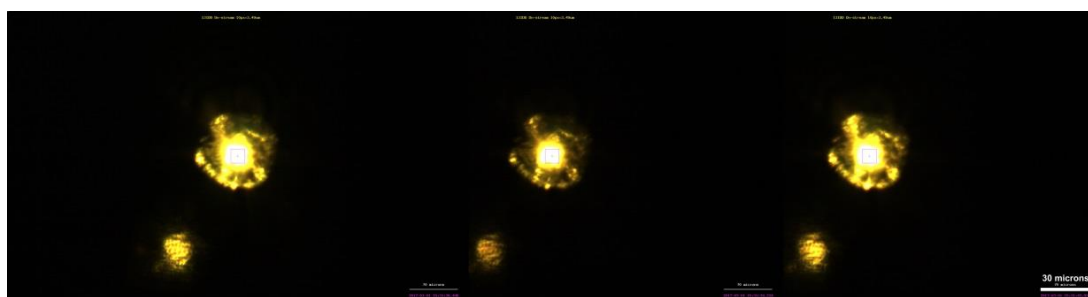


Figure 3.1-9 A series of photographs of a sample in a DAC (an iron foil in silicate perovskite at ~ 35 GPa) taken with an eight-degree interval upon rotation of the DAC about the ω -axis and simultaneous laser heating at 2300(150) K using a stationary laser. The position of the X-ray beam is marked by the square. No shift in the position of the heated spot with respect to the sample was detected upon rotation.

3.2. Brief outlook and perspectives

The Fe-O system shows complex crystallochemical behavior at extreme conditions that impacts properties of materials constituting the Earth's interior and redox processes operating within the planet. Properties, stability fields and phase diagram of iron oxides in the deep Earth are complex function of pressure, temperature, oxygen fugacity, bulk composition, and partitioning equilibria among coexisting minerals. Despite the large number of recent studies on the behavior of Fe-O system at extreme conditions, our understanding of this binary system is still incomplete.

The main goal of this thesis was to investigate the stability field of α -FeOOH (mineral goethite) at conditions of cold subducting slabs and describe structural and chemical properties of high-pressure iron oxides, particularly FeO₂, resulting from the decomposition of this material. In order to unravel the complex crystal chemistry of iron oxides and oxyhydroxides, and describe their properties at extreme conditions, we employed advanced *in situ* SC-XRD in LH-DACs technique together with XANES and Mössbauer spectroscopies. This thesis reports the decomposition of FeOOH and its impact on the early Earth's mantle; the formation of novel high-pressure iron oxides Fe₇O₁₀ and Fe_{6.32}O₉ and describes their structure and properties; discusses the chemical bonding features in FeO₂ phase.

In the framework of this thesis, we addressed several questions on the HP behavior in the Fe-O system. However, there are still a number of obscure aspects of the physical and chemical properties of this system at high pressure. The present thesis demonstrates the usefulness and power of SC-XRD experiments in laser-heated DACs and emphasizes that its future development can significantly help in unraveling the complexity of Fe-O system at extreme conditions.

3.3. List of manuscripts and statement of authors' contribution

[1] E.Koemets (EK), L.Yuan (LY), E.Bykova (EB), K.Glazyrin (KG), E.Ohtani (EO) and L.Dubrovinsky (LD). *Interaction between FeOOH and NaCl at extreme conditions: synthesis of novel Na₂FeCl₄OH_x compound (2020). Minerals. 10 (2020), doi:10.3390/min10010051.*

Conceptualization, EK and LD; DAC preparation, EK and LY; HP-HT synthesis, EK, LY and EO; In situ single-crystal XRD experiments EK, EB, KG; investigation, EK, LY, EB, KG, EO, and LD; resources, EO and LD; data curation, EK, LY, EB, EO, and LD; writing—original draft preparation, EK and LD; writing—review and editing, EK, LY, EB, KG, EO and LD; funding acquisition, EK, EO, LY, and LD.

[2] E. Koemets (EK), T. Fedotenko (TF), S. Khandarkhaeva (SK), M. Bykov (MB), E. Bykova (EB), M.Thielmann (MT), S. Chariton (SC), G. Aprilis (GA), I. Koemets (IK), K. Glazyrin (KG), H.-P. Liermann (H-PL), M. Hanfland (MH), E.Ohtani (EO), N. Dubrovinskaia (ND), C. McCammon (CM), L. Dubrovinsky (LD). *Role of FeOOH in oxygen recycling in early Earth history. On review in Nature Geoscience (2019).*

EK, ND, LD designed and planned experiments. EK, TF, SK, MB, EB, SC, GA, IK, KG, MH, H-PL and LD conducted the HP-HT single-crystal X-ray diffraction experiments. EK, EB and LD analyzed the data from HP-HT single-crystal XRD experiments. MT performed numerical calculations and interpreted the results. EK, CM, EO, ND and LD wrote the manuscript with contributions of all authors.

[3]: E. Koemets (EK), M. Bykov (MB), E. Bykova (EB), S. Chariton (SC), G. Aprilis (GA), T. Fedotenko (TF), S. Clément (SCI), J. Rouquette (JR), J. Haines (JH), V. Cerantola (VC), K. Glazyrin (KG), A. Abakumov (AA), L. Ismailova (LI), C. McCammon (CM), V. B. Prakapenka (VBP), M. Hanfland (MH), H.-P. Liermann (H-PL), V. Svitlyk (VS), A.D. Rosa (ADR), T. Irifune (TI), I. Leonov (IL), A. V. Ponomareva (AVP), I. A. Abrikosov (IA), N. Dubrovinskaia (ND), L. Dubrovinsky (LD).

Variation of oxygen oxidation state at the base of the Earth's lower mantle. Submitted to Science (2019).

EK, ND, LD designed and planned experiments. EK, SCI and JR performed cryogenic loading of a sample. EK, MB, EB, SC, GA, TF, SCI, JR, JH, KG, LI, VS, VP, MH, H-PL and LD conducted the HP-HT single-crystal X-ray diffraction experiments. EK, MB, EB and LD analyzed data from HP-HT single-crystal XRD experiments. EK, GA, SC, VC, CM collected the SMS spectra; EK, CM and LD interpreted the results. EK, GA, TF, ADR performed XANES experiments. TI has provided nanopolycrystalline diamond anvils for XANES measurements. AA performed TEM measurements on recovered samples. IL, AP, IA performed theoretical calculations and interpreted the results. EK, CM, ND and LD wrote the manuscript with contributions of all authors.

[4] Leonid Dubrovinsky (LD), Egor Koemets (EK), Maxim Bykov (MB), Elena Bykova (EB), Georgios Aprilis (GA), Anna Pakhomova (AP), Konstantin Glazyrin (KG), Alexander Laskin (AL), Vitali B. Prakapenka (VP), Eran Greenberg (EG), and Natalia Dubrovinskaia (ND). *Diamond anvils with a round table designed for high pressure experiments in DAC. High Press. Res.* **37**, 475–485 (2017).

LD and ND proposed the DART-anvil design, planned and led the research, and wrote the manuscript; EK made technical design, AL provided optical engineering expertise; MB, EB, EK, GA, AP, VP, EG, KG, and LD performed test experiments.

Chapter 4. Interaction between FeOOH and NaCl at extreme conditions: synthesis of novel Na₂FeCl₄OH_x compound

4.1. Abstract

Iron(III) oxide-hydroxide, FeOOH, is abundant in the banded iron formations (BIFs). Recent studies indicate that BIFs may carry water down to the lower mantle with subducting slabs. The previous experiments investigating the properties of FeOOH at extreme pressures (P) and temperatures (T) were performed in diamond anvil cells (DACs), where it was compressed inside alkali metal halide pressure-transmitting media (95). Alkali metal halides such as NaCl or KCl are expected to be chemically inert; therefore, they are widely used in DAC experiments. Here, we report the chemical interaction between FeOOH and NaCl pressure medium at 107(2) GPa and 2400(200) K. By means of single-crystal X-ray diffraction (SC-XRD) analysis applied to a multigrain sample, we demonstrate the formation of a Na₂FeCl₄OH_x phase and provide its structural solution and refinement. Our results demonstrate that at high P - T conditions, the alkali metal halides could interact with hydrous phases and thus cannot be used as a pressure transmitting and thermal insulating medium in DAC experiments dedicated to studies of hydroxyl or water-bearing materials at high P - T .

4.2. Introduction

Hydrous phases have been attracting great interest in the geological community due to their importance for the behavior and physical properties of the Earth's mantle (83, 148). One of such compounds, α -FeOOH (stabilized as goethite at the ambient conditions, which is a common material in the banded iron formations, or BIFs), is expected to submerge into the lower mantle with subducting slabs, bringing water to the lowermost mantle and the core-mantle boundary (CMB), as it was suggested in some publications (69, 72). Recently, a number of studies were

dedicated to studying the behavior of FeOOH at high P - T conditions, which show that FeOOH undergoes a series of phase transitions. A “pyrite-type” FeO₂H_x phase is expected to be stable at the P - T conditions of lowermost part of a mantle and core–mantle boundary (68, 69, 72, 77). This phase is attracting the attention of the community and is being intensively investigated via density functional theory calculations and spectroscopic studies (68, 77, 91, 95). In some experiments performed in DACs, alkali halides (such as KCl or NaCl, see, for example, ref. (95)) are used as a pressure transmitting medium and thermal insulator for laser heating. It is assumed that alkali halides are fully chemically inert and cannot complicate data analysis. However, at very high pressures and temperatures, the chemistry of materials may change and iron oxyhydroxide could potentially interact with the alkali halides. Information on the possible reactions between FeOOH and alkali metal halides at extreme conditions and the crystal structures of possible products is absent. Methodologically it is of great importance to verify the reactivity between these species.

4.3. Materials and Methods

A FeOOH sample (Alfa Aesar, CAS: 20344-49-4) with a lateral diameter of ~ 10 μm and thickness ~ 5 μm was loaded inside a sample chamber of a BX90-type DAC (100) equipped with two beveled Bohler-Almax type diamonds (culet diameter 80 μm). The sample chamber was made by pre-indenting Re oil-free gasket (initial thickness 200 μm , thickness after indentation ~ 15 μm) and drilling a hole of ~ 35 μm diameter in it. A NaCl powder was used as both a pressure-transmitting medium and a reactant to check its possible interaction with FeOOH. The DAC was compressed to the desired pressure (the pressure was determined using the equation of state (EoS) of B2-structured NaCl (158)) and laser-heated at BL-10XU at SPring-8 (Sayo, Hyogo, Japan) (131). The analysis of the reaction products was performed on the T -quenched sample at the P2.02 DESY beamline (159) employing the single-crystal X-ray diffraction technique for laser-heated DACs as developed at Bayreuth University (135). In order to locate the grain of a reaction product and collect the single-crystal X-ray diffraction (SC-XRD) dataset from it, the XRD mapping was

performed by scanning the sample in vertical and horizontal directions with steps of three micrometers. After localizing grain(s) of interest, the step scans were recorded on a Perkin Elmer detector (XRD1621, Waltham, Massachusetts, United States) (sets of individual photographs with equal exposure time, from 1 to 10 seconds, taken each 0.5° of DAC rotation in a range of ±36° around ω axis of the goniometer).

Analysis of collected diffraction images was performed using *CrysAlis PRO* software (Agilent Technologies, Version 1.171.37.35). The structures were solved using the dual-space method (160) and refined in the isotropic approximation by full-matrix least-squares refinements using SHELXL software package (SHELX-2019, Universität Göttingen) (160). Crystal structure visualization made with the VESTA (Version 3.4.4) software (161).

4.4. Results

The compression of FeOOH in NaCl at ambient temperature to 107(2) GPa did not result in any chemical reaction. At this pressure, after double-side laser heating of the sample at ~2400(200) K, new sets of reflections on the XRD patterns of the *T*-quenched sample were observed. Consideration of powder and single-crystal diffraction data collected from the laser-heated sample suggests that several different phases are formed in the DAC. From the powder-diffraction data (Figure 4.4-1) we identified a cubic FeO₂H_x phase with a unit cell parameter 4.403(3) Å, which is in agreement with a recent literature reports (69, 72), as well as a signal from a cubic B2-type NaCl ($a=2.911(2)$ Å) and *hcp*-structured Re ($a=2.6697(8)$ Å, $c=3.923(2)$ Å) from the gasket. Remaining peaks on the powder XRD pattern belong to an unknown phase. Through the further analysis of the single-crystal data of decent quality obtained for several grains, we were able to index reflections belonging to two different co-existing orthorhombic phases. For the first phase, we found unit cell parameters $a=2.5467(5)$ Å, $b=9.640(2)$ Å, and $c=11.580(2)$ Å, and a suggested space group *Imm2* (#44) (further denoted as “ol-phase”) as determined by analysis of the 298 unique reflections and systematic absences. Unfortunately, the intensity of the Bragg reflections of this phase is too low, and the structure solution is not possible.

For the second new phase, analysis of a single-crystal data allows determining the orthorhombic unit cell with parameters $a=8.725(2)$ Å, $b=6.180(3)$ Å, $c=3.0679(12)$ Å. Further integration of a dataset allowed extracting the intensities of 315 Bragg reflections, which belong to the single grain, and a space group *Pbam* (#55) was determined. The quality of the data (Table 1) allowed performing structure solution and refinement. We found that this phase with a chemical formula Na₂FeCl₄OH_x is the product of the chemical reaction between FeOOH and NaCl. Its crystal structure is shown in Figure 2 (crystal data, information on the data collection and structure refinement details summarized in Table 4.4-1 and Table 4.4-2). We refined atomic displacement parameters in isotropic approximation due to the limited quality of the data collected in the DAC at pressure over megabar. Due to the same reason, positions of hydrogen atoms cannot be freely refined, and we fixed H-atoms at Wyckoff 8i position with a 1 Å distance to the oxygen atoms and site occupancy fixed at 0.25.

Chapter 4. Interaction between FeOOH and NaCl at extreme conditions: synthesis of novel Na₂FeCl₄O_{H_x} compound

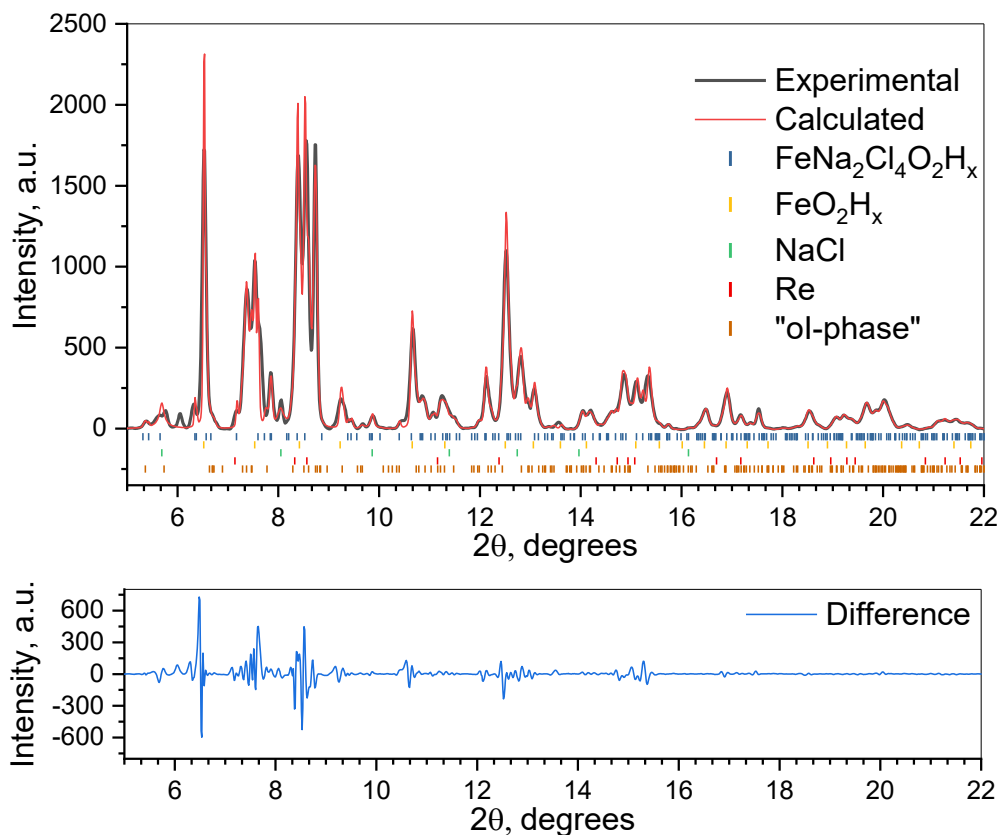


Figure 4.4-1 Le-Bail fitting of an XRD pattern of a mixture of NaCl and FeOOH at 107(2) GPa after laser-heating to 2400(200) K. Black line – convoluted experimental data from a Perkin-Elmer detector (diamond reflections masked), red line – calculated XRD signal from several phases. Color ticks below the diffraction curve represent the reflections of the phases described in a legend. Rp = 12.49 %

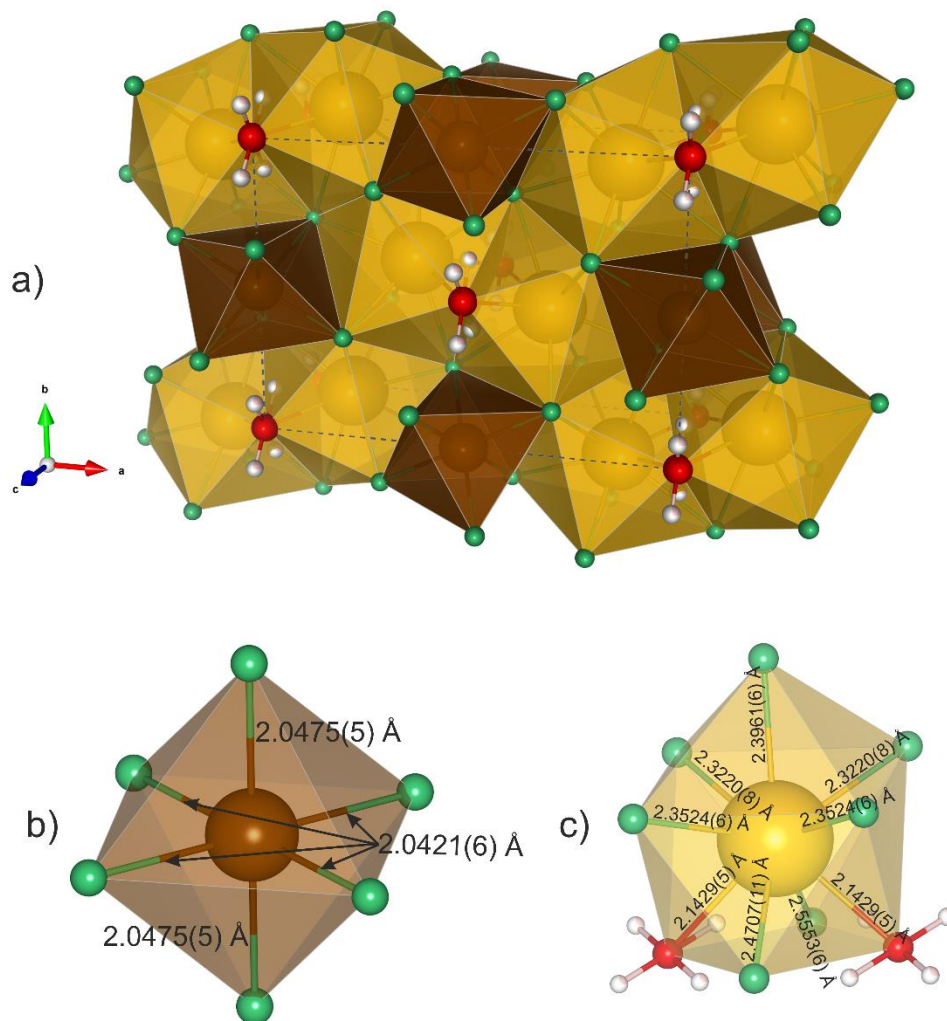


Figure 4.4-2 The crystal structure of Na₂FeCl₄OH_x at 107(2) GPa. (a) Polyhedral structural model. Yellow spheres – Na atoms, brown spheres – Fe atoms, Cl and O atoms shown as green and red spheres, correspondingly. Yellow and brown polyhedra represent the coordination of Na and Fe irons. White spheres show possible (partially occupied) positions of H atoms. Dashed black lines – unit cell boundaries. (b) Fe coordination polyhedra with bond lengths. (c) Na coordination polyhedra with bond lengths.

Table 4.4-1 Crystallographic information on the Na₂FeCl₄OH_x

Crystal Data	
Chemical formula	Na ₂ FeCl ₄ OH _x
M _r (g/mol)	260.6
Crystal system, space group	Orthorhombic, Pbam (#55)
Temperature (K), Pressure (GPa)	293, 107(2)
<i>a, b, c</i> (Å)	8.725 (2), 6.180 (3), 3.0679 (12)
<i>V</i> (Å ³)	165.41 (11)
<i>Z</i>	2
Radiation type	Synchrotron, λ = 0.2892 Å
μ (mm ⁻¹)	0.61
Crystal shape	Cube
Crystal size (mm)	0.01 × 0.01 × 0.01
Data collection	
Diffractometer	P02.2, DESY
Absorption correction	Multi-scan (ABSPACK, [15])
T _{min} , T _{max}	0.538, 1
No. of measured, independent and observed [<i>I</i> > 3σ(<i>I</i>)] reflections	894, 432, 315
R _{int}	0.038
θ values (°)	θ = 3.2–18.4
(sin θ / λ) _{max} (Å ⁻¹)	1.089
Range of <i>h, k, l</i>	<i>h</i> = -16→13, <i>k</i> = -8→10, <i>l</i> = -5→4
Refinement	
R[F ₂ > 2σ(F ₂)], wR(F ₂), S	0.070, 0.071, 2.93
No. of reflections	315
No. of parameters	27
Δρ _{max} , Δρ _{min} (eÅ ⁻³)	2.07, -1.63
Software: Crysalis PRO (132), SHELXT (126), SHELXL2014 (133)	

Table 4.4-2 Atomic coordinates in the Na₂FeCl₄OH_x structure

Atom number	Atom Name	Atomic Coordinates (x, y, z)	Occupancy	Isotropic Atomic Displacement Parameter (U, Å ²)	Wyckoff
1	Fe1	0.5, 0.0, 0.0	1	0.01	2 c
2	Cl1	0.2076, 0.3455, 0.0	1	0.012	4 g
3	Cl2	0.4251, 0.1907, 0.5	1	0.011	4 h
4	Na1	0.1645, 0.0701, 0.5	1	0.012	4 h
5	O1	0.0, 0.0, 0.0	1	0.002	2 a
6	H1	0.00380, 0.11683, 0.17495	0.25	0.0	8 i

In the orthorhombic Na₂FeCl₄OH_x compound, the iron atoms coordinated with two crystallographically distinct chlorine (Cl1 and Cl2) atoms forming just a slightly distorted octahedra (distortion index = 0.00125) with an average bond length 2.044 Å. These FeCl₆ octahedra are stacked into the columns along the *c* direction, sharing the edges (Figure 4.4-2). The Na atoms are coordinated with seven chlorine atoms and two oxygen atoms, forming a monocapped antiprismatic polyhedron (Figure 4.4-2)). Two oxygen and two chlorine atoms form a parallelogram base of antiprism (with an O1-Cl2-O1 angle of 74.42(8)°). These polyhedra are connected to each other through a common triangular and parallelogram faces and share the common edges with FeCl₆ octahedra (Figure 4.4-2)). The coordination of Na in FeNa₂Cl₄O is unusual for the Na and resembles the one described for La in LaOCl oxyhalides (162).

4.5. Discussion

While the stoichiometry of heavier atoms in the Na₂FeCl₄OH_x compound is uniquely defined by structural refinement, the amount of hydrogen is not known. One could assign common (usual) oxidation states for Na, Cl, and O atoms (+1, -1 and -2, correspondingly), but for iron as a transition metal, several oxidation states are known to range from 0 to the +4. The trivial charge balance considerations could not be easily implemented: the refinement of hydrogen atoms' positions and occupancies directly from the SC-XRD data is a complex task even at ambient conditions; for the experiments performed in the DACs, it is practically impossible in the most

cases. Mössbauer or X-ray absorption near edge structure (XANES) spectroscopies could help to define the oxidation state of iron and therefore establish the amount of hydrogen in phase; however, in case of multi-phase samples, the interpretation of spectroscopy data would be most probably ambiguous.

Another way would be to perform the crystallochemical analysis and compare the bond distances in Na₂FeCl₄OH_x with Fe-Cl distances in other known compounds. Unfortunately, such a type of analysis is greatly complicated by very limited data on the high-*P* behavior of Fe,Cl-bearing compounds. By fitting the pressure-volume literature data on Fe²⁺Cl₂ and Fe³⁺OCl with the Birch-Murnaghan equation of state (EoS), we described the Fe-Cl bond evolution in FeCl₆ octahedra upon compression. Assuming that the structures of these compounds remain the same at high pressures, we compare extrapolated Fe-Cl bond lengths for Fe²⁺Cl₂ and Fe³⁺OCl and our experimental values at 107 GPa (Figure 3). The observed average Fe-Cl bond length in FeCl₆ octahedra in the Na₂FeCl₄OH_x is 2.044 Å (see above). Extrapolated values for the Fe-Cl contact in FeOCl and FeCl₂ are ~2.6 Å and ~2.0 Å at 107 GPa.

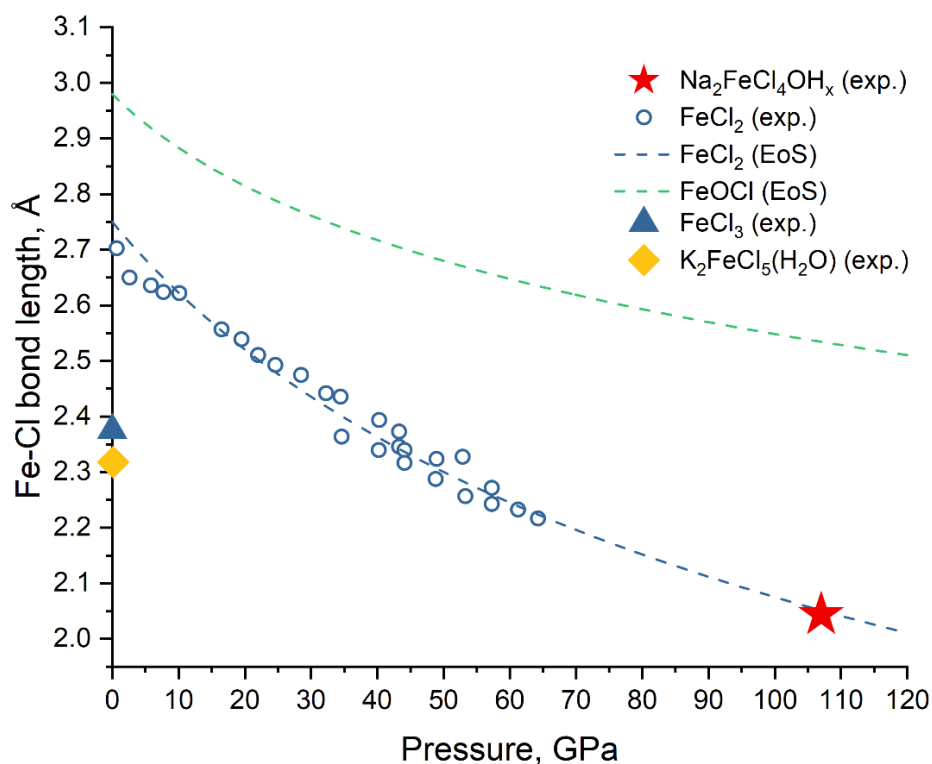


Figure 4.5-1. The estimation of a Fe-Cl bond length in different compounds at high pressures. FeCl₂ data are from (163), FeOCl - from (164). Experimental values of Fe-Cl bond length for FeCl₃ and K₂FeCl₅H₂O are from (165) and (166), correspondingly. Red star – experimental point for Na₂FeCl₄OH_x

While the coordination of iron in FeOCl is not the same as in Na₂FeCl₄OH_x and the extrapolated Fe-Cl bond length is much higher, the iron in FeCl₂ is coordinated similarly, and the estimated Fe-Cl bonds of ~2 Å are very close to the observed Fe-Cl contact in our experiment. Therefore, one could suggest that iron in Na₂FeCl₄OH_x is in the 2+ oxidation state, and therefore x=2. Still, the iron oxidation state 3+ cannot be excluded: the reported values of Fe-Cl bond lengths for ferric iron in Fe³⁺Cl₆ octahedra of FeCl₃ and K₂FeCl₅(H₂O) compounds are obviously much lower than those of ferrous iron chlorides at ambient conditions are. Unfortunately, the lack of information on the compressibility of Fe³⁺ atoms octahedrally coordinated by Cl does not allow us to estimate

the Fe-Cl distances at 107(2) GPa. Therefore, our crystallochemical considerations cannot confidently assign an oxidation state to the Fe atoms.

4.6. Conclusions

Our results demonstrate that at high *P-T* conditions sodium halide reacts with FeOOH forming a novel FeNa₂Cl₄OH_x compound. Thus, the alkali metal halides could interact with hydrous phases and thus cannot be used as a pressure-transmitting and thermal-insulating medium in DAC experiments dedicated to studies of hydroxyl or water-bearing materials at high pressure – high temperature conditions.

Supplementary Materials: The following are available online at <http://>, Figure S1: Representative X-ray diffraction pattern collected after laser-heating of FeOOH in NaCl at 2000(200) K and 107(2) GPa ($\lambda = 0.2892 \text{ \AA}$, P02.2 beamline at PETRAIII). (a) As collected 2D XRD image acquired with Perkin-Elmer detector during rotation of the DAC from -20° to $+20^\circ$ around the ω axis (“wide scan”). (b) Rolled up (“cake”) representation of a selected 2D wide scan XRD pattern. Figure S2: Examples of reconstructed reciprocal planes for one of the domains of Na₂FeCl₄OH_x phase at 107(2) GPa. (a), (b), and (c) panels show (hk-1), (h1l), and (2kl) planes correspondingly.

Acknowledgments: Authors thank the Deutsches Elektronen-Synchrotron for the provision of synchrotron beamtimes (P02.2). Authors are grateful for the SPring-8 for provision of synchrotron beamtime at BL10XU.

4.7. Supplementary materials

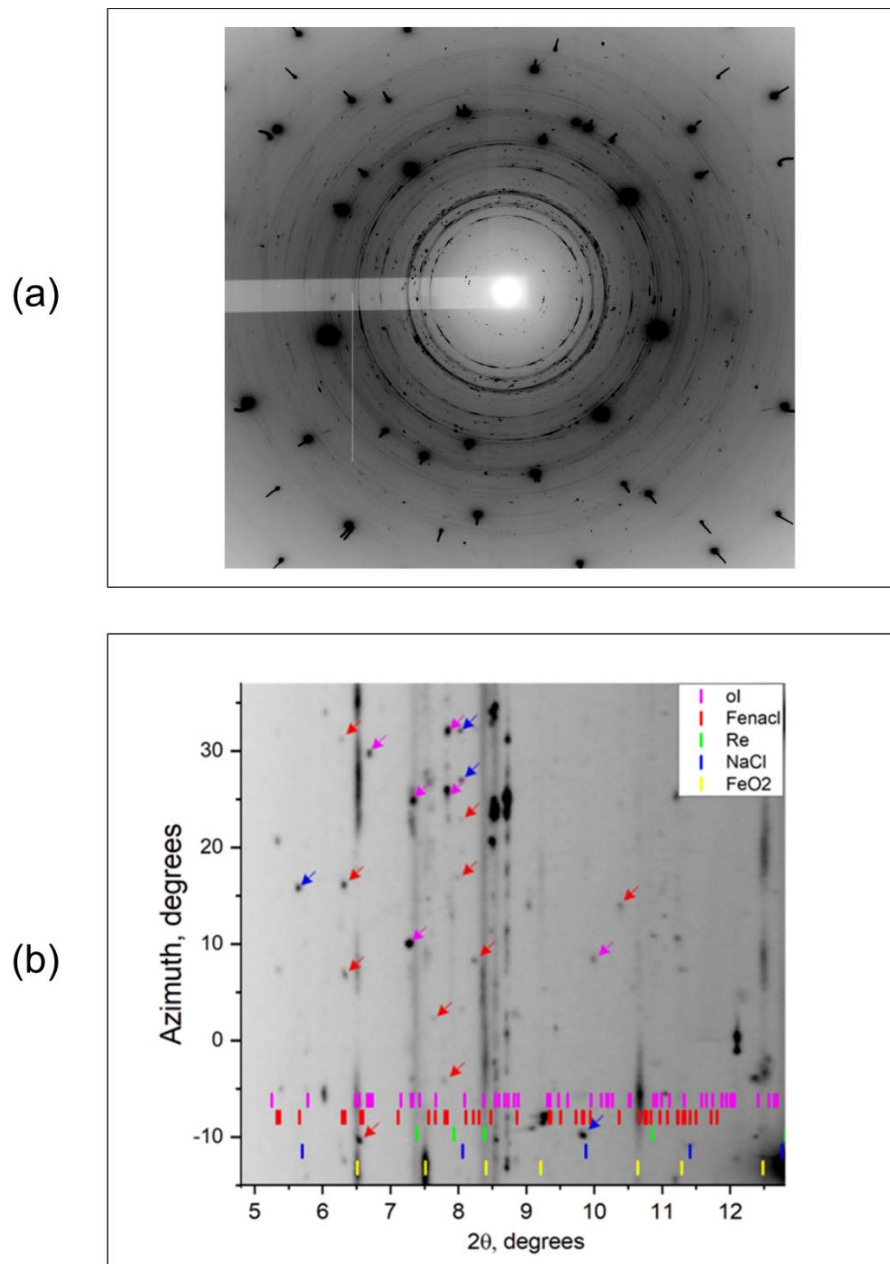


Figure 4.7-1 The 2d representation of XRD signal of FeOOH after laser heating to 2000(200) K at 107(2) GPa. (a) Raw XRD image from Perkin-Elmer detector during the rotation of a DAC from -20° to +20° around the ω axis. $\lambda=0.2892$ Å. (b) Selected 'cake' representation of a 2d raw image of XRD from the sample. The colorful ticks in the

Chapter 4. Interaction between FeOOH and NaCl at extreme conditions: synthesis of novel Na₂FeCl₄OH_x compound

bottom part of a picture denote the position of Bragg's reflections of phases, the colorful arrows denote a signal from single-crystal domains of crystalline phases (color codes are described in a legend).

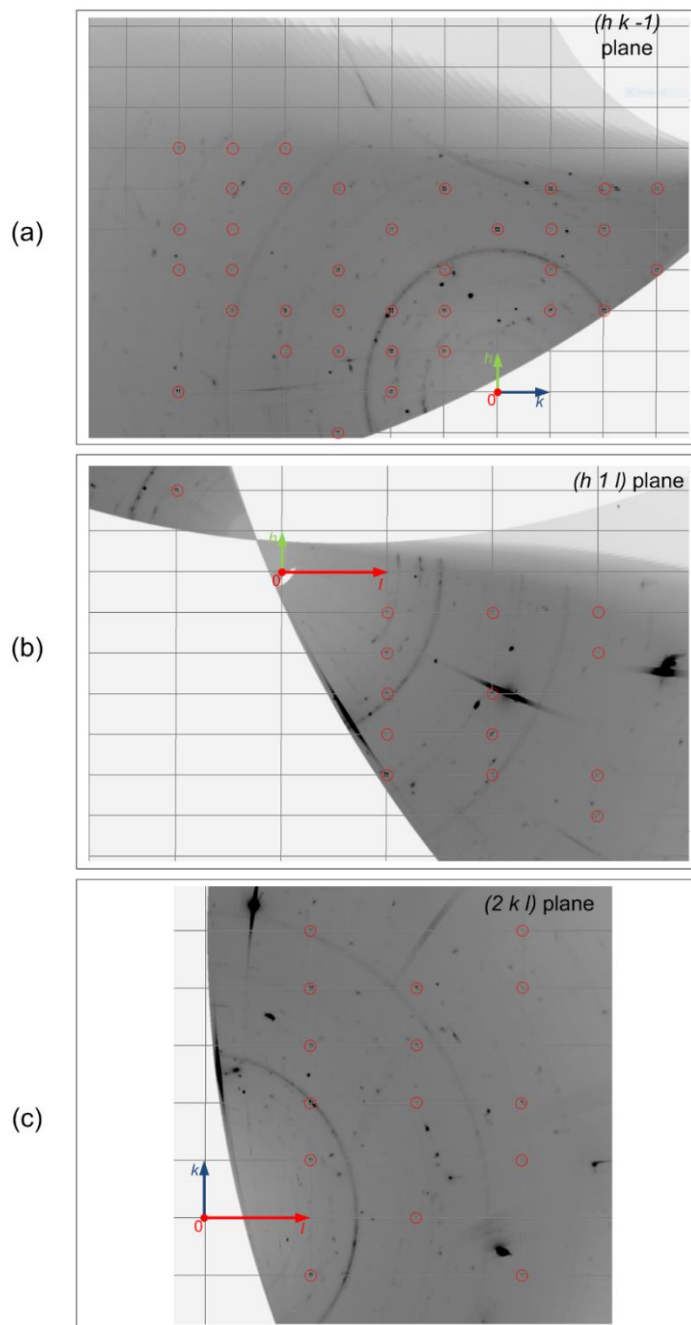


Figure 4.7-2 The selected reconstructed reciprocal planes for one of a domains of Na₂FeCl₄OH_x phase at 107(2) GPa. (a), (b) and (c) panels represent $(hk-1)$, $(h1l)$ and $(2kl)$ planes correspondingly. Grey grid and colorful arrows

represent the reciprocal lattice and its basis vectors correspondingly and serve as a guide for the eye. Red circles denote the positions of reflections. Additional features on the reconstructions are produced by the diffraction from different grains of phases present in the sample, and sample surroundings (diamonds, Re gasket and B2-type NaCl P-transmitting medium).

Chapter 5. Role of FeOOH in oxygen recycling in early Earth's history

5.1. Abstract

Goethite, α -FeOOH, is a major phase among oxidized iron species, commonly called rust, which can be formed in many ways including as a byproduct of anoxygenic prokaryote metabolism (65, 66) that took place from about 3.8 billion years (Ga) ago until the Great Oxidation Event (GOE) roughly 2.2 Ga ago. Rust was buried on the ocean floor (65, 66) and was transported into the mantle as a consequence of plate tectonics that started at least 2.8 Ga ago (10). The fate and the geological role of rust at pressure and temperature conditions of the lower mantle have been unknown up to now. We studied the behavior of FeOOH up to 82(2) GPa and 2300(100) K using *in situ* synchrotron single-crystal X-ray diffraction. At these conditions, which correspond to the coldest slabs at depths of about 1000 km, α -FeOOH decomposes to iron oxides (Fe_2O_3 , Fe_5O_7 , Fe_7O_{10} , $\text{Fe}_{6.32}\text{O}_9$) and an oxygen-rich fluid. Our results suggest that recycling of rust in Earth's mantle could contribute to oxygen release to the atmosphere and explain the sporadic increase of oxygen levels before the GOE that have been linked to the formation of large igneous provinces(151).

5.2. Introduction

Water and water-bearing species have a strong impact on both life on Earth as well as numerous processes in Earth's interior (29, 148). The presence of water affects properties of mantle minerals and causes large-scale global phenomena such as arc volcanism and plate tectonics (73–75). Mechanisms of water circulation between geospheres are crucial for

understanding geodynamic and geochemical cycles, but still remain actively debated and discussed (148). Recent studies suggest that iron-bearing minerals present in Banded Iron Formations (BIFs), such as goethite, could transport water to Earth's deep interior through subducting slabs (68–70). Hu et al. (69) and Nishi et al. (71) reported that FeOOH remains stable in the sinking slab until it reaches the lowermost part of the lower mantle. Their studies revealed by means of *in situ* powder X-ray diffraction that at pressures corresponding to depths of ~1500–1800 km and at moderately high temperatures, FeOOH undergoes a phase transition to form the stable pyrite-type phase FeO_2H_x with $0 \leq x \leq 1$ (Py-phase) (69, 72). Goethite and its high-pressure polymorphs have therefore been considered to be candidates for water and/or hydrogen transfer to the lower mantle and the core-mantle boundary (68). While FeOOH was intensively studied at the conditions of the upper mantle and core-mantle boundary, there is a lack of data on its behavior in the P-T range between these values. Here we present a detailed study of the behavior of FeOOH at conditions of the subducting slab using advanced *in situ* single-crystal X-ray diffraction (XRD) techniques in laser-heated diamond anvil cells (LH-DACs).

The behavior and stability of hydrous phases at specific depths depend on their pressure-temperature (P-T) conditions. While the pressure profile of Earth's interior is well defined (14), the temperature distribution within subducting slabs remains the subject of discussion (167). Thus, a reliable estimation of slab geotherms is a key question in studying the stability of FeOOH and its transport to the lower mantle. Recent studies on FeOOH stability (69) were performed at “cold slab” conditions, suggesting that the temperature inside the slab barely reaches 1700 K at 120 GPa (~2700 km depth). This estimation of the slab geotherm was based on the extrapolation of data of Eberle et al. (168), who modeled slab behavior to depths of only about 800 km.

A simple extrapolation of slab temperature from 800 to 2900 km is problematic, however, and leads to underestimation of temperature and large errors. We, therefore, estimated the lower boundary of temperature distribution in sinking slabs by numerical modeling calculations (see *Supplementary Information* for details). According to geodynamic analysis (169), the average vertical velocity of sinking slabs (as a component of angular slab immersion speed towards the

core, not to be confused with the plate speed) can hardly be higher than 1 cm/year (“cold slab”), but we also considered the case of 2 cm/year (“ultra-cold slab”) to estimate the lowest possible temperatures across the slab. The results of the temperature estimation (Figure 5.3-1) provide constraints on the pressure-temperature conditions for LH-DAC experiments aimed at investigation of FeOOH stability in the present work (see *Methods*, Table 5.6-1).

5.3. Experimental results

We performed a series of *in situ* synchrotron single-crystal XRD experiments in LH-DACs at pressures up to about 81 GPa and over a wide temperature range (Figure 5.3-1, Table 5.6-1). Heating a starting FeOOH crystal to 1500(100) K at 40(2) GPa (run 1, Table 5.6-1), corresponding to the P-T conditions of a cold slab at ~1000 km depth, leads to a transformation of initial α -FeOOH to ϵ -FeOOH (space group *Pnmm*) and its partial decomposition that forms the Rh₂O₃-II type structured iron oxide ι -Fe₂O₃ (25, 53) (Figure 5.3-1, Table 5.6-2, Figure 5.3-2). At a slightly higher temperature of 1600(100) K at 41(2) GPa (run 2, Table 5.6-1), the decomposition yields two iron oxides: ι -Fe₂O₃ and monoclinic Fe₅O₇ (53) (Figure 5.3-1, Table 5.6-2, Figure 5.3-2). Heating at 52(1) GPa and 1200 K (run 3.1, Table 5.6-1) results in the formation of three iron oxides: Fe₅O₇ and η -Fe₂O₃ (CaIrO₃-type Fe₂O₃ (53)) and an additional hexagonal phase (Figure 5.3-1, Table 5.6-2, Figure 5.3-2). The latter phase, according to single-crystal XRD, has chemical composition Fe_{6.3}O₉ and the hollandite-like structure (NaLi₂Ru₆O₁₂ (170)) (Figure 5.3-1, Figure 5.3-2, Figure 5.6-4 and supplementary information (SI)). Heating another FeOOH crystal in the same DAC at 1550(100) K (run 3.2, Table 5.6-1) leads to the formation of η -Fe₂O₃ and Fe₅O₇, while no traces of Fe_{6.32}O₉ are detected (Figure 5.3-1). Heating FeOOH (run 3.3, Table 5.6-1) at about 2000 K at 52(1) GPa leads to the formation of a single iron oxide, orthorhombic HP-Fe₃O₄ (53) (Figure 5.3-1, Table 5.6-2, Figure 5.3-2). During experiments at 64(2) GPa we observe the decomposition of FeOOH with formation of η -Fe₂O₃ at 1500(100) K (run 4, Table 5.6-1). On further iterative heating of the sample to 2100(100) K (run 4, Figure 5.3-1, Table 5.6-1) we observe formation of η -Fe₂O₃ and novel orthorhombic iron oxide, Fe₇O₁₀ (space group *Cmcm*), (Figure 5.3-2, Table 5.6-2 and SI). On laser heating at 81(2) GPa and 1500(100) K (run 5, Figure

5.3-1) FeOOH transforms into cubic FeO_2H_x as reported earlier (69) and partially decomposes into $\eta\text{-Fe}_2\text{O}_3$ and $\text{Fe}_{6.32}\text{O}_9$. Cubic FeO_2H_x has a unit cell volume that is larger than that of hydrogen-free FeO_2 ($86.94(8) \text{ \AA}^3$ versus $81.7(2) \text{ \AA}^3$ (72), respectively) so that the estimated amount of hydrogen incorporated into the structure (x) is calculated to be 0.64(5) if consider FeO_2 and FeO_2H as the end-members (86, 171).

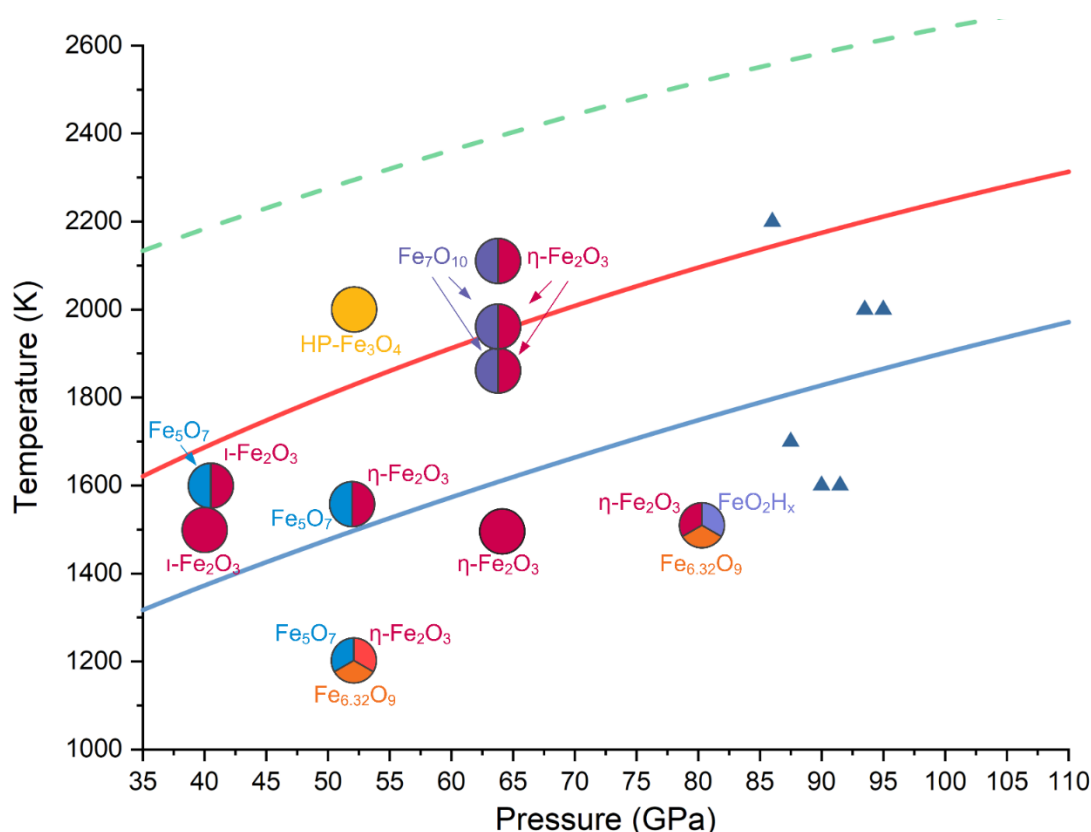


Figure 5.3-1 **Experimental conditions of high P-T treatment of FeOOH and results of phase analysis.** The position of filled circles represents P-T conditions of FeOOH treatment; different colors represent phases synthesized at these P-T conditions (sector size is arbitrary). Error bars of pressure are within the size of the symbols. Blue solid triangles represent synthesis conditions of FeO_2H_x according to (70). The dashed green line is a mantle geotherm (149), while solid red and blue lines are the calculated lowest temperatures across slabs sinking at vertical speeds of 1 and 2 cm/year, respectively (for details see Supplementary Information). We observed goethite decomposition that formed previously described $l\text{-Fe}_2\text{O}_3$, $\eta\text{-Fe}_2\text{O}_3$, $\text{HP-Fe}_3\text{O}_4$, and Fe_5O_7 , and newly reported mixed-valence iron oxides Fe_7O_{10} and $\text{Fe}_{6.32}\text{O}_9$. Formation of iron (II,III) oxides with release of oxygen upon treatment of Fe_2O_3 at pressures well above 50 GPa and heating over 2700 K was reported by Bykova et al. (18). We observed appearance of iron(II)

bearing oxides (particularly Fe_5O_7 , Fe_7O_{10} , $\text{Fe}_{6.32}\text{O}_9$, etc.) at significantly lower pressures and temperatures than those required for decomposition of pure Fe_2O_3 . This suggests that water is either directly involved in or facilitates the reduction of ferric iron. Thus, water- and ferric iron-bearing phases become unstable upon heating at high pressure due to self-redox reactions.

Summarizing our experimental observations, we have found that FeOOH is not stable even at relatively low temperatures (see Figure 5.3-1, Table 5.6-1). In the pressure range 40-81 GPa and temperatures of 1200-2100 K, it decomposes to form various iron oxides: ι - Fe_2O_3 , η - Fe_2O_3 , HP- Fe_3O_4 , and Fe_5O_7 as previously reported in the literature (53), and Fe_7O_{10} and $\text{Fe}_{6.32}\text{O}_9$ as newly described in the present work. Due to the potential inhomogeneity of experimental conditions in LH-DACs, the question of thermodynamic stability and equilibrium of the phases observed at specific P-T conditions remains unclear. Nevertheless, our observations unambiguously indicate that one or more oxidation-reduction reactions occur that produce Fe^{2+} .

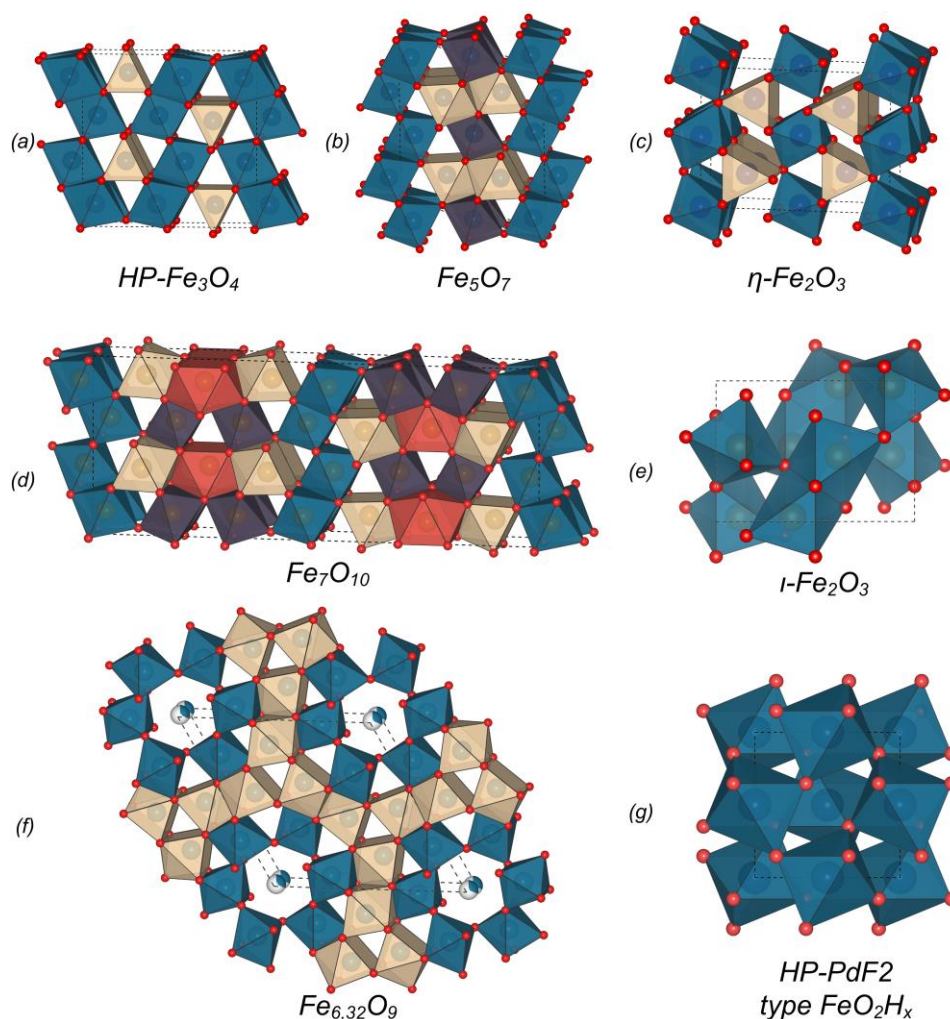


Figure 5.3-2 Structures of iron oxides synthesized from goethite during high P-T treatment based on in situ single-crystal XRD. Blue spheres are iron atoms while red spheres are oxygen atoms. Building blocks are octahedra (blue and dark purple) and trigonal prisms (pale yellow and orange). (a) $HP\text{-Fe}_3\text{O}_4$ (Bbmm) with the CaTi_2O_4 structural type, where edge-shared FeO_6 octahedra are ordered in a zigzag motif and interconnected via stacking layers of triangular prisms with shared bases; (b) Fe_5O_7 ; (c) post-perovskite $\eta\text{-Fe}_2\text{O}_3$; (d) novel Fe_7O_{10} ($\eta\text{-Fe}_2\text{O}_3$ and Fe_7O_{10} are members of the homologous series $\text{FeO} \cdot m\text{Fe}_2\text{O}_3$ (53), where prisms are connected through common triangular faces and octahedra are connected only via shared edges); (e) $\iota\text{-Fe}_2\text{O}_3$ with the $\text{Rh}_2\text{O}_3\text{-II}$ structure type (25, 53); (f) novel $\text{Fe}_{6.32}\text{O}_9$ which can be described as hexagonal hollandite-like, with chains of apices-sharing FeO_6 octahedra forming hexagonal channels that are partially occupied by iron cations. A three-dimensional framework of mono-capped prisms separates the channels. (g) FeO_2H_x (Pa-3) with the HP-PdF₂-type structure. The apices-sharing FeO_6 octahedra form a framework in which the shortest O-O distance is 2.267(5) Å at 82(1) GPa. For details of the crystal structures of Fe_7O_{10} , $\text{Fe}_{6.32}\text{O}_9$, and FeO_2H_x see Supplementary Materials.

5.4. Discussion

In order to explore the possibility that hydrogen is present in the resulting mixed-valence iron oxides, we analyzed their densities based on XRD experimental data (Figure 5.4-1). Incorporation of hydrogen into the structure drastically affects density, for example, at 40(2) GPa the density of hydrogen-bearing ϵ -FeOOH (5.34 g/cm³, (172)) is significantly lower than that of hydrogen-free FeO₂ (6.59 g/cm³, (72)). The density of ι -Fe₂O₃ (6.25 g/cm³) synthesized from FeOOH at 40(2) and 41(2) GPa matches the value for hydrogen-free iron oxide (53) at the same pressure within experimental uncertainty. Fe₅O₇ synthesized at 41(2) GPa can be approximated as a mechanical mixture of FeO (173) and Fe₃O₄ (174), so its density should be an average of FeO and Fe₃O₄ values. If it were hydrogen-free, its density should be 6.50 g/cm³, which matches well the experimental value of 6.48 g/cm³ for Fe₅O₇. These density considerations strongly suggest that iron oxides obtained in the present work do not contain a significant amount of hydrogen (Figure 5.4-1). Densities of the new phases, Fe₇O₁₀ and Fe_{6.32}O₉, match the linear composition-density trend established for various hydrogen-free iron oxides at the appropriate pressures (Figure 5.4-1). Notably, Fe₇O₁₀ synthesized at relatively high temperatures (Figure 5.4-1, Table 5.6-2) is even slightly denser than expected from the trend (Figure 5.4-1). The smaller density of Fe_{6.32}O₉ might indicate that the material contains a small amount of hydrogen located, for example, in channels of the structure (Figure 5.3-2), but even if it were present, the amount of hydrogen in Fe_{6.32}O₉ would be very small. Since this phase was not observed at temperatures higher than 1500 K (Figure 5.3-1), it is unlikely to carry water into the deep interior.

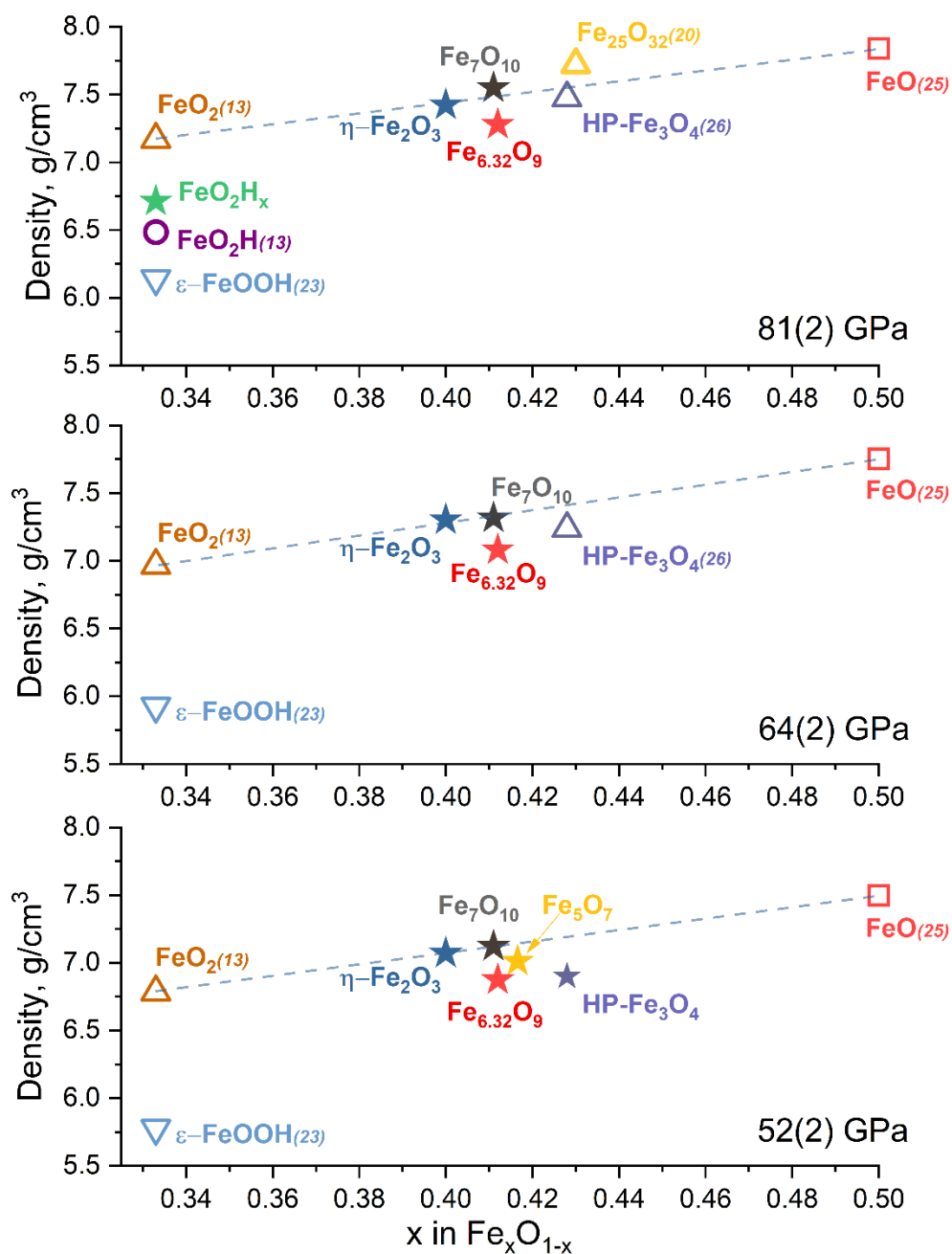
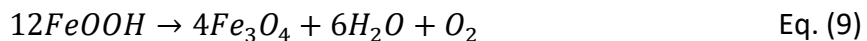


Figure 5.4-1 Density of iron-oxygen compounds as a function of chemical composition at high pressure. Data were collected at 300 K and the pressures indicated. Solid stars represent iron oxides obtained in the present work, while open symbols indicate literature data. Error bars are less than the size of symbols which are as follows: purple triangles – HP-Fe₃O₄ calculated from EOS (174); yellow triangle – Fe₂₅O₃₂ at 80.1(5) GPa (53); blue stars – η-Fe₂O₃; red squares – cubic FeO calculated from EOS (173); blue inverted triangles – ε-FeOOH calculated from EOS (171); brown triangles – FeO₂ calculated from EOS (71); purple open circle – FeO₂H (71). Dashed blue lines are guides for

the eye showing the density-stoichiometry dependence for iron oxides that connect FeO and FeO₂ end-members. Densities of previously unknown iron oxides synthesized in the present work do not deviate significantly from this trend, leading to the conclusion that these iron oxides are nominally anhydrous. This highlights the dehydration/dehydrogenation of FeOOH during its decomposition.

Our observations have important implications for water transport (as H-bearing component(s) of complex oxides) into the lower mantle and geochemistry of Earth's interior. We observed that FeOOH is not stable at depths of 1000 km, not even at conditions of "super-cold" slabs, hence iron oxyhydroxide is unlikely to be the carrier of water to deep Earth regions such as the bottom of the lower mantle and the core-mantle boundary under realistic slab subduction conditions.

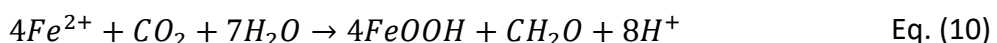
The appearance of iron(II)-bearing oxides (particularly Fe₅O₇, Fe₇O₁₀, Fe_{6.32}O₉, etc.) can lead to release of free oxygen by analogy with the high P-T behavior of Fe₂O₃ reported by Bykova et al. (53). Considering that Fe₃O₄ has the highest amount of Fe²⁺ among observed compounds, schematically this process can be described as:



Since this process for FeOOH is observed at significantly lower pressures and temperatures than required for decomposition of pure Fe₂O₃ (53), water is either directly involved in or facilitates the reduction of ferric iron. Thus, we propose that water- and ferric iron-bearing phases become unstable upon heating at high pressure due to self-redox reactions.

Our experiments demonstrate that the depth of 1000 km acts as a "chemical boundary" below which water- and ferric iron-bearing compounds produce an oxidizing fluid. Different phases of FeOOH are obvious candidates as the source of such a fluid, but in the present day the amount of iron(III) oxyhydroxides on Earth's surface is too small to be considered a global geochemical component. This situation may have been different in the past, however. Before the advent of oxygenic photosynthesis, Earth's biosphere was driven by anaerobic metabolism starting from about 3.8 Ga ago as evidenced by the earliest preserved marine sediments (65). During this period, iron(III) oxyhydroxides were probably a common byproduct of the vital functions of iron-

oxidizing phototrophs (65). Schematically, this process in early oceans can be expressed (65) by the following reaction:



where "C·H₂O" denotes organic material produced in biochemical processes.

The amount of ferric iron produced and buried as a result of ferrous iron oxidation due to anoxygenic photosynthesis is estimated to be $1.1 \cdot 10^{13}$ mol/year (65). If the predominant mineral form of ferric iron in sediments was FeOOH (commonly called "rust" (150)), it would take less than 5 Ma to accumulate the amount of oxygen present in the modern atmosphere.

When plate tectonics became active (currently considered to have started 3.2 to 2.5 Ga ago, (10)), subduction brought sediments rich in iron oxyhydroxides down to Earth's deep interior (Figure 5.4-2). Even if some part of subducted FeOOH-bearing sediments were consumed by metamorphic processes and reactions with surrounding mantle material, the same arguments that favor their preservation during subduction hold, as well as those relevant for banded iron formations (BIFs) sinking down to the core-mantle boundary(53, 175). Assuming that the sinking speed was the same as in modern slabs (around 1 cm/year for the vertical component of slab subduction speed), the time needed to reach 1000 km was only 0.1 Ga. Thus, a significant part of FeOOH-enriched material produced by phototrophs could reach the "chemical boundary" and release oxygen-rich fluids. These oxidizing fluids rising to Earth's surface could then contribute to (or even be one of the main causes of) the sequence of events known as the Great Oxidation Event (GOE). As demonstrated by recent studies (151), the GOE is a time-distributed process that occurred about 2.5 Ga ago and is associated with the formation of large igneous provinces. Additionally, recent studies on Xe isotope distribution (176–178) that suggest massive mantle degassing ~2.7-2.5 Ga ago support the hypothesis of oxygen release from the lower mantle.

Our hypothesis implies that formation of Earth's oxygen-rich atmosphere resulted from processes in the early anaerobic biosphere, plate tectonics, and decomposition of ferric iron

oxyhydroxides in Earth's mantle. The oxygen-based life that we know today could be the result early life forms adapting to the rising oxygen content in the atmosphere due to geological processes.

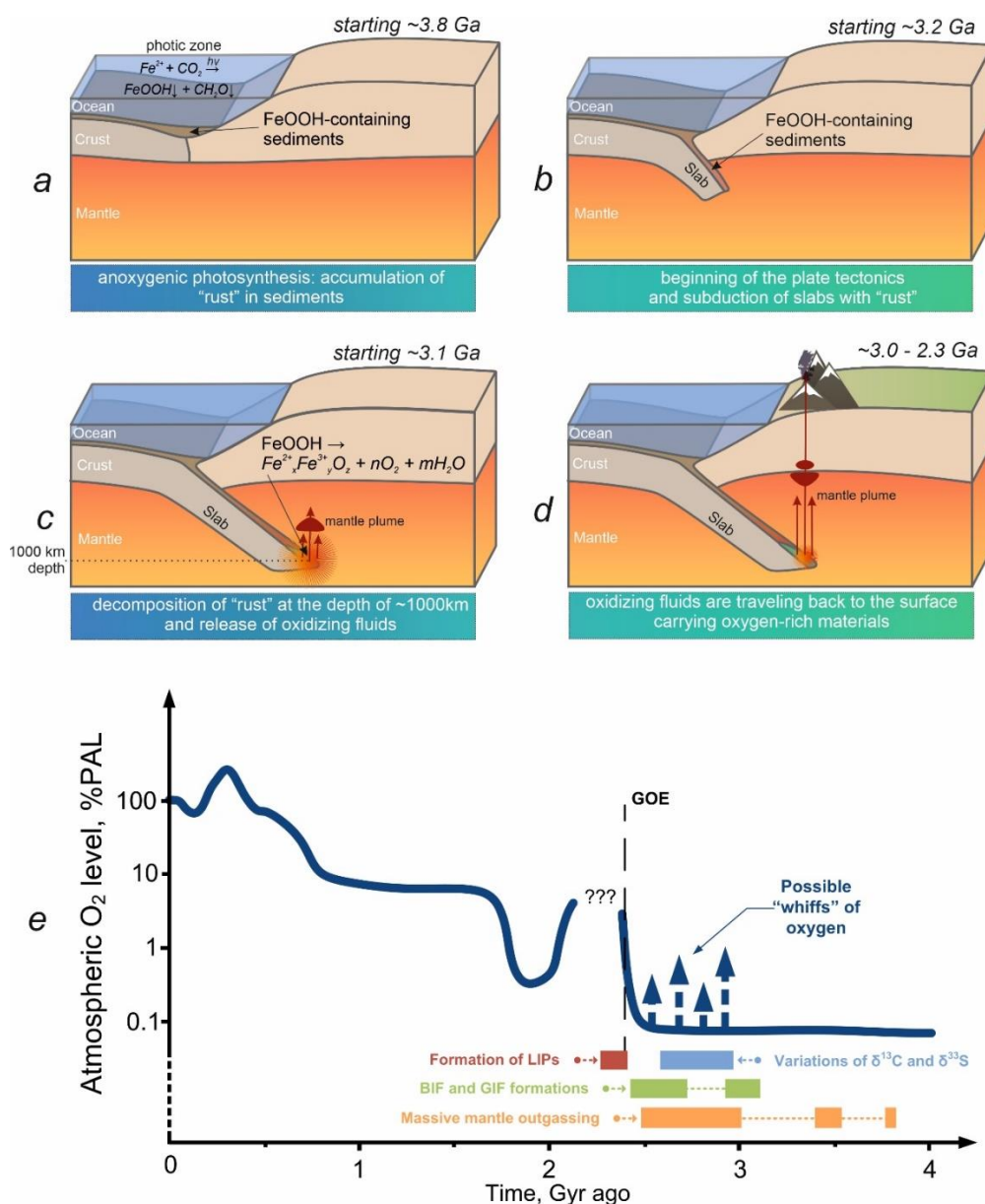


Figure 5.4-2 Schematic illustration of accumulation and recycling of iron oxyhydroxide-rich materials in Earth's mantle and relation to the Great Oxidation Event (GOE). The vertical depth scale is exaggerated. (a) Accumulation of FeOOH in sediments starting ~3.8 Ga ago (65) and driven by anoxygenic early life. (b) Beginning of plate tectonics 3.2 – 2.5 Ga ago. Subducting slabs containing FeOOH sank into the mantle. The estimated time required for a slab

descending to 1000 km depth at 1 cm/year vertical speed is ~ 0.1 Ga. (c) Reaching 1000 km, FeOOH starts to decompose into iron oxides and water/oxygen. Further sinking intensifies this process. (d) Finally, oxygen-rich fluids were released to the Earth's surface through uprising plume(s). This process is estimated to have a duration of ~ 0.1 Ga, which is similar to the subduction speed. The proposed cycle should therefore take place roughly 0.8 – 1 Ga after the appearance of the first anoxygenic life. (e) History of atmospheric oxygen concentration modified after (179). Before the GOE ~ 2.4 Ga ago, oxygen fluctuations may have taken place as evidenced by carbon and sulfur isotope variations (180), as well as the appearance of banded and granulated iron formations (150). Recent studies on Xe isotopes suggest that massive mantle degassing occurred before the GOE (176–178); additionally, significant mantle outgassing is associated with the formation of LIPs that occurred at the beginning of the GOE.

5.5. Methods

5.5.1. Sample preparation and DAC assembly

Single crystals of natural goethite with an average size of $\sim 0.01 \times 0.01 \times 0.01$ mm³ (172) were used in this study. In all runs, crystals were placed inside BX-90 diamond anvil cells (DACs) (100) equipped with Boehler-Almax type anvils. We used oil-free Re gaskets pre-indented to ~ 20 μ m thickness. Sample chambers with diameter half the diameter of anvil culets were drilled into gaskets using a laser. The cells were loaded with Ne as a pressure-transmitting medium using the gas-loading system installed at Bayerisches Geoinstitut. Pressure determination inside the DAC was performed using the Raman shift of diamond (109) and the equation of state (EOS) of Ne (158). All cells were cold compressed to the desired pressure and then goethite crystals were heated using different laser-heating systems. Subsequently, the samples were investigated *in situ* using synchrotron source single-crystal XRD. For more technical details, please see supplementary Table 5.6-1.

5.5.2. X-ray diffraction

The single-crystal XRD experiments were conducted on the ID15B beamline at the European synchrotron radiation facility (ESRF), Grenoble, France (MAR555 detector, $\lambda=0.4126$ – 0.4130 Å) and on the extreme conditions beamline P02.2 at PETRA III, Hamburg, Germany (PerkinElmer XRD1621 flat panel detector, $\lambda=0.2898$ – 0.2902 Å). The X-ray spot size depended on the beamline

settings and varied from 4 to 30 μm diameter, where typically a smaller beam was used for laser heating experiments. A portable double-sided laser heating system was used for experiments on ID15B (ESRF) to collect *ex situ* single-crystal XRD. A state-of-the art stationary double-sided laser heating set-up at P02.2 (PETRA III) was used for *in situ* high temperature single-crystal XRD along with temperature-quenched single-crystal XRD. The laser spot size on the sample covered the entire crystal and there were no measurable temperature gradients within the samples. In the case of prolonged heating experiments, temperature variation during the heating did not exceed ± 100 K. Pressures before and after laser heating were determined using the EOS of Ne (158). XRD images were collected during continuous rotation of DACs typically from -38° to $+38^\circ$ on ω , while data collection experiments were performed by narrow 0.5° scanning of the same ω range.

5.5.3. Data analysis

The goethite single crystal starting material gave characteristic Bragg peaks in the diffraction pattern after laser heating in solidified neon; however we also clearly observed well defined, sharp diffraction spots belonging to multiple grains of other high-pressure phases. Using the Ewald^{Pro} reciprocal space viewing tool for CrysAlis^{Pro} software (132), we were able to identify the diffraction spots belonging to specific domains, find their matrices of orientation and refine the unit cell parameters within subsequent intensity extractions (data integration). The crystal structures were solved using SHELXT software that employs a dual-space algorithm for the solution of a phase problem (160). The general output of the structure solution program was the crystallographic position(s) of iron atom(s), while the locations of oxygen atoms were assigned based on analysis of residual electron density maps. Crystal structures were refined against single-crystal XRD using JANA2006 software (see Table 5.6-2 for crystallographic information on the phases in the present paper). The general procedure for the analysis of multigrain diffraction datasets is described in (135).

5.6. Supplementary information

Table 5.6-1 Description of synchrotron XRD experimental runs

Run No	Anvil size, μm	P, GPa	T, K	Crystal No	Observed phases	Facility	XRD regime	Actions after synthesis
1	250	40	1500	1	$\eta\text{-Fe}_2\text{O}_3$ $\varepsilon\text{-FeOOH}$	DESY P2.02	<i>in situ</i> <i>ex situ</i>	T-quench
2	250	41	1600	1	$\eta\text{-Fe}_2\text{O}_3$ $\varepsilon\text{-FeOOH}$ Fe_5O_7	DESY P2.02	<i>ex situ</i>	T-quench
3.1	250	52	1200	1	$\eta\text{-Fe}_2\text{O}_3$ Fe_5O_7 $\text{Fe}_{6.32}\text{O}_9$	DESY P2.02 ESRF ID-15	<i>ex situ</i>	T-quench, Decompression for EOS
3.2	250	52	1550	2	$\eta\text{-Fe}_2\text{O}_3$ Fe_5O_7	DESY P2.02 ESRF ID-15	<i>ex situ</i>	T-quench, Decompression for EOS
3.3	250	52	2000	3	HP- Fe_3O_4	DESY P2.02 ESRF ID-15	<i>ex situ</i>	T-quench, Decompression for EOS
4	250	64	1500 -- 2100	1	$\eta\text{-Fe}_2\text{O}_3$ Fe_7O_{10}	DESY P2.02	<i>ex situ</i>	T-quench
5	120	81	1500	1	$\eta\text{-Fe}_2\text{O}_3$ $\text{Fe}_{6.32}\text{O}_9$ FeO_2H_x	DESY P2.02	<i>ex situ</i>	T-quench, Decompression for EOS

Table 5.6-2 Selected crystallographic information on observed phases

Chemical formula	Fe ₃ O ₄	Fe ₅ O ₇	i-Fe ₂ O ₃	FeO ₂ H _x	Fe ₇ O ₁₀	Fe _{6.32} O ₉
<i>M_r</i>	231.6	391.25	159.7	87.85	550.95	247.55
Crystal system, space group	Orthorhombic, <i>Cmcm</i>	Monoclinic, <i>C2/m</i>	Orthorhombic, <i>Pbcn</i>	Cubic, <i>Pa-3</i>	Orthorhombic, <i>Cmcm</i>	Hexagonal, <i>P6₃/m</i>
P-T conditions of XRD experiment	52(2) GPa, 300 K	52(2) GPa, 300 K	41(2) GPa, 300 K	81(2) GPa, 300 K	64(2) GPa, 300 K	81(2) GPa, 300 K
Unit cell parameters (Å)	a=2.6652, b=9.1029, c=9.1854	a=8.924(4), b=2.6699(4), c=8.076 (12), β (°) =105.90(9)	a=7.047(9), b=4.818(4), c=5.000 (4)	a=4.4301(1)	a=2.6523 (5), b=8.767 (3), c=21.960 (4)	a=9.9975(4), c=2.6041 (9)
<i>V</i> (Å ³)	222.85	185.1 (3)	169.8 (3)	86.94 (8)	510.6 (2)	225.41 (8)
<i>Z</i>	4	2	4	4	4	4
<i>F</i> (000)	440	372	304	168	1048	472
<i>D_x</i> (Mg m ⁻³)	6.901	7.021	6.248	6.711	7.167	7.295
Synchrotron wavelength	λ = 0.2903 Å	λ = 0.2903 Å	λ = 0.2904 Å	λ = 0.2907 Å	λ = 0.41113 Å	λ = 0.4111 Å
μ (mm ⁻¹)	1.44	9.86	1.36	8.45	4.14	4.03
Diffractionmeter	Esperanto-CrysAlis PRO-abstract goniometer imported esperanto images					
Monochromator	Synchrotron					
Scan method	ω-scans					
Absorption correction	CrysAlis PRO 1.171.39.46, SCALE3 ABSPACK scaling algorithm.					
No. of measured, independent and observed [<i>I</i> > 3σ(<i>I</i>)] reflections	629, 629, 462	569, 270, 222	1131, 545, 219	421, 99, 64	532, 332, 297	643, 198, 172
<i>R</i> _{int}	0.057	0.066	0.111	0.088	0.021	0.042
θ values (°)	θ _{max} = 17.3, θ _{min} = 1.8	θ _{max} = 17.6, θ _{min} = 3.3	θ _{max} = 18.9, θ _{min} = 2.1	θ _{max} = 17.5, θ _{min} = 3.3	θ _{max} = 20.4, θ _{min} = 4.6	θ _{max} = 20.5, θ _{min} = 2.4
Range of <i>h, k, l</i>	<i>h</i> = -4→4, <i>k</i> = -18→18, <i>l</i> = -17→13	<i>h</i> = -16→16, <i>k</i> = -5→5, <i>l</i> = -8→10	<i>h</i> = -13→11, <i>k</i> = -8→8, <i>l</i> = -8→10	<i>h</i> = -7→7, <i>k</i> = -3→4, <i>l</i> = -7→8	<i>h</i> = -3→3, <i>k</i> = -7→11, <i>l</i> = -33→26	<i>h</i> = -15→16, <i>k</i> = -13→13, <i>l</i> = -1→1
Refinement on	<i>F</i>	<i>F</i> ²	<i>F</i> ²	<i>F</i> ²	<i>F</i> ²	<i>F</i> ²
<i>R</i> [<i>F</i> ² > 2σ(<i>F</i> ²)], <i>wR</i> (<i>F</i> ²), <i>S</i>	0.081, 0.083, 2.09	0.049, 0.122, 1.03	0.077, 0.177, 0.88	0.057, 0.150, 1.06	0.082, 0.229, 1.13	0.042, 0.098, 0.95
No. of reflections	462	270	545	99	332	198
No. of parameters	25	18	24	6	52	25
No. of restraints	0	0	0	0	0	0
Δρ _{max} , Δρ _{min} (eÅ ⁻³)	2.92, -4.24	1.61, -1.72	2.23, -2.01	1.06, -1.43	3.60, -2.71	0.81, -0.97

5.6.1. Compressibility of novel Fe₇O₁₀ and Fe_{6.32}O₉

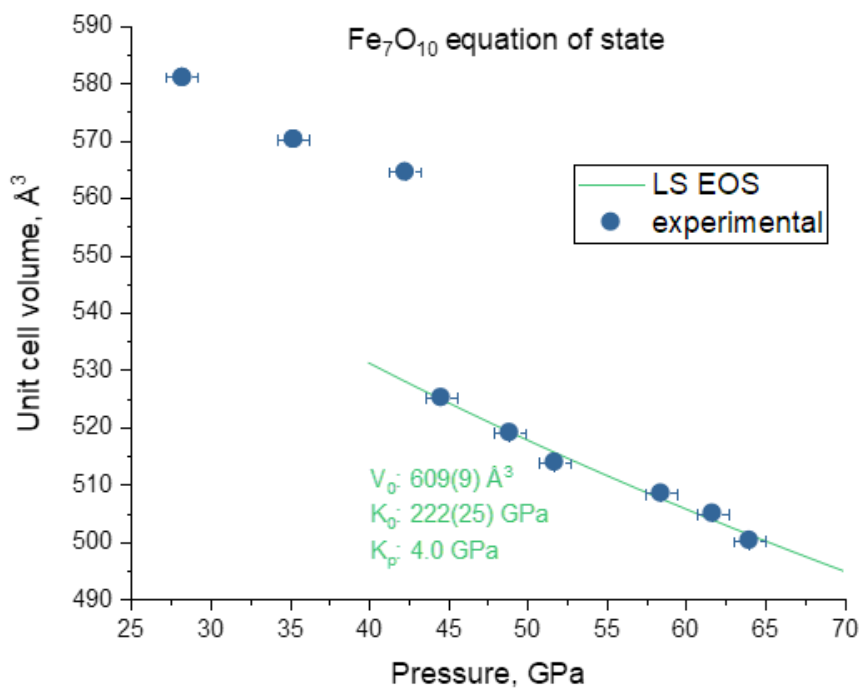


Figure 5.6-1 Equation of state of novel Fe₇O₁₀. Blue circles – experimentally determined unit cell parameters. Errors in unit cell volumes are within the size of symbols. Between 42 and 44 GPa the spin transition occurs, collapsing the volume by ~7%. Green indicates the EOS fit and derived EOS parameters for the low spin state of Fe₇O₁₀ (3rd order Birch-Murnaghan EOS; K_p is fixed to 4). High-spin state data were not fitted due to their small number.

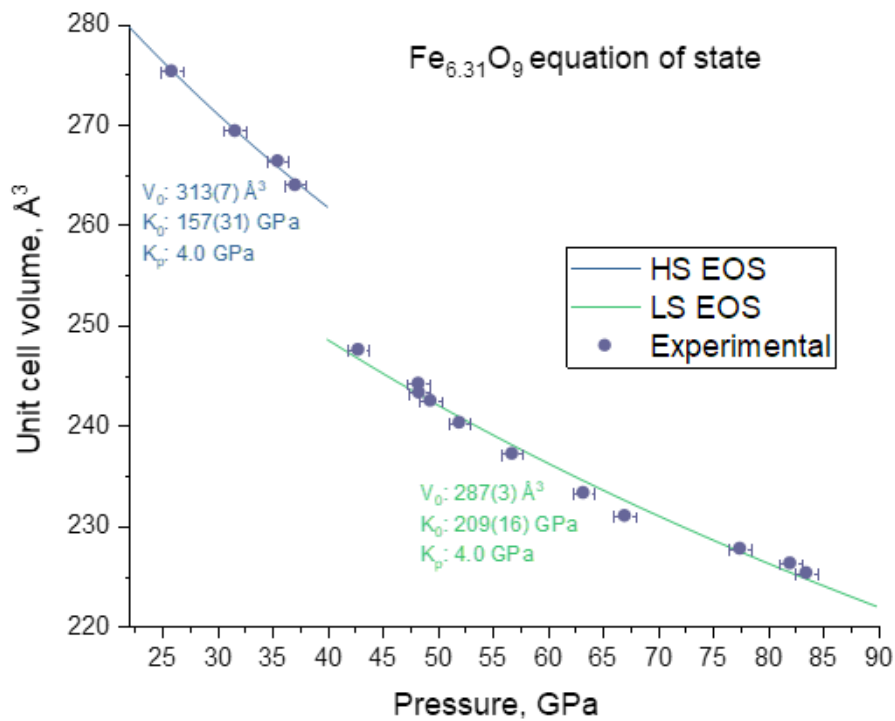


Figure 5.6-2 Equation of state of novel Fe_{6.32}O₉. Purple circles – experimentally determined unit cell parameters. Errors in unit cell volumes are within the size of symbols. Between 37 and 43 GPa the spin transition occurs and volume collapses by ~7%. Green indicates the EOS fit and derived EOS parameters for the low spin state (3rd order Birch-Murnaghan EOS; K_p is fixed to 4) while blue indicates the high spin state.

5.6.2. Crystallochemical discussion on novel Fe₇O₁₀ iron oxide

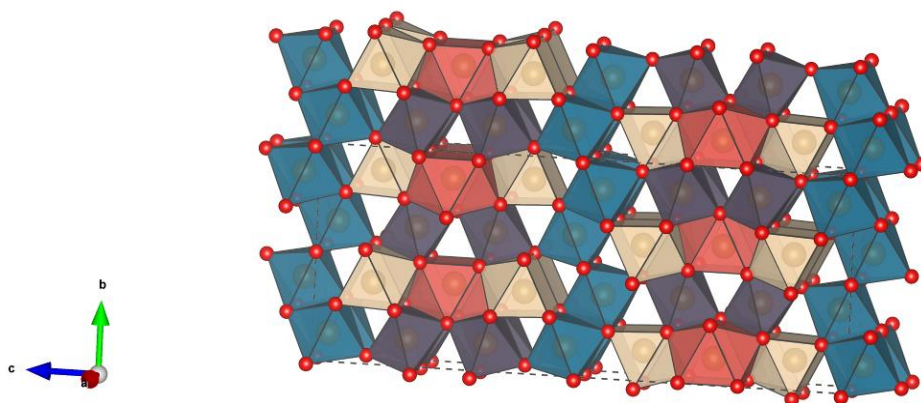


Figure 5.6-3 Crystal structure of Fe₇O₁₀ iron oxide

Synthesized at 64(1) GPa and 2100 (100) K from goethite, Fe₇O₁₀ is a novel iron oxide existing at HP-HT conditions that follows the homologous iron oxide series FeO · mFe₂O₃ (1). The phase is orthorhombic, space group *Cmcm* (N_o63), Z=4, with a remarkably large unit cell *c* parameter: $a=2.6523(5) \text{ \AA}$, $b=8.767(3) \text{ \AA}$, $c=21.960(4) \text{ \AA}$ at 64(1) GPa. The general structural motif is based on an assemblage of prisms (bicapped orange and capped pale-yellow) with stacking on a triangular base along the *a* direction separated by FeO₆ octahedra (purple) that share edges with the prisms. This assemblage is sandwiched between layers of FeO₆ octahedra creating a zig-zag pattern along the *b* direction similar to the HP-Fe₃O₄ (1) structure. Analysis of crystallographic positions and coordination supports the assignment of an Fe²⁺ oxidation state to iron atoms located in the orange bicapped prisms and Fe³⁺ for atoms located in all other polyhedra.

5.6.3. Crystallochemical discussion on novel Fe₇O₁₀ iron oxide

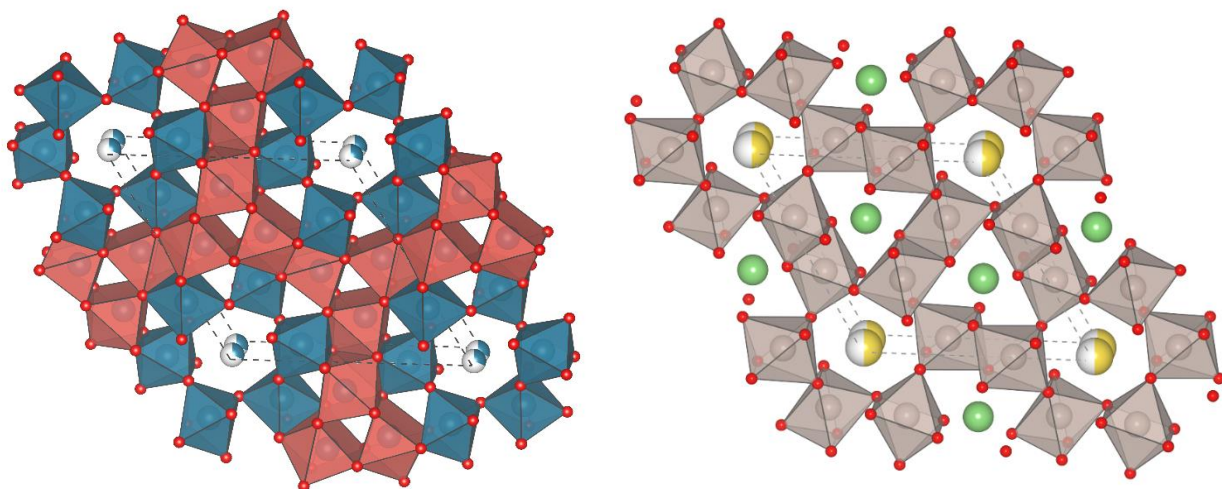


Figure 5.6-4 Crystal structure of Fe_{6.32}O₉ (left) and pseudohexagonal hollandite-like (right) NaLi₂Ru₆O₁₂ (170).

Novel Fe_{6.32}O₉ was synthesized by decomposition of goethite in two independent runs, at 52(2) GPa and 1200(100) K, and at 82(1) GPa and 1500(100) K. The structure of Fe_{6.32}O₉ can be described as hexagonal hollandite-like, which has chains of corner-sharing FeO₆ octahedra forming a three-dimensional framework with hexagonal channels that are occupied by iron cations. Through common faces, FeO₆ octahedra are connected to the framework of capped prisms sharing common triangular faces. Fe ions reside in hexagonal channels where their positions are disordered. Nonstoichiometry of iron atoms in the hexagonal tunnels is indicated, but definite conclusions cannot be drawn from X-ray refinements due to experimental uncertainties associated with XRD data collection in a DAC.

5.6.4. Computational details

To obtain a rough estimate of the temperature distribution in a subducting slab, we modeled the temperature evolution of a 100 km thick vertically descending slab with a constant sinking velocity v_s . The adiabatic temperature profile of the mantle is given by (167), with the temperature distribution in the overlying lithosphere increasing linearly from the surface to the

lithosphere-asthenosphere boundary. Neglecting vertical heat transport, the thermal evolution in the slab is given by a simple one-dimensional equation:

$$\frac{dT}{dt} = \kappa \frac{d^2T}{dx^2} \quad \text{Eq. (11)}$$

where T is temperature and κ is thermal conductivity; t and x are time and distance across the slab, respectively. Both geotherm (167) and thermal diffusivity (based on (15, 181)) are shown in Figure 5.6-6.

The evolution of the temperature profile is computed using a finite difference scheme. Slab thickness is resolved using 1001 nodes. The thermal evolution of the slab is computed to a depth of 2800 km using 5000 time steps. The results of this modeling are shown in Figure 5.6-5. As expected, the temperature distribution in the slab is strongly influenced by the sinking speed. Minimal temperatures are located within the slab core and are shown in Figure 5.3-1 of the main text. Temperature distributions are considered to be only rough estimates due to the simple assumptions used.

Uncertainties in the applied model arise from the assumption of an initial linear temperature gradient, a constant sinking speed, the mantle geotherm (here a present-day mantle geotherm is used, whereas mantle temperatures in the Archean were likely 200-300 K higher) and the chosen material parameters. Additionally, the assumption of a purely vertical slab motion, the slab not being stretched or eroded during its descent as well as the neglect of vertical heat transport, result in an underestimation of the possible temperature field in the slab. As such, model results can be interpreted as a conservative lower bound on slab temperatures.

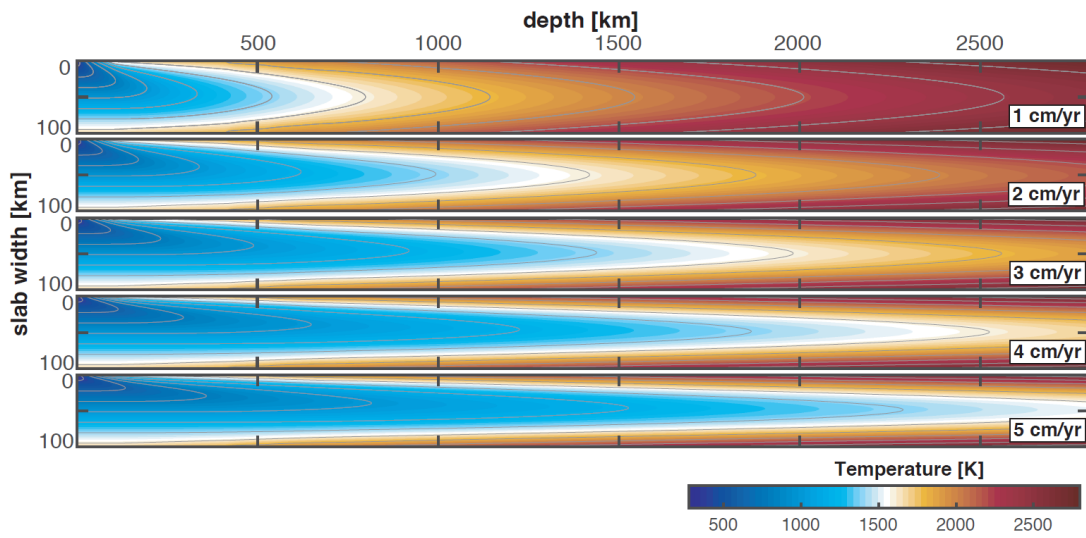


Figure 5.6-5 Temperature distribution within the descending slab as a function of sinking speed v_s (as the vertical component of angular slab subduction). Colors denote temperatures, with grey contours indicated for better readability.

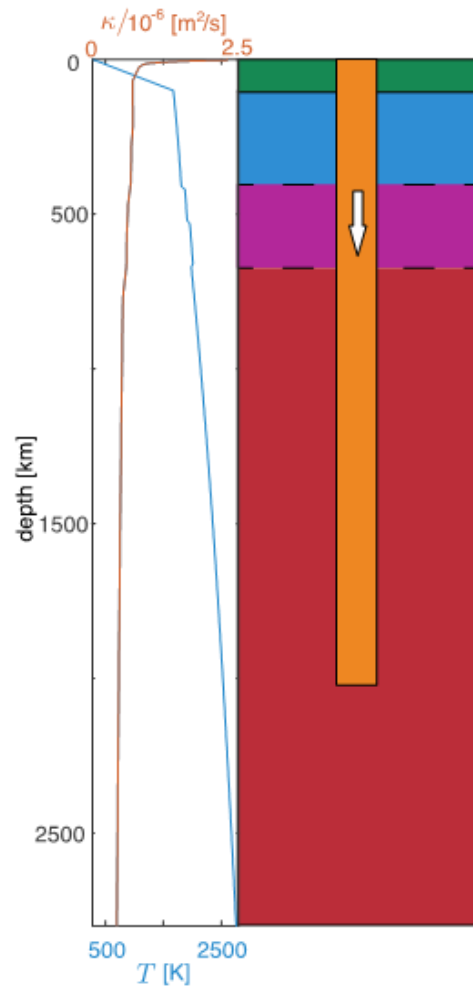


Figure 5.6-6 Model setup for numerical temperature estimation. The blue line represents the geotherm, the orange line represents the value of heat diffusivity coefficient, colorful blocks on the right represent the model setup used. Green-crust, blue-upper mantle, purple – transition zone, red – lower mantle, orange – subducting slab with fixed thickness.

Chapter 6. Variation of oxygen oxidation state at the base of the Earth's mantle

6.1. Abstract

Iron-oxygen interactions control oxygen fugacity and thus most of the geochemical processes. We found that at pressure-temperature conditions of the lowermost mantle, the oxidation state of oxygen in iron-oxygen and in major iron-bearing silicate phases varies from 1.5- to 2-. Consequently, crystal chemistry of Fe,Al-bearing bridgmanite and silicate post-perovskite change considerably, affecting the amount of iron accommodated by silicates, its partitioning, and structural positions. Our results suggest that apart from different phase assemblage in the D'' layer compared to the rest of the lower mantle, the nature of chemical bonding is also different due to reduced negative charge on oxygen atoms, with implications for global-scale phenomena such as the stability of large low shear velocity provinces. In iron-bearing bridgmanite and silicate post-perovskite in D'' layer can deviate from -2.

6.2. Introduction

Iron, the most abundant element by mass in Earth, was considered until recently to be the only geochemically abundant element in Earth's interior with a variable oxidation state. While oxygen (the most abundant element according to number of atoms) is also known to form species with several oxidation states (for example, O^0 in atmosphere, O^{2-} in oxides and silicates, O_2^{2-} in peroxides, O_2^{3-} in electrochemically oxidized transition metals oxides (152, 153)), but so far only valence state -2 was considered for materials forming in Earth's mantle. Synthesis (25, 26, 57, 58) at high pressures and high temperatures (HP-HT) yields numerous iron oxides with unexpected compositions (for example, Fe_4O_5 , Fe_5O_6 , Fe_7O_9 , Fe_5O_7 , $Fe_{25}O_{32}$, and especially FeO_2), unusual crystal structures, and intriguing physical properties, indicate that oxygen may have variable oxidation state in deep Earth interior. X-ray Absorption Spectroscopy (XAS, (77, 95)) and nuclear forward scattering (NFS, (77)) studies of cubic high pressure FeO_2H_x ($x=0$ to 1, (69, 72))

compounds were used to argue that iron is ferrous even at strongly oxidized conditions and thus oxygen can form peroxide (O^{2-}) ions under deep mantle conditions. However, the chemical nature of FeO_2 (and FeO_2H_x) remains highly uncertain. Theoretical work (91, 92, 154) suggests that iron is ferric, while XAS data were interpreted to indicate that it is ferrous (77, 95), yet NFS data of cubic FeO_2 (77) shows center shifts (~ 0.15 mm/s at 80 GPa) that are unrealistic for any ferrous compound. Moreover, all experimental structural data are from powder diffraction (6), which makes an accurate analysis of O-O distances difficult. Even if the peroxide anion did form stable compounds at high pressure, it is not clear to what extent this would affect the behavior of major mantle phases (ferropericlase, bridgmanite, silicate post-perovskite). Thus, the goals of the present work are to clarify the oxidation state of oxygen (particularly in the case of FeO_2) and look for evidence that it deviates from 2- in silicate perovskite and/or post-perovskite. In order to achieve these goals, we employed synchrotron-based single-crystal X-ray diffraction, X-ray absorption and Mössbauer spectroscopy using laser-heated diamond anvil cells (see *Methods in Supplementary Materials*, Figure 6.7-1, Table 6.7-1).

6.3. Results

Iron and oxygen react at high pressures and temperatures. Compression of iron in oxygen at ambient temperature to 25(1) GPa did not produce any chemical reaction, but laser heating of the sample at this pressure to $\sim 1500(100)$ K led to the formation of Fe_2O_3 (space group $R\bar{3}c$, lattice parameters $a = 6.271(7)$ Å, $c = 7.662(4)$ Å) (Figure 6.7-2), in agreement with literature data (25). After further pressure increase to 46(1) GPa, we laser heated the sample at $\sim 1200(100)$ K. The XRD pattern of the temperature-quenched product appeared to be drastically changed. XRD analysis showed cubic FeO_2 with unit cell parameter $a = 4.4313(14)$ Å, which is close to the values previously reported for “pyrite-type” FeO_2 (69, 92).

Iterative heating of the samples at different pressures resulted in the growth of single-crystal domains of cubic FeO_2 that enabled data of sufficient quality for *in situ* single-crystal XRD approach to be performed and further structure solution and refinement to be obtained

(Methods, Table 6.7-1, Table 6.7-2, Table 6.7-3). Structural analysis showed that the shortest O-O distance varies from 2.203(4) Å to 2.090(10) Å within the pressure range ~36 to ~73 GPa. From a crystal-chemical point of view, such a large value for the shortest O-O distance suggests the absence of chemical bonding between these oxygen atoms. Thus, the cubic FeO₂ structure (Figure 6.3-1) belongs to the HP-PdF₂ structure type (89, 90) (see also *Supplementary Comments*), rather than to the pyrite-type.

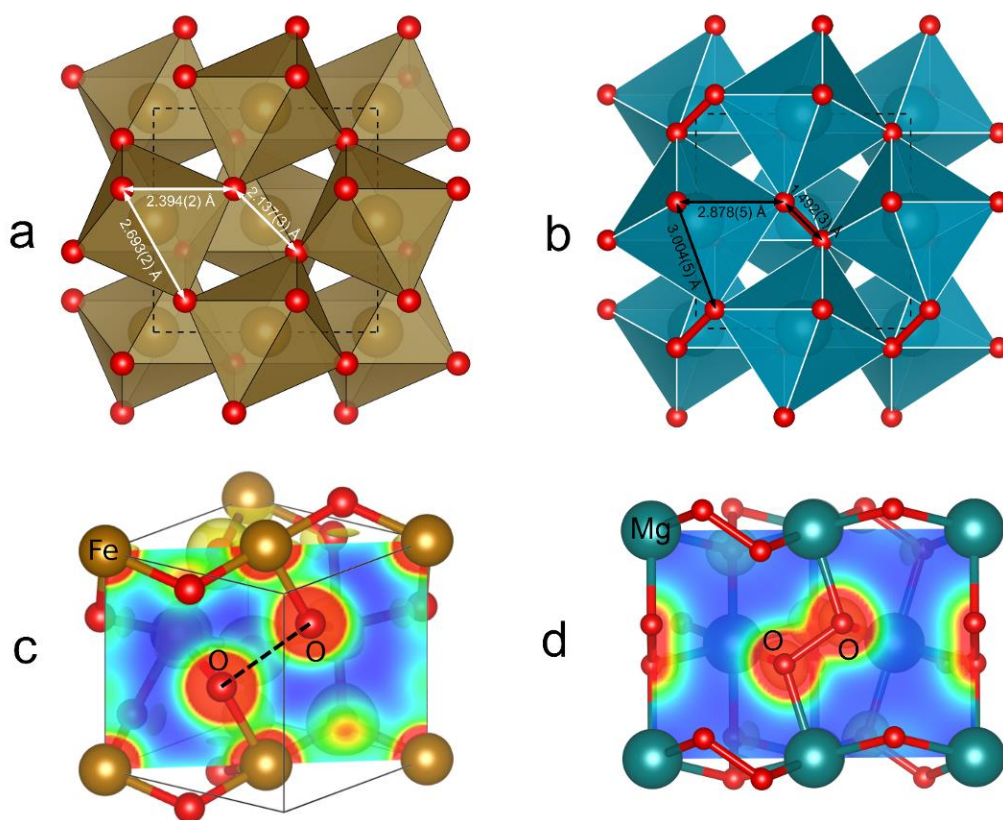


Figure 6.3-1. Comparison of crystal structures of HP-PdF₂-type FeO₂ and pyrite-type MgO₂ peroxide. (a) Crystal structure of cubic (HP-PdF₂-type) FeO₂ as refined from single-crystal XRD data (iron – brown, oxygen – red). XRD data were taken from the temperature quenched sample obtained after heating iron in oxygen at 58(2) GPa and 1800(100) K in a DAC (Table 6.7-1, Table 6.7-2). The shortest experimentally determined O-O distance is 2.137(2) Å, which is too large for a peroxide-type structure. (b) Crystal structure of pyrite-type MgO₂ peroxide (magnesium atoms – blue-green) at ambient conditions (26). The shortest O-O distance is 1.492(3) Å. (c) Valence electron density plot for cubic FeO₂ for the unit cell volume 83.0 Å³ (corresponding to 69 GPa) (see also Methods, Figure 6.7-9, Figure 6.7-10). The theory confirms that the shortest O-O bond length even at 180 GPa remains sufficiently large (1.86 Å),

suggesting the absence of covalent 'molecular' $(O_2)^{3-}$ bonding in FeO_2 . (d) Valence electron density plot for cubic MgO_2 for the unit cell volume 113.3 \AA^3 (ambient pressure) as obtained by DFT (HSE03) calculations. For MgO_2 the formation of 'molecular' $(O_2)^{2-}$ bonds, with 21% of a maximal electron density value in the center of the O-O contact, is evident. For cubic FeO_2 the value is only 5% and thus the calculations support the $Fe^{3+}(O^{1.5-})_2$ electronic configuration.

An explicit examination of the calculated electronic structure (*see Methods*, Figure 6.7-10, Figure 6.7-11) and charge density distribution (Figure 6.3-1) confirms that the oxidation state of Fe in HP-PdF₂-type FeO_2 is close to 3+ and that there is a noticeable absence of O-O bonding to at least 180 GPa. Mössbauer spectroscopy data (Figure 6.7-4) are consistent with iron in the Fe^{3+} state (53, 156) (we note that the center shift that we obtained for cubic FeO_2 at 58(2) GPa (0.06(5) mm/s) is in good agreement with the value of Liu et al. (77)). Our experimental and theoretical results (Figure 6.3-1 and *Supplementary Information*) thus imply that the oxidation state of oxygen in HP-PdF₂-type FeO_2 is equal to 1.5- due to oxygen-metal negative charge transfer (Figure 6.7-10). Such a charge transfer is expected to shorten the Fe-O distance and consequently reduce the volume of FeO_6 octahedra, which should cause both iron polyhedra and the entire structure to become highly incompressible. Indeed, fitting the pressure-volume data for cubic FeO_2 with a 3rd order Birch-Murnaghan equation of state (EoS) gave EoS parameters with a large bulk modulus: $V_0=97.6(3) \text{ \AA}^3/\text{unit cell}$, bulk modulus $K_0=305(9) \text{ GPa}$, and $K'=4.0$ (fixed). Compressibility of FeO_6 octahedra is low ($K_{O,\text{octahedron}}=350(4) \text{ GPa}$) and the octahedral volume is significantly smaller than that known for any other compound, including those with ferric iron in the low-spin state (Figure 6.3-2).

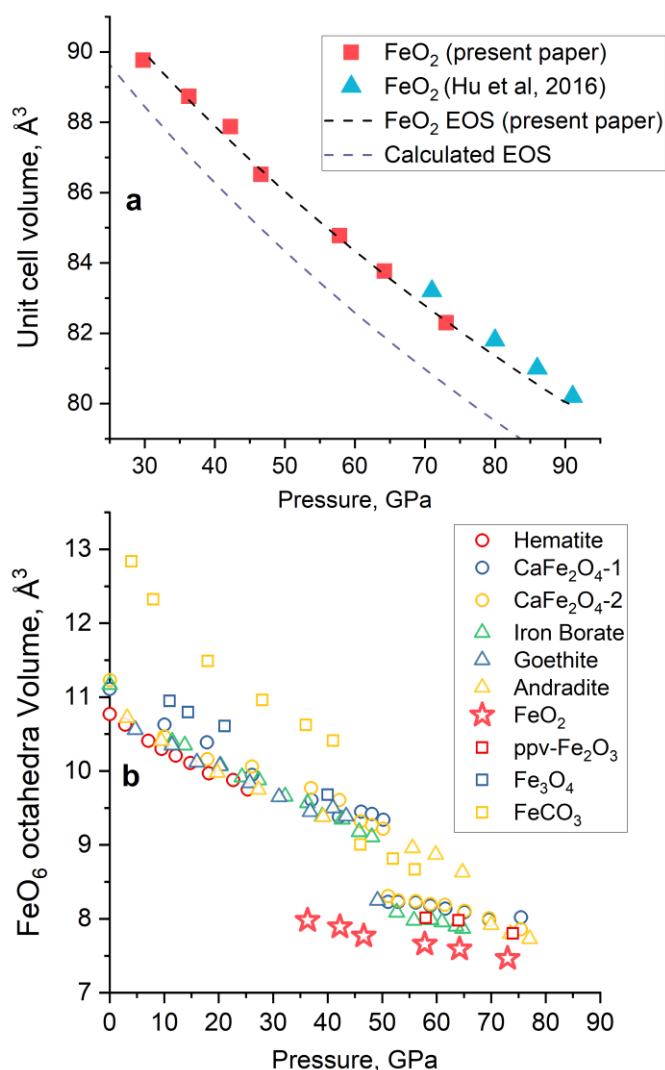


Figure 6.3-2. **Compressional behaviour of HP-PdF₂-structured cubic FeO₂.** **(a)** Variation of the unit cell volume as a function of pressure: red squares – single-crystal XRD data, dashed black line – fit of this P-V data with the Birch-Murnaghan equation of state ($V_0=97.6(3) \text{ \AA}^3$, $K_0=305(9) \text{ GPa}$, $K'=4.0$ (fixed)); blue triangles – powder XRD data according to Hu et al. (69). The EoS parameters obtained on the basis of our experimental data are close to those theoretically calculated by the DFT+DMFT method ($V_0=99.6 \text{ \AA}^3$, $K_0=270 \text{ GPa}$, $K'=4.0$; dashed grey line) which are in agreement with earlier simulations (182). **(b)** Pressure dependence of volumes of FeO₆ octahedra in various compounds according to (30) and references therein. Red stars designate the data for HP-PdF₂-structured cubic FeO₂; red circles – hematite (α -Fe₂O₃); blue and yellow circles – two different octahedra in calcium ferrite (CaFe₂O₄-1) and (CaFe₂O₄-2), respectively; green triangles – iron borate (FeBO₃); blue triangles – goethite (α -FeOOH); yellow triangles – andradite (Ca₃Fe₂(SiO₄)₃); red squares – CalrO₃-type structured η -Fe₂O₃ (ppv-Fe₂O₃); blue squares – magnetite (Fe₃O₄); yellow squares – iron carbonate (FeCO₃).

Laser heating of goethite, α -FeOOH, at $\sim 81(2)$ GPa and $\sim 1500(100)$ K resulted in formation of a cubic phase with lattice parameter $a=4.43(1)$ Å. The structure was solved and refined from single crystal XRD data (Supplementary Information, Table 6.7-2), and arrangement of Fe and O was found to be identical with the HP-PdF₂-type. The lattice parameter corresponds to the composition FeO₂H_{0.4} (72). A relatively high value of the shortest O-O distance ($\sim 2.267(5)$ Å) rules out peroxide-type chemical bonding between oxygen atoms. Consideration of the volumes of FeO₆ octahedra in FeO₂H_{0.4} (7.74 Å³, Figure 6.3-2) allows the oxidation state of iron to be assigned as 3+.

In order to confirm the oxidation state of iron in cubic FeO₂H_x, a new sample was synthesized by laser heating of goethite at $86(2)$ GPa and $1700(200)$ K in a DAC equipped with anvils made of polycrystalline diamond (183). Powder XRD data confirmed synthesis of the material with lattice parameter $a=4.449(5)$ Å (Figure 6.7-6), which corresponds to the composition FeO₂H_{0.5}. XANES data obtained from this sample unambiguously confirms that iron is ferric (Figure 6.7-7 and Figure 6.7-8). Thus, oxygen in FeO₂H_{0.5} has oxidation state -1.75.

Generalizing our observations on cubic HP-PdF₂-structured FeO₂ and FeO₂H_x phases and taking into account that compounds with x up to 1 have been described in the literature, we conclude that at pressures above ~ 50 GPa, the oxidation state of oxygen can significantly deviate from -2. Prominent changes in oxygen chemistry could affect the behavior of major lower mantle phases, particularly those containing iron (such as bridgmanite, Brg), where the effect would be most pronounced (and more easily detected) in iron-rich compounds.

Formation of pure Fe-bridgmanite with composition Fe_{0.88}SiO₃ (generalized perovskite formula ABO₃, A=Fe²⁺_{0.64}Fe³⁺_{0.24}, B=Si) was reported (184) to result from transformation of skiaegite-majorite garnet Fe_{1.19}Si_{0.81}O₃ at high temperatures between 45 and 110 GPa. Heating this garnet to $\sim 2500(150)$ K above 125 GPa resulted in the formation of a mixture of perovskite- and post-perovskite-structured phases, and of pure post-perovskite above ~ 145 GPa (see *Supplementary Materials*). In Fe-bridgmanite synthesized below 110 GPa the iron content is lower than the silicon content and iron is absent from the B-site. However the refinement of

single-crystal XRD data for Fe-bridgmanite at 141(4) GPa, for example, resulted in the composition $\text{Fe}_{0.92(2)}(\text{Si}_{0.85(4)}\text{Fe}_{0.15(4)})\text{O}_3$, and $\text{Fe}_{0.92(4)}(\text{Si}_{0.88(2)}\text{Fe}_{0.12(4)})\text{O}_3$ for post-perovskite at 144(3) GPa (Table 6.7-4; oxygen positions are fully occupied according to XRD). This means that (a) iron enters octahedrally coordinated B-sites, (b) within measurement uncertainty the transformation from skiaigite-majorite garnet to high-pressure phases is isochemical, and (c) pure iron silicate post-perovskite does exist (Figure 6.3-3).

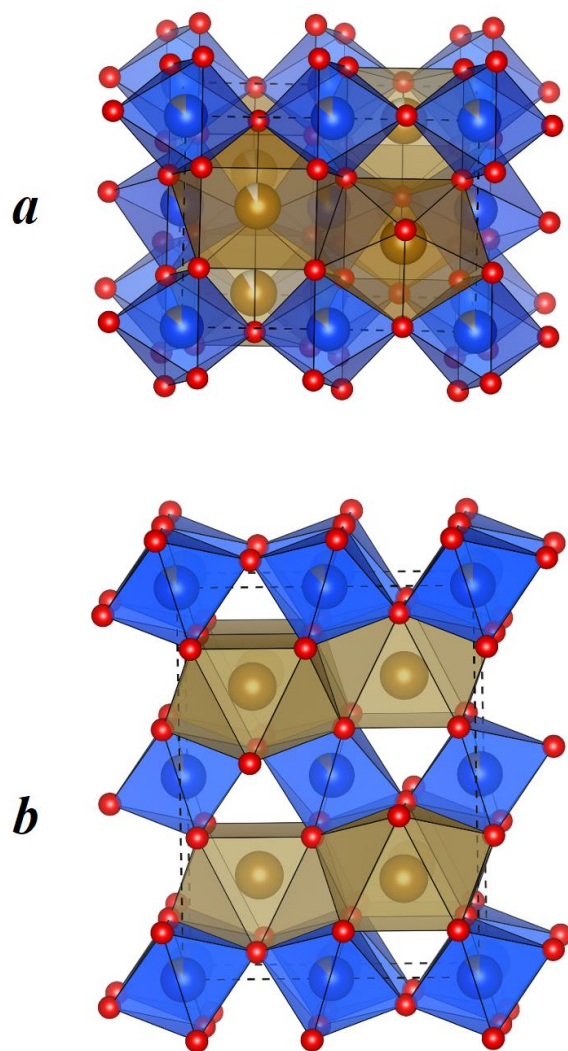


Figure 6.3-3. Experimentally determined crystal structures of pure-iron CaIrO_3 -structured silicate post-perovskite and GaFeO_3 -structured orthorhombic silicate perovskite bridgmanite. (a) Iron post-perovskite synthesized at 144(3) GPa and 2700(150) K with chemical composition $\text{Fe}_{0.92(4)}(\text{Si}_{0.88(2)}\text{Fe}_{0.12(4)})\text{O}_3$. (b) Fe-bridgmanite synthesized at 141(4)

GPa and 2500(150) K with chemical composition $\text{Fe}_{0.92(2)}(\text{Si}_{0.85(4)}\text{Fe}_{0.15(4)})\text{O}_3$ (see also Table 6.7-1 and Table 6.7-4). Crystal structures of both materials are built up from bi-capped prisms (“A-site”, light brown) and octahedra (“B-site”, blue) formed by oxygen atoms (red spheres). In Fe-bridgmanite octahedra are linked through vertices forming a 3D network, and in post-perovskite edge-sharing octahedra are arranged in columns that are combined through vertices to form 2D layers. Fe cations are shown as brown spheres, and Si as blue spheres. According to single-crystal XRD data, iron cations enter B-sites (Si-positions) of the structures (designated by brown segments in the blue spheres).

Such drastic changes in crystal chemistry suggest that chemical bonding in silicate phases at conditions of the lower part of the lower mantle have also changed. Indeed, for both perovskite and post-perovskite $\text{Fe}(\text{Si}_{0.75}\text{Fe}_{0.25})\text{O}_3$ phases in which the B-site is 25% occupied by iron atoms, DFT+DMFT simulations (see *Methods and Supplementary Comments*) with unit cell volume corresponding to ~140 GPa predict that Fe^{+2} and Fe^{+3} will be located in the A and B sites, respectively, and that the oxygen oxidation state (which is equal to 2- in FeSiO_3) will change and become ~ 1.9- due to formation of an electronic hole on oxygen sites. The change in oxidation state of oxygen is similar to that found for FeO_2 , although mechanisms of the change are different for the silicate and oxide systems (see *Methods*, Figure 6.7-12).

Single-crystal XRD supported by Mössbauer spectroscopy (see *Methods and Supplementary Comments*) allows determination of the amount of ferric iron in Fe-bridgmanite and post-perovskite. For example, Fe-bridgmanite synthesized at 100(2) GPa shows a composition of $\text{Fe}^{2+}_{0.71}\text{Fe}^{3+}_{0.17}\text{SiO}_3$. The total cation charge is thus equal to 5.93+, which within uncertainty implies an oxygen oxidation state equal to 2-. In the case of Fe,Al-bearing post-perovskite synthesized at 155(3) GPa, the analysis (Figure 6.7-5) gives the formula $\text{Mg}_{0.86}\text{Fe}^{2+}_{0.12}\text{Fe}^{3+}_{0.02}\text{Si}_{0.91}\text{Al}_{0.04}\text{O}_3$ and a total cation charge of 5.78+; thus the formal charge on oxygen is less than 2- in accordance with theoretical predictions.

Laser heating of single crystal silicate perovskite $\text{Mg}_{0.60}\text{Fe}_{0.40}\text{Si}_{0.63}\text{Al}_{0.37}\text{O}_3$ (see *FE40* in Table 6.7-4 and *Supplementary Materials*) at 153(5) GPa and 2700(150) K resulted in formation of several single-crystal domains with lattice parameters of bridgmanite and post-perovskite (Table 6.7-4). Post-perovskite domains (for example, $(\text{Mg}_{0.77},\text{Fe}_{0.23})(\text{Si}_{0.62},\text{Al}_{0.37})\text{O}_3$, Table 6.7-4) show an

iron depletion by nearly a factor of two compared to the initial bridgmanite. Even if all iron in post-perovskite were ferric, the oxygen oxidation state is 1.94-.

6.4. Discussion

Experiments on single crystals of Fe,Al-bearing bridgmanite with different compositions ($\text{Mg}_{1-x}\text{Fe}_x(\text{Si}_{1-y}\text{Al}_y)\text{O}_3$ ($x=0.12-0.17$; $y=0.03-0.06$) (*particularly the samples designated as FE17 and FE14 in (184) and Table 6.7-4*) were performed at 137 to 155 GPa and 2400 – 2700 K. In all cases, the formation of only silicate perovskite and post-perovskite phases was observed, but due to the small overall iron concentration and the relatively large uncertainties associated with harsh experimental conditions, it is difficult to draw quantitative conclusions regarding the chemical composition of the products of reactions and the oxidation state of iron. Formation of domains of phases with slightly different unit cell parameters/volumes was observed in all experiments (Table 6.7-4), and, as a rule, the amount of iron in post-perovskite is smaller than in co-existing (or starting) perovskite. Nevertheless, by combining results of single crystal diffraction and Mössbauer (SMS) spectroscopy (Table 6.7-4, Figure 6.7-5) for post-perovskite synthesized at 155(3) GPa, we found an oxygen charge of -1.92(3), even for a total iron content of ~ 0.14 .

Variable oxygen oxidation state is important not only for the chemistry of the Fe-O system, but it affects the physico-chemical properties of iron-bearing silicate phases at lowermost Earth's mantle conditions (Figure 6.4-1). Our *in situ* single-crystal diffraction data show that at pressures relevant for the D'' layer at the CMB, silicate post-perovskite is depleted in iron with respect to the initial (or co-existing) Fe,Al-bearing bridgmanite. This agrees with reports of a drastic increase in iron partitioning into ferropericlase compared to silicate in the stability field of post-perovskite (185, 186), probably associated with changes in the oxidation states of iron and oxygen (186, 187). Variations in the oxidation state of iron and partitioning of differently oxidized species between co-existing phases can be one reason for the large transformation pressure range across the bridgmanite-post-perovskite boundary (188). A densities difference of $\sim 3\%$ between co-

existing bridgmanites and post-perovskites (for example, in FE17 (Table 6.7-4), the densities of co-existing silicate perovskite and post-perovskite are $6.00(3) \text{ g/cm}^3$ and $5.84(3) \text{ g/cm}^3$, respectively) could result in phase differentiation over geological time-scales. This, in turn, may lead to dynamic instabilities at the bottom of the lower mantle, formation of rising plumes and accumulation of dense material forming global-scale heterogeneities such as large low-shear-velocity provinces (LLSVPs) detected by seismic observations (189), nearly antipodal beneath the Pacific Ocean and Africa. Evidence for chemical differences between these regions and the surrounding mantle includes sharp margins and anti-correlated anomalies between bulk and shear sound velocities in LLSVPs. Although the identity and origin of these regions is still unknown, the likely high density of LLSVPs may be explained by enrichment in iron (190) and be linked to changes in oxygen chemical behavior.

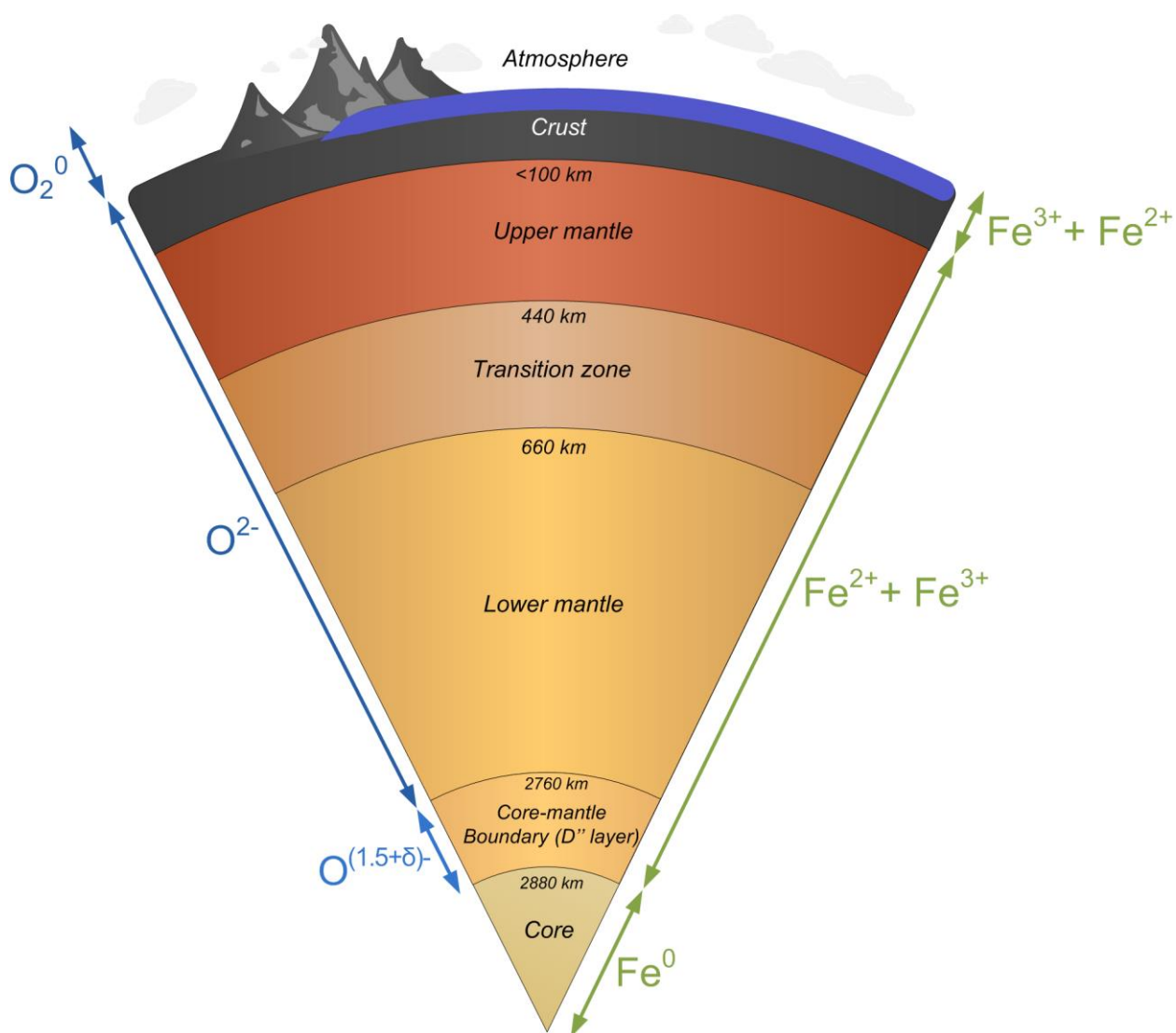


Figure 6.4-1. **Schematic diagram showing variation of iron and oxygen oxidation states through different geospheres.** Iron and oxygen interactions control oxygen fugacity and thus most of global geochemical processes (29, 191). So far, iron has been considered to be the only geochemically abundant element within the solid Earth to have a variable oxidation state. In the crust and the upper mantle, the proportion of ferric iron is lower than in the lower mantle (29), while the Earth's core is formed of iron alloys. Our experiments and earlier data (69) demonstrate that at pressures up to ~ 45 GPa, the most oxygen-rich oxide is Fe_2O_3 . At higher pressures HP-PdF₂-structured cubic FeO_2 with $\text{O}^{1.5-}$ becomes stable. While the crust and mantle are dominated by O^{2-} , near the core-mantle boundary the oxidation state of oxygen changes and may be described as $\text{O}^{(1.5+\delta)-}$ ($\delta < 0.5$; $\delta \sim 0.43$ in silicate post-perovskite). For clarity the thickness of Earth layers is not drawn to scale.

6.5. Acknowledgments

We thank the European Synchrotron Radiation Facility for provision of synchrotron radiation facilities (ID15, ID18, ID24, ID27). Authors thank the Deutsches Elektronen-Synchrotron for provision of synchrotron beamtimes (P02.2). Portions of this work were performed at GeoSoilEnviroCARS (The University of Chicago, Sector 13), Advanced Photon Source (APS), Argonne National Laboratory. GeoSoilEnviroCARS is supported by the National Science Foundation - Earth Sciences (EAR - 1634415) and Department of Energy- GeoSciences (DE-FG02-94ER14466). This research used resources of the Advanced Photon Source, a U.S. Department of Energy (DOE) Office of Science User Facility operated for the DOE Office of Science by Argonne National Laboratory under Contract No. DE-AC02-06CH11357. Support provided by the Swedish Research Council project No. 2015-04391, the Swedish Government Strategic Research Areas in Materials Science on Functional Materials at Linköping University (Faculty Grant SFO-Mat-LiU No. 2009-00971) and the Swedish e-Science Research Centre (SeRC) is gratefully acknowledged. Authors are grateful to DFG for financial support through International Research training Group "Deep Earth Volatile Cycles" (GRK 2156/1), DU 393/9-2, and BY 101/1-1. Theoretical simulations of the electronic structure and analysis of chemical bonding was supported by the Russian Science Foundation (Project No. 18-12-00492).

6.6. Experimental

6.6.1. Materials

For HP-HT synthesis of FeO₂ the following materials were used in the present work: oxygen (99.999% purity, Riessner-Gase GmbH); iron (Goodfellow Inc., 99.999 % purity).

Single crystals of bridgmanite with different compositions, Mg_{0.83}Fe_{0.17}Al_{0.06}Si_{0.94}O₃ (referred to as FE17 below), Mg_{0.86}Fe_{0.14}Al_{0.04}Si_{0.96}O₃ (FE14), and Mg_{0.60}Fe_{0.40}Si_{0.63}Al_{0.37}O₃ (FE40), as determined from Single Crystal X-ray Diffraction (SCXRD) structural refinement and microprobe analysis, were selected from samples synthesized in a multianvil (MA) apparatus at 25 GPa and

1300°C (184). According to Mössbauer spectroscopy, the ratio $\text{Fe}^{3+}/\Sigma\text{Fe}$ is 0.93(3) in FE40 and 0.20(4) in FE17 and FE14. Before being loaded into a DAC, crystals with sizes from $\sim 10 \times 10 \times 5 \mu\text{m}^3$ to $\sim 20 \times 20 \times 7 \mu\text{m}^3$ were selected and tested with an in-house high-brilliance rotating anode diffractometer.

6.6.2. DAC preparations

A BX-90 (100) Diamond-anvil cell (DAC) equipped with Boehler-Almax diamonds with flat culets and size of 250 μm (in experiments below 80 GPa) or beveled with culets of 120 μm (in experiments above 80 GPa) glued on tungsten carbide seats were used as a pressure generator. A rhenium gasket with indentation thickness of $\sim 15 \mu\text{m}$ was drilled in order to create a sample chamber of approx. diameter 110 μm or 60 μm in different experiments. Thin pieces of Fe with approximate lateral sizes of 15 μm and thickness of $\sim 3 \mu\text{m}$ were placed inside the sample chamber for synthesis of FeO_2 , and the cells were loaded cryogenically with oxygen which served as a chemical reactant and pressure-transmitting medium; pressure determination before heating was made according to the equation of state of hcp-iron. Experiments with bridgmanites of different compositions were performed in DACs loaded with Ne (see ref. (1) for more details).

6.6.3. Data acquisition

Monochromatic XRD experiments with laser-heated diamond anvil cells were performed at 13-IDD (APS), ID-15b (192) and ID-27 (ESRF), and at P02.2 (PETRA III, DESY (159)) beamlines. These beamlines are equipped with state-of-the-art double-sided laser heating systems allowing the collection of *in situ* XRD data from samples inside the DAC during laser heating as well as after quenching.

The XRD patterns at 13-IDD were collected with a Pilatus 1M CdTe detector. The X-ray beam with wavelength of 0.2952 Å was focused to $\sim 3 \times 3$ micrometer² spot. The calibration of the detector was made using LaB_6 and the procedure realized in the DIOPTAS software (193). During heating still-scans (no oscillations) were collected *in situ*; after heating mapping was done and

stepped ω -scans were collected for the points containing single-crystal domains. Step scans consisted of individual exposures taken over 0.5° intervals of DAC rotation to constrain the ω angle of maximum intensity of each peak.

The XRD patterns at ID-27 were registered using Perkin Elmer and MAR165 planar detectors. The wavelength of X-ray radiation used was 0.3738 \AA . The beam was focused to about $2.5 \times 2.5 \text{ \mu m}^2$. The calibration of the detector was made using CeO_2 and procedure realized in the program FIT2D (Hammersley et al. 1996).

Synchrotron Mössbauer Source (SMS) spectroscopy experiments were performed at the Nuclear Resonance beamline (ID18) at the ESRF. Monochromatisation on ID18 is based on the usage of nuclear reflections of an iron borate ($^{57}\text{FeBO}_3$) crystal. The source provides ^{57}Fe resonant radiation at energy 14.4 keV within a bandwidth of 15 neV which is tunable in energy over a range of $\pm 0.6 \text{ meV}$. Calibration of velocity scales of Mössbauer spectra was done with a 25 \mu m -thick α -Fe foil. Fitting of the spectra was performed using the software package MossA (165). Lorentzian lines were used to fit all Mössbauer spectra and a linear function was applied to model the background.

Synchrotron X-ray Absorption Near-Edge Spectroscopy (XANES) experiments were carried out at the ESRF XAS beamline (ID24) at the iron K-edge in-situ at high P/T conditions using the online double sided laser-heating system. The beam was focused to $3 \times 3 \text{ (hvx) \mu m}^2$ using a set of Si mirrors and a Si (311) polychromatic crystal. The latter ensured an energy resolution of 1 eV . This high energy-resolution was necessary for constraining the pre-edge and edge features in the XANES and to determine the oxidation state of iron.

6.6.4. Structure solution and refinement

Analysis of collected diffraction images with further data processing (cell refinement and data reduction) was performed using *CrysAlis PRO* software (Agilent Technologies, Version 1.171.37.35). The structures were solved using the dual-space method (160) and refined in the

isotropic approximation by full matrix least-squares refinements using SHELXL software (160). Molecular graphics is made with a VESTA software (161).

6.6.5. Computational details

For calculations of the electronic structure, magnetic state and crystal structure properties of FeO_2 and $\text{Fe}(\text{Si}_{0.75}\text{Fe}_{0.25})\text{O}_3$ we employed a state-of-the-art fully self-consistent in charge density DFT+DMFT approach (DMFT: dynamical mean-field theory) (194–196). To model the chemical substitution in $\text{Fe}(\text{Si}_{0.75}\text{Fe}_{0.25})\text{O}_3$, we constructed a supercell (with periodic boundary conditions) containing 4 f.u. of the host material FeSiO_3 in which one of the Si ions is replaced with Fe. The DFT+DMFT method describes the quantum dynamics of the many-electron problem exactly (neglecting non-local effects) and allows one to include the effect of electronic correlations on the electronic properties of correlated materials (194–199). For the partially filled Fe 3d and O 2p orbitals we constructed a basis set of atomic-centered symmetry-constrained Wannier functions (200). To solve the realistic many-body problem, we employed the continuous-time hybridization-expansion quantum Monte-Carlo algorithm (201). The calculations were performed in the paramagnetic state at electronic temperature $T_{el} = 1160$ K. We used the average Coulomb interaction $U=6$ eV and Hund's exchange $J=0.89$ eV for the Fe 3d shell as estimated previously (91). The Coulomb interaction was treated in the density-density approximation. The spin-orbit coupling was neglected in these calculations. The DFT+DMFT approach was implemented within the plane-wave pseudopotentials with the generalized gradient approximation in DFT. We employed the fully localized double-counting correction, evaluated from the self-consistently determined local occupancies, to account for the electronic interactions already described by DFT. To define valence, we computed the reduced density matrix for the Fe 3d states; its eigenvalues gave the probability of different 3d-electron atomic (valence) configurations.

For calculations of MgO_2 we employed the all electron projector-augmented-wave (PAW) method as implemented in the VASP code (202–204). The nonlocal screened Coulomb potential hybrid density Heyd-Scuseria-Ernzerhof (HSE03) functional was used (205). We used the Gaussian

smearing method with a smearing width of 0.10 eV. The energy cutoff for the plane waves included in the expansion of wave functions was set to 500 eV. The calculated value of the band gap at ambient pressure is about 5.5 eV.

6.6.6. Evolution of the crystal structure parameters with pressure

We have performed a full structural optimization of the lattice parameters (determined the lattice volume and the fractional position of oxygen) and computed the electronic properties of the HP-PdF₂-type crystal structure of FeO₂ under pressure, using a fully charge self-consistent DFT+DMFT approach (194–197). In order to evaluate pressure, we fitted our total-energy results to the third-order Birch-Murnaghan equation of state. Our results for the pressure evolution of the crystal structure parameters are summarized in Figure 6.7-9. The calculated lattice volume $V=83.042 \text{ \AA}^3$, interatomic distances (1.794 Å, 2.390 Å, and 2.09 Å for Fe-O, O-O₆ and O-O bonds, respectively) and oxygen fractional position $z=0.362$ at ~70 GPa are in good agreement with experimental values ($V=83.768 \text{ \AA}^3$, 1.790 (7) Å, 2.384(6) and 2.084(14) for Fe-O, O-O₆ and O-O bonds, respectively).

6.7. Supplementary Information

6.7.1. Pyrite vs HP-PdF₂-type structures

For peroxides (in molecular or crystalline forms), the distances between the closest oxygen atoms at ambient pressure are very characteristic – from about 1.2 to 1.5 Å (88), and under compression these distances are not expected to increase. The shortest O-O contact reported for pyrite-type FeO₂ is ~1.9 Å (69). It is too long for peroxides, but too short for cubic dioxides with the high-pressure PdF₂-type structure (HP-PdF₂). For the latter, the shortest O-O distance is ~2.5 Å at ambient conditions. These phases are characterized by low compressibility (see for details refs. (89, 90)). In fact, osmium and ruthenium, the neighbors of iron in the VIIIb group in the Periodic System, form typical dioxides, OsO₂ and RuO₂, with the HP-PdF₂-type structure (89, 90). According to the “rule of thumb” (206), the behavior of compounds (particularly oxides) of an

element at high pressure is like compounds of elements with higher atomic number in the same periodic table group at low pressures. Thus, one could expect that FeO_2 also forms a dioxide, not a peroxide. The problem of the oxidation state of iron in FeO_2 is closely linked to the question regarding the conditions at which this compound could be formed, and in particular, if an excess of oxygen is necessary to oxidize Fe^{3+} or whether the compound contains only Fe^{2+} and competes with other oxides containing ferrous iron (7-11).

6.7.2. Electronic structure of FeO_2

Our DFT+DMFT calculations show that at a pressure of ~ 69 GPa, FeO_2 is a poor metal (Figure 6.7-10) with about 5.21 electrons in the Wannier Fe $3d$ states (4.07 electrons inside the atomic sphere with radius ~ 0.78 Å, in accord with the bond valence analysis). Oxygen states are partially occupied with ~ 0.61 hole states in the Wannier O $2p$. The local magnetic moment is $\sim 1.59 \mu_B$ (fluctuating local moment of $\sim 0.83 \mu_B$). Our results for the decomposition of electronic state into atomic configurations (valence states) show that the value for Fe is nearly $3+$ at ~ 69 GPa: $\text{Fe}^{3+} 3d^5$ configuration has a weight of $\sim 50\%$, with a $\sim 30\%$ admixture of the $\text{Fe}^{2+} 3d^6$ state ($\sim 0.5|d^5\rangle + 0.3|d^6\rangle$, see Figure 6.7-11). In Figure 6.7-10 we see that due to distorted FeO_6 octahedron symmetry, the Fe t_{2g} states split into a a_{1g} singlet and e_g doublet. Fe e_g orbitals are empty and are located well above the Fermi level at 1-4 eV. Fe t_{2g} states form weakly renormalized ($m/m^* \sim 1.6$) quasiparticle bands near E_F . Importantly, our fully relaxed and charge self-consistent DFT-DMFT calculations lead to a different bonding picture of FeO_2 in comparison to the analysis by Streltsov *et al.* (91). In fact, our results reveal the absence of a molecular $(\text{O}_2)^{3-}$ bonding state, i.e., in FeO_2 iron has effective charge $3+$, and oxygen $1.5-$. We see that the bonding O-O σ states appear at ~ -2 eV, while the anti-bonding σ^* states due to mixing with the Fe t_{2g} states at the Fermi level split into the $t_{2g} \pm \sigma^*$ combinations (seen as two peaks at -1 and +1 eV in Figure 6.7-10). Importantly, the empty $t_{2g} - \sigma^*$ O-O band is located ~ 1 eV above the Fermi level, confirming the formation of a localized hole at the O sites. At the same time, the bonding-antibonding splitting of the O $2p$ orbitals is small, just $\sim 2-3$ eV, indicating negligible bonding between the two oxygen atoms. This is in agreement with the analysis of charge density

distribution in Figure 6.3-1, strengthening the conclusion regarding the absence of a molecular $(O_2)^{2-}$ or $(O_2)^{3-}$ bonding state in FeO_2 in the studied interval of pressure.

6.7.3. Electronic structure of $Fe(Si_{0.75}Fe_{0.25})O_3$

Our DFT+DMFT calculations demonstrate that $Fe(Si_{0.75}Fe_{0.25})O_3$ is a metal (Figure 6.7-13) with sufficiently distinct Fe A/B 3d charges (5.94/5.28 electrons) and local magnetic moments 4.02/1.44 (fluctuating local moments 3.9/1.07 μ_B), respectively. $Fe_A t_{2g}$ and z^2 orbital occupations are nearly half-filled (~ 0.52), while the $Fe_A x^2-y^2$ states are ~ 0.81 . $Fe_A x^2-y^2$ states show a quasiparticle peak at the Fermi level, with a lower Hubbard band satellite at about -3 eV. $Fe_B a_{1g}$ and orbital occupations are 0.77-0.9. $Fe_B e_g$ states are empty and are located well above Fermi level at about 2-4 eV.

We note that iron in the Fe_A sites is 2+ with a valence configuration $\sim 0.73 |d^6\rangle + 0.15 |d^7\rangle$, whereas in the Fe_B sites it is nearly 3+ ($0.30 |d^6\rangle + 0.54 |d^5\rangle$). Furthermore, a structural relaxation of the oxygen positions surrounding the Fe_B sites (performed within DFT+U) tends to decrease charge disproportion to 5.87/5.56, shifting the electronic configuration of the Fe ions in the Fe_B sites to nearly a mixed valence state ($\sim 0.42 |d^6\rangle + 0.44 |d^5\rangle$). But this does not affect either the electronic structure or the magnetic state: $Fe(Si_{0.75}Fe_{0.25})O_3$ remains metallic and the calculated local magnetic moments are ~ 4.08 and $1.19 \mu_B$ for the Fe A and B sites, respectively. Most importantly, our results indicate that absolute value of oxygen oxidation state in $Fe(Si_{0.75}Fe_{0.25})O_3$ ($\sim 1.85-1.9+$) is lower than that in $FeSiO_3$ (2+) due to negative oxygen-metal charge transfer, resulting in the formation of a hole at the O sites. Note that the hole at the oxygen sites due to the formation of the Fe^{+3}_B cation is delocalized, and it is distributed over 12 oxygen sites.

6.7.4. Electronic structure of MgO_2

The band gap of MgO_2 calculated within hybrid-DFT has a value of ~ 5.5 eV at ambient pressure. The calculated equilibrium volume is 113.3 \AA^3 . Under a pressure of ~ 70 GPa, the O-O bond

distance in MgO₂ shrinks by ~4 %, to 1.43 Å, resulting in a slight increase of the relative valence electron density in the center of the O-O bond to $\rho(r)/\rho_{max} \sim 23\%$.

6.7.5. Composition of Fe-bearing silicate post-perovskite at conditions of the Earth's lower mantle.

Mössbauer spectroscopy in combination with single-crystal XRD allows one to determine the relative amount of ferric iron in Fe-bridgmanite or post-perovskite. For example, SMS spectra of Fe-bridgmanite (Figure 6.7-5) synthesized at 100(2) GPa are characterized by two components with center shifts (CS) 0.62 and 0.88 mm/s assigned to Fe²⁺ (~81% of total iron), and two components with CS -0.071 and 0.34 mm/s assigned to Fe³⁺ (~19% of total iron). According to X-ray diffraction data (184), bridgmanite contains 0.88 at% of iron per formula unit, and thus the composition of the material is Fe²⁺_{0.71}Fe³⁺_{0.17}SiO₃. The total charge of cations is 5.93(9)+, and thus, within uncertainty, the oxidation state of oxygen is 2-. For Fe-post-perovskite synthesized at 144(3) GPa with the composition Fe_{1.04}Si_{0.88}O₃ (Table 6.7-4), SMS spectra (Figure 6.7-5) show three components – a doublet with CS 0.06 mm/s (assigned to Fe³⁺, ~15% of total iron), a doublet with CS 0.58 mm/s and a sextet with CS 0.78 mm/s (assigned to Fe²⁺, ~85% of total iron). Thus, the composition of the material is Fe²⁺_{0.88}Fe³⁺_{0.16}Si_{0.88}O₃. The total charge of cations is 5.76+, which strongly suggests that the oxidation state of oxygen is different from 2-. Similarly, for Fe,Al-bearing post-perovskite synthesized at 155(3) GPa, the analysis of single-crystal XRD and Mössbauer spectroscopy data (Figure 6.7-5) gives the formula Mg_{0.86}Fe²⁺_{0.12}Fe³⁺_{0.02}Si_{0.91}Al_{0.04}O₃, and a total charge of cations of 5.78+, which also suggests that the oxidation state of oxygen is different from 2-.

Single-crystal X-ray diffraction data provide information on the content of iron in the sample, but do not allow the oxidation state of a cation to be assigned. Nevertheless, considering Si⁴⁺, Al³⁺, and Mg²⁺ and assuming that all Fe has oxidation state 3+, we can estimate the “upper limit” of the absolute value of the oxidation state of oxygen. For example, HP-HT treatment of a single crystal of silicate perovskite Mg_{0.60}Fe_{0.40}Si_{0.63}Al_{0.37}O₃ (FE40, see (184)) at 153(5) GPa and

2600(100) K resulted in the formation of several single-crystal domains with the lattice parameters of bridgmanite and post-perovskite (Table 6.7-4). No other phases (apart from Ne, present as a pressure medium, and Re from the gasket) were detected by single-crystal or powder XRD. The analysis of the data obtained from a domain with the strongest diffraction (the best data-set) gave a chemical composition $\text{Mg}_{0.77}\text{Fe}_{0.23}\text{Si}_{0.99}\text{O}_3$. The conclusion regarding the iron content is robust because X-ray scattering factors of silicon, magnesium, and iron are very different (184); Al and Si in the B-site cannot be distinguished, but there is no evidence that Al enters the A-site. The crystal-chemical formula of the material is $(\text{Mg}_{0.77},\text{Fe}_{0.23})(\text{Si}_{0.62},\text{Al}_{0.37})\text{O}_3$; the sum of formal charges of cations (with all iron Fe^{3+}) is 5.82+. Similarly, in experiments with silicate perovskite with the composition FE14 (see (184)) after heating at 2650(150) K at 155(3) GPa, a domain of post-perovskite with the composition $(\text{Mg}_{0.89},\text{Fe}_{0.11})(\text{Si}_{0.87},\text{Al}_{0.04})\text{O}_3$ was found; the sum of formal charges of cations (with Fe^{3+}) is 5.71+. These observations support the theoretical prediction of the presence of oxygen with a formal charge lower than 2.

6.7.6. Figures and Tables

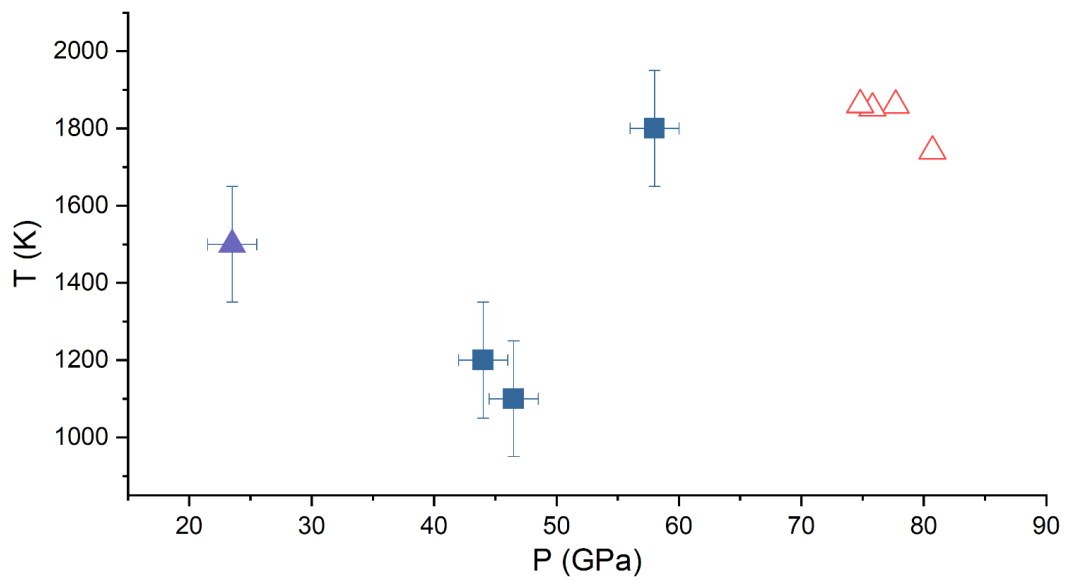


Figure 6.7-1 LH-DAC FeO_2 and Fe_2O_3 synthesis conditions from Fe and $\epsilon\text{-O}_2$ in the present work (solid squares and solid triangle, respectively). Open red triangles show the synthesis conditions of FeO_2 from the interaction between Fe_2O_3 and $\epsilon\text{-O}_2$ (69).

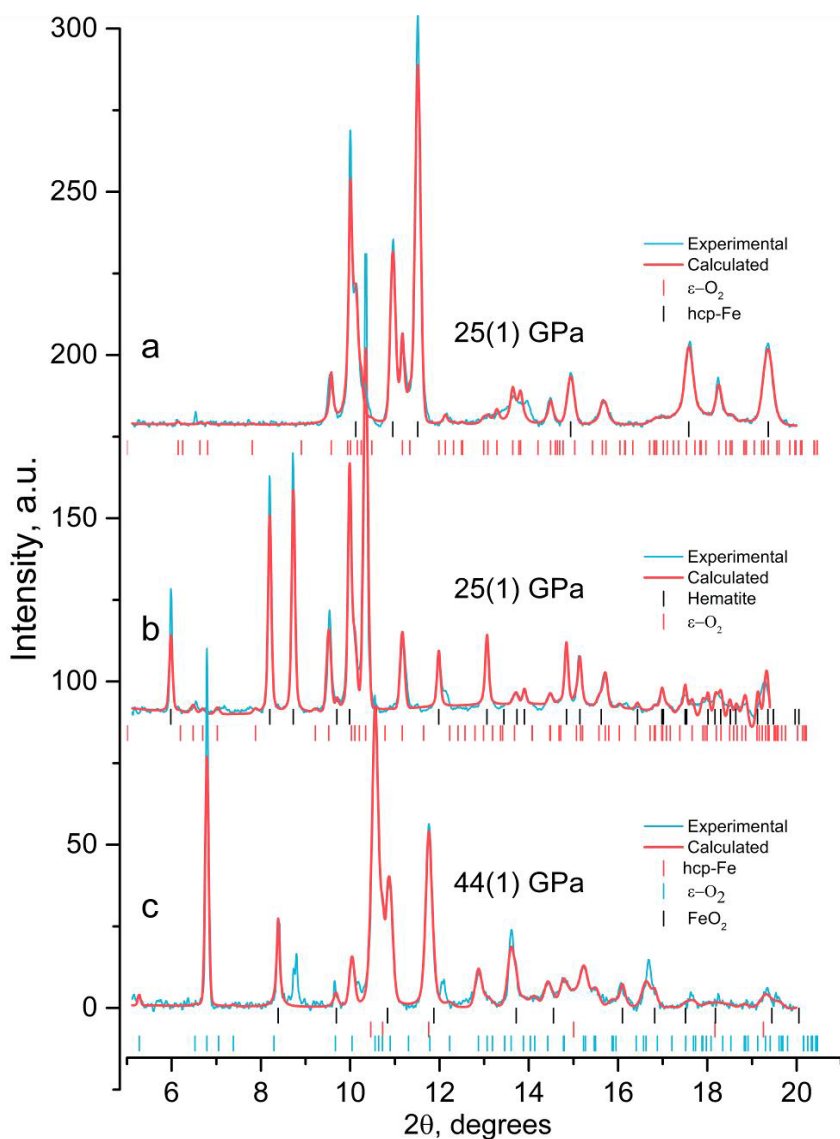


Figure 6.7-2 LeBail fit of convoluted 2D XRD patterns of starting materials and temperature-quenched products of reaction between Fe and ϵ -O₂ after laser-heating to 1200K at 25 GPa ($\lambda=0.3738$ Å). (a) Starting materials at 25(1) GPa. Black ticks – hcp-Fe peak positions ($P6_3/mmc$, cell parameters: $a=2.44555(2)$ Å, $c=3.91572(4)$ Å); red ticks - ϵ -O₂ peak positions ($C2/m$, $a=7.71051(8)$ Å, $b=5.47545(7)$ Å, $c=3.6419(1)$ Å, $\beta=116.061(2)^\circ$). (b) Temperature-quenched products of reaction between hcp-Fe and O₈ after laser heating to 1200 K at 25(1) GPa; Black ticks - Fe₂O₃ peak positions ($R\bar{3}c$, cell parameters: $a=4.91496(3)$ Å, $c=13.2579(1)$ Å); red ticks - O₈ (ϵ -O₂) peak positions ($C2/m$, $a=7.5876(2)$ Å, $b=5.4911(1)$ Å, $c=3.85594(6)$ Å, $\beta=115.328(2)^\circ$). (c) Reaction products after laser heating to 1500 K at 46(1) GPa. Black ticks – FeO₂ ($Pa\bar{3}$, $a=4.42641(77)$ Å); red ticks – hcp-Fe ($P6_3/mmc$, $a=2.36771(5)$ Å, $c=3.9940(2)$ Å); light blue ticks - ϵ -O₂ peak positions ($C2/m$, $a=7.3117(2)$ Å, $b=5.1644(1)$ Å, $c=3.50936(8)$ Å, $\beta=115.964(2)^\circ$)

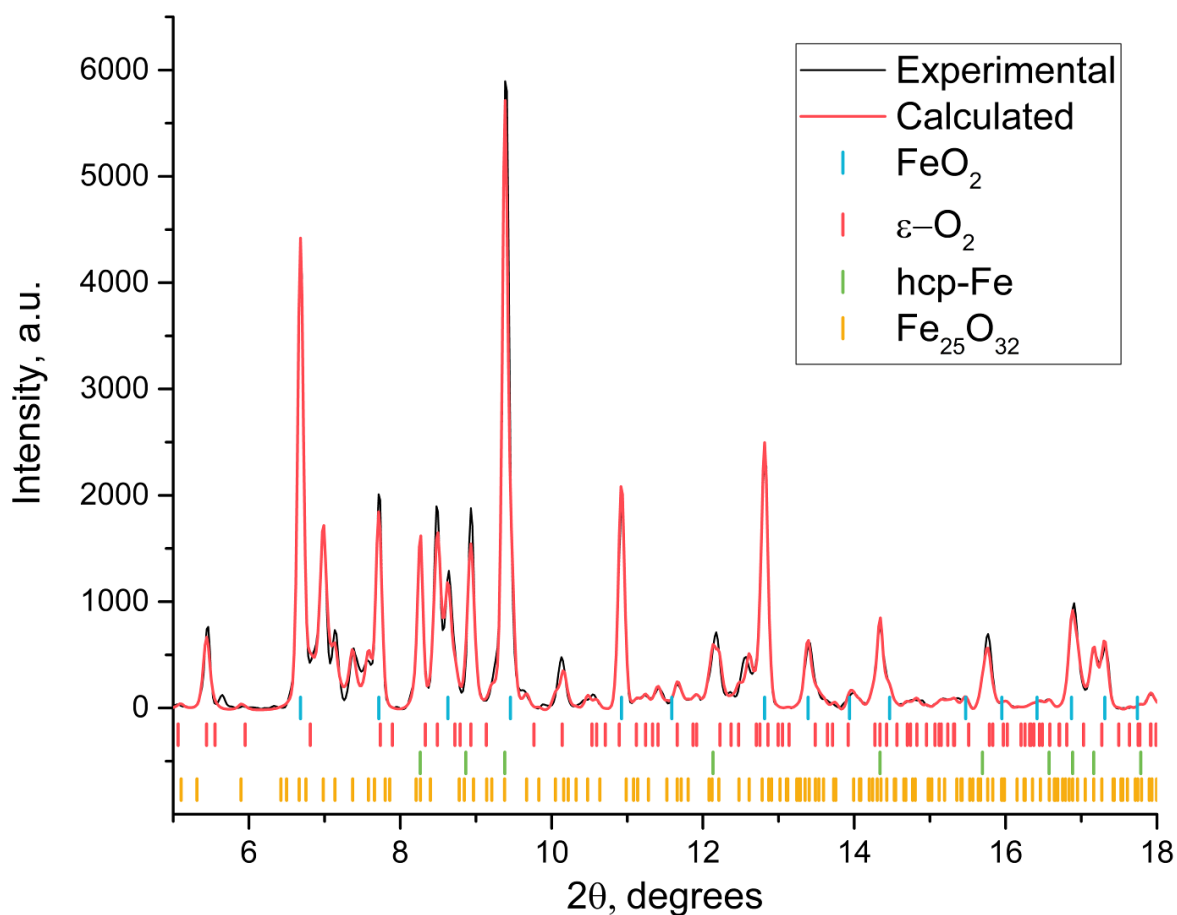


Figure 6.7-3 LeBail fit of convoluted 2D XRD pattern of temperature-quenched products of reaction between Fe and ϵ -O₂ after laser-heating to 1200K at 58(2) GPa. Black line – experimental data, red line – calculated pattern; light blue ticks correspond to FeO₂ peak positions ($Pa\bar{3}$ - $Pa\bar{3}$), cell parameter $a = 4.3849(4)$ Å; red ticks correspond to O₈ (ϵ -O) ($C2/m$, $a = 7.480(5)$ Å, $b = 4.966(2)$ Å, $c = 3.475(2)$ Å, $\beta = 116.67(5)^\circ$); green ticks correspond to hcp-Fe peak positions ($P6_3/mmc$, $a = 2.36615(36)$ Å, $c = 3.7925(11)$ Å); orange ticks correspond to Fe₂₅O₃₂ ($P6-2m\bar{P}\bar{6}2m$, $a = 13.2292(34)$ Å, $c = 2.60658(88)$ Å). $R_p = 10.92$.

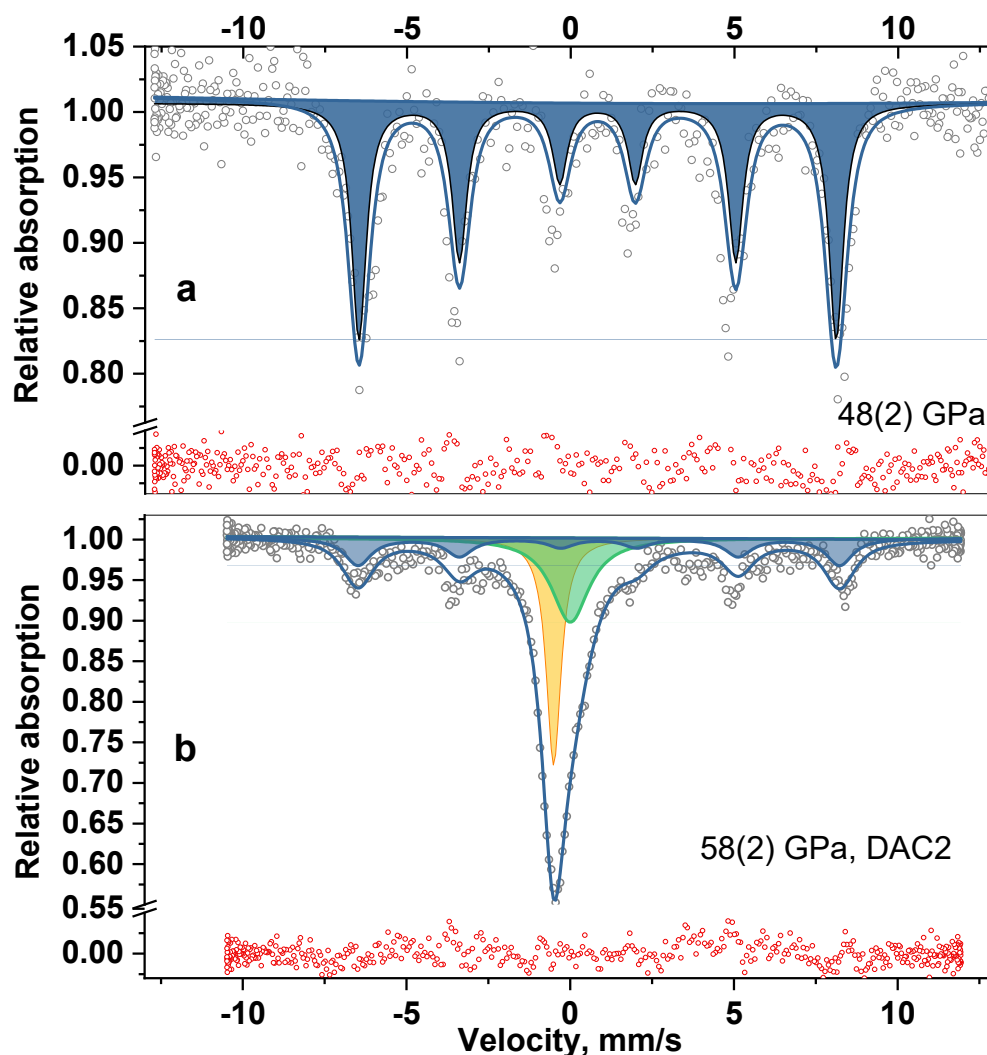


Figure 6.7-4 Mössbauer spectra of laser heated $\text{Fe}_{25}\text{O}_{32}$ and FeO_2 obtained at ID-18 ESRF. Normally Mössbauer spectroscopy would be the ideal method to determine the oxidation state of iron in cubic FeO_2 . Unfortunately, the diameter of the beam of even the SMS (about $20\ \mu\text{m}$) is too large to avoid signals from the starting material and products of reaction between iron and oxygen. (a) Mössbauer spectrum of $\text{Fe}_{25}\text{O}_{32}$ obtained after heating FeO at $48(2)\ \text{GPa}$ (53). The spectrum shows one sextet (shaded blue) with center shift (CS)= $0.82(2)\ \text{mm/s}$ and magnetic field splitting $45.2(16)\ \text{T}$. (b) Mössbauer spectrum of the contents of DAC2 after laser heating at $58(2)\ \text{GPa}$. The spectrum shows a signal from the starting material (hcp-Fe, singlet with CS = $-0.49(1)\ \text{mm/s}$, shaded yellow), intermediate products of reaction between iron and oxygen, particularly $\text{Fe}_{25}\text{O}_{32}$ (53), identified from characteristic spectral features such as a sextet (shaded blue) with CS= $0.84(1)\ \text{mm/s}$ and magnetic field splitting $45.68(6)\ \text{T}$ and powder XRD data, see Figure 6.7-3), and of HP-PdF₂-type FeO_2 (singlet with CS= $0.06(5)\ \text{mm/s}$, shaded green). The value of the center shift of the singlet due to FeO_2 is consistent with Fe(III) in the low spin state.

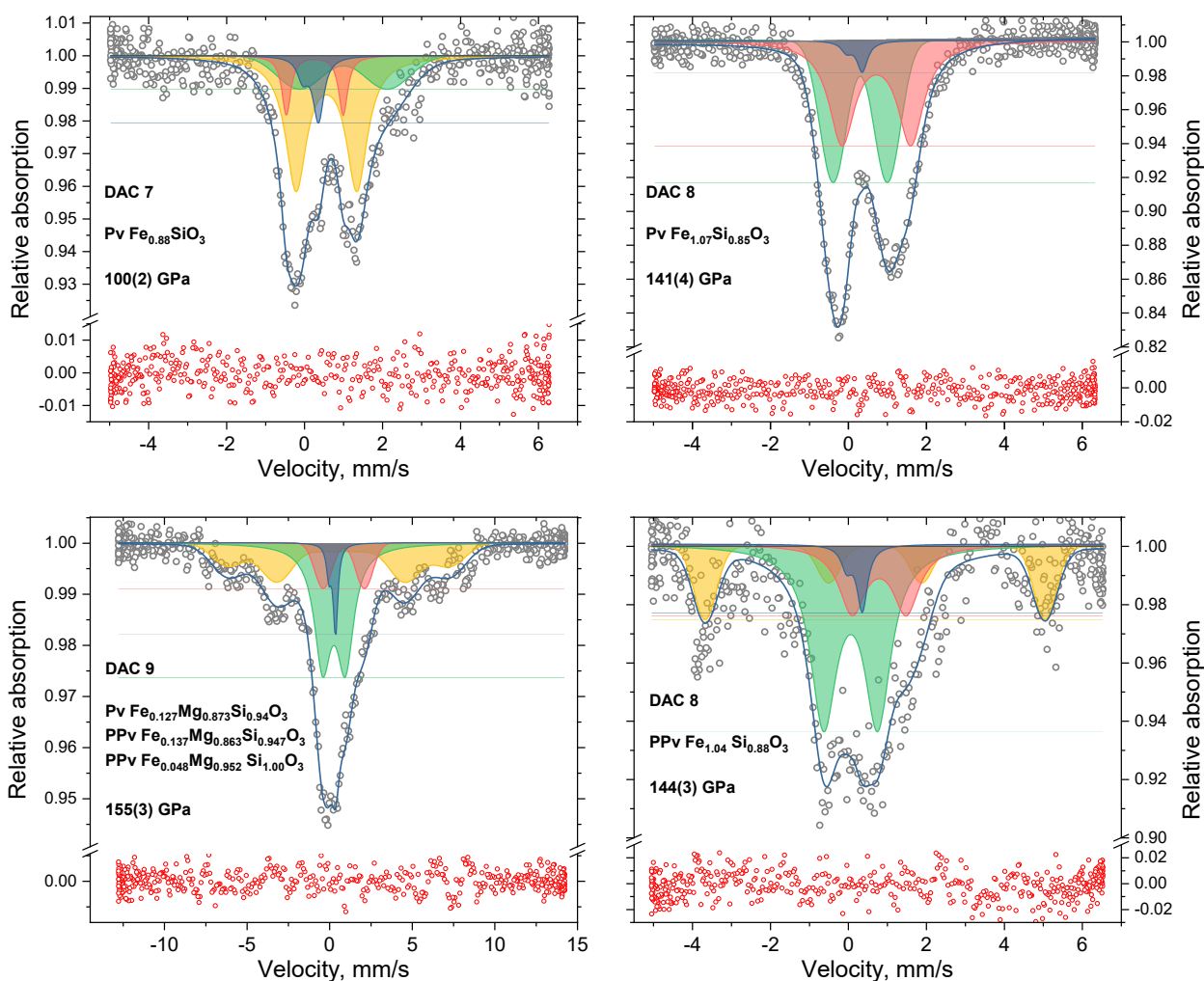


Figure 6.7-5 Examples of Mössbauer (SMS) spectra of silicate perovskites and post-perovskites. In all spectra, the blue asymmetric doublet indicates the contribution from Fe in the Be lenses. Upper left: Mössbauer spectrum of Fe-bridgmanite synthesized at 100(2) GPa. We cannot distinguish individual sites of silicate perovskite from the SMS fit, but can assign one component (red doublet, CS=0.26(6) mm/s, QS=1.46(10) mm/s, area 11 %) to high spin Fe³⁺, and another component (green doublet, CS=1.0(1) mm/s, QS=2.2(4) mm/s, area 21%) to Fe²⁺ in either the intermediate- or high-spin state. Fe³⁺/ΣFe of silicate perovskite based on the SMS fit is 0.34(10) and the calculated oxygen charge is 2.02(5). There is a large contribution from a component with intermediate valence state (yellow doublet, CS=0.56(10) mm/s, QS=1.56(5) mm/s, area 58%), which could be from a Fe-rich phase such as Fe₄O₅. Since the starting material has Fe:Si = 1.47 and silicate perovskite has Fe:Si of 0.88, it is not surprising to observe an additional Fe-rich phase. Upper right: Mössbauer spectrum of Fe-bridgmanite at 141(4) GPa. We cannot distinguish individual sites of silicate perovskite from the SMS fit, but can assign one component (green doublet, CS=0.31(4) mm/s,

QS=1.40(4) mm/s, area 47%) to high-spin Fe³⁺ and another component (red doublet, CS=0.72(4) mm/s, QS=1.77(10) mm/s, area 49%) to Fe²⁺ in either the intermediate- or high-spin state. Fe³⁺/ΣFe of silicate perovskite based on the SMS fit is 0.49(5) and the calculated oxygen charge is 2.02(10). The difference between Fe:Si of the starting material (1.47) and run product (1.18) according to X-ray diffraction is not large (within uncertainties of the method), so we assume that all absorption is due to silicate perovskite. Lower right: Mössbauer spectrum of Fe-silicate post-perovskite synthesized at 144(3) GPa. We cannot distinguish individual sites of silicate post-perovskite from the SMS fit, but can assign one component (green doublet, CS=0.06(7) mm/s, QS=1.39(9) mm/s, area 46%) to low-spin Fe³⁺ and two components (paramagnetic red doublet, CS=0.79(19) mm/s, QS=1.39(23) mm/s, area 18%; yellow magnetic sextet, CS=0.69(6) mm/s, magnetic hyperfine splitting 46.7(7) T, area 32%) to high-spin Fe²⁺. Fe³⁺/ΣFe of silicate post-perovskite based on the SMS fit is 0.48(20) and the calculated oxygen charge is 2.03(10). The difference between Fe:Si of the starting material (1.47) and run product (1.26) according X-ray diffraction (within uncertainties of the method) is not large, so we assume that all absorption is due to silicate post-perovskite. Lower left: Mössbauer spectrum of silicate perovskite and post-perovskites at 155(3) GPa. The dominant components are similar to those in the lower right spectrum, so are assigned to low-spin Fe³⁺ (green doublet, CS=0.27(11) mm/s, QS=1.38(28) mm/s, area 34%) and high-spin Fe²⁺ (paramagnetic red doublet, CS=0.9(3) mm/s, QS=2.5(5) mm/s, area 9%; yellow magnetic sextet, CS=0.6(1) mm/s, magnetic hyperfine splitting 42(1) T, area 52%). The calculated oxygen charge is 1.92(3), nearly independent of Fe³⁺/ΣFe due to the low concentration of total iron.

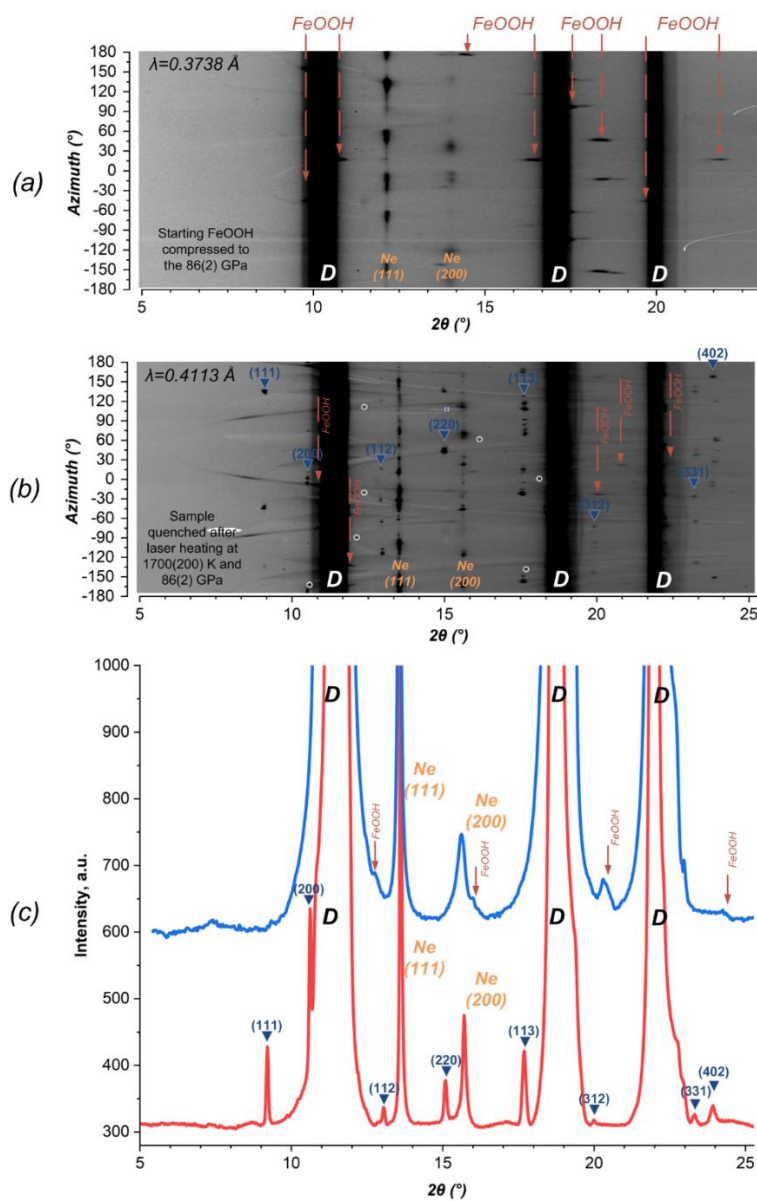


Figure 6.7-6 XRD patterns of FeOOH before and after laser heating at 86(2) GPa (DAC11, see Table 6.7-1). (a) Starting single-crystal of goethite was compressed to 86(2) GPa at ambient temperature in a DAC equipped with nano-polycrystalline diamond anvils allowing glitch-free X-ray Absorption Spectroscopy (183). Positions of FeOOH reflections are marked with red arrows. Diamond reflections are marked with “D”, and reflections of the pressure-transmitting medium are marked with “Ne”. (b) After laser-heating FeOOH transformed to the cubic FeO_2H_x phase ($a = 4.44(5) \text{ \AA}$, $x=0.53$ (69), position of reflections are marked with blue inverted triangles with indices). Diamond reflections are marked with “D”, and reflections of the pressure-transmitting medium are marked with “Ne”. White circles indicate bad detector pixels. The few remaining very weak reflections of FeOOH are marked with red. (c) \AA -X-

ray wavelength integrated 2D patterns corresponding to those shown on (a) and (b) were convoluted and normalized to 0.4113. The blue line shows powder diffraction from FeOOH before heating at 86(2) GPa, and the red line shows the pattern after laser heating at 1700(200) K and 86(2) GPa. The $\text{FeO}_2\text{H}_{0.5}$ reflections are marked by inverted triangles with indices.

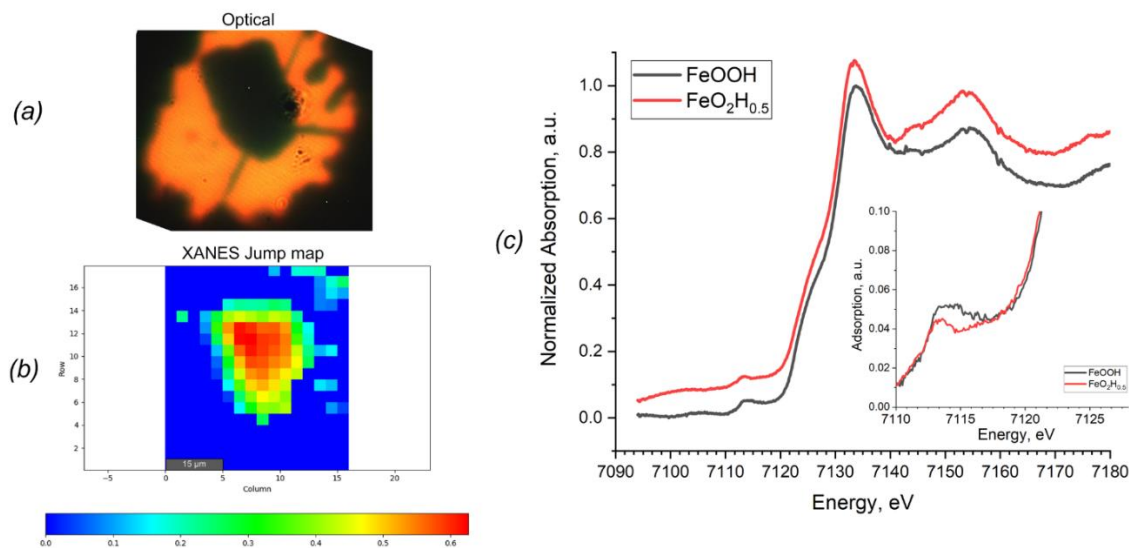


Figure 6.7-7 Results of X-ray absorption spectroscopy measurements on FeOOH before and after laser heating at 1700(200) K and 86(2) GPa (DAC11, see Table 6.7-1). (a) Microphotograph of FeOOH after laser heating. (b) XANES jump map (spectra collected at room temperature with steps of 3 μm covering the whole sample). Column and row numbers denote the number of the step along the corresponding direction; color coding reflects the value of the XAS jump. (c) Normalized X-ray absorption spectra of FeOOH cold-compressed to 86(2) GPa (gray line) and $\text{FeO}_2\text{H}_{0.5}$ (red line) that were synthesized by laser-heating of the starting material at 1700(200) K at the same pressure. Both spectra were collected at the center of the sample. The inset shows the enlarged pre-jump XANES region of the spectra. After laser heating the pre-jump peak narrows and a pronounced change in the edge feature is observed. However, the position of the XAS jump does not change after laser heating, so we infer that iron does not alter its oxidation state. The initial FeOOH transforms into cubic oxhydroxide; therefore iron in FeO_2H_x is in the ferric state.

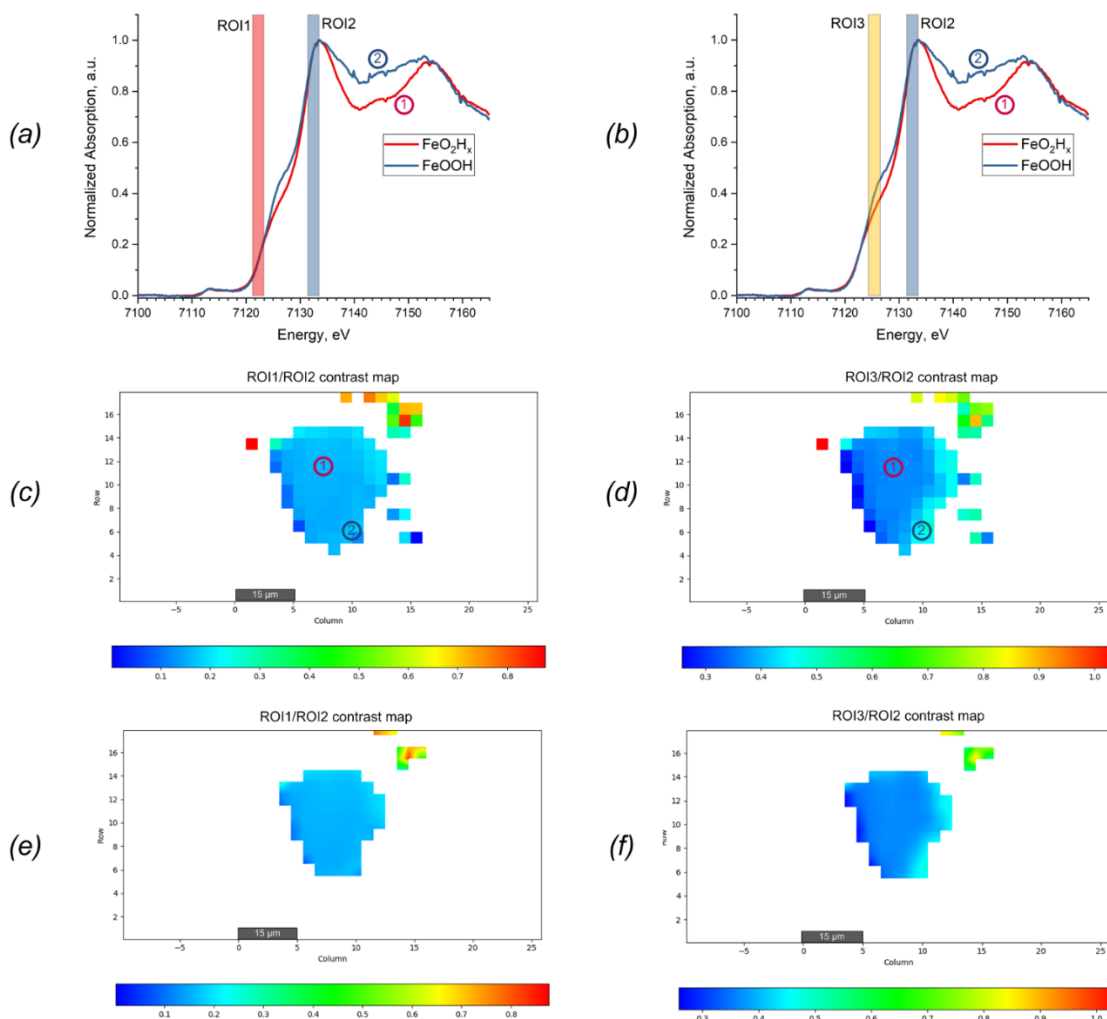


Figure 6.7-8 XAS spectra and maps of FeOOH in Ne pressure transmitting medium after laser heating at 1700(200) K and 86(2) GPa (DAC11, see Table 6.7-1). (a) and (b): XAS spectra collected at different spots of the sample (denoted by red and blue circles with numbers). The red line corresponds to the spectrum of cubic $\text{FeO}_2\text{H}_{0.5}$, and the blue spectrum resembles those taken from the sample edge (the area was difficult to heat and probably experienced lower temperatures) belonging to FeOOH which is characterized by a pronounced shoulder at ~ 7125 eV. Regions of Interest (ROI) highlighted in color designate the three energy regions: ROI1 — beginning of the edge (red), ROI2 — spectral maximum (blue), ROI3 (yellow) — edge feature. This set of ROIs was further used to build comparative contrast maps (c) and (d) as described in (207). The comparative contrast XANES map (c) and the map with bilinear filtration (e) built on the ROI1/ROI2 ratio indicates that there is no significant variation of jump position within the whole sample, so all iron in the sample is ferric after laser heating at 1700(200) K and 86(2) GPa. The comparative contrast XANES map (d) and the map with bilinear filtration (f) built on the ROI3/ROI2 ratio indicates that there is a

variation in the XAS edge feature near the sample boarder which could be explained by the remaining FeOOH phase that did not transform into FeO_2H_x due to temperature gradients. This conclusion is in agreement with our XRD observations (see Figure 6.7-6).

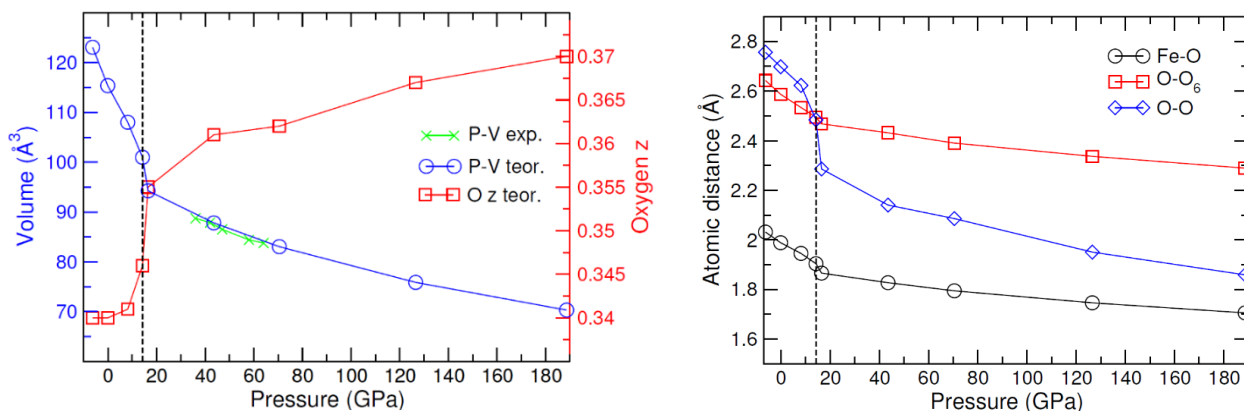


Figure 6.7-9 Evolution of the crystal structure parameters: (a) lattice volume and fractional z coordinate of oxygen, and (b) interatomic Fe-O, O-O₆, and O-O bond distances of FeO_2 under pressure as obtained by DFT+DMFT calculations at $T=1160$ K. Note that below ~ 14 GPa, PdF_2 -type FeO_2 shows a low-spin to high-spin phase transition, associated with the formation of local moments.

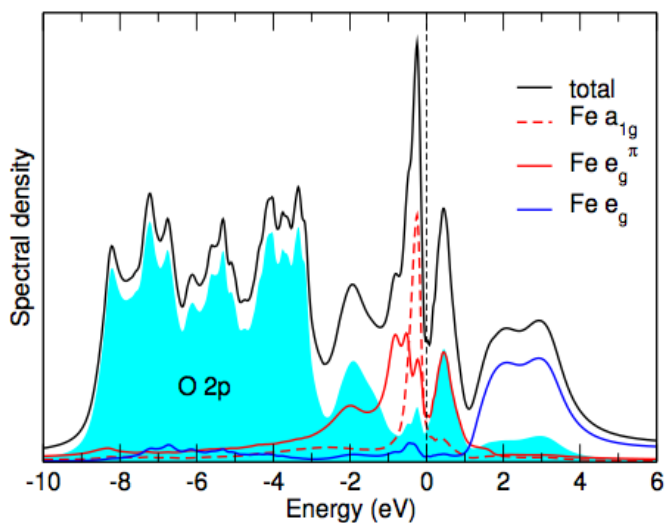


Figure 6.7-10 Orbitally-resolved spectral functions of FeO_2 for Fe 3d (delineated by colored lines) and O 2p (blue shaded area) obtained by DFT+DMFT at 1160 K and ~ 70 GPa. The electronic temperature is set to $T = 1160$ K. The Fermi energy ($E_F = 0$ eV) is taken as energy zero, and is shown by a vertical dashed line. Due to distorted FeO_6 octahedron symmetry, the Fe t_{2g} states split into an a_{1g} singlet and e_g doublet. Fe e_g orbitals are empty and are located well above the Fermi level between 1 to 4 eV. Fe t_{2g} states form weakly renormalised ($m/m^* \sim 1.6$)

quasiparticle bands near E_F . The bonding-antibonding splitting of the O 2p orbitals is ~ 2 -3 eV. The bonding σ states appear at ~ -2 eV, while the anti-bonding σ^* states due to mixing with the Fe t_{2g} states at the Fermi level split into the $t_{2g} \pm \sigma^*$ combinations (two peaks at -1 and +1 eV). Note the empty $t_{2g} - \sigma^*$ O-O band located ~ 1 eV above the Fermi level. Our results show the O 2p states crossing the Fermi level, implying that FeO₂ belongs to the class of negative charge-transfer gap materials in the Zaanen-Sawatzky-Allen scheme (excitation energy for the transfer of electrons from the O 2p to Fe 3d states is negative). In such materials, instead of having an electronic configuration corresponding to the formal valence state, e.g. Fe⁴⁺ (3d⁴) and O²⁻ (2p⁶) configuration in FeO₂, the system prefers to have a configuration with higher occupation of the 3d-shell, creating holes on oxygen. This behavior can be attributed to the known high resistance of transition metal ions to extremely elevated valence (which is energetically unfavorable, e.g., due to a large Coulomb interaction U value between the electrons in the 3d shell) and prefer to retain a lower valence (higher occupation of the 3d-shell) at the expense of creating holes on oxygen.

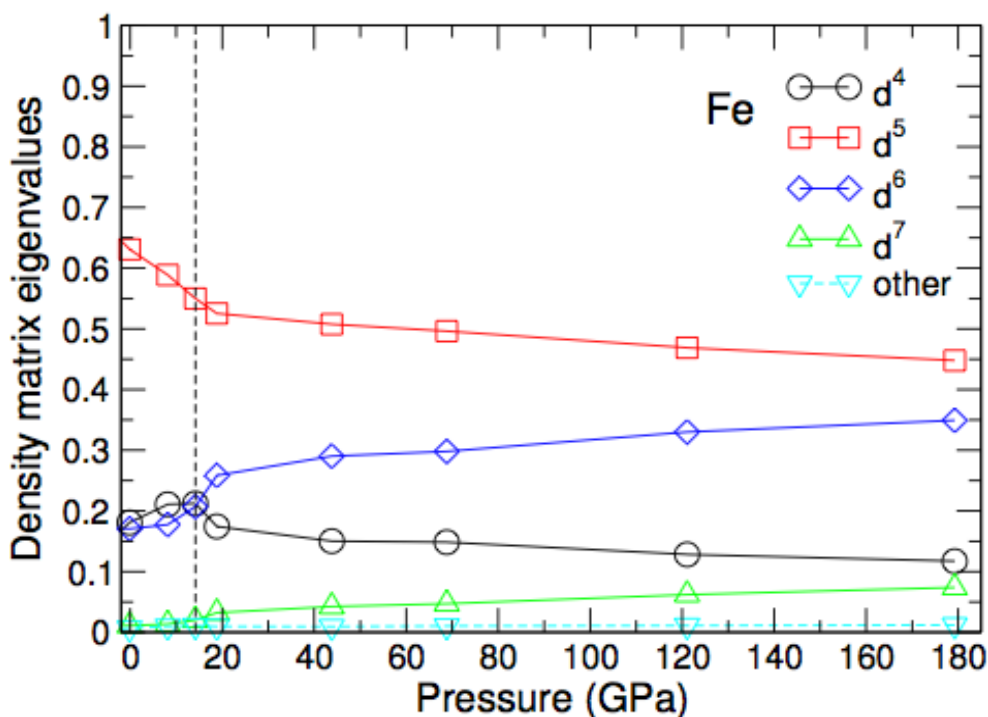


Figure 6.7-11. Projection of the DFT+DMFT electronic state to various Fe 3d atomic configurations (d⁴, d⁵, d⁶, and others) for FeO₂ as a function of compression. The oxidation state of the Fe ion is close to 3+ with a 3d⁵ electronic configuration

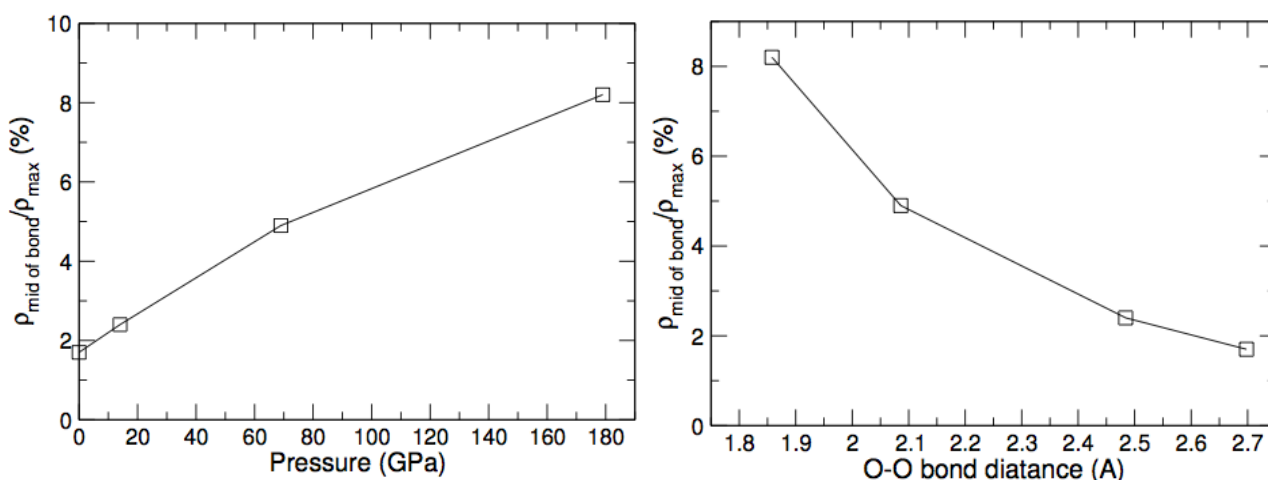


Figure 6.7-12 Evolution of the valence electron density $\rho(r)/\rho_{\text{max}}$ of FeO_2 in the center of the O-O bond as a function of pressure (left) and of the corresponding O-O bond distance (right). Note, that the peroxide bond in MgO_2 exhibits an O-O bond length of ~ 1.49 Å at ambient pressure, which corresponds to a $\rho(r)/\rho_{\text{max}}$ of $\sim 21\%$

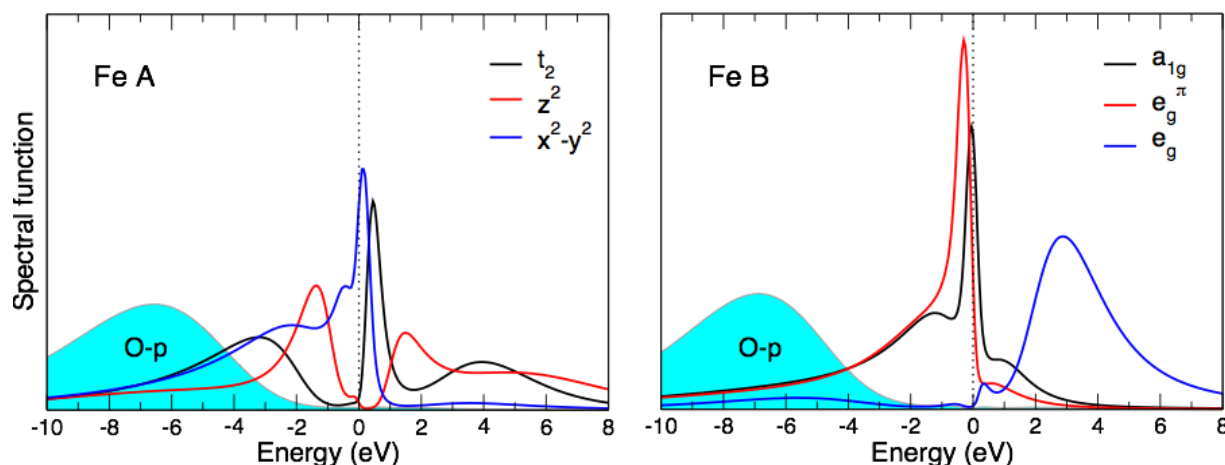


Figure 6.7-13 Orbitally-resolved spectral functions of $\text{Fe}_A(\text{Si}_{0.75}\text{Fe}_{0.25})\text{O}_3$ for Fe $3d$ (delineated by colored lines and O $2p$ (blue shaded area in A and B) obtained by DFT+DMFT at 1160 K and ~ 140 GPa. The Fermi energy E_F is set to zero and is shown by a vertical dashed line. In the A site Fe t_2 and z^2 states are nearly half-filled (orbital occupation ~ 0.52), while orbital occupations of the Fe x^2-y^2 states are ~ 0.81 . Fe x^2-y^2 states show a quasiparticle peak at the Fermi level, with a lower Hubbard band satellite at about -3 eV. In the B site: Fe a_{1g} and e_g^π orbital occupations are 0.77-0.9. Fe e_g states are empty and are located well above the Fermi level at about 2-4 eV. Fe a_{1g} and e_g^π states show a quasiparticle peak near the Fermi level with a lower Hubbard band at about -2 eV. The calculated local magnetic moments are ~ 4.08 and $1.19 \mu_B$ for the states listed in A and B, respectively.

Chapter 6. Variation of oxygen oxidation state at the base of the Earth's mantle

Table 6.7-1 Description of experimental runs on FeO₂ and (Fe,Al)-bearing silicate perovskite and post-perovskite synthesis in the present work.

DAC 1

P, GPa	T, K	Observed phases	Facility	Details
25(1) GPa	300	hcp-Fe, ϵ -O ₂	ESRF ID-27	Characterization of starting materials
25(1) GPa	1200 K	Fe ₂ O ₃ , hcp-Fe, ϵ -O ₂	ESRF ID-27	Laser heating of cell contents, XRD mapping of T-quenched products
46(1) GPa	1500 K	FeO ₂ , hcp-Fe, ϵ -O ₂	ESRF ID-27	Reheating of cell contents, XRD mapping of T-quenched products, Single-crystal data collection

DAC 2

P, GPa	T, K	Observed phases	Facility	Details
55(2) GPa	300	hcp-Fe, ϵ -O ₂	APS IDD13	Characterization of starting materials
55(2) to 58(2) GPa	1200 K to 1800 K	FeO ₂ , Fe ₂₅ O ₃₂ , hcp-Fe, ϵ -O ₂	APS IDD13	4 cycles of laser heating with temperature increase in steps, XRD mapping of T-quenched products
58(2) GPa	300 K	FeO ₂	APS IDD13	Single crystal data collection
58(2) GPa	300 K	FeO ₂ , Fe, Fe ₂₅ O ₃₂	ESRF ID-18	<i>in situ</i> Synchrotron Mössbauer Source spectroscopy data collection.
64(2) GPa	300 K	FeO ₂	ESRF ID-27	Single crystal data collection
73(2) GPa	300 K	FeO ₂	ESRF ID-27	Single crystal data collection

DAC 3

P, GPa	T, K	Observed phases	Facility	Comments
44(2) GPa	300 K	hcp-Fe, ϵ -O ₂	ESRF ID-27	Characterization of starting materials
44(2) GPa	1200 K	FeO ₂ , hcp-Fe, ϵ -O ₂	ESRF ID-27	Laser heating of cell contents, XRD mapping of T-quenched products
42(2) GPa	300 K	FeO ₂ , hcp-Fe, ϵ -O ₂	ESRF ID-27	Single crystal data collection
36(2) GPa	300 K	FeO ₂ , hcp-Fe, ϵ -O ₂	ESRF ID-27	Single crystal data collection

DAC 4

P, GPa	T, K	Observed phases	Facility	Comments
129(1) GPa	300	Mg _{0.86} Fe _{0.14} Al _{0.04} Si _{0.96} O ₃ (FE14), Ne	PETRAIII P02	Characterization of starting material
137(1) GPa	2500(100) K**	Pv Fe _{0.013} Mg _{0.987} Si _{0.905} O ₃ * PPv Fe _{0.093} Mg _{0.875} Si _{1.032} O ₃	PETRAIII P02	Laser heated, XRD mapping of T-quenched products, single crystal data collection

* Here and in all other single crystal refinements "Si" means total silicon and aluminum content

** Temperature of the heat treatment, data collected at ambient temperature.

DAC 5

P, GPa	T, K	Observed phases	Facility	Comments
--------	------	-----------------	----------	----------

Chapter 6. Variation of oxygen oxidation state at the base of the Earth's mantle

110(2) GPa	2550(100) K	Pv Fe _{0.172} Mg _{0.828} Si _{0.971} O ₃ (FE17), Ne	ESRF, ID09	Laser heated, XRD mapping of T-quenched products, single crystal data collection
142(3) GPa	2600(100) K	Pv Fe _{0.263} Mg _{0.816} Si _{0.921} O ₃ Pv Fe _{0.149} Mg _{0.851} SiO ₃ PPv Fe _{0.191} Mg _{0.84} Si _{0.969} O ₃	ESRF, ID09	Laser heated, XRD mapping of T-quenched products, single crystal data collection

DAC 6

P, GPa	T, K	Observed phases	Facility	Comments
148(4) GPa	300 K	Mg _{0.60} Fe _{0.40} Si _{0.63} Al _{0.37} O ₃ (FE40), Ne	ESRF, ID09	Characterization of starting material
153(5) GPa	2550(150) K	Pv Fe _{0.638} Mg _{0.423} Si _{0.939} O ₃ PPv Fe _{0.058} Mg _{0.942} Si _{0.91} O ₃ PPv Fe _{0.17} Mg _{0.83} Si _{0.865} O ₃ PPv Fe _{0.228} Mg _{0.772} Si _{1.00} O ₃	ESRF, ID09	Laser heated, XRD mapping of T-quenched products, single crystal data collection

DAC 7

P, GPa	T, K	Observed phases	Facility	Comments
100(2) GPa	2300(150) K	Pv Fe _{0.88} SiO ₃ , Ne	APS IDD-13 ESRF, ID18	Synthesis of Pv from skiaigite-majorite garnet (Fe _{1.19} Si _{0.81} O ₃) and its characterization by X-ray diffraction and SMS

DAC 8

P, GPa	T, K	Observed phases	Facility	Comments
141(4) GPa	2500(150) K	Pv Fe _{1.07} Si _{0.85} O ₃ , Ne	APS, IDD-13	Synthesis of Pv from skiaigite-majorite garnet (Fe _{1.19} Si _{0.81} O ₃) and its characterization by X-ray diffraction and SMS
144(3) GPa	2550(150) K	PPv Fe _{1.04} Si _{0.88} O ₃	APS, IDD-13 ESRF, ID18	Laser heated, XRD mapping of T-quenched products, single crystal data collection Mössbauer spectroscopy (SMS)

DAC 9

P, GPa	T, K	Observed phases	Facility	Comments
141(4) GPa	2400(150) K	Pv Fe _{0.111} Mg _{0.889} Si _{0.907} O ₃ , Ne	ESRF, ID27	Starting material FE14, laser heated, XRD mapping of T-quenched products, single crystal data collection
155(3) GPa	2700(150) K	Pv Fe _{0.127} Mg _{0.873} Si _{0.94} O ₃ PPv Fe _{0.137} Mg _{0.863} Si _{0.947} O ₃ PPv Fe _{0.048} Mg _{0.952} Si _{1.00} O ₃	ESRF, ID27 ESRF, ID18	Laser heated, XRD mapping of T-quenched products, single crystal data collection Mössbauer spectroscopy (SMS)

DAC 10

P, GPa	T, K	Observed phases	Facility	Comments
81(2)	1500(100)	FeO ₂ H _{0.4}	ESRF, ID27	Starting material goethite. Single-crystal data collection

DAC 11

P, GPa	T, K	Observed phases	Facility	Comments
86(2)	1700(200) K	FeO ₂ H _{0.5} , FeOOH (minor)	ESRF, ID24	Starting material goethite. XANES data collection before and after heating
86(2)	300 K	FeO ₂ H _{0.5} , FeOOH (minor)	ESRF, ID15	Powder XRD data collection. Confirmation of FeO ₂ H _x synthesis

Chapter 6. Variation of oxygen oxidation state at the base of the Earth's mantle

 Table 6.7-2 Details of crystal structure refinements and atomic coordinates of FeO₂ at different pressures

Pressure	36(1) GPa	42(1) GPa	47(1) GPa	58(2) GPa	64(1) GPa	73(1) GPa	81(2)
Chemical formula	FeO ₂	FeO ₂ H _{0.4}					
Mr	87.85	87.85	87.85	87.85	87.85	87.85	87.85
Crystal system, space group	Cubic, Pa3-						
Temperature (K)	293						
a (Å)	4.4603 (7)	4.4459 (9)	4.4123 (14)	4.3868 (9)	4.3755 (9)	4.3522 (7)	4.43(1)
V (Å ³)	88.73 (4)	87.88 (5)	86.81 (8)	84.42 (5)	83.77 (5)	82.44 (4)	86.94(8)
Z	4	4	4	4	4	4	4
F(000)	168	168	168	168	168	168	618
Dx (Mg m ⁻³)	6.576	6.64	6.722	6.912	6.966	7.078	6.711
Radiation type	Synchrotron, λ = 0.373 Å	Synchrotron, λ = 0.373 Å	Synchrotron, λ = 0.373 Å	Synchrotron, λ = 0.295 Å	Synchrotron, λ = 0.373 Å	Synchrotron, λ = 0.3738 Å	synchrotron, λ = 0.2907 Å
μ (mm ⁻¹)	8.28	8.36	8.46	1.45	8.77	8.91	8.45
Absorption correction	–	–	–	–	–	–	–
No. of measured, independent and observed [I > 2σ(I)] reflections	126, 47, 37	128, 49, 38	64, 26, 26	126, 69, 53	102, 43, 28	133, 41, 33	421, 99, 64
R _{int}	0.035	0.018	0.010	0.05	0.097	0.061	0.088
θ values (°)	θ _{max} = 16.3, θ _{min} = 4.2	θ _{max} = 17.5, θ _{min} = 4.2	θ _{max} = 17.5, θ _{min} = 4.2	θ _{max} = 15.4, θ _{min} = 3.3	θ _{max} = 17.8, θ _{min} = 4.2	θ _{max} = 16.0, θ _{min} = 4.3	θ _{max} = 17.5, θ _{min} = 3.3
Range of h, k, l	-5 < h < 6 -6 < k < 6 -4 < l < 5	-5 < h < 6 -6 < k < 6 -4 < l < 5	-6 < h < 6 -5 < k < 5 -5 < l < 4	-5 < h < 6 -7 < k < 7 -5 < l < 7	-6 < h < 6 -6 < k < 6 -4 < l < 5	-5 < h < 5 -6 < k < 6 -3 < l < 4	h = -7→7, k = -3→4, l = -7→8
Refinement on	F2	F2	F2	F2	F2	F2	F ²
R[F2 > 2σ(F2)], wR(F2), S	0.065, 0.183, 1.16	0.059, 0.170, 1.28	0.074, 0.171, 1.28	0.036, 0.101, 1.05	0.063, 0.168, 1.12	0.078, 0.203, 1.15	0.057, 0.150, 1.06
Parameters/restraints	8/0	8/0	8/0	6/0	7/0	7/0	6/0
Δρ _{max} , Δρ _{min} (e/Å ⁻³)	1.43, -1.77	1.12, -1.69	1.46, -1.43	1.00, -1.72	1.65, -1.95	1.57, -1.56	1.06, -1.43
Atomic coordinates (xyz) and Wyckoff position							
Fe1 (4a)	0.0000	0.0000	0.0000	0.0000	0.0000	0.0000	0.0000
O1 (8c)	0.3574(6)	0.3567(8)	0.354(3)	0.3594(3)	0.3611(16)	0.3618 (16)	0.3523(6)

Table 6.7-3 Details of crystal structure refinements and atomic coordinates of trigonal FeO₂ at different pressures

Pressure	25(1)
Chemical formula	FeO ₂
Mr	87.85
Crystal system, space group	Trigonal, R3-
Temperature (K)	293
a (Å)	6.271 (7)
c(Å)	7.662 (4)
V (Å ³)	260.9 (6)
Z	12
F(000)	504
Dx (Mg m ⁻³)	6.709
Radiation type	Synchrotron, λ = 0.3738 Å
μ (mm ⁻¹)	8.45
Atomic coordinates (x,y,z)	
Fe1	0.5, 0.0, 0.0
Fe2	0.0, 0.0, 0.0
O1	0.0, 0.0, 0.363(2)
O2	0.234(3), 0.261(3), 0.102(2)
No. of measured, independent and observed [I > 2σ(I)] reflections	127, 87, 43
R _{int}	0.038
θ values (°)	θ _{max} = 17.7, θ _{min} = 3.4
Range of h, k, l	-10 < h < 9 -6 < k < 7 -9 < l < 11
Refinement on	F ₂
R[F ₂ > 2σ(F ₂)], wR(F ₂), S	0.066, 0.187, 1.08
No. of parameters	12
No. of restraints	0
Δρ _{max} , Δρ _{min} (e/Å ⁻³)	1.35, -1.04

Chapter 6. Variation of oxygen oxidation state at the base of the Earth's mantle

Table 6.7-4 Details of crystal structure refinements of silicate perovskite and post-perovskites at different pressures

Sample, DAC #	FE14, DAC4	FE14, DAC4	FE17, DAC5	FE17, DAC5	FE17, DAC5	FE17, DAC5	FE40, DAC6	FE40, DAC6	FE40, DAC6
Chemical formula	Fe _{0.013} Mg _{0.987} Si _{0.905} O ₃	Fe _{0.093} Mg _{0.875} Si _{1.032} O ₃	Fe _{0.191} Mg _{0.84} Si _{0.969} O ₃	Fe _{0.172} Mg _{0.828} Si _{0.971} O ₃	Fe _{0.263} Mg _{0.816} Si _{0.921} O ₃	Fe _{0.149} Mg _{0.851} SiO ₃	Fe _{0.228} Mg _{0.772} SiO ₃	Fe _{0.17} Mg _{0.83} Si _{0.865} O ₃	Fe _{0.058} Mg _{0.942} Si _{0.91} O ₃
Pressure, GPa	137(1)	137(1)	142(1)	110(2)	142(3)	142(3)	153(5)	153(5)	153(5)
<i>M_r</i>	98.1	103.4	106.3	103.4	108.4	105.1	107.2	102	99.7
Crystal system, space group	Orthorho mbic <i>Pbnm</i>	Orthorho mbic <i>Cmcm</i>	Orthorho mbic <i>Cmcm</i>	Orthorho mbic <i>Pbnm</i>	Orthorho mbic <i>Pbnm</i>	Orthorho mbic <i>Pbnm</i>	Orthorho mbic <i>Cmcm</i>	Orthorho mbic <i>Cmcm</i>	Orthorho mbic <i>Cmcm</i>
Temperature (K)	293	293	293	293	293	293	293	293	293
<i>a</i> , <i>b</i> , <i>c</i> (Å)	4.2249(2), 4.5387(2), 6.249 (4)	2.4511(6), 8.020(2), 6.0731 (5)	2.4500(7), 8.0037(9), 6.0652(4)	4.343(2), 4.617(3), 6.339(2)	4.2377(1), 4.5419(1), 6.2254(1)	4.251(3), 4.556(4), 6.256(6)	2.4643(6), 8.0087(7), 6.1065(4)	2.453(5), 7.9736(8), 6.0791 (7)	2.473(2), 7.988(5), 6.097(5)
<i>V</i> (Å ³)	119.83 (10)	119.38 (7)	118.93 (4)	127.08 (11)	119.82 (5)	121.16 (18)	120.52 (11)	118.9(1)	120.46 (16)
<i>Z</i>	4	4	4	4	4	4	4	4	4
<i>F</i> (000)	195	205	210	205	214	206	212	202	198
Wavelength	0.28965 Å	0.28965 Å	0.41454 Å	0.41454 Å	0.41454 Å	0.41454 Å	0.41453 Å	0.41453 Å	0.41453 Å
θ range (°)	3–14.3	2.7–16.6	3.0–18.3	3.3–18.0	3.4–17.9	3.4–16.7	3.9–18.3	4.9–15.7	5.9–17.4
μ (mm ⁻¹)	0.22	0.29	0.88	0.67	1.03	0.77	0.93	0.8	0.55
No. of measured, independent and observed [<i>I</i> > 3 σ (<i>I</i>)] reflections	524, 154, 122	308, 166, 115	144, 67, 66	259, 129, 108	223, 118, 113	228, 115, 70	140, 73, 70	108, 56, 35	133, 59, 38
<i>R</i> _{int}	0.04	0.046	0.015	0.024	0.011	0.097	0.009	0.063	0.056
θ range values (°)	2.7 – 14.5	2.7 – 19.9	3.0 – 18.9	3.3 – 19.1	3.4 – 18.7	3.4 – 18.1	3.9 – 18.8	3.0 – 17.9	3.6 – 18.7
Range of <i>h</i> , <i>k</i> , <i>l</i>	-7 < <i>h</i> < 7 -7 < <i>k</i> < 7 5 < <i>l</i> < 4	-5 < <i>h</i> < 5, -9 < <i>k</i> < 4, -13 < <i>l</i> < 13	-1 < <i>h</i> < 1, -11 < <i>k</i> < 10, -8 < <i>l</i> < 9	-5 < <i>h</i> < 6, -4 < <i>k</i> < 5, -7 < <i>l</i> < 8	-4 < <i>h</i> < 5, -5 < <i>k</i> < 4, -8 < <i>l</i> < 7	-5 < <i>h</i> < 5, -4 < <i>k</i> < 6, -6 < <i>l</i> < 7	-3 < <i>h</i> < 3, -7 < <i>k</i> < 6, -9 < <i>l</i> < 9	-3 < <i>h</i> < 3, -10 < <i>k</i> < 9, -4 < <i>l</i> < 6	-2 < <i>h</i> < 3, -9 < <i>k</i> < 9, -7 < <i>l</i> < 5
<i>R</i> [<i>F</i> ² > 2 σ (<i>F</i> ²)], <i>wR</i> (<i>F</i> ²), <i>S</i>	0.069, 0.081, 2.69	0.052, 0.056, 1.35	0.074, 0.099, 7.16	0.084, 0.090, 3.12	0.090, 0.113, 7.69	0.139, 0.143, 2.87	0.074, 0.093, 6.51	0.142, 0.141, 3.27	0.087, 0.088, 3.01
No. of parameters	15	11	12	15	15	15	12	12	12

Chapter 6. Variation of oxygen oxidation state at the base of the Earth's mantle

Sample, DAC #	FE40, DAC6	Fe-ski, DAC8	Fe-ski, DAC8	Fe-ski, DAC8	FE14, DAC9	FE14, DAC9	FE14, DAC9	FE14, DAC9
Chemical formula	Fe _{0.638} Mg _{0.423} Si _{0.939} O ₃	Fe _{1.04} Si _{0.88} O ₃	Fe _{1.04} Si _{0.88} O ₃	Fe _{1.07} Si _{0.85} O ₃	Fe _{0.137} Mg _{0.863} Si _{0.947} O ₃	Fe _{0.048} Mg _{0.952} SiO ₃	Fe _{0.111} Mg _{0.889} Si _{0.907} O ₃	Fe _{0.127} Mg _{0.873} Si _{0.94} O ₃
Pressure, GPa	153(5)	144(3)	144(3)	141(4)	155(3)	155(3)	141(4)	155(3)
<i>M_r</i>	120.3	105.93	105.93		103.2	101.9	101.3	102.7
Crystal system, space group	Orthorhombic, <i>Pbnm</i>	Orthorhombic, <i>Cmcm</i>	Orthorhombic, <i>Cmcm</i>	Orthorhombic, <i>Pbnm</i>	Orthorhombic, <i>Cmcm</i>	Orthorhombic, <i>Cmcm</i>	Orthorhombic, <i>Pbnm</i>	Orthorhombic, <i>Pbnm</i>
Temperature (K)	293	293	293	293	293	293	293	293
<i>a, b, c</i> (Å)	4.232 (13), 4.575 (2), 6.251 (7)	2.4680 (12), 8.196 (5), 6.120 (3)	2.4714 (14), 8.188 (7), 6.133 (3)	4.2970 (9), 4.6062 (13), 6.305 (2)	2.4434 (7), 7.9745 (6), 6.0651 (4)	2.4405 (4), 7.9703 (17), 6.061 (3)	4.2266 (10), 4.5295 (8), 6.218 (5)	4.2280 (6), 4.5384 (5), 6.198 (2)
<i>V</i> (Å ³)	121.0 (4)	123.79 (11)	124.10 (14)	124.80 (6)	118.18	117.89 (7)	119.04 (10)	118.92 (4)
<i>Z</i>	4	4	4	4	4	4	4	4
<i>F</i> (000)	235	207	207	207	205	203	201	204
Wavelength	$\lambda = 0.41453$ Å	$\lambda = 0.2952$ Å	$\lambda = 0.2952$ Å	$\lambda = 0.2952$ Å	$\lambda = 0.3738$ Å	$\lambda = 0.3738$ Å	$\lambda = 0.3738$ Å	$\lambda = 0.3738$ Å
θ range (°)	5.5–18.8	3.4–17.9	3.4–17.9	3.4–17.9	4.6–16.0	4.6–16.0	3.5–17.1	3.5–17.1
μ (mm ⁻¹)	1.87	4.39	4.38	4.36	0.58	0.44	0.53	0.56
No. of measured, independent and observed [<i>I</i> > 3 σ (<i>I</i>)] reflections	236, 102, 77	168, 76, 60	158, 74, 63	308, 119, 104	125, 66, 60	134, 67, 61	236, 115, 104	223, 117, 111
<i>R</i> _{int}	0.011	0.071	0.078	0.067	0.014	0.016	0.027	0.017
θ range values (°)	3.8 – 19.0	2.5 – 11.2	2.5 – 11.2	2.4 – 11.2	4.6 – 16.6	4.6 – 16.6	3.1 – 17.2	3.5 – 17.1
Range of <i>h, k, l</i>	-2 < <i>h</i> < 3, -6 < <i>k</i> < 6, -7 < <i>l</i> < 8	-2 < <i>h</i> < 3, -9 < <i>k</i> < 9, -7 < <i>l</i> < 7	-2 < <i>h</i> < 3, -10 < <i>k</i> < 9, -7 < <i>l</i> < 7	-5 < <i>h</i> < 5, -5 < <i>k</i> < 5, -6 < <i>l</i> < 6	-3 < <i>h</i> < 3, -11 < <i>k</i> < 11, -5 < <i>l</i> < 2	-3 < <i>h</i> < 3, -11 < <i>k</i> < 11, -5 < <i>l</i> < 2	-6 < <i>h</i> < 6, -6 < <i>k</i> < 6, -2 < <i>l</i> < 5	-6 < <i>h</i> < 6, -6 < <i>k</i> < 6, -2 < <i>l</i> < 5
<i>R</i> [<i>F</i> ² > 2 σ (<i>F</i> ²)], <i>wR</i> [<i>F</i> ²], <i>S</i>	0.070, 0.077, 3.46	0.076, 0.176, 1.33	0.075, 0.183, 1.34	0.053, 0.136, 1.06	0.076, 0.110, 9.98	0.064, 0.106, 9.48	0.098, 0.136, 10.84	0.079, 0.105, 9.48
No. of parameters	14	13	13	14	12	11	15	15

Chapter 7. Diamond anvils with a round table (DART-anvils) designed for high-pressure experiments in DAC

Leonid Dubrovinsky^{a*}, Egor Koemets^a, Maxim Bykov^a, Elena Bykova^b, Georgios Aprilis^c, Anna Pakhomova^b, Konstantin Glazyrin^b, Alexander Laskin^d, Vitali B. Prakapenka^e, Eran Greenberg^e, and Natalia Dubrovinskaia^{c*}

^aBayerisches Geoinstitut, University of Bayreuth, D-95440 Bayreuth, Germany

^bPhoton Science, Deutsches Elektronen-Synchrotron, Notkestrasse 85, D-22607 Hamburg, Germany

^cMaterial Physics and Technology at Extreme Conditions, Laboratory of Crystallography, University of Bayreuth, D-95440 Bayreuth, Germany

^dAdlOptica GmbH, Rudower Chaussee 29, D-12489 Berlin, Germany

^eCenter for Advanced Radiation Sources, University of Chicago, 9700 South Cass Avenue, Argonne, IL 60437, USA

7.1. Abstract

Here, we present new Diamond Anvils with a Round Table (DART-anvils) designed for applications in diamond anvil cell (DAC) technique. The main features of the new DART-anvil design are a spherical shape of both the crown and the table of a diamond and the position of the centre of the culet position exactly in the centre of the sphere. The performance of DART-anvils was tested in a number of high-pressure high-temperature (HP-HT) experiments at different synchrotron beamlines. These experiments demonstrated a number of advantages, which are unavailable with any of hitherto known anvils designs. Use of DART-anvils enables to realise *in situ* single-crystal X-ray diffraction experiments with laser heating using stationary laser-

heating setups; eliminating flat-plate design of conventional anvils, DART-anvils make the cell alignment easier; working as solid immersion lenses, they provide additional magnification of the sample in a DAC and improve the image resolution.

7.2. Introduction

Single-crystal diamonds were introduced as ‘Bridgman anvils’ in 1959 (Figure 7.2-1). Two major types of diamond anvil cells (DACs) – opposite plate and piston-cylinder – were designed, and their different modifications have been dominating in the scientific practice hitherto (208). Subsequent decades of development turned a diamond anvil cell into a universal high-pressure device providing the capability for a wide range of *in situ* measurements of properties of matter at pressure-temperature conditions corresponding to the entire Earth interior and beyond (98). Already in the beginning of the 1970s, the DAC technique demonstrated broad opportunities for high-pressure research dealing with Mössbauer, infrared and Raman spectroscopies, resistivity measurements, X-ray diffraction (XRD), and inelastic scattering.

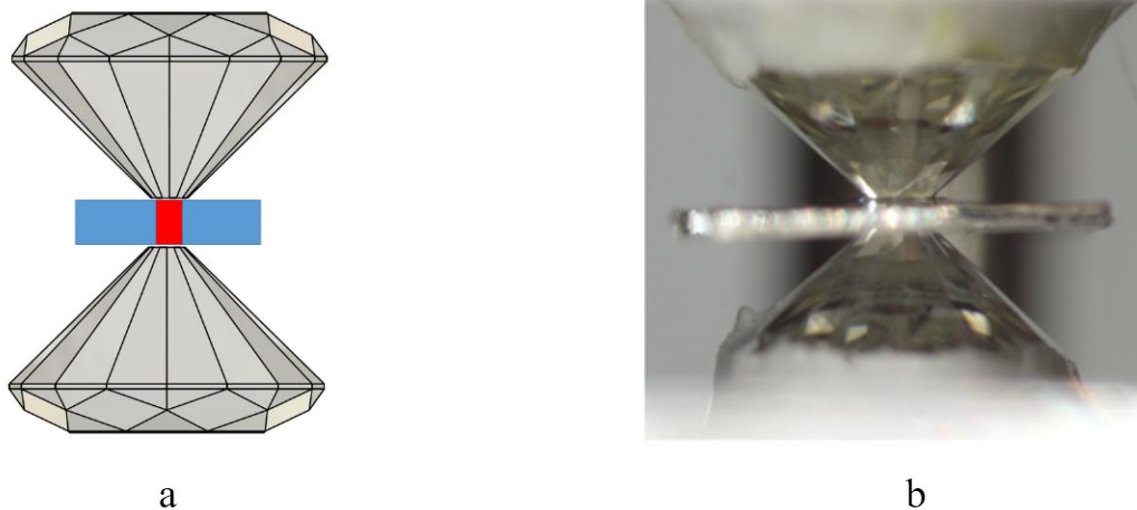


Figure 7.2-1 A schematic (a) and a microscope image (b) of an opposed diamond anvil assembly, the main part of a DAC. Two gem quality diamonds squeeze a sample (red) placed into a hole in a metallic gasket (blue).

Diamond anvils are obviously the most important components of a DAC, and with the development of new analytical techniques used to study materials at extreme conditions, anvil design evolved as well. Rapidly growing areas of DACs applications – single crystal and powder X-ray diffraction, in-house and synchrotron-based spectroscopic techniques (Brillouin spectroscopy, inelastic X-ray scattering, nuclear inelastic scattering, etc.) – require diamond anvils with a large optical aperture. Widely available on the market over decades are classical diamond anvils of ‘standard Drukker’ or ‘modified Brilliant’ cut (Figure 7.2-2a). They have, however, a number of limitations, especially in modern applications. For example, in order to achieve pressures in the range of 100 GPa, the diamonds should be rather thick (of about 2 mm or more) that leads to a significant absorption of X-rays (particularly those of relatively low energies, below 25 keV). The optical opening larger than 60° is difficult to achieve with such thick diamonds. A solution was found due to making crowns of diamond anvils conical (209, 210) (Figure 7.2-2b), and later spherical (211) (Figure 7.2-2c). In these cases, anvils are not anymore glued on the surface of a flat supporting plate (Figure 7.2-1b), but instead, their crowns of a conical or spherical shape are fixed inside a conical (spherical) cavity of identical size drilled in the hard metal or tungsten carbide (WC) support. Such anvils are usually thin (of about 1.4-1.5 mm) and can provide up to about 90° optical opening (85° X-ray aperture) (211). Note that the table of all currently used diamond anvil designs is flat. In (212) it was suggested that truncated sapphire balls can serve as anvils in a high pressure cell and as focusing optical elements.

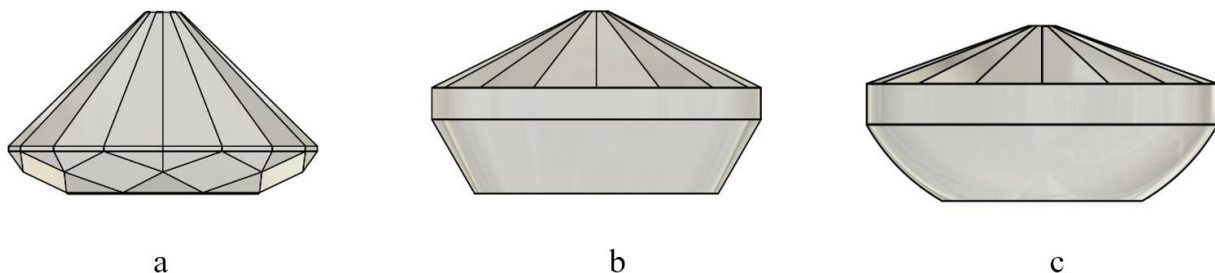


Figure 7.2-2 Examples of diamond anvils of different designs: (a) modified Brilliant, (b) Bohler Almax, and (c) diamond anvil with a spherical support.

Most of the novel and quickly developing methods of *in situ* investigations of pressurised materials (single-crystal X-ray diffraction, inelastic X-ray scattering, Brillouin spectroscopy, etc.) require moving DACs with respect to the beam of electromagnetic radiation (e.g., X-ray and laser), which is used for heating, exciting, or probing materials properties at extreme pressure and variable temperature conditions. Conventional anvils have “flat plate” geometry, and rotation of a cell at any angle with respect to the stationary beam leads to strong refraction, as diamond is a material with a high refractive index ($n = 2.425$ at 532 nm). This destroys the alignment of the sample with respect to the optical beam. Special procedures (sometimes quite complicated, time and labour consuming) are required to maintain the alignment with respect to X-rays and optical systems, but still certain types of experiments, which involve DAC rotations, cannot be performed while keeping lasers or optical components stationary. For example, immobile laser heating of a sample in a DAC with conventional (flat-table) anvils during single-crystal X-ray diffraction data collection is impossible, as the sample is getting out of the focus of the laser beam upon rotation of the cell.

In this work, we present new design of diamond anvils, the Diamond Anvil with a Round Table (DART), which enables to eliminate a number of problems associated with the use of conventional anvils in DACs. The major feature of the new DART-anvil design is a spherical shape of both the crown and the table of a diamond with the centre of the culet located exactly in the centre of the sphere.

7.3. Diamond anvil with a round table (DART-anvil)

To realise the new DART-anvil design, one should polish a diamond as shown in Figure 7.3-1. The crown and the table are not distinguished anymore, and the anvil has a spherical surface below the girdle circle. The lower girdle circle (as shown in Figure 7.3-1a) is the latitude of the sphere, whose center is at the culet of the diamond (Figure 7.3-1). To distinguish the design of our anvil from previously known ones, we call it a “diamond anvil with a round table” (DART) to underline that the table has a convex shape.

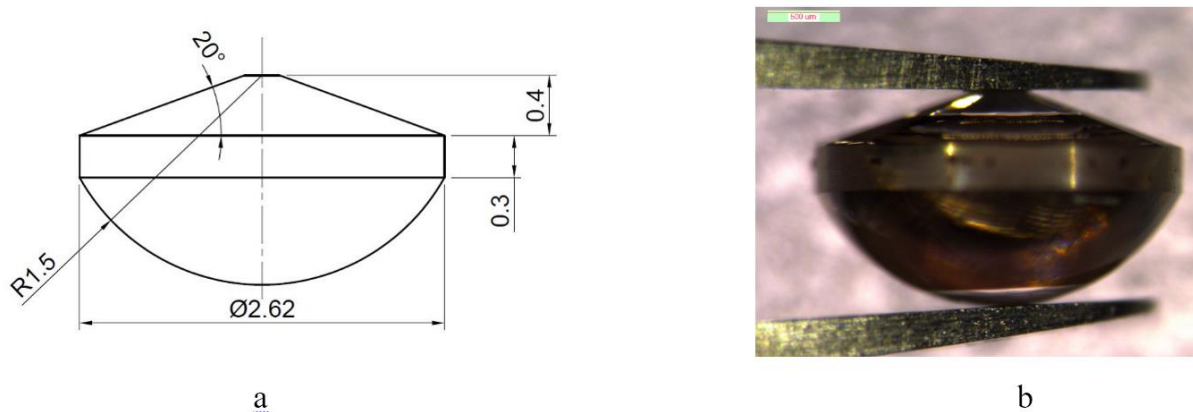


Figure 7.3-1 A schematic (a) and a microscope image (b) of the DART-anvil (Diamond Anvil with a Round Table). (Dimensions may be scaled/adjusted in accordance with experimental needs.)

The DART-anvils, to be mounted in a DAC, require special seats. A schematic of a seat for the DART-anvil, suitable for the BX90 type cells (100), and its three-dimensional image are shown in Figure 7.3-2.

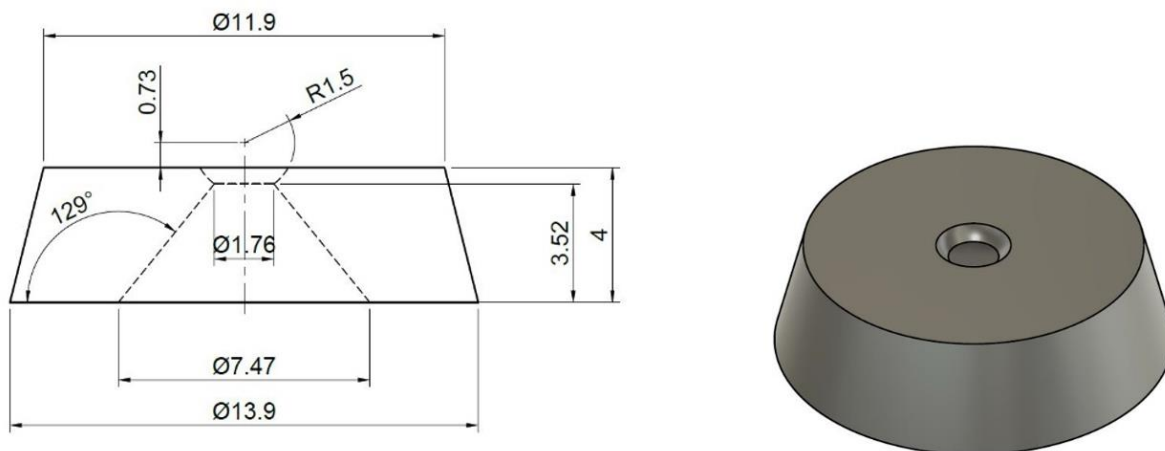


Figure 7.3-2 A schematic of a seat for the DART-anvil and its three-dimensional image.

DART-anvils provide a number of advantages, which are unavailable with any of hitherto known types of anvils. First, they enable ~ 2.4 times enlargement of the image of a sample in a DAC. Indeed, according to Abbe invariant (213):

$$n y \sin(\omega) = n' y' \sin(\omega') \quad \text{Eq. (12)}$$

where n and n' are refractive indexes of media, y is the object size, y' is the image size, ω and ω' are slope angles, i.e. angles between a ray and the optical axis. In case of a DART-anvil, which effectively acts as a lens, $n = \sim 2.4$ (diamond), $n' = 1$ (air), $\omega = \omega'$ since the centre of the spherical surface coincides with the object plane. Consequently, the magnification is $y'/y = n/n' = \sim 2.4$. Thus, a DART-anvil acts as a solid immersion lens (213) and significantly magnifies the image of a sample in the pressure chamber. It also enhances the physical resolution of the imaging which is proportional to the numerical aperture, $NA = n \sin(\omega)$, of the observation channel (213) being essentially increased due to high refractive index of the lens material (diamond).

Imaging from the center of a spherical lens is also characterized by a remarkable feature from the point of view of aberrations - for the practically used NA the image is free of not only spherical aberration, but also from coma and astigmatism in a zone around the surface centre. This simplifies drastically the alignment procedure and provides high quality imaging even in case of certain misalignments or de-focusing. In contrast to diamond anvils of known design, which have two parallel optical surfaces and thus the image of an object observed through the anvils does not coincide with the objects' physical position along the optical axis, the DART is free of that problem. As a result, the optical and x-ray alignment of the DACs equipped with DART-anvils (e.g., with respect to the goniometer axes) becomes much more simple and accurate; no refraction correction is needed once the sample is aligned to the optical focal point, thus simplifying the procedure of aligning to the x-ray focus. Providing this advantage in combination with the higher magnification of the objects confined in the pressure chamber and enhanced

physical resolution, DART-anvils have a great potential for applications in different spectroscopies, including Raman, IR, and Brillouin.

The major effect DART-anvils promise is applications requiring laser heating. In particular, DART-anvils allow performing *in situ* high-pressure high-temperature single-crystal XRD experiments in DACs using *stationary lasers*. With the design we propose, a laser beam remains focused on the sample even if the cell is rotating: due to the spherical shape of the anvil, the direction of the incoming laser beam is maintained perpendicular to the anvil's surface, while the DAC is rotated during the XRD data collection (Figure 7.3-3).

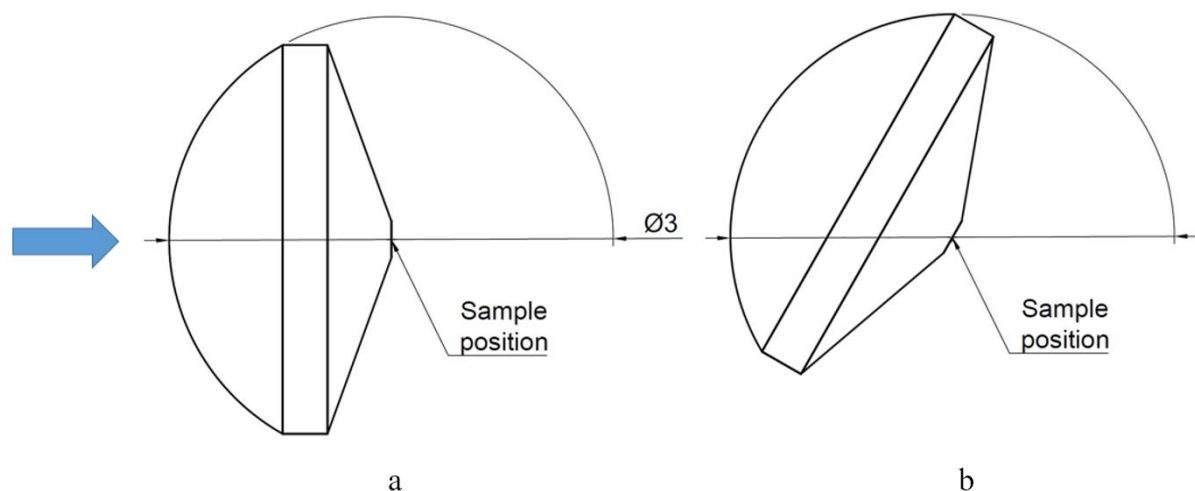


Figure 7.3-3 A schematic view of a DART-anvil aligned with respect to the incoming beam before rotation (a) and after rotation (b). The arrow shows the direction of optical observation and/or the direction of a laser beam. The samples remains in focus upon rotation.

7.4. Examples of applications of DART-anvils

We have conducted a number of high-pressure high-temperature (HP-HT) experiments with DACs equipped with DART-anvils aimed at demonstrating their possible applications and advantages. The XRD experiments we describe below were performed using existing laser-heating setups. In all of the experiments Re gaskets with the initial thickness of 200 μm were

used. The gaskets were indented to the thickness of 20 to 25 μm . Gases (He, Ne, or N_2) were loaded at pressure of 1.3-1.4 kbar (105). In all cases, the culet size of DART-anvils was 250 μm .

7.4.1. Performance of DART-anvils on compression at ambient temperature

To check the stability of DART-anvils, we assembled a DAC with one DART-anvil and one Bohler-Almax-type anvil (250 μm culet, 4.0 mm outer diameter). In this cell, a powder of iron was compressed up to ~ 70 GPa at ambient temperature in a He pressure transmitting medium. After decompression, we opened the cell and inspected the anvils under a microscope. Both anvils remained intact; no problems in the course of compression or decompression appeared.

In this experiment pressure was measured not only using ruby fluorescence, but also on a Raman signal from the centres of the culets of both of the diamond anvils, employing the existing correlation between the high frequency edge of the Raman band with the normal stress at the culet face (214). For this purpose, a LabRam spectrometer (He-Ne laser, x50 long working objective, 200 μm confocal hole) was used. Interestingly, the signals from the DART and the standard “flat” Bohler-Almax anvils have a different shape (Figure 7.4-1). The position of a sharp peak observed in the spectrum from the DART-anvil indeed corresponds to the most stressed part of the anvil, so that the pressure estimation on a Raman signal from the center of the culet (214) appears to be more accurate for DART-anvils when compared to conventional flat ones.

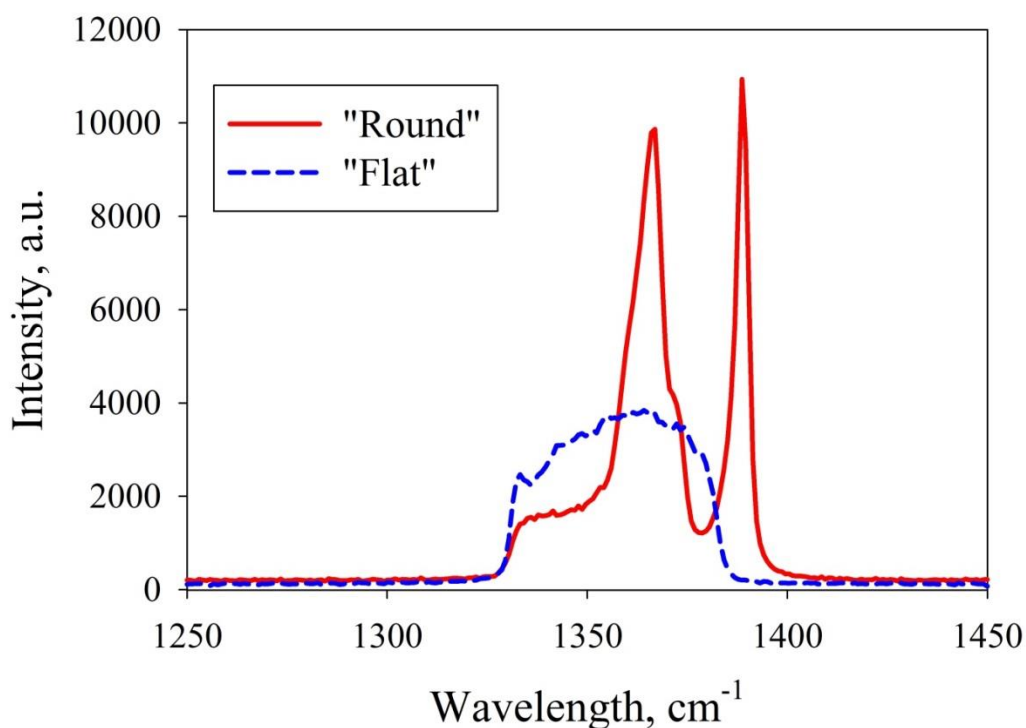


Figure 7.4-1 Examples of Raman spectra collected from the diamond-to-sample interface of the DART- (red continuous line) and Bohler-Almax- (blue dashed line) anvils at 24(1) GPa.

7.4.2. Single-crystal XRD data collection during laser heating at IDD-13 at GSECARS (APS, USA)

The experiment described below was performed at 13-IDD (GSECARS) at the APS. We used the flat-top laser-heating setup standard for this beamline (128). X-ray beam with a wavelength of $\sim 0.295 \text{ \AA}$ was focused to about $2 \times 3 \text{ \mu m}^2$ FWHM. Data were collected using a Pilatus 1M CdTe detector (DECTRIS). A mini-BX90 cell (30 mm outer diameter) (100) was equipped with two DART-anvils. This cell was mounted in a standard water-cooled holder, which was not yet optimized for the actual laser optical system and allowed rotation in the range of -4 to 20 degrees during laser heating (while opening of the cell was 68 degrees). The three-layer sample consisted of an iron foil (about 3 \mu m thick and 50 \mu m in diameter) compressed between two layers of powdered

bridgmanite ($\text{Mg}_{0.88}\text{Fe}_{0.12}$)($\text{Si}_{0.96}\text{Al}_{0.04}$) O_3 pre-synthesised in a large volume press. This “sandwiched” sample was loaded into a hole of 125 μm in diameter and 20 μm thick made in a Re gasket. Pressure was measured using the thermal equation of state of iron (215).

The cell was aligned with respect to the rotational (ω) axis using X-ray beam and applying the standard for the 13-IDD beamline procedure. After the alignment, the cell was rotated about the ω -axis, while the sample was observed using the optics of the laser-heating system; no visible changes in the position of the sample were detected upon rotation (Figure 7.4-2). Upon laser heating, no shift in the position of the heated spot was observed (Figure 7.4-3), and the temperature, measured spectroradiometrically, was reasonably stable (for example, in one run it maintained within 1600 – 1850 K, and in another run, within 2200 – 2400 K).



Figure 7.4-2 A series of photographs of a sample in a DAC (an iron foil in silicate perovskite at ~ 35 GPa) taken with a five-degree interval upon rotation of the DAC about the ω -axis. Beforehand the cell was aligned with respect to the rotational centre of the goniometer at 13-IDD beamline at the APS (USA). The position of the X-ray beam is marked by the yellow square. No visible changes in the position of the sample were detected upon rotation.

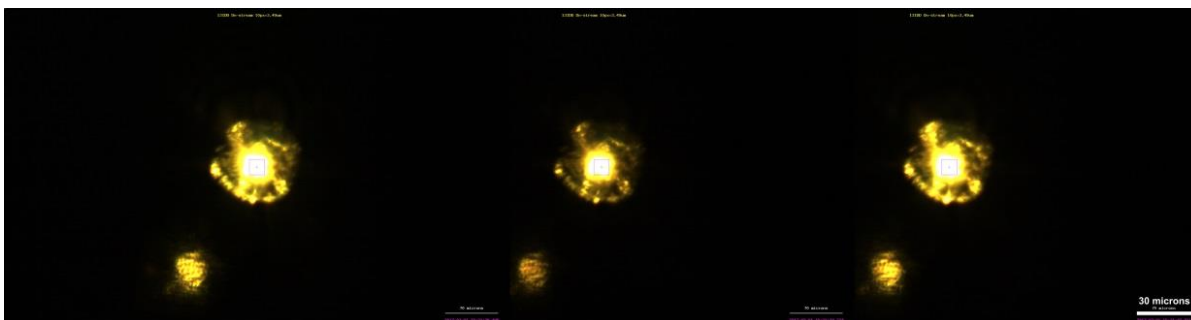


Figure 7.4-3 A series of photographs of a sample in a DAC (an iron foil in silicate perovskite at ~ 35 GPa) taken with an eight-degree interval upon rotation of the DAC about the ω -axis and simultaneous laser heating at 2300(150) K using a stationary laser. Beforehand the cell was aligned with respect to the rotational centre of the goniometer at 13-IDB beamline at the APS (USA). The position of the X-ray beam is marked by the square. No shift in the position of the heated spot with respect to the sample was detected upon rotation.

Several crystallites of bridgmanite formed already after the first annealing of the sample at temperatures of 1300–1700 K. Unfortunately, the X-ray diffraction from individual crystallites was rather weak, and, in combination with a relatively small rotational angle (24°), it was not easy to collect data sets suitable for single-crystal structure refinement. Still, after collecting ω -step scans (0.25° step with 0.25 s/step), we were able to find a single-crystal domain, which gave about 90 unique reflections (about 50 of them with $F_o > 4\sigma(F_o)$). Integration in *CrysAlis^{Pro}*© gave $R_{\text{int}} \sim 9\%$, and the structure was refined using SHELXL (160) with $R_1 \sim 10\%$ (14 parameters to refine; Table 7.4-1). It is remarkable that the quality of the diffraction data collected during heating (1700(150) K) was practically similar to that collected at ambient temperature (Table 7.4-1).

Table 7.4-1 Results of the single-crystal structure refinement of bridgmanite ($\text{Mg}_{0.88}\text{Fe}_{0.12}$)($\text{Si}_{0.96}\text{Al}_{0.04}$) O_3 (silicate perovskite ABO_3 , where $A=(\text{Mg}_{0.88}\text{Fe}_{0.12})$ and $B=(\text{Si}_{0.96}\text{Al}_{0.04})$; space group $Pbnm$, #62) at different pressures and temperatures.

P , GPa	T , K	$R_{\text{int}}/R_1/R_{1\text{all}}$, %	Lattice parameters				Atomic parameters (x, y, z, U)
			a , Å	b , Å	c , Å	V , Å ³ /unit cell	
35(1)	298	8.6/9.6/12.7	4.578(8)	4.764(4)	6.692(9)	145.95(37)	A: -0.026(4), 0.4381(14), 0.25, 0.039(3) B: 0.0, 0.0, 0.0, 0.041(2) O1: 0.105(5), 0.028(2), 0.25, 0.026(3) O2: 0.205(8), 0.306(2), -0.057(2), 0.049(4)
43(1)	1700(150)	9.6/8.2/9.4	4.606(9)	4.759(7)	6.708(13)	147.0(5)	A: -0.024(2) 0.442(1) 0.25 0.024(2) B: 0.0, 0.0, 0.0, 0.019(1) O1: 0.105(5), 0.040(2), 0.25, 0.015(2) O2: 0.174(4), 0.299(1), -0.046(1), 0.017(2)

7.4.3. Single-crystal XRD data collection during laser heating at Extreme Conditions Beam Line (ECB P02.2) at PETRA III (DESY, Germany)

A small (about 10 μm in diameter and 5 μm thick) piece of commercially available polycrystalline chromium (Sigma Aldrich Inc.) was placed inside a hole drilled in a Re gasket. A mini-BX90 DAC equipped with DART-anvils was used. The sample chamber was loaded with nitrogen, which served as both a pressure-transmitting medium and a possible reactant. A ruby sphere was also placed into the chamber as a pressure gauge. The sample was compressed to the desired pressure of 38(1) GPa.

Figure 7.4-4 shows the sample in the pressure chamber after compression. The DART-anvil with its spherical surface acts as a solid immersion lens and all visible objects are magnified. The microscope scale of 50 μm corresponds indeed to the value of ~ 21 μm (Figure 7.4-4) due to additional magnification by $\times 2.4$ of the diamond spherical lens, which also improves optical resolution, so that individual grains (crystals) of solid nitrogen become visible (Figure 7.4-4).

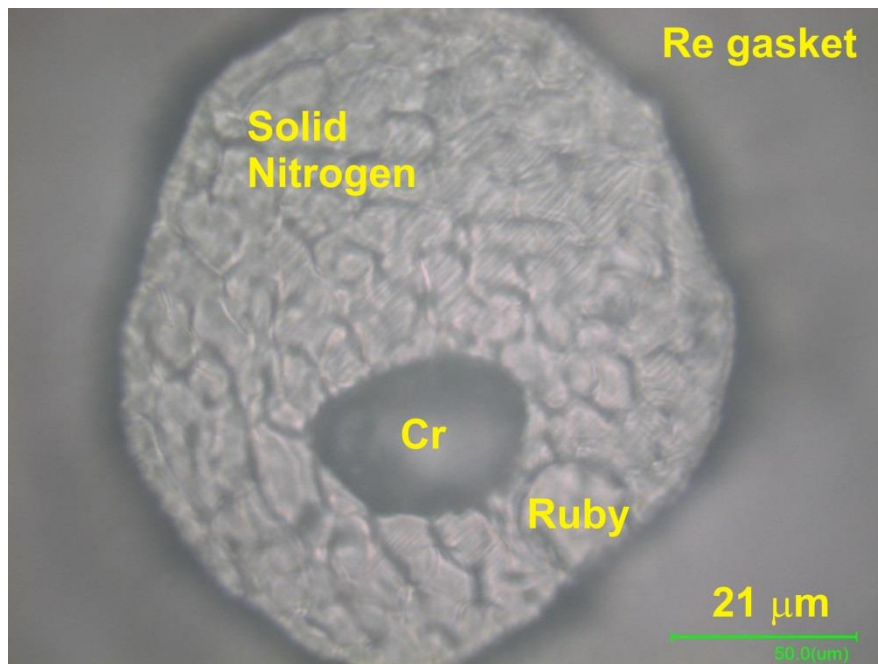


Figure 7.4-4 A sample of Cr compressed in N₂ medium to 38(1) GPa. Sizes of the ruby ball and the Cr particle were measured before compression and compared with “apparent sizes” in the DAC. All objects in the pressure chamber are additionally magnified by ~2.4 times. The corrected scale (21μm) is designated. Due to improved resolution, individual grains (crystals) of solid nitrogen (of a few microns in dimension) are clearly visible.

Single-crystal X-ray diffraction experiments on this sample were performed at the ECB beamline (P02.2) at PETRA III (DESY, Hamburg) ($\lambda = 0.2904 \text{ \AA}$, Perkin Elmer XRD1621 flat panel detector) (159). All operations at the beamline were performed “as usual”, without any specific modifications for the DART-anvils implementation. X-ray diffraction images were collected upon continuous rotation of the cell from -20° to $+20^\circ$ about the ω -axis (wide scans) and with a narrow 0.5° scanning step in the range from -38° to $+38^\circ$ ω (step scans). Due to the limitations implied by the mirrors of the laser-heating system, upon heating the cell was rotated in the angular ω range from -24° to $+35^\circ$. Data integration and semi-empirical absorption correction were performed using *CrysAlis^{Pro}*®. The crystal structures were solved and refined using the computer program JANA2006 (125).

Before, during and after laser heating we could observe single-crystal domains of Cr. The crystal structure of Cr was refined against single-crystal X-ray diffraction data (Table 7.4-2). Cr maintains its *bcc* structure up to the temperature of 2800(100) K at 38(1) GPa. We could clearly observe the linear thermal expansion of chromium manifesting in the increase of the unit cell parameter by ca. 0.55% and enlargement of thermal ellipsoids (Table 7.4-2).

Table 7.4-2 Crystallographic data for Cr before (“cold”) and during (“hot”) laser heating at 38(1) GPa.

	“Cold”	“Hot”
Chemical formula	Cr	Cr
Pressure (GPa)	38(1)	
Temperature (K)	293	2350(150)
Space group	<i>Im</i> $\bar{3}$ <i>m</i>	<i>Im</i> $\bar{3}$ <i>m</i>
<i>a</i> (Å)	2.7622(3)	2.7672(2)
<i>V</i> (Å ³)	21.075(5)	21.190(3)
Calculated density (g/cm ³)	8.194	8.149
Observed reflections	54	56
Unique reflections	15	14
Unique reflections [<i>I</i> > 2σ(<i>I</i>)]	15	14
Parameters	2	2
R _{int}	18.06	19.70
R ₁	0.0623	0.0409
wR ₂	0.0756	0.0506
U _{iso} (Å ²)	0.0075(11)	0.0111(9)

7.5. Conclusions

We have developed a new design of diamond anvils, “diamond anvils with a round table” (DART-anvils), in assembly with a spherical support (anvil’s seat). Their performance was tested

in a number of HP-HT experiments at different synchrotron beamlines. Use of DART-anvils provides a number of advantages, which are unavailable with any of hitherto known anvils designs. In particular, they allow considerable (~ 2.4) enlargement of the image of a sample in a DAC and improve its resolution, as a DART-anvil works as a solid immersion lens. Use of the DART anvils improves the precision of the pressure measurement in DACs on a Raman signal from the centre of the culet of a diamond anvil. The procedure of the sample alignment on the rotational stage is greatly simplified for the cells with DART-anvils. *In situ* single-crystal XRD experiments with laser heating can be realised with stationary laser-heating setups, i.e. the laser beam needs not be moved simultaneously with the rotating sample. Due to the spherical shape of the DART-anvil surface, the angle of incidence of the incoming laser beam remains normal to this surface and focused to the sample, while the DAC is rotated during the XRD data collection.

7.6. Acknowledgments

N.D. thanks the German Research Foundation (Deutsche Forschungsgemeinschaft, DFG, projects no. DU 954-8/1 and DU 954-11/1) and the Federal Ministry of Education and Research, Germany (BMBF, grants no. 5K13WC3 and 5K16WC1) for financial support. L.D. acknowledges DFG funding through projects the CarboPaT Research Unit FOR2125. We thank **Dutch Diamond Technologies BV** and **Almax easyLab** Group Ltd for producing the DART-anvils according to our design. Technical support of S. Übelhack (Bayerisches Geoinstitut) is gratefully acknowledged. Portions of this work were performed at GeoSoilEnviroCARS (The University of Chicago, Sector 13), Advanced Photon Source (APS), Argonne National Laboratory. GeoSoilEnviroCARS is supported by the National Science Foundation - Earth Sciences (EAR - 1634415) and Department of Energy- GeoSciences (DE-FG02-94ER14466). This research used resources of the Advanced Photon Source, a U.S. Department of Energy (DOE) Office of Science User Facility operated for the DOE Office of Science by Argonne National Laboratory under Contract No. DE-AC02-06CH11357.

Chapter 8. Bibliography

1. R. W. Carlson, E. Garnero, T. M. Harrison, J. Li, M. Manga, W. F. McDonough, S. Mukhopadhyay, B. Romanowicz, D. Rubie, Q. Williams, S. Zhong, *How did early Earth become our modern world?* (2014), vol. 42.
2. B. J. Wood, M. J. Walter, J. Wade, Accretion of the Earth and segregation of its core. *Nature*. **441**, 825–833 (2006).
3. K. Lodders, Solar system abundances of the elements. *Astrophys. Sp. Sci. Proc.*, 379–417 (2010).
4. E. Kokubo, S. Ida, Formation of protoplanet systems and diversity of planetary systems. *Astrophys. J.* **581**, 666–680 (2002).
5. F. Albarède, Volatile accretion history of the terrestrial planets and dynamic implications. *Nature*. **461**, 1227–1233 (2009).
6. R. M. Canup, E. Asphaug, Origin of the Moon in a giant impact near the end of the Earth's formation. *Nature*. **412**, 708–712 (2001).
7. D. P. O'Brien, A. Izidoro, S. A. Jacobson, S. N. Raymond, D. C. Rubie, The delivery of water during terrestrial planet formation. *Space Sci. Rev.* **214** (2018), doi:10.1007/s11214-018-0475-8.
8. B. Nath, Water on Earth. *Resonance*. **24**, 575–582 (2019).
9. A. Morbidelli, J. Chambers, J. I. Lunine, J. M. Petit, F. Robert, G. B. Valsecchi, K. E. Cyr, Source regions and timescales for the delivery of water to the Earth. *Meteorit. Planet. Sci.* **35**, 1309–1320 (2000).
10. O. Nebel, F. A. Capitanio, S. A. Pisarevsky, P. A. Cawood, C. J. Hawkesworth, B. Dhuime, Geological archive of the onset of plate tectonics. *Philos. Trans. R. Soc. A Math. Phys. Eng. Sci.* **376**, 20170405 (2018).
11. K. C. Condie, *Plate tectonics & crustal evolution* (Elsevier, 2013).
12. J. W. Morgan, E. Anders, Chemical composition of Earth, Venus, and Mercury. *Proc. Natl. Acad. Sci.* **77**, 6973–6977 (1980).
13. W. F. McDonough, S. s. Sun, The composition of the Earth. *Chem. Geol.* **120**, 223–253 (1995).
14. A. M. Dziewonski, D. L. Anderson, Preliminary reference Earth model. *Phys. Earth Planet. Inter.* **25**, 297–356 (1981).

15. D. L. Anderson, *Theory of the Earth* (Blackwell scientific publications, 1989; <http://linkinghub.elsevier.com/retrieve/pii/003192019090182W>), vol. 62.
16. G. R. Helffrich, B. J. Wood, The Earth's mantle. **412**, 501–507 (2001).
17. T. Ishii, R. Huang, H. Fei, I. Koemets, Z. Liu, F. Maeda, L. Yuan, L. Wang, D. Druzhbin, T. Yamamoto, S. Bhat, R. Farla, T. Kawazoe, N. Tsujino, E. Kulik, Y. Higo, Y. Tange, T. Katsura, Complete agreement of the post-spinel transition with the 660-km seismic discontinuity. *Sci. Rep.* **8**, 6–11 (2018).
18. F. V. Kaminsky, *The Earth's lower mantle composition and structure* (2017).
19. A. Sheyko, C. Finlay, J. Favre, A. Jackson, Scale separated low viscosity dynamos and dissipation within the Earth's core. *Sci. Rep.* **8**, 1–7 (2018).
20. Mineral physics and seismic constraints on Earth's structure and dynamics Earth structure, mineralogy, elasticity. (available at <https://slideplayer.com/slide/7057700/>).
21. V. Dols, F. Paresce, F. Paresce, Y. Fei, H.-K. Mao, In situ determination of the NiAs phase of FeO at high pressure and temperature. *Science* (80-.). **266**, 1992–1994 (1994).
22. E. Bykova, M. Bykov, V. Prakapenka, H. Liermann, N. Dubrovinskaia, L. Dubrovinsky, A novel high pressure monoclinic Fe₂O₃ polymorph revealed by single-crystal synchrotron X-ray diffraction studies. *High Press. Res.*, 37–41 (2013).
23. M. P. Pasternak, G. K. Rozenberg, G. Machavariani, O. Naaman, R. D. Taylor, R. Jeanloz, Breakdown of the Mott-Hubbard state in Fe₂O₃: a first-order insulator-metal transition with collapse of magnetism at 50 GPa. *Phys. Rev. Lett.* **82**, 4663–4666 (1999).
24. S. Ono, T. Kikegawa, Y. Ohishi, High-pressure phase transition of hematite, Fe₂O₃. *J. Phys. Chem. Solids.* **65**, 1527–1530 (2004).
25. E. Ito, H. Fukui, T. Katsura, D. Yamazaki, T. Yoshino, Y. I. Aizawa, A. Kubo, S. Yokoshi, K. Kawabe, S. Zhai, A. Shatzkiy, M. Okube, A. Nozawa, K. I. Funakoshi, Determination of high-pressure phase equilibria of Fe₂O₃ using the Kawai-type apparatus equipped with sintered diamond anvils. *Am. Mineral.* **94**, 205–209 (2009).
26. A. B. Woodland, J. Kornprobst, A. Tabit, Ferric iron in orogenic Iherzolite massifs and controls of oxygen fugacity in the upper mantle. *Lithos.* **89**, 222–241 (2006).
27. J. F. Lin, A. G. Gavriliuk, V. V. Struzhkin, S. D. Jacobsen, W. Sturhahn, M. Y. Hu, P. Chow, C. S. Yoo, Pressure-induced electronic spin transition of iron in magnesiowustite - (Mg,Fe)O. *Phys. Rev. B - Condens. Matter Mater. Phys.* **73**, 73–76 (2006).
28. Y. Fei, L. Zhang, A. Corgne, H. Watson, A. Ricolleau, Y. Meng, V. Prakapenka, Spin transition and equations of state of (Mg,Fe)O solid solutions. *Geophys. Res. Lett.* **34**, 1–5 (2007).

29. D. J. Frost, C. A. McCammon, The redox state of Earth's mantle. *Annu. Rev. Earth Planet. Sci.* **36**, 389–420 (2008).
30. A. B. Woodland, The oxygen fugacity of the Earth's mantle: variations with depth. *Elev. Annu. V. M. Goldschmidt Conf.*, 3148 (2001).
31. B. J. Wood, L. T. Bryndzia, K. E. Johnson, Mantle oxidation state and its relationship to tectonic environment and fluid speciation. *Science (80-.)*. **126**, 337–346 (1990).
32. E. J. Garnero, A. K. McNamara, Structure and dynamics of Earth's lower mantle. *Science (80-.)*. **320**, 626–628 (2008).
33. S. Rost, E. J. Garnero, Q. Williams, Fine-scale ultralow-velocity zone structure from high-frequency seismic array data. **111**, 1–14 (2006).
34. J. Revenaugh, Q. Williams, T. Lay, L. H. Kellogg, in *The core-mantle boundary region* (1998), pp. 319–334.
35. E. J. Garnero, A. K. McNamara, S. H. Shim, Continent-sized anomalous zones with low seismic velocity at the base of Earth's mantle. *Nat. Geosci.* **9**, 481–489 (2016).
36. Z. Zhang, S. M. Dorfman, J. Labidi, S. Zhang, M. Manga, L. P. Stixrude, W. F. McDonough, Q. C. Williams, in *AGU Fall Meeting Abstracts* (2014), vol. 2014, pp. DI41A-4320.
37. C. Huang, W. Leng, Z. Wu, The continually stable subduction, iron-spin transition, and the formation of LLSVPs from subducted oceanic crust. *J. Geophys. Res. Solid Earth.* **125**, 1–20 (2020).
38. C. Huang, W. Leng, Z. Wu, Iron-spin transition controls structure and stability of LLSVPs in the lower mantle. *Earth Planet. Sci. Lett.* **423**, 173–181 (2015).
39. H. K. Mao, Q. Hu, L. Yang, J. Liu, D. Y. Kim, Y. Meng, L. Zhang, V. B. Prakapenka, W. Yang, W. L. Mao, When water meets iron at Earth's core-mantle boundary. *Natl. Sci. Rev.* **4**, 870–878 (2017).
40. G. Morard, D. Andrault, D. Antonangeli, Y. Nakajima, A. L. Auzende, E. Boulard, S. Cervera, A. Clark, O. T. Lord, J. Siebert, V. Svitlyk, G. Garbarino, M. Mezouar, Fe–FeO and Fe–Fe₃C melting relations at Earth's core–mantle boundary conditions: implications for a volatile-rich or oxygen-rich core. *Earth Planet. Sci. Lett.* **473**, 94–103 (2017).
41. J. Liu, J. Li, R. Hrubciak, J. S. Smith, Origins of ultralow velocity zones through slab-derived metallic melt. *Proc. Natl. Acad. Sci. U. S. A.* **113**, 5547–5551 (2016).
42. G. Graziano, Geochemistry: A journey to the oxidized centre of the Earth. *Nat. Rev. Chem.* **1**, 41570 (2017).

43. J. B. Dixon, S. B. Weed, U. Schwertmann, R. M. Taylor, *Iron Oxides* (1989), doi:10.2136/sssabookser1.2ed.c8.
44. P. Tartaj, M. P. Morales, T. Gonzalez-Carreño, S. Veintemillas-Verdaguer, C. J. Serna, The iron oxides strike back: From biomedical applications to energy storage devices and photoelectrochemical water splitting. *Adv. Mater.* **23**, 5243–5249 (2011).
45. D. Faivre, *Iron Oxides: From Nature to Applications* (2016).
46. X. Zhu, H. Tang, X. Sun, Genesis of banded iron formations: a series of experimental simulations. *Ore Geol. Rev.* (2014), doi:10.1016/j.oregeorev.2014.03.009.
47. N. M. Rose, D. Bridgwater, H. S. Thomsen, Earliest part of Earth's stratigraphic record: a reappraisal of the >3.7 Ga Isua (Greenland) supracrustal sequence (1996).
48. A. Polat, A. W. Hofmann, M. T. Rosing, Boninite-like volcanic rocks in the 3.7-3.8 Ga Isua greenstone belt, West Greenland: geochemical evidence for intra-oceanic subduction zone processes in the early Earth. *Chem. Geol.* **184**, 231–254 (2002).
49. D. P. Dobson, J. P. Brodholt, Subducted banded iron formations as a source of ultralow-velocity zones at the core-mantle boundary. *Nature.* **434**, 371–374 (2005).
50. S. Ono, Y. Ohishi, In situ X-ray observation of phase transformation in Fe₂O₃ at high pressures and high temperatures. **66**, 1714–1720 (2005).
51. H. Ozawa, K. Hirose, S. Tateno, N. Sata, Y. Ohishi, Phase transition boundary between B1 and B8 structures of FeO up to 210 GPa. *Phys. Earth Planet. Inter.* **179**, 157–163 (2010).
52. L. S. Dubrovinsky, N. A. Dubrovinskaia, C. McCammon, G. K. Rozenberg, R. Ahuja, J. M. Osorio-Guillen, V. Dmitriev, H. P. Weber, T. Le Bihan, B. Johansson, The structure of the metallic high-pressure Fe₃O₄ polymorph: experimental and theoretical study. *J. Phys. Condens. Matter.* **15**, 7697–7706 (2003).
53. E. Bykova, L. Dubrovinsky, N. Dubrovinskaia, M. Bykov, C. McCammon, S. V. Ovsyannikov, H.-P. Liermann, I. Kuppenko, A. I. Chumakov, R. Ruffer, M. Hanfland, V. Prakapenka, Structural complexity of simple Fe₂O₃ at high pressures and temperatures. *Nat. Commun.* **7**, 10661 (2016).
54. C. Malgrange, C. Ricolleau, M. Schlenker, Symmetry and physical properties of crystals. *Symmetry Phys. Prop. Cryst.* (2014), doi:10.1007/978-94-017-8993-6.
55. I. Kuppenko, G. Aprilis, D. M. Vasiukov, C. McCammon, S. Chariton, V. Cerantola, I. Kantor, A. I. Chumakov, R. Ruffer, L. Dubrovinsky, C. Sanchez-Valle, Magnetism in cold subducting slabs at mantle transition zone depths. *Nature.* **570**, 102–106 (2019).
56. K. Hikosaka, R. Sinmyo, K. Hirose, T. Ishii, Y. Ohishi, The stability of Fe₅O₆ and Fe₄O₅ at high

- pressure and temperature. *Am. Mineral.* **104**, 1356–1359 (2019).
57. B. Lavina, P. Dera, E. Kim, Y. Meng, R. T. T. Downs, P. F. F. Weck, S. R. S. R. Sutton, Y. Zhao, Discovery of the recoverable high-pressure iron oxide Fe₄O₅. *Proc. Natl. Acad. Sci. U. S. A.* **108**, 17281–17285 (2011).
 58. B. Lavina, Y. Meng, Unraveling the complexity of iron oxides at high pressure and temperature: Synthesis of Fe₅O₆. *Sci. Adv.* **1**, e1400260–e1400260 (2015).
 59. R. Sinmyo, E. Bykova, S. V. Ovsyannikov, C. Mccammon, I. Kuppenko, L. Ismailova, L. Dubrovinsky, Discovery of Fe₇O₉: a new iron oxide with a complex monoclinic structure. *Nat. Publ. Gr.*, 1–7 (2016).
 60. T. Ishii, L. Uenver-Thiele, A. B. Woodland, E. Alig, T. B. Ballaran, Synthesis and crystal structure of Mg-bearing Fe₉O₁₁: New insight in the complexity of Fe-Mg oxides at conditions of the deep upper mantle. *Am. Mineral.* **103**, 1873–1876 (2018).
 61. J. Guignard, W. a. Crichton, Synthesis and recovery of bulk Fe₄O₅ from magnetite, Fe₃O₄. A member of a self-similar series of structures for the lower mantle and transition zone. *Mineral. Mag.* **78**, 361–371 (2014).
 62. R. Myhill, D. O. Ojwang, L. Ziberna, D. J. Frost, T. B. Ballaran, N. Miyajima, On the P–T–fO₂ stability of Fe₄O₅, Fe₅O₆ and Fe₄O₅-rich solid solutions. *Contrib. to Mineral. Petrol.* **171**, 1–11 (2016).
 63. L. Uenver-Thiele, A. B. Woodland, T. B. Ballaran, N. Miyajima, D. J. Frost, Phase relations of MgFe₂O₄ at conditions of the deep upper mantle and transition zone. *Am. Mineral.* **102**, 632–642 (2017).
 64. T. B. Ballaran, L. Uenver-Thiele, A. B. Woodland, Complete substitution of Fe²⁺ by Mg in Fe₄O₅: The crystal structure of the Mg₂Fe₂O₅ end-member. *Am. Mineral.* **100**, 628–632 (2015).
 65. D. E. Canfield, M. T. Rosing, C. Bjerrum, Early anaerobic metabolisms. *Philos. Trans. R. Soc. B Biol. Sci.* **361**, 1819–1834 (2006).
 66. S. A. Crowe, L. N. Døssing, N. J. Beukes, M. Bau, S. J. Kruger, R. Frei, D. E. Canfield, Atmospheric oxygenation three billion years ago. *Nature.* **501**, 535–538 (2013).
 67. A. E. Gleason, R. Jeanloz, M. Kunz, Pressure-temperature stability studies of FeOOH using X-ray diffraction. *Am. Mineral.* **93**, 1882–1885 (2008).
 68. H. K. Mao, Q. Hu, L. Yang, J. Liu, D. Y. Kim, Y. Meng, L. Zhang, V. B. Prakapenka, W. Yang, W. L. Mao, When water meets iron at Earth’s core-mantle boundary. *Natl. Sci. Rev.* **4**, 870–878 (2017).

69. Q. Hu, D. Y. Kim, W. Yang, L. Yang, Y. Meng, L. Zhang, H. K. Mao, FeO₂ and FeOOH under deep lower-mantle conditions and Earth's oxygen–hydrogen cycles. *Nature*. **534**, 241–244 (2016).
70. J. Liu, Q. Hu, D. Young Kim, Z. Wu, W. Wang, Y. Xiao, P. Chow, Y. Meng, V. B. Prakapenka, H. K. Mao, W. L. Mao, Hydrogen-bearing iron peroxide and the origin of ultralow-velocity zones. *Nature*. **551**, 494–497 (2017).
71. M. Nishi, Y. Kuwayama, J. Tsuchiya, T. Tsuchiya, The pyrite-type high-pressure form of FeOOH. *Nature*. **547**, 205–208 (2017).
72. Q. Hu, D. Y. Kim, J. Liu, Y. Meng, L. Yang, D. Zhang, W. L. Mao, H. Mao, Dehydrogenation of goethite in Earth's deep lower mantle. *Proc. Natl. Acad. Sci.* **114**, 201620644 (2017).
73. D. R. Bell, G. R. Rossman, The role of Earth's mantle: *Science (80-)*. **255**, 1391–1397 (1992).
74. K. Litasov, E. Ohtani, Phase relations and melt compositions in CMAS-pyrolite-H₂O system up to 25 GPa. *Phys. Earth Planet. Inter.* **134**, 105–127 (2002).
75. S. D. Jacobsen, S. Van Der Lee, *Earth's Deep Water Cycle* (2013), vol. 168.
76. E. Boulard, M. Harmand, F. Guyot, G. Lelong, G. Morard, D. Cabaret, S. Boccato, A. D. Rosa, R. Briggs, S. Pascarelli, G. Fiquet, Ferrous iron under oxygen-rich conditions in the deep mantle. *Geophys. Res. Lett.* **46**, 1348–1356 (2019).
77. J. Liu, Q. Hu, W. Bi, L. Yang, Y. Xiao, P. Chow, Y. Meng, V. B. Prakapenka, H. K. Mao, W. L. Mao, Altered chemistry of oxygen and iron under deep Earth conditions. *Nat. Commun.* **10**, 1–8 (2019).
78. S. Mei, D. . Kohlstedt, Influence of water on plastic deformation of olivine aggregates: 1. Diffusion creep regime. *J. Geophys. Res.* **105**, 21457–21469 (2000).
79. S. D. Jacobsen, J. R. Smyth, Effect of water on the sound velocities of ringwoodite in the transition zone. *Geophys. Monogr. Ser.* **168**, 131–145 (2006).
80. T. Kubo, E. Ohtani, T. Kato, T. Shinmei, K. Fujino, Effects of water on the alpha-beta transformation kinetics in San Carlos olivine. *Science (80-)*. **281**, 85–87 (1998).
81. G. Hirth, D. L. Kohlstedt, Water in the oceanic upper mantle: implications for rheology, melt extraction and the evolution of the lithosphere. *Earth Planet. Sci. Lett.* **144**, 93–108 (1996).
82. M. Murakami, K. Hirose, H. Yurimoto, S. Nakashima, N. Takafuji, Water in Earth's lower mantle. *Science (80-)*. **295**, 1885–1887 (2002).
83. A. H. Peslier, M. Schönbächler, H. Busemann, S. I. Karato, Water in the Earth's Interior:

- Distribution and Origin. *Space Sci. Rev.* **212**, 1–68 (2017).
84. E. Ohtani, Hydrous minerals and the storage of water in the deep mantle. *Chem. Geol.* **418**, 6–15 (2015).
85. E. Ohtani, L. Yuan, I. Ohira, A. Shatskiy, K. Litasov, Fate of water transported into the deep mantle by slab subduction. *J. Asian Earth Sci.* (2018), doi:10.1016/j.jseae.2018.04.024.
86. L. Yuan, E. Ohtani, D. Ikuta, S. Kamada, J. Tsuchiya, H. Naohisa, Y. Ohishi, A. Suzuki, Chemical reactions between Fe and H₂O up to megabar pressures and implications for water storage in the Earth's mantle and core. *Geophys. Res. Lett.* **45**, 1330–1338 (2018).
87. J. Liu, Q. Hu, D. Young Kim, Z. Wu, W. Wang, Y. Xiao, P. Chow, Y. Meng, V. B. Prakapenka, H. K. Mao, W. L. Mao, Hydrogen-bearing iron peroxide and the origin of ultralow-velocity zones. *Nature.* **551**, 494–497 (2017).
88. W.-K. Li, G.-D. Zhou, T. C. W. Mak, *Advanced structural inorganic chemistry* (Oxford University Press, 2008), vol. 10.
89. J. Haines, J. M. Leger, M. W. Schmidt, J. P. Petit, a S. Pereira, J. a H. Da Jornada, S. Hull, Structural characterisation of the pa3-type, high pressure phase of ruthenium dioxide. *J. Phys. Chem. Solids.* **59**, 239–243 (1998).
90. Y. Shirako, X. Wang, Y. Tsujimoto, K. Tanaka, Y. Guo, Y. Matsushita, Y. Nemoto, Y. Katsuya, Y. Shi, D. Mori, H. Kojitani, K. Yamaura, Y. Inaguma, M. Akaogi, Synthesis, crystal structure, and electronic properties of high- pressure PdF₂ - Type Oxides MO₂ (M = Ru, Rh, Os, Ir, Pt). *Inorg. Chem.* **2**, 11616–11625 (2014).
91. S. S. Streltsov, A. O. Shorikov, S. L. Skornyakov, A. I. Poteryaev, D. I. Khomskii, *Sci. Rep.*, in press, doi:10.1038/s41598-017-13312-4.
92. A. T. Garcia-Sosa, M. Castro, Density functional study of FeO₂, FeO₂⁺, and FeO₂⁻. *Int. J. Quantum Chem.* **80**, 307–319 (2000).
93. B. G. Jang, J. Liu, Q. Hu, K. Haule, H. K. Mao, W. L. Mao, D. Y. Kim, J. H. Shim, Electronic spin transition in FeO₂: Evidence for Fe(II) with peroxide O₂²⁻. *Phys. Rev. B.* **100**, 17–19 (2019).
94. S. V. Ovsyannikov, V. V. Shchennikov, M. A. Shvetsova, L. S. Dubrovinsky, A. Polian, Tuning of the stoichiometry of Fe_{1-x}O wüstite by compression. *Phys. Rev. B - Condens. Matter Mater. Phys.* **81**, 11–14 (2010).
95. E. Boulard, M. Harmand, F. Guyot, G. Lelong, G. Morard, D. Cabaret, S. Boccato, A. D. Rosa, R. Briggs, S. Pascarelli, G. Fiquet, Ferrous iron under oxygen-rich conditions in the deep mantle. *Geophys. Res. Lett.* **46**, 1348–1356 (2019).
96. E. Bykova, G. Aprilis, M. Bykov, K. Glazyrin, M. Wendt, S. Wenz, A. Ehnes, N. Dubrovinskaia,

- Single-crystal diffractometer coupled with double-sided laser heating system at the Extreme Conditions Beamline P02.2 at PETRA III. **073907** (2019), doi:10.1063/1.5108881.
97. N. Dubrovinskaia, L. Dubrovinsky, N. A. Solopova, A. Abakumov, S. Turner, M. Hanfland, E. Bykova, M. Bykov, C. Prescher, V. B. Prakapenka, S. Petitgirard, I. Chuvashova, B. Gasharova, Y. L. Mathis, P. Ershov, I. Snigireva, A. Snigirev, Terapascal static pressure generation with ultrahigh yield strength nanodiamond. *Sci. Adv.* **2** (2016), doi:10.1126/sciadv.1600341.
 98. W. A. Bassett, Diamond anvil cell, 50th birthday. *High Press. Res.* **29**, 163–186 (2009).
 99. L. Merrill, W. A. Bassett, Miniature diamond anvil pressure cell for single crystal x-ray diffraction studies. *Rev. Sci. Instrum.* **45**, 290 (1974).
 100. I. Kantor, V. Prakapenka, A. Kantor, P. Dera, A. Kurnosov, S. Sinogeikin, N. Dubrovinskaia, L. Dubrovinsky, BX90: A new diamond anvil cell design for X-ray diffraction and optical measurements. *Rev. Sci. Instrum.* **83**, 125102 (2012).
 101. H. K. Mao, P. M. Bell, Design and varieties of the megabar cell. *Carnegie Inst. Washingt. Yearb.* **77**, 904–908 (1978).
 102. R. Letoullec, J. P. Pinceaux, P. Loubeyre, The membrane diamond anvil cell: a new device for generating continuous pressure and temperature variations. *High Press. Res.* **1**, 77–90 (1988).
 103. R. Miletich, D. R. Allan, W. F. Kuhs, in *High-temperature and high-pressure crystal chemistry*, R. M. Hazen, R. T. Downs, Eds. (The Mineralogical Society of America, Washington, DC, 2001), pp. 445–520.
 104. C. Prescher, L. Dubrovinsky, E. Bykova, I. Kuppenko, K. Glazyrin, K. Anastasia, N. Miyajima, C. McCammon, M. Mookherjee, V. Prakapenka, V. Cerantola, Y. Nakajima, N. Dubrovinskaia, R. Rüffer, A. Chumakov, M. Hanfland, Carbon in the Earth's core accounts for its high Poisson's ratio. *Submitt. to Nat. Geosie.* (2014).
 105. A. Kurnosov, I. Kantor, T. Boffa-Ballaran, S. Lindhardt, L. Dubrovinsky, A. Kuznetsov, B. H. Zehnder, A novel gas-loading system for mechanically closing of various types of diamond anvil cells. *Rev. Sci. Instrum.* **79**, 045110 (2008).
 106. H. K. Mao, J. Xu, P. M. Bell, Calibration of the ruby pressure gauge to 800 kbar under quasi-hydrostatic conditions. *J. Geophys. Res.* **91**, 4673–4676 (1986).
 107. A. D. Chijioke, W. J. Nellis, a. Soldatov, I. F. Silvera, The ruby pressure standard to 150 GPa. *J. Appl. Phys.* **98**, 114905 (2005).
 108. N. J. Hess, D. Schiferl, Pressure and temperature dependence of laser-induced fluorescence of Sm:YAG to 100 kbar and 700 °C and an empirical model. *J. Appl. Phys.* **68**,

- 1953–1961 (1990).
109. Y. Akahama, H. Kawamura, Pressure calibration of diamond anvil Raman gauge to 410 GPa. *J. Phys. Conf. Ser.* **215** (2010), doi:10.1088/1742-6596/215/1/012195.
110. S. M. Dorfman, V. B. Prakapenka, Y. Meng, T. S. Duffy, Intercomparison of pressure standards (Au, Pt, Mo, MgO, NaCl and Ne) to 2.5 Mbar. *J. Geophys. Res.* **117**, B08210 (2012).
111. Y. Fei, A. Ricolleau, M. Frank, K. Mibe, G. Shen, V. Prakapenka, Toward an internally consistent pressure scale. *Proc. Natl. Acad. Sci. U. S. A.* **104**, 9182–9186 (2007).
112. A. Dewaele, M. Torrent, P. Loubeyre, M. Mezouar, Compression curves of transition metals in the Mbar range: Experiments and projector augmented-wave calculations. *Phys. Rev. B.* **78**, 104102 (2008).
113. A. Dewaele, A. B. Belonoshko, G. Garbarino, F. Occelli, P. Bouvier, M. Hanfland, M. Mezouar, High-pressure–high-temperature equation of state of KCl and KBr. *Phys. Rev. B.* **85**, 214105 (2012).
114. M. Mezouar, R. Giampaoli, G. Garbarino, I. Kantor, A. Dewaele, G. Weck, S. Boccato, V. Svitlyk, A. D. Rosa, R. Torchio, O. Mathon, O. Hignette, S. Bauchau, Methodology for in situ synchrotron X-ray studies in the laser-heated diamond anvil cell. *High Press. Res.* **37**, 170–180 (2017).
115. R. Giampaoli, I. Kantor, M. Mezouar, S. Boccato, A. D. Rosa, R. Torchio, G. Garbarino, O. Mathon, S. Pascarelli, Measurement of temperature in the laser heated diamond anvil cell: comparison between reflective and refractive optics. *High Press. Res.* **38**, 250–269 (2018).
116. I. Kuppenko, L. Dubrovinsky, N. Dubrovinskaia, C. McCammon, K. Glazyrin, E. Bykova, T. Boffa Ballaran, R. Sinmyo, A. I. Chumakov, V. Potapkin, I. Kantor, R. Rüffer, M. Hanfland, W. Crichton, M. Merlini, Portable double-sided laser-heating system for Mössbauer spectroscopy and X-ray diffraction experiments at synchrotron facilities with diamond anvil cells. *Rev. Sci. Instrum.* **83**, 124501 (2012).
117. R. Boehler, H. G. Musshoff, R. Ditz, G. Aquilanti, a Trapananti, Portable laser-heating stand for synchrotron applications. *Rev. Sci. Instrum.* **80**, 045103 (2009).
118. T. Fedotenko, L. Dubrovinsky, G. Aprilis, E. Koemets, A. Snigirev, I. Snigireva, A. Barannikov, P. Ershov, F. Cova, M. Hanfland, N. Dubrovinskaia, Laser heating setup for diamond anvil cells for in situ synchrotron and in house high and ultra-high pressure studies. *Rev. Sci. Instrum.* **90**, 104501 (2019).
119. G. Aprilis, C. Strohm, I. Kuppenko, S. Linhardt, A. Laskin, D. M. Vasiukov, V. Cerantola, E. G. Koemets, C. McCammon, A. Kurnosov, A. I. Chumakov, R. Rüffer, N. Dubrovinskaia, L.

- Dubrovinsky, Portable double-sided pulsed laser heating system for time-resolved geoscience and materials science applications. *Rev. Sci. Instrum.* **88** (2017), doi:10.1063/1.4998985.
120. G. Hildebrandt, The discovery of the diffraction of X-rays in crystals — a historical review. *Cryst. Res. Technol.* **28**, 747–766 (1993).
121. G. S. Girolami, *X-ray Crystallography* (University Science Books, 2016).
122. C. Stan, C. Beavers, M. Kunz, N. Tamura, X-Ray diffraction under extreme conditions at the Advanced Light Source. *Quantum Beam Sci.* **2**, 4 (2018).
123. I.-E. Benrabah, H. P. Van Landeghem, F. Bonnet, F. Robaut, A. Deschamps, Use of space-resolved in-situ high energy X-ray diffraction for the characterization of the compositional dependence of the austenite-to-ferrite transformation kinetics in steels. *Quantum Beam Sci.* **4**, 1 (2019).
124. X. Ou, J. Li, F. Zheng, P. Wu, Q. Pan, X. Xiong, C. Yang, M. Liu, In situ X-ray diffraction characterization of NiSe₂ as a promising anode material for sodium ion batteries. *J. Power Sources.* **343**, 483–491 (2017).
125. V. Petříček, M. Dušek, L. Palatinus, Crystallographic computing system JANA2006: General features. *Zeitschrift für Krist.* **229**, 345–352 (2014).
126. G. M. Sheldrick, SHELXT - Integrated space-group and crystal-structure determination. *Acta Crystallogr. Sect. A Found. Crystallogr.* **71**, 3–8 (2015).
127. J. S. Smith, G. Shen, Multimode scanning X-ray diffraction microscopy for diamond anvil cell experiments. *Rev. Sci. Instrum.* **025109** (2019), doi:10.1063/1.5057518.
128. V. B. Prakapenka, A. Kubo, A. Kuznetsov, A. Laskin, O. Shkurikhin, P. Dera, M. L. Rivers, S. R. Sutton, Advanced flat top laser heating system for high pressure research at GSECARS: application to the melting behavior of germanium. *High Press. Res.* **28**, 225–235 (2008).
129. I. Kantor, C. Marini, O. Mathon, S. Pascarelli, A laser heating facility for energy-dispersive X-ray absorption spectroscopy. *Rev. Sci. Instrum.* **89**, 013111 (2018).
130. I. Kuppenko, thesis, Universität Bayreuth (2014).
131. Y. Ohishi, N. Hirao, N. Sata, K. Hirose, M. Takata, Highly intense monochromatic X-ray diffraction facility for high-pressure research at SPring-8. *High Press. Res.* **28**, 163–173 (2008).
132. O. D. Rigaku, CrysAlisPro Software System, Version 1.171. 38.41 I, Rigaku Cooperation (2015).

133. G. M. Sheldrick, Crystal structure refinement with SHELXL. *Acta Crystallogr. Sect. C Struct. Chem.* **71**, 3–8 (2015).
134. L. J. Barbour, XSEED: A graphical interface for use with the SHELX97 program suite. *J. Supramol. Chem.* **1**, 189 (2001).
135. E. Bykova, Single-crystal X-ray diffraction at extreme conditions in mineral physics and material sciences. *Thesis. Bayreuther Graduiertenschule für Math. und Naturwissenschaften.*, 282 (2015).
136. L. J. Barbour, X-Seed - A software tool for supramolecular crystallography. *J. Supramol. Chem.* **1**, 189–191 (2001).
137. M. Marszalek, *Mössbauer spectroscopy: basic principles and practical guide to exotic Mössbauer isotopes* (2017), vol. 2.
138. N. N. Greenwood, *Mössbauer spectroscopy* (Springer Science & Business Media, 2012).
139. P. Gütllich, Mössbauer Spectroscopy – Principles and Applications (Lecture) (2005) (available at http://www.ak-guetlich.chemie.uni-mainz.de/Dateien/Moessbauer_Lectures.pdf).
140. C. A. McCammon, Insights into phase transformations from Mössbauer spectroscopy. *Transform. Process. Miner.* **39**, 241–264 (2019).
141. V. Potapkin, A. I. Chumakov, G. V. Smirnov, J. P. Celse, R. Rüffer, C. McCammon, L. Dubrovinsky, The ^{57}Fe synchrotron Mössbauer source at the ESRF. *J. Synchrotron Radiat.* **19**, 559–569 (2012).
142. M. Kotrbová, S. Kadečková, J. Novák, J. Brádlér, G. V. Smirnov, Y. V. Shvydko, Growth and perfection of flux grown FeBO_3 and $^{57}\text{FeBO}_3$ crystals. *J. Cryst. Growth.* **71**, 607–614 (1985).
143. M. Newville, Fundamentals of XAFS. *Rev. Mineral. Geochemistry.* **78**, 33–74 (2014).
144. J. Rothe, A. Léon, X-ray Absorption Fine Structure (XAFS) Spectroscopy. *Hydrog. Technol.*, 603–622 (2008).
145. M. Munoz, S. Pascarelli, G. Aquilanti, O. Narygina, A. Kurnosov, L. Dubrovinsky, Hyperspectral-XANES mapping in the diamond-anvil cell: analytical procedure applied to the decomposition of (Mg,Fe)-ringwoodite at the upper/lower mantle boundary. *High Press. Res.* **28**, 665–673 (2008).
146. A. Mottana, A. Marcelli, The historical development of X-ray Absorption Fine Spectroscopy and of its applications to materials science. *Hist. Mech. Mach. Sci.* **27**, 275–301 (2015).
147. S. Pascarelli, O. Mathon, M. Munõz, T. Mairs, J. Susini, Energy-dispersive absorption

- spectroscopy for hard-X-ray micro-XAS applications. *J. Synchrotron Radiat.* **13** (2006), pp. 351–358.
148. M. M. Hirschmann, Water, melting, and the deep Earth H₂O cycle. *Annu. Rev. Earth Planet. Sci.* **34**, 629–653 (2006).
149. T. Katsura, A. Yoneda, D. Yamazaki, Adiabatic temperature profile in the mantle. **183**, 212–218 (2010).
150. D. E. Canfield, *Oxygen: a four billion year history* (Princeton Uni Press, 2014), vol. 51.
151. U. Söderlund, K. R. Chamberlain, W. Bleeker, A. Bekker, E. R. Larsson, M. O. de Kock, A. P. Gumsley, Timing and tempo of the Great Oxidation Event. *Proc. Natl. Acad. Sci.* **114**, 1811–1816 (2017).
152. S. S. Lobanov, Q. Zhu, N. Holtgrewe, C. Prescher, V. B. Prakapenka, A. R. Oganov, A. F. Goncharov, Stable magnesium peroxide at high pressure. *Sci. Rep.* **5**, 1–8 (2015).
153. D.-H. Seo, J. Lee, A. Urban, R. Malik, S. Kang, G. Ceder, The structural and chemical origin of the oxygen redox activity in layered and cation-disordered Li-excess cathode materials. *Nat. Chem.* **8**, 692–7 (2016).
154. C. Lu, M. Amsler, C. Chen, Unraveling the structure and bonding evolution of the newly discovered iron oxide FeO₂. *Phys. Rev. B.* **98**, 1–7 (2018).
155. Q. Hu, D. Y. Kim, W. Yang, L. Yang, Y. Meng, L. Zhang, H. K. Mao, FeO₂ and FeOOH under deep lower-mantle conditions and Earth's oxygen-hydrogen cycles. *Nature.* **534**, 241–244 (2016).
156. P. Gütlich, E. Bill, A. X. Trautwein, Mössbauer spectroscopy and transition metal chemistry. *Clim. Chang. 2013 - Phys. Sci. Basis.* **53** (2011), pp. 1–30.
157. D. M. Vasiukov, L. Dubrovinsky, I. Kupenko, V. Cerantola, G. Aprilis, L. Ismailova, E. Bykova, C. McCammon, C. Prescher, A. I. Chumakov, N. Dubrovinskaia, Pressure-induced spin pairing transition of Fe³⁺ in oxygen octahedra, 1–41 (2017).
158. Y. Fei, A. Ricolleau, M. Frank, K. Mibe, G. Shen, V. Prakapenka, High-Pressure Geoscience Special Feature: Toward an internally consistent pressure scale. *Proc. Natl. Acad. Sci.* **104**, 9182–9186 (2007).
159. H. P. Liermann, Z. Konôpková, W. Morgenroth, K. Glazyrin, J. Bednarčík, E. E. McBride, S. Petitgirard, J. T. Delitz, M. Wendt, Y. Bican, A. Ehnes, I. Schwark, A. Rothkirch, M. Tischer, J. Heuer, H. Schulte-Schrepping, T. Kracht, H. Franz, The extreme conditions beamline P02.2 and the extreme conditions science infrastructure at PETRA III. *J. Synchrotron Radiat.* **22**, 908–924 (2015).

160. G. M. Sheldrick, Crystal structure refinement with SHELXL. *Acta Crystallogr. Sect. C Struct. Chem.* **71**, 3–8 (2015).
161. K. Momma, F. Izumi, VESTA 3 for three-dimensional visualization of crystal, volumetric and morphology data. *J. Appl. Crystallogr.* **44**, 1272–1276 (2011).
162. J. Hölsä, E. Säilynoja, K. Koski, H. Rahiala, J. Valkonen, X-ray powder diffraction study of the stability of solid solutions in $(\text{La}_{1-x}\text{Gd}_x)\text{OCl}$. *Powder Diffr.* **11**, 129–133 (1996).
163. G. K. Rozenberg, M. P. Pasternak, P. Gorodetsky, W. M. Xu, L. S. Dubrovinsky, T. Le Bihan, R. D. Taylor, Pressure-induced structural, electronic, and magnetic phase transitions in FeCl_2 studied by x-ray diffraction and resistivity measurements. *Phys. Rev. B - Condens. Matter Mater. Phys.* **79**, 1–7 (2009).
164. M. Bykov, Structural aspects of pressure- and temperature-induced phase transitions in low-dimensional systems, 179 (2015).
165. C. Prescher, C. McCammon, L. Dubrovinsky, MossA: A program for analyzing energy-domain Mössbauer spectra from conventional and synchrotron sources. *J. Appl. Crystallogr.* **45**, 329–331 (2012).
166. A. J. Schultz, R. L. Carlin, Single-crystal pulsed neutron diffraction structure of the antiferromagnet $\text{K}_2[\text{FeCl}_5(\text{H}_2\text{O})]$ with and without applied pressure. *Acta Crystallogr. Sect. B.* **51**, 43–47 (1995).
167. T. Katsura, A. Yoneda, D. Yamazaki, T. Yoshino, E. Ito, D. Suetsugu, C. Bina, T. Inoue, D. Wiens, M. Jellinek, Adiabatic temperature profile in the mantle. *Phys. Earth Planet. Inter.* **183**, 212–218 (2010).
168. M. A. Eberle, O. Grasset, C. Sotin, A numerical study of the interaction between the mantle wedge, subducting slab, and overriding plate. *Phys. Earth Planet. Inter.* **134**, 191–202 (2002).
169. N. P. Butterworth, A. S. Talsma, R. D. Müller, M. Seton, H. P. Bunge, B. S. A. Schuberth, G. E. Shephard, C. Heine, Geological, tomographic, kinematic and geodynamic constraints on the dynamics of sinking slabs. *J. Geodyn.* **73**, 1–13 (2014).
170. M. L. Foo, T. He, Q. Huang, H. W. Zandbergen, T. Siegrist, G. Lawes, A. P. Ramirez, R. J. Cava, Synthesis and characterization of the pseudo-hexagonal hollandites $\text{ALi}_2\text{Ru}_6\text{O}_{12}$ ($A=\text{Na}, \text{K}$). *J. Solid State Chem.* **179**, 941–948 (2006).
171. A. E. Gleason, C. E. Quiroga, A. Suzuki, R. Pentcheva, W. L. Mao, Symmetrization driven spin transition in $\epsilon\text{-FeOOH}$ at high pressure. *Earth Planet. Sci. Lett.* **379**, 49–55 (2013).
172. W. Xu, E. Greenberg, G. K. Rozenberg, M. P. Pasternak, E. Bykova, T. Boffa-Ballaran, L. Dubrovinsky, V. Prakapenka, M. Hanfland, O. Y. Vekilova, S. I. Simak, I. A. Abrikosov,

- Pressure-induced hydrogen bond symmetrization in iron oxyhydroxide. *Phys. Rev. Lett.* **111**, 1–5 (2013).
173. R. A. Fischer, A. J. Campbell, G. A. Shofner, O. T. Lord, P. Dera, V. B. Prakapenka, Equation of state and phase diagram of FeO. *Earth Planet. Sci. Lett.* **304**, 496–502 (2011).
174. E. Greenberg, W. M. Xu, M. Nikolaevsky, E. Bykova, G. Garbarino, K. Glazyrin, D. G. Merkel, L. Dubrovinsky, M. P. Pasternak, G. K. Rozenberg, High-pressure magnetic, electronic, and structural properties of MFe_2O_4 ($M = Mg, Zn, Fe$) ferric spinels. **195150**, 1–13 (2017).
175. D. P. Dobson, J. P. Brodholt, Subducted banded iron formations as a source of ultra-low velocity zones at the core-mantle boundary. *Nature*. **434**, 371–374 (2005).
176. D. V. Bekaert, M. W. Broadley, F. Delarue, G. Avice, F. Robert, B. Marty, Archean kerogen as a new tracer of atmospheric evolution: implications for dating the widespread nature of early life. *Sci. Adv.* **4**, 1–9 (2018).
177. G. Avice, B. Marty, R. Burgess, A. Hofmann, P. Philippot, K. Zahnle, D. Zakharov, Evolution of atmospheric xenon and other noble gases inferred from Archean to Paleoproterozoic rocks. *Geochim. Cosmochim. Acta.* **232**, 82–100 (2018).
178. G. Avice, B. Marty, R. Burgess, The origin and degassing history of the Earth’s atmosphere revealed by Archean xenon. *Nat. Commun.* **8**, 1–9 (2017).
179. D. E. Canfield, The early history of atmospheric oxygen: Homage to Robert M. Garrels. *Annu. Rev. Earth Planet. Sci.* **33**, 1–36 (2005).
180. T. W. Lyons, C. T. Reinhard, N. J. Planavsky, The rise of oxygen in Earth’s early ocean and atmosphere. *Nature*. **506**, 307–315 (2014).
181. D. W. Waples, J. S. Waples, A review and evaluation of specific heat capacities of rocks, minerals, and subsurface fluids. Part 2: Fluids and porous rocks. *Nat. Resour. Res.* **13**, 123–130 (2004).
182. A. O. Shorikov, S. V. Streltsov, Equation of state of FeO_2 . *J. Magn. Magn. Mater.* (2017), doi:10.1016/j.jmmm.2017.10.061.
183. N. Ishimatsu, K. Matsumoto, H. Maruyama, N. Kawamura, M. Mizumaki, H. Sumiya, T. Irifune, Glitch-free X-ray absorption spectrum under high pressure obtained using nanopolycrystalline diamond anvils. *J. Synchrotron Radiat.* **19**, 768–772 (2012).
184. L. Ismailova, E. Bykova, M. Bykov, V. Cerantola, C. Mccammon, T. B. Ballaran, A. Bobrov, R. Sinmyo, N. Dubrovinskaia, K. Glazyrin, H. Liermann, I. Kuppenko, M. Hanfland, C. Prescher, V. Prakapenka, V. Svitlyk, L. Dubrovinsky, Stability of Fe,Al-bearing bridgmanite in the lower mantle and synthesis of pure Fe-bridgmanite. *Sci. Adv.* **2**, 1–8 (2016).

185. R. Sinmyo, K. Hirose, Iron partitioning in pyrolitic lower mantle. *Phys. Chem. Miner.* **40**, 107–113 (2013).
186. H. Piet, J. Badro, F. Nabiei, T. Dennenwaldt, S.-H. Shim, M. Cantoni, C. Hébert, P. Gillet, Spin and valence dependence of iron partitioning in Earth's deep mantle. *Proc. Natl. Acad. Sci.* **113**, 11127–11130 (2016).
187. C. Prescher, F. Langenhorst, L. S. Dubrovinsky, V. B. Prakapenka, N. Miyajima, The effect of Fe spin crossovers on its partitioning behavior and oxidation state in a pyrolitic Earth's lower mantle system. *Earth Planet. Sci. Lett.* **399**, 86–91 (2014).
188. K. Catalli, S. H. Shim, V. Prakapenka, Thickness and Clapeyron slope of the post-perovskite boundary. *Nature.* **462**, 782–785 (2009).
189. A. M. Dziewonski, V. Lekic, B. A. Romanowicz, Mantle anchor structure: an argument for bottom up tectonics. *Earth Planet. Sci. Lett.* **299**, 69–79 (2010).
190. J. Trampert, F. Deschamps, J. Resovsky, D. Yuen, Probabilistic tomography maps chemical heterogeneities throughout the lower mantle. *Science (80-.).* **306**, 853–856 (2004).
191. C. Ballhaus, R. F. Berry, D. H. Green, Oxygen fugacity controls in the Earth's upper mantle. *Nature.* **348**, 437 (1990).
192. M. Merlini, M. Hanfland, Single-crystal diffraction at megabar conditions by synchrotron radiation. *High Press. Res.* **33**, 511–522 (2013).
193. C. Prescher, V. B. Prakapenka, DIOPTAS: A program for reduction of two-dimensional X-ray diffraction data and data exploration. *High Press. Res.* **35**, 223–230 (2015).
194. A. Georges, G. Kotliar, W. Krauth, M. Rozenberg, Dynamical mean-field theory of strongly correlated fermion systems and the limit of infinite dimensions. *Rev. Mod. Phys.* **68**, 13–125 (1996).
195. L. V. Pourovskii, B. Amadon, S. Biermann, A. Georges, Self-consistency over the charge density in dynamical mean-field theory: a linear muffin-tin implementation and some physical implications. *Phys. Rev. B - Condens. Matter Mater. Phys.* **76**, 1–15 (2007).
196. I. Leonov, V. I. Anisimov, D. Vollhardt, Metal-insulator transition and lattice instability of paramagnetic V₂O₃. *Phys. Rev. B - Condens. Matter Mater. Phys.* **91**, 1–5 (2015).
197. I. Leonov, L. Pourovskii, A. Georges, I. A. Abrikosov, Magnetic collapse and the behavior of transition metal oxides at high pressure. *Phys. Rev. B.* **94**, 1–6 (2016).
198. I. Leonov, S. L. Skornyakov, V. I. Anisimov, D. Vollhardt, Correlation-driven topological Fermi surface transition in FeSe. *Phys. Rev. Lett.* **115**, 1–6 (2015).

199. E. Greenberg, I. Leonov, S. Layek, Z. Konopkova, M. P. Pasternak, L. Dubrovinsky, R. Jeanloz, I. A. Abrikosov, G. K. Rozenberg, Pressure-induced site-selective Mott insulator-metal transition in Fe₂O₃. *Phys. Rev. X*, **8**, 31059 (2018).
200. G. Trimarchi, I. Leonov, N. Binggeli, D. Korotin, V. I. Anisimov, LDA+DMFT implemented with the pseudopotential plane-wave approach. *J. Phys. Condens. Matter*, **20** (2008), doi:10.1088/0953-8984/20/13/135227.
201. E. Gull, A. J. Millis, A. I. Lichtenstein, A. N. Rubtsov, M. Troyer, P. Werner, Continuous-time Monte Carlo methods for quantum impurity models. *Rev. Mod. Phys.* **83**, 349–404 (2011).
202. G. Kresse, J. Furthmüller, Efficiency of ab-initio total energy calculations for metals and semiconductors using a plane-wave basis set. *Comput. Mater. Sci.* **6**, 15–50 (1996).
203. D. Joubert, From ultrasoft pseudopotentials to the projector augmented-wave method. *Phys. Rev. B - Condens. Matter Mater. Phys.* **59**, 1758–1775 (1999).
204. G. Kresse, J. Furthmüller, Efficient iterative schemes for ab initio total-energy calculations using a plane-wave basis set. *Phys. Rev. B - Condens. Matter Mater. Phys.* **54**, 11169–11186 (1996).
205. J. Heyd, G. E. Scuseria, M. Ernzerhof, Hybrid functionals based on a screened Coulomb potential. *J. Chem. Phys.* **118**, 8207–8215 (2003).
206. C. T. Prewitt, R. T. Downs, Chapter 9 HIGH-PRESSURE CRYSTAL CHEMISTRY. *Rev. Mineral. Geochemistry*, **37**, 283–317 (1998).
207. G. Aprilis, I. Kantor, I. Kuppenko, V. Cerantola, A. Pakhomova, I. E. Collings, R. Torchio, T. Fedotenko, S. Chariton, M. Bykov, E. Bykova, E. Koemets, D. M. Vasiukov, C. McCammon, L. Dubrovinsky, N. Dubrovinskaia, Comparative study of the influence of pulsed and continuous wave laser heating on the mobilization of carbon and its chemical reaction with iron in a diamond anvil cell. *J. Appl. Phys.* **125** (2019), doi:10.1063/1.5067268.
208. M. I. Eremets, *High pressure experimental methods* (Oxford University Press, 1996).
209. R. Boehler, K. De Hantsetters, New anvil designs in diamond-cells. *High Press. Res.* **24**, 391–396 (2004).
210. R. Boehler, New diamond cell for single-crystal x-ray diffraction. *Rev. Sci. Instrum.* **77**, 115103 (2006).
211. N. Dubrovinskaia, L. Dubrovinsky, M. Hanfland, M. Hofmann, Diamond anvils with a spherical support designed for X-ray and neutron diffraction experiments in DAC. *High Press. Res.* **32**, 537–543 (2012).
212. K. Syassen, Ruby under pressure. *High Press. Res.* **28**, 75–126 (2008).

213. M. Born, E. Wolf Principles of optics. *Pergamon Press*. **6**, 36–111 (1980).
214. Y. Akahama, H. Kawamura, Pressure calibration of diamond anvil Raman gauge to 310 GPa
Advertisement : Pressure calibration of diamond anvil Raman gauge to 310 GPa. **043516**
(2006), doi:10.1063/1.2335683.
215. L. S. Dubrovinsky, S. K. Saxena, F. Tutti, S. Rekhi, T. LeBehan, In situ X-ray study of thermal expansion and phase transition of iron at multimegabar pressure. *Phys. Rev. Lett.* **84**, 1720–1723 (2000).

(Eidesstattliche) Versicherungen und Erklärungen

(§ 9 Satz 2 Nr. 3 PromO BayNAT)

Hiermit versichere ich eidesstattlich, dass ich die Arbeit selbstständig verfasst und keine anderen als die von mir angegebenen Quellen und Hilfsmittel benutzt habe (vgl. Art. 64 Abs. 1 Satz 6 BayHSchG).

(§ 9 Satz 2 Nr. 3 PromO BayNAT)

Hiermit erkläre ich, dass ich die Dissertation nicht bereits zur Erlangung eines akademischen Grades eingereicht habe und dass ich nicht bereits diese oder eine gleichartige Doktorprüfung endgültig nicht bestanden habe.

(§ 9 Satz 2 Nr. 4 PromO BayNAT)

Hiermit erkläre ich, dass ich Hilfe von gewerblichen Promotionsberatern bzw. -vermittlern oder ähnlichen Dienstleistern weder bisher in Anspruch genommen habe noch künftig in Anspruch nehmen werde.

(§ 9 Satz 2 Nr. 7 PromO BayNAT)

Hiermit erkläre ich mein Einverständnis, dass die elektronische Fassung meiner Dissertation unter Wahrung meiner Urheberrechte und des Datenschutzes einer gesonderten Überprüfung unterzogen werden kann.

(§ 9 Satz 2 Nr. 8 PromO BayNAT)

Hiermit erkläre ich mein Einverständnis, dass bei Verdacht wissenschaftlichen Fehlverhaltens Ermittlungen durch universitätsinterne Organe der wissenschaftlichen Selbstkontrolle stattfinden können.

.....
Ort, Datum, Unterschrift